



UNIVERSITÀ  
DEGLI STUDI  
FIRENZE  
DIPARTIMENTO  
DI INGEGNERIA  
INDUSTRIALE

UNIVERSITÀ DEGLI STUDI DI FIRENZE  
Scuola di Ingegneria

---

DOTTORATO DI RICERCA IN  
INGEGNERIA INDUSTRIALE  
CICLO XXIX

COORDINATORE Prof. Maurizio DE LUCIA

# Development and Validation of an Efficient TEHD Model of Tilting Pad Journal Bearings

*Settore scientifico disciplinare ING-IND/13*

**Dottorando**

Dott. Nocciolini Daniele

**Tutore**

Prof. Rindi Andrea

**Coordinatore**

Prof. De Lucia Maurizio

ANNI 2013/2016

*«La vita fa paura! Ci si abitui. Non esiste nessun rimedio miracoloso, dipende tutto da noi. Quindi metta i piedi a terra, esca da qui e cominci ad impegnarsi sul serio.*

*Perchè nella vita, le cose che contano, non si ottengono mai con facilità.»*

*Dr. Robert Kelso*

*Innanzitutto vorrei ringraziare la mia famiglia, perchè senza il loro sostegno non avrei mai raggiunto questo importante traguardo.*

*Un sentito ringraziamento va al Professor Andrea Rindi per avermi dato la possibilità di svolgere questo stimolante lavoro di ricerca, e all'Ingegnere Enrico Meli per la disponibilità dimostrata durante tutto il percorso di dottorato.*

*Un caloroso ringraziamento va senz'altro all'Ingegnere Roberto Conti che dal periodo di tesi magistrale ad oggi mi ha dato un importante sostegno sia ingegneristico che morale. Un enorme ringraziamento va all'amico, compagno di studi ed infine collega Ing. Amedeo Frilli senza cui sia il periodo di studi che il percorso di dottorato non sarebbero mai stati così proficui e sereni. Infine un grazie a tutte le persone che hanno contribuito a rendere piacevole la mia permanenza nel MDM Lab ed a tutti coloro che mi hanno accompagnato nel mio percorso universitario.*

*Un grande ringraziamento va a Luca, sempre presente in ogni mio momento di sconforto ma anche di gioia. The last but not the least, desidero ringraziare Alessia, che dal 2010 mi accompagna in questo stupendo percorso di vita, regalandomi ogni giorno serenità, risate ed amore.*

## **Abstract**

The constant increase of turbomachinery rotational speed has brought the design and the use of journal bearings to their very limits: tilting pad journal bearings (TPJBs) have been introduced for high-speed/high-load applications due to their intrinsic stability properties and can be used both in transient and steady-state operations obtaining superior performances. TPJBs operation involves different physical aspects, like the pads flexibility and the heat exchange between solids and fluids. An accurate analysis of the TPJBs behavior is essential for a successful design and operation of the system; however, it is necessary to reach a compromise between the accuracy of the results provided by the TPJB model and its computational cost.

The present thesis exposes the development of an innovative and efficient quasi-3D TPJB modeling approach that allows an accurate analysis of the interactions between the fluid dynamic and thermal phenomena with the elastic behaviour of the solid components (ThermoElastoHydroDynamic analysis); the majority of existing models describes these aspects separately but their complex interactions must be taken into account to obtain a more accurate characterization of the system.

The main objective of the proposed model is to provide accurate 3D results with low computational times; furthermore, it is characterized by a strong modularity, allowing for complex transient simulations of the complete plant and for the representation of different kinds of bearings.

In this thesis, the whole model has been developed and experimentally validated in collaboration with Nuovo Pignone General Electric S.p.a., which provided the required technical and experimental data.

# Contents

<b>1</b>	<b>Introduction</b>	<b>1</b>
1.1	State of the art . . . . .	3
1.1.1	Fluid dynamical modeling . . . . .	10
1.1.2	Rotor dynamical modeling . . . . .	14
1.1.3	ThermoElastoHydroDynamic modeling . . . . .	18
1.2	Goals of the thesis . . . . .	26
<b>2</b>	<b>Models architecture</b>	<b>27</b>
2.1	Step 1: Fluid dynamical aspects . . . . .	28
2.2	Step 2: Rotor dynamical aspects . . . . .	30
2.3	Step 3: ThermoElastoHydroDynamic aspects . . . . .	34
<b>3</b>	<b>Step 1: Fluid dynamical aspects</b>	<b>38</b>
3.1	Softwares . . . . .	39
3.2	Model structure . . . . .	41
3.3	Oil film modeling . . . . .	44

---

3.3.1	Lubrication theory . . . . .	44
3.3.2	Oil film sub-model . . . . .	51
3.4	Supply sump modeling . . . . .	62
3.4.1	Lumped parameters modeling approach . . . . .	62
3.4.2	Sump sub-model . . . . .	67
3.5	Pad sub-model . . . . .	70
3.6	Rotor modeling . . . . .	71
3.6.1	Rotordynamics . . . . .	71
3.6.2	Rotor fraction sub-model . . . . .	77
3.7	Numerical solvers . . . . .	79
3.7.1	ode15s . . . . .	79
3.7.2	BiCGStab . . . . .	81
<b>4</b>	<b>Step 2: Rotor dynamical aspects</b>	<b>84</b>
4.1	Software . . . . .	85
4.2	Model structure . . . . .	88
4.3	Rotor modeling . . . . .	91
4.3.1	Rotor FEM modeling . . . . .	91
4.3.2	Complete rotor dynamical model . . . . .	95
4.4	Numerical solvers . . . . .	100
4.4.1	Double Dogleg . . . . .	100
<b>5</b>	<b>Step 3: ThermoElastoHydroDynamic aspects</b>	<b>102</b>
5.1	Software . . . . .	103

---

5.2	Model structure . . . . .	105
5.3	Oil film modeling . . . . .	108
5.3.1	Thermal modeling . . . . .	108
5.4	Supply sump modeling . . . . .	112
5.4.1	Thermal modeling . . . . .	112
5.5	Pad modeling . . . . .	114
5.5.1	Pad FEM modeling . . . . .	114
5.5.2	Theory of the thermal modeling . . . . .	115
5.5.3	Thermal modeling . . . . .	128
5.5.4	Elastic modeling . . . . .	130
5.6	Rotor modeling . . . . .	136
5.6.1	Elastic modeling . . . . .	136
5.6.2	Thermal modeling . . . . .	138
5.7	Numerical solvers . . . . .	141
<b>6</b>	<b>Experimental data</b>	<b>144</b>
6.1	Test case 1: Fluid dynamical characteristics . . . . .	145
6.2	Test case 2: Rotor dynamical characteristics . . . . .	148
6.3	Test case 3: ThermoElastoHydroDynamic characteristics . . . . .	150
<b>7</b>	<b>Models numerical validation</b>	<b>157</b>
7.1	Step 1: Fluid dynamical characteristics . . . . .	158
7.1.1	Model performances . . . . .	163
7.2	Step 2: Rotor dynamical characteristics . . . . .	167

---

7.2.1	Model performances . . . . .	174
7.3	Step 3: ThermoElastoHydroDynamic characteristics . . . . .	178
7.3.1	Static results and preliminary validation . . . . .	179
7.3.2	Experimental validation of the oil film model . . . . .	181
7.3.3	Numerical results of the rotor and pad models . . . . .	185
7.3.4	Model performances . . . . .	189
<b>8</b>	<b>Conclusions and future developments</b>	<b>191</b>
<b>A</b>	<b>Publications</b>	<b>196</b>
	<b>Bibliography</b>	<b>204</b>



# List of Figures

1.1	Tilting pad journal bearing . . . . .	3
1.2	Oil whirl and oil whip . . . . .	4
1.3	TPJB components . . . . .	5
1.4	TPJB scheme . . . . .	6
1.5	Spherical pivot . . . . .	6
1.6	Pressure field and oil film thickness inside a TPJB oil film . . . . .	7
1.7	Bearing geometrical characteristics and preload . . . . .	7
1.8	Generic rotor orbit . . . . .	8
1.9	TPJB selection map based on geometrical and energetic parameters . . . . .	9
1.10	Lubricant supply system . . . . .	11
1.11	Michell bearing . . . . .	14
1.12	Bearing stiffness and damping coefficients . . . . .	16
1.13	Mass-spring-damper lumped parameters system . . . . .	16
1.14	Scheme of the bearing linearized model . . . . .	17
1.15	Orbit described by the rotor. . . . .	19

---

1.16	Bearing geometry with three pad studied by Chang [12]. . . . .	21
1.17	Two pads bearing studied by Hashimoto [15]. . . . .	22
1.18	Pad model with flexible pivot [19]. . . . .	24
2.1	Constructive drawing for the GEJB200M-05 bearing. All data are “owned and reserved” and obtained by permission of GE O&G Nuovo Pignone “GE ©2014 - All Rights Reserved” . . . . .	29
2.2	Conceptual map of the developed model . . . . .	30
2.3	Constructive drawing for the considered <i>Kingsbury</i> <sup>®</sup> bearing. All data are “owned and reserved” and obtained by permission of GE O&G Nuovo Pignone “GE ©2014 - All Rights Reserved” . . . . .	31
2.4	Rotor scheme. All data are “owned and reserved” and obtained by permission of GE O&G Nuovo Pignone “GE ©2014 - All Rights Reserved” . . . . .	32
2.5	Complete model scheme . . . . .	33
2.6	General architecture of the complete model. . . . .	35
2.7	Constructive drawing for the considered rotor of a centrifugal compressor. All data are “owned and reserved” and obtained by permission of GE O&G Nuovo Pignone “GE ©2014 - All Rights Reserved” . . . . .	37
3.1	Typical analyses with the <i>Thin Film Flow</i> interface . . . . .	39
3.2	<i>Thin Film Flow</i> model scheme . . . . .	40
3.3	Developed model . . . . .	41
3.4	Stribeck diagram . . . . .	45
3.5	Bi-dimensional motion of the fluid inside the oil film . . . . .	46
3.6	Physical system analyzed according to the Reynolds equation . . . . .	47

---

3.7	3D pad model with 2D oil film mesh . . . . .	51
3.8	Reference systems . . . . .	52
3.9	Rotor peripheral velocity . . . . .	53
3.10	Bearing preload and reference angles . . . . .	56
3.11	Oil film thickness . . . . .	57
3.12	Lubricant viscosity as a function of temperature . . . . .	58
3.13	Control volume . . . . .	59
3.14	Generic dynamic system . . . . .	62
3.15	Variables for lumped parameters modeling approach . . . . .	63
3.16	Control volume for the $n$ -th element . . . . .	64
3.17	Generic capacitive element . . . . .	64
3.18	Generic inertial element . . . . .	66
3.19	Generic resistive element . . . . .	67
3.20	Scheme of the sump interposed between two adjacent pads . . . . .	68
3.21	Calculation of pad moments of inertia . . . . .	70
3.22	Pressure and forces acting on the tilting pad . . . . .	71
3.23	Simple rotor scheme . . . . .	73
3.24	Campbell diagram . . . . .	74
3.25	Unbalance response . . . . .	74
3.26	Waterfall plot of the rotor forced response . . . . .	75
3.27	Rotor with 4 degrees of freedom . . . . .	75
3.28	Reference systems used for the analysis of a 4 DOFs rotor model . . . . .	76
3.29	Rotor fraction and forces acting on it . . . . .	77

---

3.30	Newton's method for the solution of nonlinear systems . . . . .	83
4.1	Cross section of the <i>BEAM</i> element . . . . .	86
4.2	Element local reference system . . . . .	86
4.3	Complete rotor dynamical model . . . . .	89
4.4	Typical FEM elements . . . . .	92
4.5	Scheme of the <i>BEAM</i> element . . . . .	94
4.6	Rotor discretization . . . . .	94
4.7	Bearing with five tilting pads and oil film mesh . . . . .	95
4.8	Example of a centrifugal impeller schematized as a Disk element . . . . .	96
4.9	Gyroscopic moments . . . . .	97
4.10	Unbalance loads . . . . .	98
4.11	Rotor supported by two bearings . . . . .	98
4.12	Double Dogleg method . . . . .	100
5.1	Modules available in the software <i>COMSOL Multiphysics</i> <sup>®</sup> 4.4. . . . .	104
5.2	Structure of the developed model. . . . .	106
5.3	Trend of the density-temperature relationship for a generic lubricant. . . . .	109
5.4	TPJB structure, lubricant supply plant and control volume. . . . .	111
5.5	Scheme of a <i>BRICK</i> element. . . . .	115
5.6	Heat exchange typologies. . . . .	116
5.7	Heat flux through a cylinder . . . . .	118
5.8	Energy balance of infinitesimal element $dV$ . . . . .	119
5.9	Schematization of the natural convection (a) and of the forced convection (b). . . . .	122

---

5.10	Transition between laminar and turbulent flow on a flat plate. . . . .	123
5.11	Convection on the flat plate. . . . .	125
5.12	Pads Surfaces concerned by the convective heat transfer with the lubricant. . . . .	128
5.13	Pads Surfaces subjected to heat exchange and adiabatic surfaces. . . . .	129
5.14	Reference system of the considered 3D solid. . . . .	132
5.15	Spherical pivot surfaces with zero displacement. . . . .	133
5.16	Rotor discretization with BEAM elements and rotor solid fractions. . . . .	136
5.17	Rotor and rotor fractions modeled by solid elements. . . . .	137
5.18	Part of the rotor fraction that exchanges heat with the fluid film by convection. . .	138
5.19	Parts of the rotor that exchange heat through conduction process. . . . .	139
5.20	Conceptual map of the realized model. . . . .	141
5.21	Modeling approach used by the <i>Segregated</i> solver. . . . .	142
6.1	Scheme of the experimental plant located in Massa-Carrara. All data are “owned and reserved” and obtained by permission of GE O&G Nuovo Pignone “GE ©2014 - All Rights Reserved” . . . . .	145
6.2	Experimental procedure concerning the 3BLC1005 centrifugal compressor. All data are “owned and reserved” and obtained by permission of GE O&G Nuovo Pignone “GE ©2014 - All Rights Reserved” . . . . .	148
6.3	Run up phase for the 3BLC1005 compressor. All data are “owned and reserved” and obtained by permission of GE O&G Nuovo Pignone “GE ©2014 - All Rights Reserved” . . . . .	149
6.4	Unbalance response for the 3BLC1005 compressor. All data are “owned and reserved” and obtained by permission of GE O&G Nuovo Pignone “GE ©2014 - All Rights Reserved” . . . . .	150

---

6.5	Test rig. . . . .	151
6.6	Simplified scheme of the experimental test rig. . . . .	153
6.7	Sensors and signal acquisition system. . . . .	154
6.8	Experimental procedure to evaluate the onset of the thermal instability. . . . .	155
7.1	Rotor fraction X and Y displacements. . . . .	158
7.2	Rotor fraction trajectory. . . . .	160
7.3	Pads tilt angles. . . . .	160
7.4	Sumps pressures. . . . .	161
7.5	Lubricant supply flow rate for the complete bearing. . . . .	162
7.6	Pressure field inside the oil films. . . . .	163
7.7	Velocity field inside the oil films. . . . .	164
7.8	Pads mean lines (for the pressure measurement). . . . .	164
7.9	Pressure level in the pads mean lines. . . . .	165
7.10	Oil film thickness in the pads mean lines. . . . .	166
7.11	Comparison between the experimental, theoretical and numerical flow rates (50°C). All data are “owned and reserved” and obtained by permission of GE O&G Nuovo Pignone “GE ©2014 - All Rights Reserved” . . . . .	167
7.12	Comparison between the experimental, theoretical and numerical flow rates (65°C). All data are “owned and reserved” and obtained by permission of GE O&G Nuovo Pignone “GE ©2014 - All Rights Reserved” . . . . .	168
7.13	Relative errors (50°C) . . . . .	169
7.14	Relative errors (65°C) . . . . .	169
7.15	Mesh for the CFD analysis of the considered bearing . . . . .	170

---

7.16	Unbalance load on the rotor end . . . . .	170
7.17	Dynamical characteristics of the considered bearings . . . . .	172
7.18	Rotor frequency response obtained with the complete model . . . . .	172
7.19	Vibration amplitude for the rotor drive-end . . . . .	173
7.20	Generic rotor deformation (transient simulation) . . . . .	173
7.21	Generic pressure field inside the oil films (transient simulation) . . . . .	173
7.22	Rotor displacements time history . . . . .	174
7.23	Rotor displacements time history (drive-end) . . . . .	175
7.24	Pads tilt angles time history . . . . .	175
7.25	Rotor orbit (drive-end bearing) . . . . .	176
7.26	Fourier transform of the rotor vibration (bearings locations) . . . . .	176
7.27	Fourier transform of the rotor vibration (rotor drive-end) . . . . .	177
7.28	Comparison between the static eccentricity of the bearing obtained with the proposed model and that obtained from the experimental tests. . . . .	179
7.29	Comparison between the numerical and experimental values of the temperature range shown in [33], and the results obtained by the proposed THD model and the TEHD model (4000 rpm and an applied load of 10 kN). . . . .	180
7.30	Comparison between the oil film thickness obtained with the third modeling step (TEHD) and with the previously developed model (HD), with a rotor rotational velocity equal to 8000 rpm and an applied load equal to half of the rotor mass (LOP configuration) together with an unbalance force. . . . .	182

- 7.31 Comparison between the pressure field obtained with the third modelling step (TEHD) and with the previously developed model (HD), with a rotor rotational velocity equal to 8000 rpm and an applied load equal to half of the rotor mass (LOP configuration) together with an unbalance force. . . . . 183
- 7.32 Comparison between the temperature field obtained with the third modelling step (TEHD) and with the previously developed model (THD), with a rotor rotational velocity equal to 8000 rpm and an applied load equal to half of the rotor mass (LOP configuration) together with an unbalance force. . . . . 184
- 7.33 3D representation of the temperature (a) and of the thermo-elastic deformation (b) fields of the Non-Drive End bearing pads with a rotor rotational velocity equal to 8000 rpm and an applied load equal to half of the rotor mass (LOP configuration) together with an unbalance force (TEHD modelling step). . . . . 186
- 7.34 Deformation field obtained with the TEHD model on the Non-Drive End bearing pads, with a rotor rotational velocity equal to 8000 rpm and an applied load equal to half of the rotor mass (LOP configuration) together with an unbalance force. . . . . 187
- 7.35 Bearing radial clearance variation obtained with the TEHD model for the NDE bearing, with a rotor rotational velocity equal to 8000 rpm and an applied load equal to half of the rotor mass (LOP configuration) together with an unbalance force. . . . . 188
- 7.36 3D representation of the temperature field in the rotor fraction enclosed in the Non-Drive End bearing (a), of the stresses and of the temperature gradient due to the bearing (b); with a rotor rotational velocity equal to 8000 rpm and an applied load equal to half of the rotor mass (LOP configuration) together with an unbalance force. . . . . 189



---

8.1 UNIFI test rig Layout . . . . . 195

# List of Tables

6.1	Experimental flow rates for the GEJB200M-05 bearing. All data are “owned and reserved” and obtained by permission of GE O&G Nuovo Pignone “GE ©2014 - All Rights Reserved” . . . . .	147
6.2	Main characteristics and operating conditions of the test rig and of its TPJBs.	152
6.3	Main characteristics of the lubricant ISO VG 46. . . . .	153
6.4	Rotor critical velocity for the considered configurations. . . . .	155
7.1	Parameters considered for the model of a single bearing . . . . .	159
7.2	Parameters used in the orifice lumped parameters formulas . . . . .	163
7.3	Numerical solvers tolerances and mesh features (Step 1) . . . . .	165
7.4	Characteristics of the computer used for the simulations . . . . .	166
7.5	Comparison between computational times (Step 1) . . . . .	166
7.6	Parameters considered for the complete model . . . . .	171
7.7	Numerical solvers tolerances and mesh features (Step 2) . . . . .	177
7.8	Comparison between computational times (Step 2) . . . . .	178
7.9	Machine features and calculation time. . . . .	190

# Nomenclature

Symbol	Description	Unit
$a$	Thermal diffusivity	$[m^2/s]$
$\mathbf{b}$	Constant terms of the linear system	
$c_b$	Bearing clearance	$[m]$
$c_p$	Specific heat	$[J/kg \cdot K]$
$c_p$	Pad clearance	$[m]$
$d$	Supply orifice diameter	$[m]$
$d_0$	BEAM element diameter	$[m]$
$e$	Specific enthalpy	$[J/kg]$
$f$	Frequency	$[Hz]$
$\mathbf{f}(t)$	Generalized loads	
$\mathbf{f}_b$	Loads acting on the <i>channel base</i>	$[N]$
$\mathbf{f}_w$	Loads acting on the <i>solid wall</i>	$[N]$
$g$	Gravity acceleration modulus	$[m/s^2]$
$h$	Oil film thickness	$[m]$
$h$	Time step amplitude	
$h$	Heat transfer coefficient	$[W/m^2 \cdot K]$

---

$h_0$	Bearing radial clearance	[ $m$ ]
$h_b$	Channel base height	[ $m$ ]
$h_w$	Solid wall height	[ $m$ ]
$i$	Imaginary unit	[ $-$ ]
$k$	BDF order	
$l$	Length	[ $m$ ]
$m$	Bearing preload	[ $-$ ]
$m_{rot}$	Rotor fraction mass	[ $kg$ ]
$m_k$	Double Dogleg functional	
$m_p$	Lumped mass	[ $kg$ ]
$m_{res}$	Unbalance mass	[ $kg$ ]
$\mathbf{n}$	Normalized normal vector	[ $-$ ]
$n_p$	Bearing pads number	[ $-$ ]
$p$	Pressure	[ $Pa$ ]
$p_a$	Environment pressure	[ $Pa$ ]
$p_f$	Oil film overpressure	[ $Pa$ ]
$p_{ref}$	Reference pressure for fluid properties	[ $Pa$ ]
$\mathbf{q}(t)$	Generalized displacements	
$r_d$	Disk element radius	[ $m$ ]
$r\varphi z$	Cylindrical coordinates in the rotor fraction reference system	
$r\beta z$	Cylindrical coordinates in the pad preloaded reference system	
$s$	Natural frequency	[ $Hz$ ]
$s$	Double Dogleg step	
$t$	Time	[ $s$ ]
$t_0$	Initial time for the integration	[ $s$ ]
$t_f$	Final time for the integration	[ $s$ ]
$t_{fin}$	Simulation time	[ $s$ ]
$\mathbf{u}$	Displacements	[ $m$ ]

---

<b>v</b>	Velocities	$[m/s]$
$\mathbf{v}_{av}$	Mean velocity in the oil film	$[m/s]$
$\mathbf{v}_M$	Peripheral velocity of the rotor	$[m/s]$
<b>x</b>	Linear system unknowns	
$xyz$	Fixed reference system	$[m]$
<b>A</b>	Area	$[m^2]$
<b>A</b>	Linear system matrix	
<b>B</b>	Shape functions derivatives matrix	
<b>C</b>	Damping matrix	$[N \cdot s/m]$
<b>D</b>	Elastic stiffness matrix	
$C_d$	Orifice flow coefficient	$[-]$
$C_f$	Fluid capacity	$[m^5/N]$
$CC$	Pad radial clearance	$[m]$
$E$	Young's modulus	$[N/mm^2]$
<b>E</b>	Material stiffness matrix	
$\dot{E}$	Thermal power	$[W]$
$E_K$	Kinetic energy	$[J]$
$E_P$	Potential energy	$[J]$
<b>F</b>	Force	$[N]$
$G$	Shear modulus	$[mm^2 \cdot rad/N]$
<b>G</b>	Gyroscopic matrix	$[N \cdot s/m]$
$Gr$	Grashof number	$[-]$
<b>H</b>	Structural damping matrix	$[N/m]$
$I$	Moment of inertia	$[m^4]$
$I_f$	Fluid inertia	$[kg/m^4]$
<b>J</b>	Jacobian matrix	
$J_p$	Polar moment of inertia	$[kg \cdot m^2]$
$J_t$	Transverse moment of inertia	$[kg \cdot m^2]$

---

$K$	Krylov subspace	
$\mathbf{K}$	Stiffness matrix	$[N/m]$
$L$	Bearing length	$[m]$
$\mathbf{L}$	Lower triangular matrix	
$L_u$	Bearing specific load	$[N/m^2]$
$M$	Molar mass	$[kg/mol]$
$\mathbf{M}$	Moment	$[N \cdot m]$
$\mathbf{M}$	Mass matrix	
$\mathbf{M}$	Preconditioning matrix	
$\mathbf{M}^A$	Point on the rotor surface	
$N$	Rotor spin speed	$[rpm]$
$\mathbf{N}$	Shape functions matrix	
$Nu$	Nusselt number	$[-]$
$\mathbf{P}$	Point on the pad surface	
$Pr$	Prandtl number	$[-]$
$Q$	Volumetric flow rate	$[m^3/s]$
$\dot{Q}$	Thermal power	$[W]$
$R$	Bearing radius	$[m]$
$R$	Ideal gas constant	$[J/kg \cdot K]$
$\mathbf{R}$	Rotation matrix	$[-]$
$R_f$	Fluid resistance	$[kg/m^4 \cdot s]$
$R_p$	Pad radius	$[m]$
$R_s$	Rotor fraction radius	$[m]$
$Re$	Reynolds number	$[-]$
$S$	Generic control volume surface	$[m^2]$
$So$	Sommerfeld number	$[-]$
$T$	Temperature	$[K]$
$T_{ref}$	Reference temperature for fluid properties	$[K]$

---

$U_s$	Rotor peripheral velocity modulus	$[m/s]$
$\mathbf{U}$	Upper triangular matrix	
$V$	Volume	$[m^3]$
$\dot{W}$	Mechanical power	$[W]$
$W_j$	Bearing load	$[N]$
$W_t$	Flexural modulus	$[m^3]$
$\mathbf{Y}$	Model state vector	

### Greek letters

$\alpha$	Unbalance phase	$[rad]$
$\alpha$	Pad pivot angular position	$[rad]$
$\alpha_T$	Thermal expansion tensor	
$\beta$	Compressibility modulus	$[Pa]$
$\gamma$	Pad tilt angle	$[rad]$
$\gamma_k$	NDF coefficient	
$\delta_{ij}$	Kronecker delta	$[-]$
$\epsilon$	Unbalance eccentricity	$[m]$
$\epsilon$	Strain tensor	$[-]$
$\eta$	Pivot offset	$[-]$
$\theta$	Angular coordinate for rotor rotation	$[rad]$
$\lambda_p$	Thermal conductivity	$[W/m \cdot K]$
$\mu$	Dynamic viscosity	$[Pa \cdot s]$
$\nu$	Poisson's coefficient	$[-]$
$\nu_s$	Specific volume	$[m^3/kg]$
$\xi\eta\zeta$	Reference system for the rigid body	
$\rho$	Density	$[kg/m^3]$
$\rho$	BiCGStab tolerance	

---

$\sigma$	Stress tensor	[MPa]
$\tau$	Viscous stress tensor	[MPa]
$\phi_{X'}$	Rotor pitch	[rad]
$\phi_Y$	Rotor yaw	[rad]
$\chi$	Pad pitch	[rad]
$\chi$	Rotor angular unbalance	[rad]
$\psi_{pad}$	Pad opening angle	[rad]
$\psi_{piv}$	Pivot angular offset	[rad]
$\omega$	Rotation speed	[rad/s]
$\Omega$	Spin speed	[rad/s]

---



# Introduction

The present thesis deals with the development of an innovative numerical model for the simulation of the ThermoElastoHydroDynamic (TEHD) behavior of a fluid dynamical tilting pad journal bearing (TPJB). This type of bearing is widely used in the turbomachinery field due to its important dynamical properties and so a TPJB model plays a fundamental role in the study of the phenomena involved in the operation of a turbomachine.

A tilting pad journal bearing, in order to perform its supporting function for the rotor, needs to be supplied with a flow of pressurized lubricant fluid; consequently the bearing must be included within the hydraulic fluid network that surrounds the machine, in order to be able to control and adjust the flow rates and pressure levels. The work exposed in this thesis stems from the need expressed by General Electric Oil & Gas to develop an advanced tool for the analysis of the hydraulic performance of the bearings; the proposed model can be used as an alternative to the classical simplified models to obtain predictions closer to the experimental results and to avoid the onset of dangerous situations during off-design operation of the machine.

In addition, to perform a complete and accurate analysis of the rotor-bearing system, the mechanical behavior of the system must be considered: the bearing, to adequately

support the rotor, is constrained to a supporting structure (base-plate) that as a first approximation can be considered rigid but actually is subjected to complex vibratory phenomena similarly to the rotor. The bearing is the element that links the motions and the modes of vibration of the moving parts and their fixed base.

The existing models for the study of TPJBs are for the most part simplified models based on the lumped parameters approach and can provide results in only one of the above mentioned areas. The objective of this work is therefore to develop a model that can provide reliable predictions on a complete analysis of the behavior of the bearing, so that it may be included in a global model including all the various elements present in a plant, while maintaining the calculation times within the limits imposed by the industry.

The bearings and rotors considered for the development of the models are currently used by General Electric Oil & Gas, which provided the technical data needed for the development phase and the experimental data necessary to validate the models.

## 1.1 State of the art

The continuous increase of the rotational speed typical in the turbomachinery field, with the aim to improve the machines aerodynamic performances, has brought the classical fixed geometry journal bearing to the limits of their operating range: the intrinsic problems in operating at high speed with fixed geometry bearings have led to the introduction of tilting pad journal bearings in order to achieve satisfactory performances even in very challenging operating regimes. The principal limit of fixed geometry journal

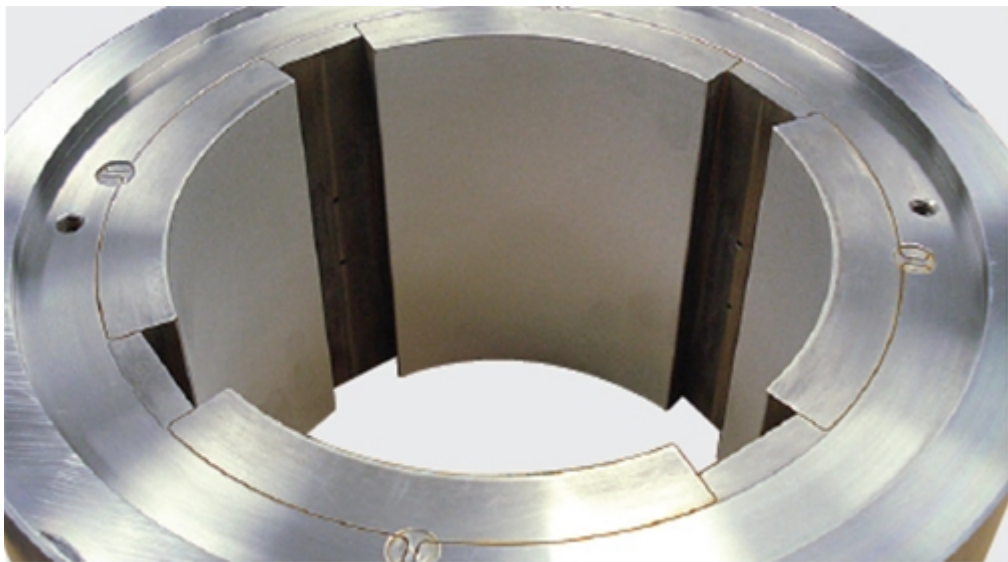


Figure 1.1: Tilting pad journal bearing

bearings is the onset of instability phenomena (*oil whip* and *oil whirl*) due to the coupling between the forces exerted by the bearing on the rotor in the  $x$  and  $y$  directions.

In particular, the *oil whirl* is a rotor vibration that occurs at a frequency equal to about half of the rotor spin speed and overlaps with other oscillatory motions, in particular the synchronous oscillations due to the rotor unbalance; the amplitude of these vibrations is reduced and generally does not constitute a problem. Increasing the speed of rotation to about twice the first rotor critical speed, the motion becomes more violent and can quickly degenerate into vibrations at frequency equal to the first natural frequency of

the rotor and independent of the rotational speed which often prove destructive for the machine; this motion is denominated *oil whip*.

A simplified interpretation of the phenomenon is based on the fact that the lubricant in the bearing circulates with a velocity equal to half the rotor peripheral velocity, generating a sort of rotating damping. In the region of the Campbell diagram below the line  $\omega = \Omega/2$  the system is unstable; if the lower branch of the diagram is a horizontal line, as in the simple case of the Jeffcott rotor, the threshold of instability corresponds to twice the first critical speed of the rotor. However, an accurate modeling of the phenomenon must

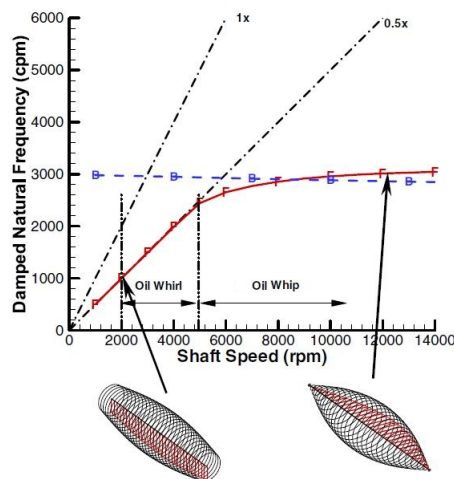


Figure 1.2: Oil whirl and oil whip

take into account the real stiffness of the bearings and their anisotropy (which makes important the distinction between forward and backward vibrations), as well as the behavior of the lubricant, considering so the different non-linear characteristics of the bearing [1].

Due to their intrinsic instability, fixed geometry journal bearings are difficult to use with supercritical rotational speed: tilting pad journal bearings completely solve this problem, despite a lower damping at low rotational speeds and a greater complexity. In numerical terms, the *oil whirl* and *oil whip* phenomena represent limits on the specific load which can

be applied to the bearing:

$$L_u = \frac{W_j}{2 \cdot L \cdot R}, \quad (1.1)$$

where  $W_j$  is the load applied to the bearing, due to the rotor weight,  $L$  and  $R$  are respectively the bearing length and radius; another limit concerns the rotor peripheral speed:

$$U_s = \left( \frac{\pi}{30} \right) \cdot (N \cdot R), \quad (1.2)$$

where  $N$  is the rotor spin speed (expressed in *rpm*). A tilting pad journal bearing is a particular fluid dynamical journal bearing where the surface delimiting the oil film is not a complete cylinder but is divided in a certain number of sectors capable, through appropriate constraints, of one or more rotations. The bearing geometry is no more fixed



Figure 1.3: TPJB components

and is able to follow the rotor motion and to adjust to the dynamic loads applied to the system. Tilting pad thrust bearings are also widely used; their characteristics are similar to those reported for the TPJBs.

The pad constraint, denominated *pivot*, can be a cylindrical or spherical hinge, leaving the pad respectively with one or two degrees of freedom (DOFs); typically the pivot is not located in the center of the pad: this makes the tilting pad bearing an unidirectional device, where a single direction of rotation for the rotor is possible, the one for which the pivot is placed in the second half of the pad.

The rotor motion generates on each pad an overpressure that has the qualitative trend



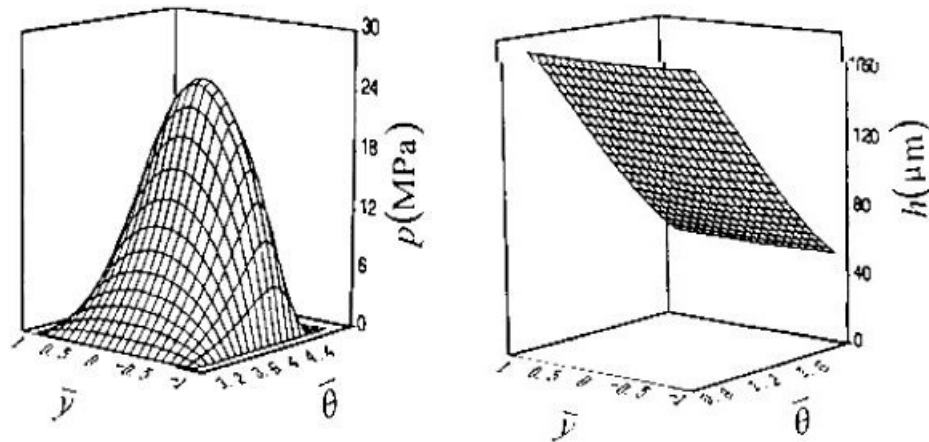


Figure 1.6: Pressure field and oil film thickness inside a TPJB oil film

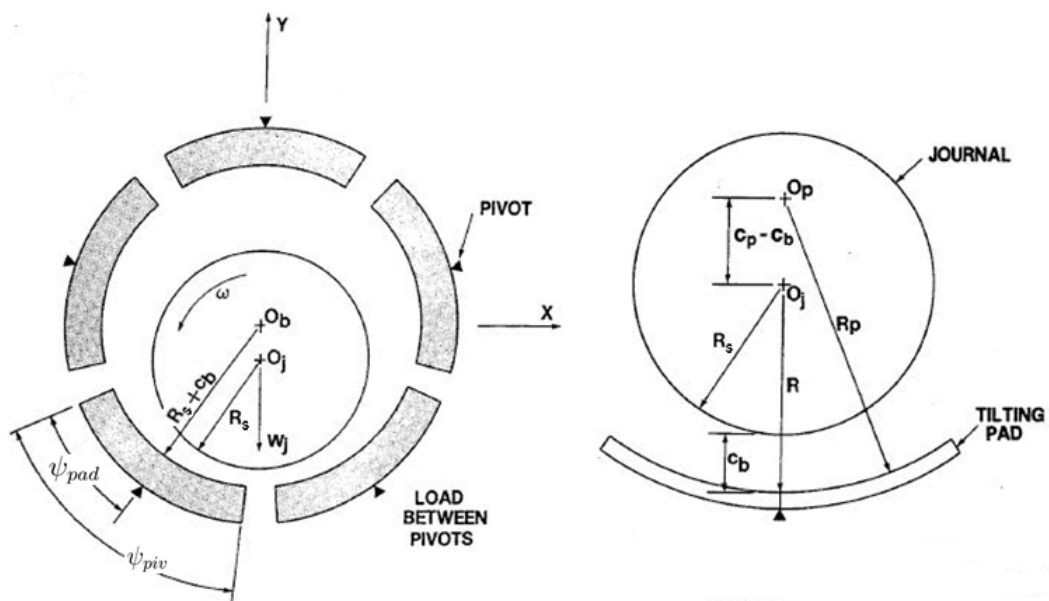


Figure 1.7: Bearing geometrical characteristics and preload

from that in which the load is applied in correspondence of a single pad: the first case is characterized by more symmetrical stiffness and damping matrices (in the modeling of the linearized bearing), involving a greater circularity of the rotor orbits, with amplitudes smaller with respect to the elliptical orbits performed in correspondence of the critical

speeds. The offset of the pivot with respect to the pad centerline is defined as follows:

$$\eta = \frac{\psi_{piv}}{\psi_{pad}}, \quad (1.3)$$

where  $\psi_{pad}$  is the pad opening angle and  $\psi_{piv}$  is the angle included between the pad leading edge and the pivot; generally,  $\eta$  assumes values of about 0,6. The pivot offset

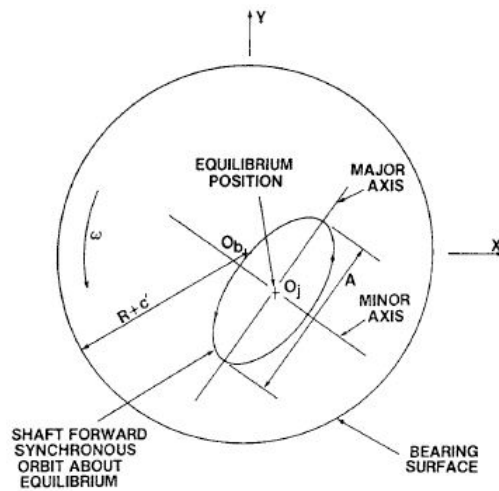


Figure 1.8: Generic rotor orbit

increases the oil film thickness, leading to a decrease of the operating temperature and to an increase of the bearing load capacity.

One of the most important factors for a TPJB analysis is the preload. Referring to Figure 1.7, it is defined as follows:

$$m = 1 - \left( \frac{c_b}{c_p} \right), \quad (1.4)$$

where:

$$c_b = (R - R_s), \quad (1.5)$$

and

$$c_p = (R_p - R_s), \quad (1.6)$$

are respectively the bearing and the pad clearance,  $R_s$  is the rotor fraction radius and  $R_p$  is the pad radius of curvature. The bearing clearance allows for the possible thermal



expansion of the components and leaves sufficient space for the pads tilting and for the oil film; it also influences the lubricant flow rate required for the operation of the bearing and the temperatures within the oil film. The preload is mainly due to the non-concentricity between the shaft and pads, when pads are placed with a zero tilt angle. A preload equal to zero corresponds to a pad radius of curvature constant and equal to that in correspondence of the pivot ( $R_p = R$ ) and a pad clearance equal to the bearing clearance ( $c_P = c_b$ ). Typically the preload values (positive if  $c_P > c_b$ ) vary between 0.2 and 0.6. In presence of preload there is always a converging portion of the oil film and the pad can generate lift even with small applied loads. On the other hand a bearing with zero preload generates a greater damping, thus being more effective in suppressing the rotor vibration and hence in its stabilization [2].

The problem that arises with not preloaded bearings is the inability to cover a wide

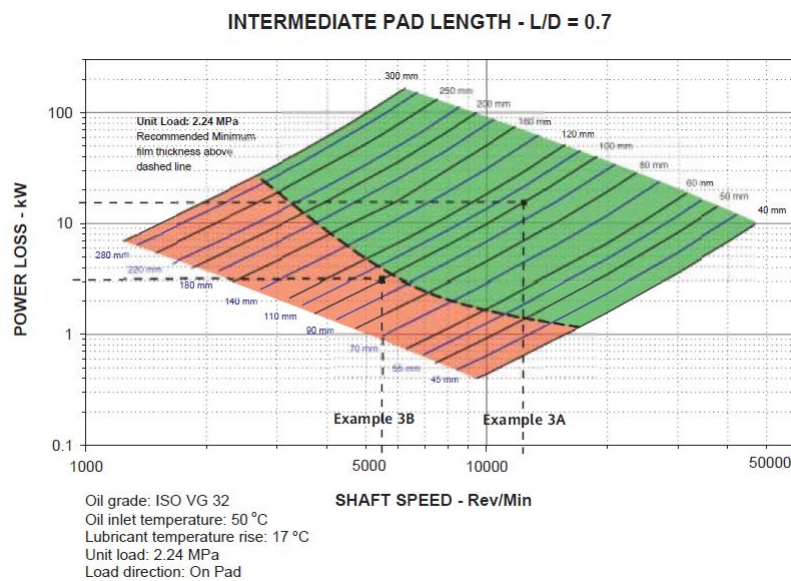


Figure 1.9: TPJB selection map based on geometrical and energetic parameters

operating range: since the presence of a convergent oil film is not always assured, low applied loads can lead to situations in which the upper pads are unloaded and, being unable to find a dynamic equilibrium, establish *flutter* motions; in these cases, the rotor instability is obviously intensified.

Another important geometric parameter of the bearing is the ratio  $L/D$  between the axial length of the bearing and its diameter: an increase of this factor results in an increase of the actual damping of the bearing. To obtain this effect it is more practical for the designer to increase the length of the bearing, although this modification can lead to a more severe misalignment between shaft and bearing, and to the need to use pads with two degrees of freedom.

In the selection and design of the bearing, the designer must take into account the normal force due to the oil film and the torque required to start up the rotor after a period of stop. The designer who must select the appropriate bearing for a specific application is guided in the selection by special maps in which the operation of the bearing is related to its geometric characteristics.

### 1.1.1 Fluid dynamical modeling

Tilting pad journal bearings are devices that exert their supporting action through a pressurized lubricant fluid, which also performs the secondary function to remove the heat generated in the rotor-bearing system. A first fundamental distinction can be made between bearings with fluid dynamical sustenance and bearings with fluid statical sustenance: in both cases the contact between the parts in relative motion is completely eliminated but in the first case the supporting effect is present only in certain kinematic conditions, while the supporting effect for the hydrostatic bearing is due to an external pressure device and the contact is avoided even in absence of relative motion. In both types of bearings the lubricant is fed to the bearing through a series of cavities located between adjacent pads, or in some cases realized directly on the pads surfaces (*direct lube*); there are bearings where the lubricant is not fed from the outside and the bearing operates filled with pressurized fluid (*flooded*). For the direct lube bearings, the supplied lubricant flow must compensate for fluid losses which occur in correspondence of the seals enclosing the bearing. There are also bearing configurations where the oil can be

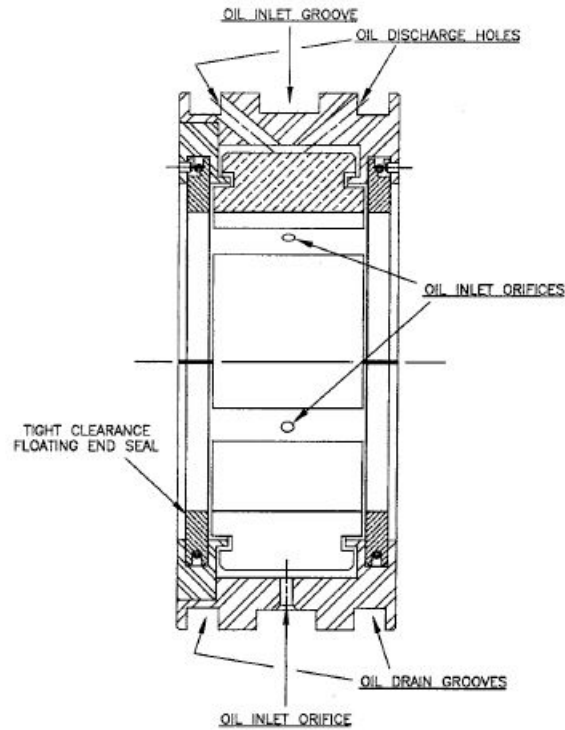


Figure 1.10: Lubricant supply system

discharged from the bearing through radial ducts realized on the top of the device.

An essential task for the designer who decides to use tilting pad journal bearings for the support of a rotating system is an estimate, as accurate as possible, of the lubricant flow rate required by the bearing for a correct operation in all its working range. A basic calculation of the lubricant flow rate needed by the tilting pad journal bearing is rather simple since its value is essentially speed and eccentricity independent. The flow rate depends essentially on the characteristics of the supply and discharge orifices, of the seals and, to a lesser extent, on the lubricant viscosity [2].

The flow rate fed to the bearing through the supply ducts, for an incompressible fluid, can be calculated using the ideal orifice model, according to the following lumped parameters formula:

$$Q = C_d A \sqrt{\frac{2\Delta p}{\rho}}, \quad (1.7)$$

where  $C_d$  is the non-dimensional flow coefficient for the considered orifice, which generally assumes a value of 0.61 in absence of more information. The considered  $\Delta p$  derives from the representation of the bearing as a lumped resistive element; consequently the pressure drop due to the presence of the bearing within the hydraulic network is given by:

$$\Delta p = p_s - p_{env}, \quad (1.8)$$

where  $p_s$  is the supply pressure for the lubricant fluid before the bearing and  $p_{env}$  is the environment pressure after the bearing, since the flow rate exiting the bearing is discharged externally; then the flow rate  $Q$  represents both the inlet and the outlet flow rate of the bearing. The flow rate for  $n$  circular supply orifices with diameter  $d$  is calculated as follows:

$$Q = 0,61 \frac{n\pi d^2}{4} \sqrt{\frac{2\Delta p}{\rho}}. \quad (1.9)$$

Using the definition of equivalent diameter:

$$d_i = \frac{4A}{l}, \quad (1.10)$$

it is then possible to calculate the flow rate with Equation 1.9 even with not circular orifices, with cross section  $A$  and perimeter  $l$ .

Clearly, in a complete study of the behavior of the machine-plant system, it can be too coarse to consider the bearing only as an ideal orifice, without taking into account the complex phenomena involved in it which define its operating range.

A first innovative step with respect to the ideal orifice is represented by the model used by General Electric Oil & Gas. The lubricant flow rate is still calculated with a single equation, analogous to the resistive element model, but a larger number of parameters is considered: the model derives from the analysis of a vast set of experimental data concerning the flow through an orifice. The flow rate is computed as follows:

$$Q = 1,265 D^2 k_{GENP} \frac{\beta^2}{\sqrt{1 - \beta^2}} \sqrt{\frac{\Delta p}{\rho_{inlet}}}, \quad (1.11)$$

where  $D$  is the diameter of the supply duct coming from the hydraulic network (measured in Inches),  $d$  is the diameter of the striction corresponding to the orifice (Inches),  $\beta$  is the ratio between  $d$  and  $D$  and:

$$k_{GENP} = (0,6014 - 0,01352D^{-0,25}) + (0,376 + 0,07257D^{-0,25}) \left( \frac{0,00025}{D^2\beta^2 + 0,0025D} + \beta^4 + 1,5\beta^{16} \right) + kLAMP_{GENP}, \quad (1.12)$$

where  $kLAMP_{GENP}$  is a term to be added to the formula in case of laminar flow:

$$kLAMP_{GENP} = \frac{1000}{\sqrt{Re \cdot d}} \left[ (0,0002 + \frac{0,0011}{D}) + (0,0038 + \frac{0,0004}{D}) (\beta^2 + (16,5 + 5D)\beta^{16}) \right]. \quad (1.13)$$

The opposite with respect to lumped parameters models is represented by fully 3D bearing models. The computing power available today allows the use of CFD (Computational Fluid Dynamics) models for the analysis of the hydraulic behavior of the bearings, in order to achieve accurate results for bearings subjected to critical loading conditions. Those 3D models, based on a complete discretization of the oil film using finite elements and volumes, are therefore an essential tool for a proper fluid dynamical modeling of the bearings. However their fundamental limitation is a deep numerical inefficiency, since the complexity of the CFD analysis of those models involves computational times incompatible with the needs of the industry (considering the fact that the bearing is only a single element of a complex system, which often includes a significant number of bearings, each needing to be analyzed according to its peculiarities. As previously mentioned, one of the objectives of this work is the development of a bearing model that could reach a compromise between the fully-3D CFD models and the simplified lumped parameters models, more efficient with respect to the firsts and more accurate than the seconds, and that allows a coupled rotordynamical and fluid dynamical analysis, in order to improve the results obtainable in both areas; the model should also be able to contain drastically the calculation time, revealing itself a critical analysis tool.

### 1.1.2 Rotor dynamical modeling

From the mechanical point of view, tilting pad journal bearings exert normal and tangential forces that support the rotor in its motion and interact with the dynamic behavior of the entire system. As will be illustrated in the following chapters, the rotor performs, overlapping its proper rotation, complex vibratory motions: this makes the forces exchanged by shaft and bearing time-dependent and variable as a function of the rotor motion, position and velocity. When using fluid dynamical bearings, the system is further complicated by the strong anisotropy that characterizes their behavior and by the dependence on the rotor spin speed.

The analysis techniques concerning the dynamic behavior of tilting pad journal bearings

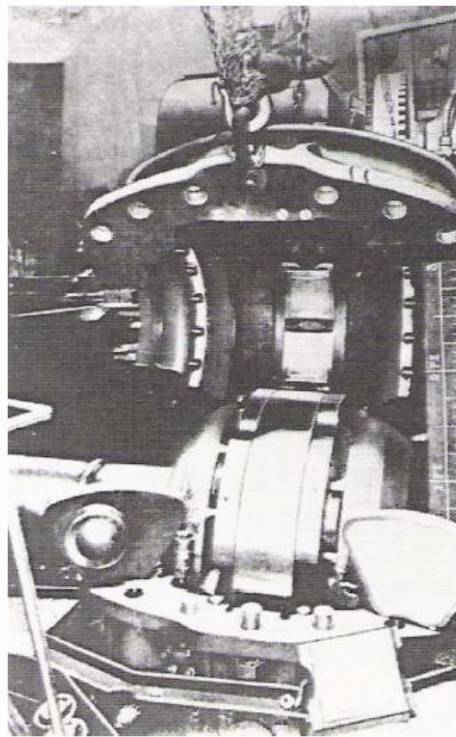


Figure 1.11: Michell bearing

have evolved considerably over the last 50 years, thanks to an increase in the available computing power. The first analyses were based on stationary calculations, neglecting

the curvature of the pads: being unable to highlight the dynamic characteristics of the bearings, the TPJBs did not seem to produce any kind of advantage over the classical fixed geometry journal bearings. The first step towards a dynamic modeling was performed by Lund, who developed a method for assembling the equations of motion of the bearing in terms of stiffness and damping. The aforementioned method was then enriched by other researchers introducing a greater number of physical effects, but maintaining its essence of lumped parameters model [3].

So historically the behavior of the bearings has been analyzed simplifying extensively the problem with the fundamental assumption that the rotor performs small oscillations with respect to its stable equilibrium position, an operating condition that leads to the linearization of the bearing behavior.

Considering a simplified case with rotor and bearing perfectly aligned, firstly it is necessary to integrate the oil film pressure to determine the radial forces acting on the rotor. It is then possible to analyze the static equilibrium of the rotor, determining the equilibrium position and the forces that the bearing exerts in correspondence of that position. Once determined the equilibrium condition, the linearization procedure is performed perturbing the position of the rotor. If the shaft moves small quantities  $\Delta x$  and  $\Delta y$  from the static equilibrium position with a velocity  $\dot{x}$  and  $\dot{y}$ , the force exerted by the bearing, which in the equilibrium position is  $\mathbf{f}_{st}$ , can be expressed as follows:

$$\mathbf{f} = \mathbf{f}_{st} - \begin{bmatrix} \frac{\partial f_x}{\partial \dot{x}} & \frac{\partial f_x}{\partial \dot{y}} \\ \frac{\partial f_y}{\partial \dot{x}} & \frac{\partial f_y}{\partial \dot{y}} \end{bmatrix}_{x_{st}, y_{st}} \begin{Bmatrix} \dot{x} \\ \dot{y} \end{Bmatrix} - \begin{bmatrix} \frac{\partial f_x}{\partial x} & \frac{\partial f_x}{\partial y} \\ \frac{\partial f_y}{\partial x} & \frac{\partial f_y}{\partial y} \end{bmatrix}_{x_{st}, y_{st}} \begin{Bmatrix} \Delta x \\ \Delta y \end{Bmatrix}. \quad (1.14)$$

Then the bearing linearized behavior can be expressed through a set of eight coefficients: the eight partial derivatives of the components of the force with respect to displacement (stiffness coefficients) and with respect to speed (damping coefficients). Those coefficients are collected in the stiffness and damping matrices:

$$\mathbf{K} = - \left[ \left( \frac{\partial f_i}{\partial x_j} \right) \right]_{x_{st}, y_{st}}, \quad (1.15)$$

$$C = - \left[ \left( \frac{\partial f_i}{\partial \dot{x}_j} \right) \right]_{x_{st}, y_{st}} \quad (1.16)$$

The obtained linearized forces are referred to a lumped parameters modeling approach

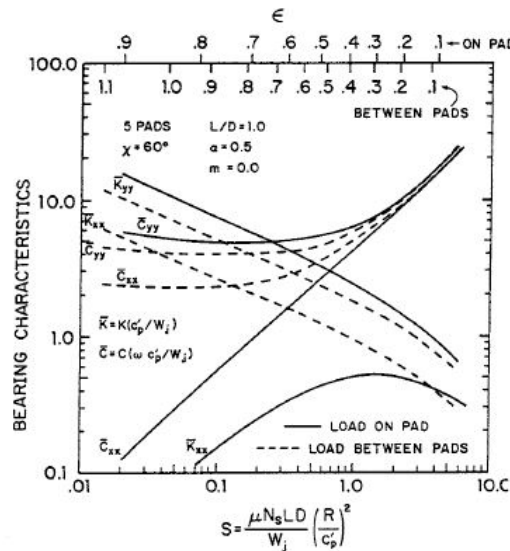


Figure 1.12: Bearing stiffness and damping coefficients

based on the use of spring and damper elements: the negative sign preceding the matrices indicates that the forces tend to bring the system (the rotor) back to its equilibrium position (springs) with zero speed (dampers) [1]. The oil film is then represented with

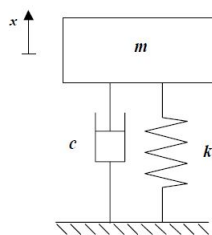


Figure 1.13: Mass-spring-damper lumped parameters system

the stiffness and damping coefficients calculated through the linearization procedure. Referring to Figure 1.14, where for the sake of synthesis only a single pad is reported,





with  $n_p$  pads:

$$\begin{aligned}
 & \begin{bmatrix} m_{rot} & 0 & 0 & 0 & \dots & 0 \\ 0 & m_{rot} & 0 & 0 & \dots & 0 \\ 0 & 0 & J_{p,1} & 0 & \dots & 0 \\ 0 & 0 & 0 & J_{p,2} & \ddots & \vdots \\ \vdots & \vdots & \vdots & \ddots & \ddots & 0 \\ 0 & 0 & 0 & \dots & 0 & J_{p,n_p} \end{bmatrix} \begin{Bmatrix} \ddot{x} \\ \ddot{y} \\ \ddot{\gamma}_1 \\ \ddot{\gamma}_2 \\ \vdots \\ \ddot{\gamma}_{n_p} \end{Bmatrix} + \begin{bmatrix} c_{xx} & c_{xy} & c_{x\gamma_1} & c_{x\gamma_2} & \dots & c_{x\gamma_{n_p}} \\ c_{yx} & c_{yy} & c_{y\gamma_1} & c_{y\gamma_2} & \dots & c_{y\gamma_{n_p}} \\ c_{\gamma_1x} & c_{\gamma_1y} & c_{\gamma_1\gamma_1} & 0 & \dots & 0 \\ c_{\gamma_2x} & c_{\gamma_2y} & 0 & c_{\gamma_2\gamma_2} & \ddots & \vdots \\ \vdots & \vdots & \vdots & \ddots & \ddots & 0 \\ c_{\gamma_{n_p}x} & c_{\gamma_{n_p}y} & 0 & \dots & 0 & c_{\gamma_{n_p}\gamma_{n_p}} \end{bmatrix} \begin{Bmatrix} \dot{x} \\ \dot{y} \\ \dot{\gamma}_1 \\ \dot{\gamma}_2 \\ \vdots \\ \dot{\gamma}_{n_p} \end{Bmatrix} + \\
 & + \begin{bmatrix} k_{xx} & k_{xy} & k_{x\gamma_1} & k_{x\gamma_2} & \dots & k_{x\gamma_{n_p}} \\ k_{yx} & k_{yy} & k_{y\gamma_1} & k_{y\gamma_2} & \dots & k_{y\gamma_{n_p}} \\ k_{\gamma_1x} & k_{\gamma_1y} & k_{\gamma_1\gamma_1} & 0 & \dots & 0 \\ k_{\gamma_2x} & k_{\gamma_2y} & 0 & k_{\gamma_2\gamma_2} & \ddots & \vdots \\ \vdots & \vdots & \vdots & \ddots & \ddots & 0 \\ k_{\gamma_{n_p}x} & k_{\gamma_{n_p}y} & 0 & \dots & 0 & k_{\gamma_{n_p}\gamma_{n_p}} \end{bmatrix} \begin{Bmatrix} x \\ y \\ \gamma_1 \\ \gamma_2 \\ \vdots \\ \gamma_{n_p} \end{Bmatrix} = \begin{Bmatrix} f_x \\ f_y \\ 0 \\ 0 \\ \vdots \\ 0 \end{Bmatrix}. \tag{1.18}
 \end{aligned}$$

These equations analyze the motion of a single element of the rotor, dynamically identified by the mass  $m_{rot}$ , and of the pads supporting it, but their shape, being that typical of dynamic problems which will be illustrated in the following chapters, allows for an easy extension of the problem in order to include a rotor model developed with the finite element method [4].

### 1.1.3 ThermoElastoHydroDynamic modeling

Some TPJB models consider, always maintaining a lumped parameter modeling, the effects that the lubricant temperature has on the whole system. Those models, offer considerable advantages from the computational point of view, but their accuracy and their ability to investigate the physical interactions that involve the bearings are not sufficient to ensure that the obtained results are able to improve the efficiency of modern rotors; furthermore the modern study of rotors involves a detailed analysis of the

couplings among the various elements of the system. These analyses arise from the designers' need to widen the operation field of the machines, and prevent the triggering of any phenomena of rotor instability; it is evident how these simplified models are inadequate to perform this type of analysis.

Most of the studies found in literature analyse a smaller number of physical phenomena coupled together, or perform a complete coupled analysis considering simpler bearings (e.g. journal bearings); this approach has been used for example by Knight and Barrett [5], who developed a thermal analysis thermo-hydrodynamic (THD) of a Tilting Pad Journal Bearing, based on a finite difference solution of the classical energy equation, able to estimate the lubricant viscosity through the average value of the temperature calculated in the fluid film. Instead, Gomiciaga and Keogh [6] analysed a rotor supported by two bearings, using CFD techniques. In this model the motion is divided into a *backward* component and in a *forward* component of the circular orbit of the rotor, and the CFD technique is used to evaluate the fluid dynamics of the lubricant and the heat exchange that this produces. The heat exchanged is evaluated by an average calculated on the  $i$ -th

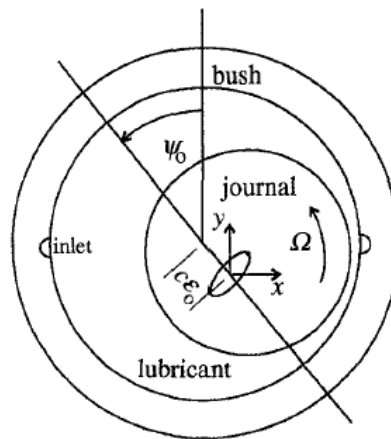


Figure 1.15: Orbit described by the rotor.

orbit, and defined as follows:

$$\bar{q}_{O_i}(\theta, z) = \frac{\Omega}{2\pi} \int_{t_{i-1}}^{t_i} q_O(\theta, z, t) dt, \quad (1.19)$$

where  $t_i = \frac{\Omega_i}{2\pi}$ ,  $\Omega$  is the rotation speed of the rotor and  $q_O(\theta, z, t)$  is the heat flow generated by the fluid film within the bearing, defined as follows:

$$q_O(\theta, z, t) = -\frac{k(\theta, z, t)}{h(\theta, t)} \cdot \frac{\partial T_l}{\partial \eta}(l, \theta, z, t), \quad (1.20)$$

where  $k$  is the thermal conductivity of the lubricant,  $h$  is the fluid film thickness,  $T_l$  is the lubricant temperature and  $\eta$  is a dimensionless radial coordinate.

A further development, compared to the previous approaches, is represented by the most recent completely three-dimensional models, which analyze many of the physical phenomena involved in the Tilting Pad Journal Bearings operation; these models couple the classic ThermoHydroDynamic study (THD) (performed on the fluid film) with studies of the elastic and thermal behaviors of the solid elements of the system, generating a ThermoElastoHydroDynamic study (TEHD) of the bearing [7], [8].

Some authors, such as Ettles [9] and Brockwell [10] proposed TEHD models through which one studies the lubrication problem and in particular the calculation of the pressure distribution in the fluid film, through the generalized Reynolds equation.

Another interesting model is that proposed by Costantinescu [11], in which the fluid film is studied inside the bearings considering the fluid motion as the sum of an average speed that this assumes and a fluctuation component, that is:

$$u_i = \bar{u}_i + u'_i, \quad (1.21)$$

where  $u_i$  is the fluctuation component and  $\bar{u}_i$  is instead the average value of the lubricant velocity, calculated as follows:

$$\bar{u}_i = \lim_{t \rightarrow \infty} \int_{t_o}^{t_o+T} u_i dt. \quad (1.22)$$

An important work is that presented by Chang [12]: he develops a TEHD model, based on the Newton-Raphson method, of a TPJB with three pads and he analyses on three dimensions both the heat transfer generated by the lubricant and the deformations, elastic and thermal, of the solid components. The analyses of the heat exchange within the

lubricant, Chang uses the energy equation, expressed in the following form:

$$\frac{\partial^2 \bar{T}}{\partial \bar{r}_p^2} + \frac{1}{\bar{r}_p} \frac{\partial \bar{T}}{\partial \bar{r}_p} + \frac{1}{\bar{r}_p^2} \frac{\partial^2 \bar{T}}{\partial \bar{\theta}^2} + \frac{\partial^2 \bar{T}}{\partial \bar{y}^2} = 0, \quad (1.23)$$

where, in accordance with Figure 1.16,  $r_{n_p}$ ,  $y_p$ ,  $\theta_p$  are cylindrical coordinates of the  $i$ -th pad. For the study of the elastic and thermal deformations, which occur in the solid

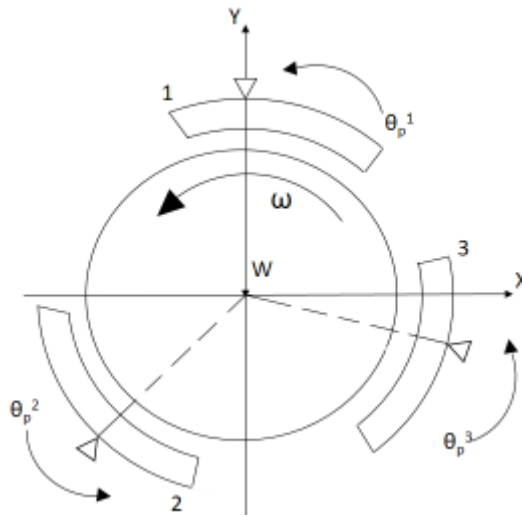


Figure 1.16: Bearing geometry with three pad studied by Chang [12].

components, Chang uses the Finite Element Method, by which it is possible to evaluate the elastic deformation matrix  $[\bar{D}]$  and the thermal expansion matrix  $[\bar{D}']$ , respectively due to the pressure and the temperature fields generated by the lubricant, ; through those matrices it is possible to calculate the variation of the fluid film thickness following the elastic deformation of the pad:

$$\bar{d}_1^{i,j}(\bar{\theta}, \bar{y}) = \sum \sum \bar{D}_{k,l}^{i,j} \cdot \bar{p}_{k,j}, \quad (1.24)$$

and the variation of the fluid film thickness as a result of thermal expansion:

$$\bar{d}_2(\bar{\theta}, \bar{y}) = \sum \sum \sum \bar{D}_{k,l,m}^{i,j} \cdot \bar{T}_{k,l,m}. \quad (1.25)$$

Other authors have investigated several aspects related to Tilting Pad Journal Bearings, such as Brugier and Pascal [13] who developed a TEHD model to estimate the

dynamic coefficients of TPJBs; in this method a small perturbation applies to the rotor in correspondence of the bearings, to evaluate the bearings response and extract consequently the respective damping  $[C]$  and stiffness  $[K]$  matrices. A further model is that proposed by Kim [14], in which the coefficients of the damping and stiffness matrices were evaluated considering both heat transfer and elastic deformation.

Instead, Hashimoto [15] developed a TEHD model able to reproduce the behaviour of large bearings. This model provided a calculation procedure made up of ten distinct steps; in accordance with Figure 1.17 the steps are the following:

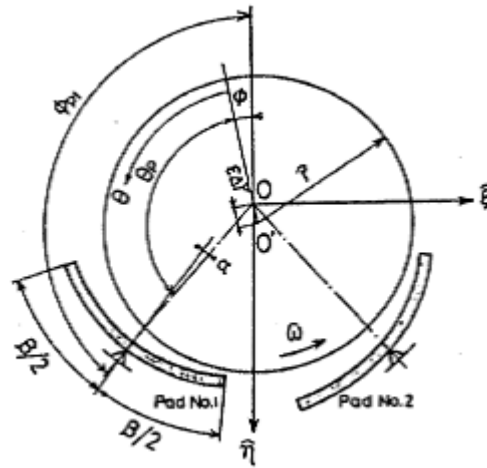


Figure 1.17: Two pads bearing studied by Hashimoto [15].

1. an attitude angle  $\phi$  is assumed;
2. a pad deformation  $v_i$  is assumed;
3. a pad tilt  $A_i$  is assumed;
4. the temperature  $T_i$  and lubricant viscosity  $\mu_i$  are calculated using the following equations:

$$\frac{\partial T_i}{\partial \theta} = \frac{2\mu_i}{h_i^2} (1 + 0.001 \cdot sR_{h_i}^{0.94}), \quad (1.26)$$

$$\mu_i = e^{-T_i}, \quad (1.27)$$

where the subscript  $i$  is referred to the  $i$ -th pad;

5. the static pressure of the fluid film  $p_{ij}$  is calculated using the following equation:

$$\frac{\partial}{\partial \theta} \left( h_i^3 \frac{G_{\theta i}}{\mu_i} \frac{\partial p_{ij}}{\partial \theta} \right) + \frac{1}{4\lambda^2} \frac{\partial}{\partial z} \left( h_i^3 \frac{G_{zi}}{\mu_i} \frac{\partial p_{ij}}{\partial z} \right) = f_{ij}, \quad (1.28)$$

where  $h$  is the fluid film thickness,  $G_{\theta i}$  and  $G_{zi}$  are the turbulence coefficients and  $\lambda$  is the bearing thickness-diameter ratio;

6. through an iterative method it is possible to obtain the correct value of the pad tilt  $A_i$  that satisfies the moments equilibrium on the  $i$ -th pad;
7. through an iterative method it is possible to obtain the correct value of pad deformation  $v_i$ . If the model does not get to convergence, the method is repeated from step 2 to step 7 until convergence;
8. through the Newton-Rapshon method it is possible to estimate the correct value of the angle  $\phi$  that satisfies the following forces balance acting on the fluid film:

$$\sum_{i=1}^2 W_{pi}(\phi) \sin \phi_{pi} = 0, \quad (1.29)$$

where  $W_{pi}$  is the load capacity of the bearing;

9. the static characteristics of the bearing (such as the Sommerfeld number) are calculated;
10. finally, with all the available data, the damping and stiffness dynamic coefficients of the bearing are calculated.

In addition, some authors have introduced in the analysis also other elements of the rotor-bearing system: Kirk and Balbadhur [16] developed a ThermoElasto model for analyzing the onset of thermal instability of the rotor; Monmousseau and Fillon [17] developed a TEHD model considering a possible flexibility of the pads pivots (an analogous model was previously developed by Kirk and Reedy [18] and led to the conclusion that to

obtain satisfactory results, the model adopted must necessarily take into account the bearing deformability); Suh and Palazzolo [19] performed *transient* tests analyzing the ThermoHydroDynamic behavior of the lubricant coupled with the rotor FEM model, considering the possibility for the cylindrical pivot of the pad to be deformed (as shown in Figure 1.18). A very important contribution due to this work is the analysis of the

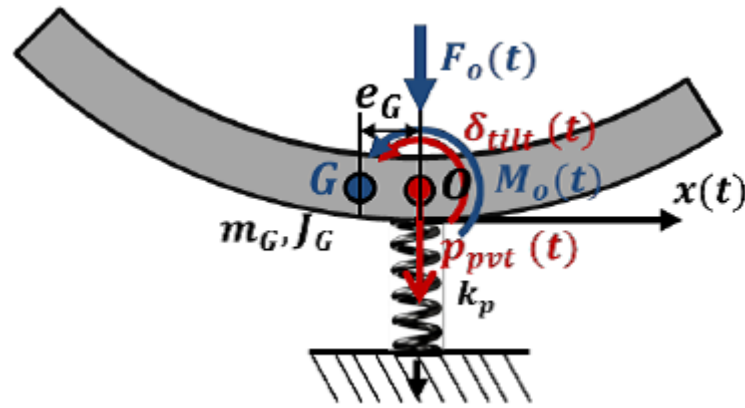


Figure 1.18: Pad model with flexible pivot [19].

distortion generated on the pads and on the rotor by the heat load generated by the fluid film within the bearing. The temperature distribution by thermal conduction that develops in the pad is evaluated as follows:

$$\frac{\partial^2 T}{\partial x^2} + \frac{\partial^2 T}{\partial y^2} + \frac{\partial^2 T}{\partial z^2} = \frac{\rho c}{k} \frac{\partial T}{\partial t}, \quad (1.30)$$

where  $x, y, z$  are the three-dimensional coordinates of the  $i$ -th pad and  $k$  is its thermal conductivity coefficient; this temperature value is directly applied to the FEM elastic models of the pads and of the rotor in order to estimate the value of the associated heat load, thus obtaining the value of the thermal expansion suffered by solid components, for which the following equation is applied:

$$\mathbf{K}_E \mathbf{X}_E = \mathbf{F}_{E,T}, \quad (1.31)$$

where  $\mathbf{K}_E$  is the stiffness matrix of the 3D FEM model and  $\mathbf{X}_E$  and  $\mathbf{F}_{E,T}$  are respectively the thermal expansion and the thermal load vectors.



All these models offer a great accuracy but their resolution times and their computational weight represent a major limitation, and therefore their use in the study of modern rotors is still limited.

## 1.2 Goals of the thesis

The present thesis aims at the development of efficient three-dimensional tilting pad journal bearings models, in order to analyze both the bearing interactions with the lubricant supply system and those with the rotor, the rotor and pads deformation and the thermal effects developed in the pads, in the rotor and inside the oil film. Furthermore, the attention was placed on the realization of a model with a high numerical efficiency, in order to perform complex simulations while keeping computational times within the limits marked by the necessities of the industry. The proposed bearing models consider all the six degrees of freedom permitted to the rotor fraction enclosed inside the bearing and aim to reach a good compromise between the simplified lumped parameters models and the fully three-dimensional ones, improving the results obtainable with the firsts and the numerical efficiency with respect to the seconds.

The goal of developing a complete tilting pad journal bearing model has been achieved through three consecutive modeling steps: the first step deals with the modeling (and experimental validation) of the fluid dynamical characteristics of the bearing, the second step addresses the rotor dynamical aspects of the system (with a further validation) while the third step analyzes the coupled effects between thermal, elastic, fluid dynamic and rotor dynamic behaviours (with a further validation).

The thesis starts with an overview of the architecture of the developed models, analyzing the inputs and outputs that characterize the different components, shown in Chapter 2. Then Chapters 3, 4 and 5 (respectively concerning the modeling Step 1,2 and 3) analyze in detail the developed models, illustrating the modeled elements in parallel with their theoretical basis; the software and algorithms used for the numerical solution are also presented. After an analysis of the experimental apparatus and results used for the models validation reported in Chapter 6, in Chapter 7 the results obtained from the simulation of the proposed models are shown, in addition to a comparison with the experimental data and to an analysis of the performances of the models.

## Models architecture

In this thesis three modeling steps have been completed in order to develop a complete three dimensional tilting pad journal bearing model and couple it efficiently with rotor dynamical models. The first developed model represents a bearing with four tilting pads and has been used to realize a validation concerning the fluid dynamical characteristics of the model. The second model is conceptually analogous to the first and can be considered its evolution: it represents a centrifugal compressor supported by two bearings, each with five tilting pads, and allows to evaluate accurately the rotor dynamical performances of the system. The last model is an evolution of the second one, adding the analysis of the thermal and elastic behaviour of rotor, pads and oil films (thus realizing a fully TEHD model). In this Chapter, the architectures and the characteristic of the three models will be introduced.

## 2.1 Step 1: Fluid dynamical aspects

The first model includes the following components:

- oil film model;
- pad dynamical model;
- rotor fraction model;
- sump model connected with a duct model (lubricant supply plant).

The sump represents the fluid cavity circumferentially interposed between two adjacent pads where the flow rates present in the bearing (the flow rates entering and exiting the oil films, the supply flow rate and the leakage flow rate connected to the bearing through appropriate ducts and orifices) mix. The oil film model and the models of the elements connected to it are repeated  $n_p$  times, where  $n_p$  is the number of pads of the considered bearing: the developed model is highly modular and allows to easily analyze different layouts of bearings by varying the number of components. The oil film model has been realized using the software *COMSOL Multiphysics*<sup>®</sup> 4.4, in order to solve the fluid dynamical problem represented by the Reynolds equation through the finite elements method. The outputs of this model are the forces and the moments that the bearing, thanks to the pressure field, exerts on rotor and pads, and the inlet and outlet flow rates, while the inputs are the positions and velocities of rotor and pads and the pressure levels on the oil film boundaries. For each integration time step, the oil film model is solved as steady state while the rotor and pads motions and the supply plant dynamics are solved as time-dependent: this assumption is correct if the time step  $\Delta t$  is sufficiently small. The other components of the model are solved with *MATLAB*<sup>®</sup> R2013a: the numerical problem is then divided into two parts, dividing the PDEs (partial differential equations) representative of the oil film from the ODEs (ordinary differential equations) concerning the dynamical behavior of the remaining components. The scheme reported in Figure 2.2

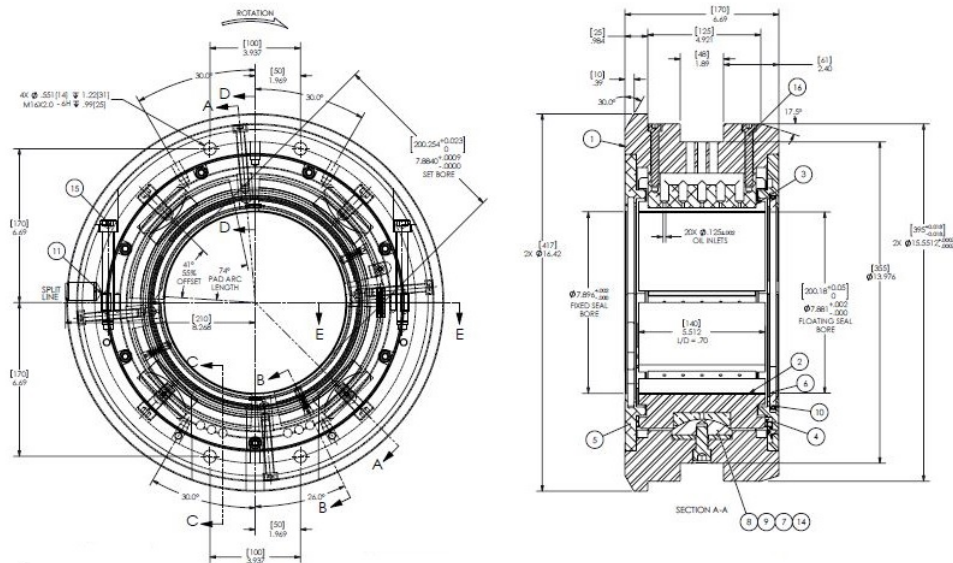


Figure 2.1: Constructive drawing for the GEJB200M-05 bearing. All data are “owned and reserved” and obtained by permission of GE O&G Nuovo Pignone “GE ©2014 - All Rights Reserved”

shows the modeling flow of the first model.

For the development of the first model, a *Lufkin*<sup>®</sup> tilting pad journal bearing with four pads used by General Electric Oil & Gas has been considered as a reference, in order to validate the model with appropriate experimental data (shown in Chapter 6). The model is handled through *MATLAB*<sup>®</sup> *R2013a*: with the *ode15s* solver, which solves a global set of ODEs (shown in the following Chapters), the four oil film steady state models are called back until the system reaches a dynamic equilibrium condition (steady state operation).

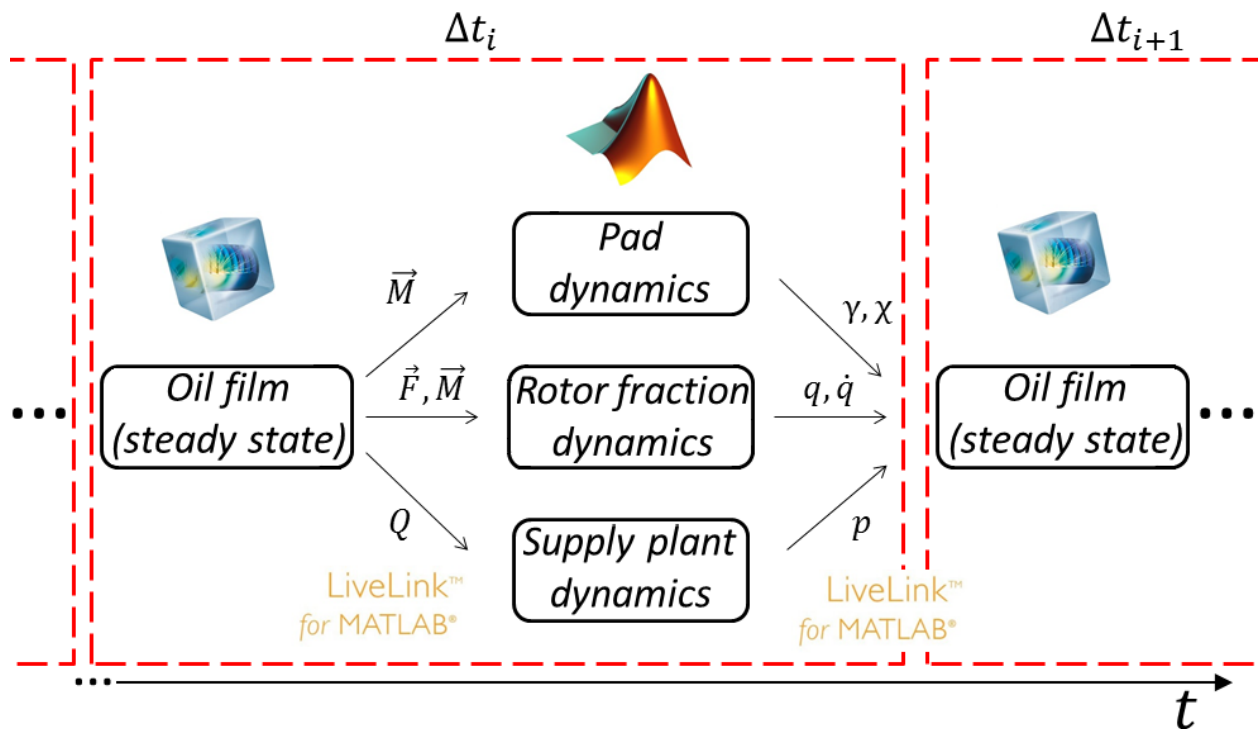


Figure 2.2: Conceptual map of the developed model

## 2.2 Step 2: Rotor dynamical aspects

In order to extend the bearing model and include rotor dynamical effects, the modeling proceeded building the whole model with *COMSOL Multiphysics*<sup>®4.4</sup>, avoiding data exchange between two softwares (this exchange can easily become a critical factor in the analysis of complex rotors). Furthermore, the use of *COMSOL Multiphysics*<sup>®4.4</sup> for the solution of the rotor motion allows to readily model complex real rotors, since *COMSOL Multiphysics*<sup>®4.4</sup> is a multiphysics FEM software. The modeling approach followed in the second step of this research work is analogous to the former; this second model is in fact an evolution of the other, developed in order to analyze the rotor dynamical behavior of the system. The model developed in this phase includes two complete *Kingsbury*<sup>®</sup>bearings, each composed by five tilting pads, and a FEM modeled rotor based on a centrifugal compressor realized by General Electric Oil & Gas. The components of the model are the following:

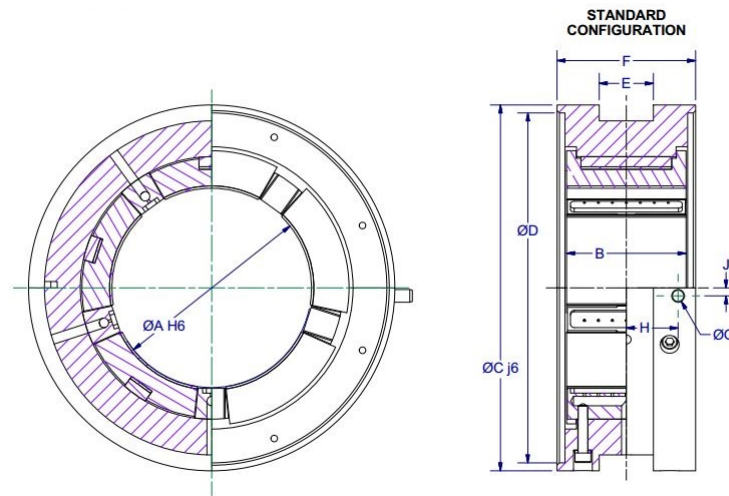


Figure 2.3: Constructive drawing for the considered *Kingsbury*® bearing. All data are “owned and reserved” and obtained by permission of GE O&G Nuovo Pignone “GE ©2014 - All Rights Reserved”

- ten oil film models;
- ten pad dynamical models;
- ten lubricant supply plant models;
- rotor FEM model (with BEAM elements).

The model is completely coupled and all its elements are solved through the same solver within *COMSOL Multiphysics*® 4.4. In Figure 2.5 the interactions between the model components are reported; the input and the outputs of the various parts are analogous to those exposed for the previous model: the bearings receive as inputs the positions and velocities of their pads and of the rotor fractions enclosed in the bearings and the supply sumps pressures, while they provide as outputs the forces and moments acting on rotor and pads and the lubricant flow rates to return to the pads, rotor and supply plant models. The primary difference with the previous model is the higher connection level between the various elements and the simultaneous solution of the whole model in the time or

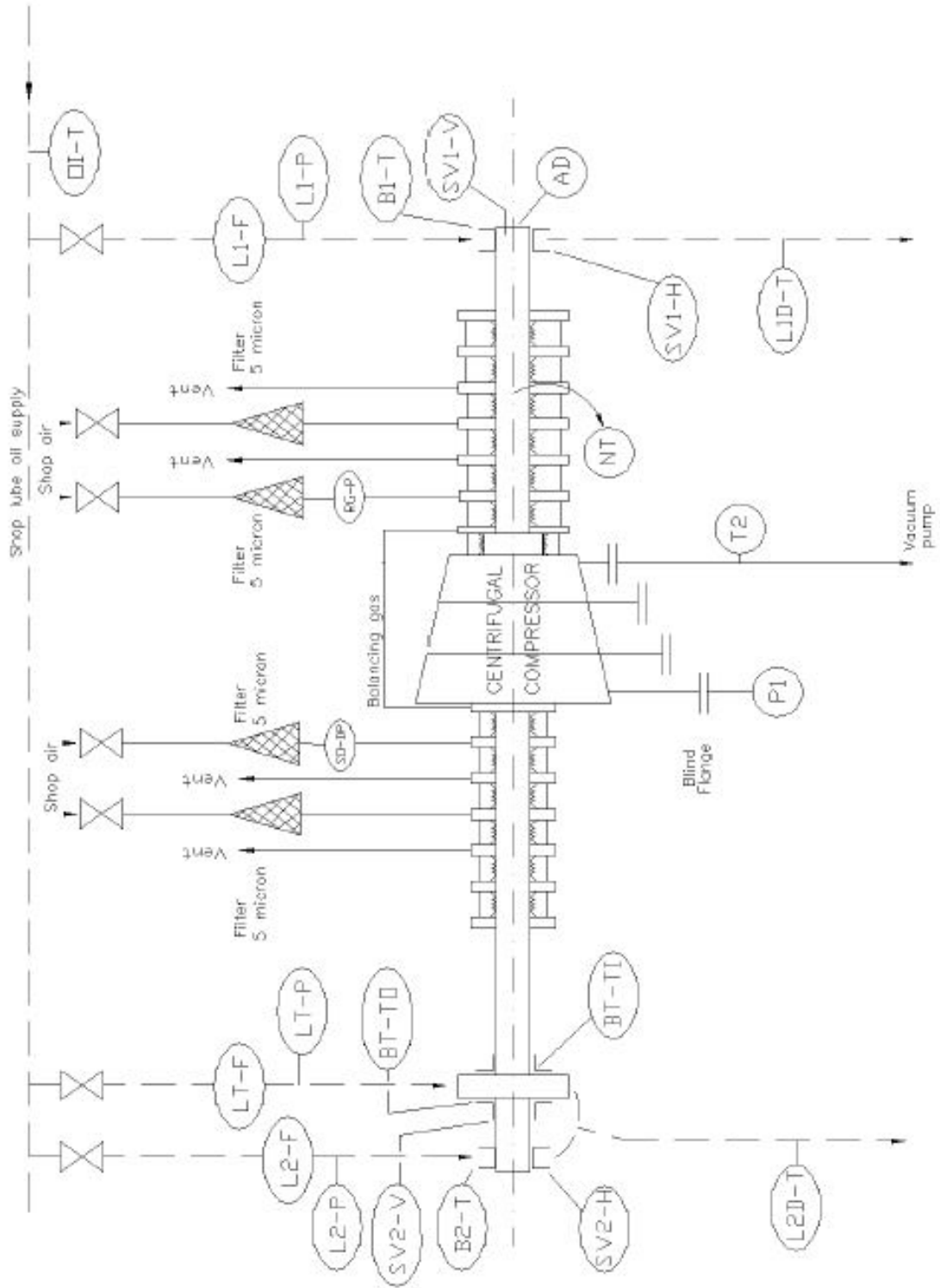


Figure 2.4: Rotor scheme. All data are “owned and reserved” and obtained by permission of GE O&G Nuovo Pignone “GE ©2014 - All Rights Reserved”



frequency domain: the solution scheme (with the oil films solved through steady state analyses for each time step) previously illustrated is no more followed and the whole model follows a simultaneous transient evolution in the time domain or is completely solved as steady state in the frequency domain.

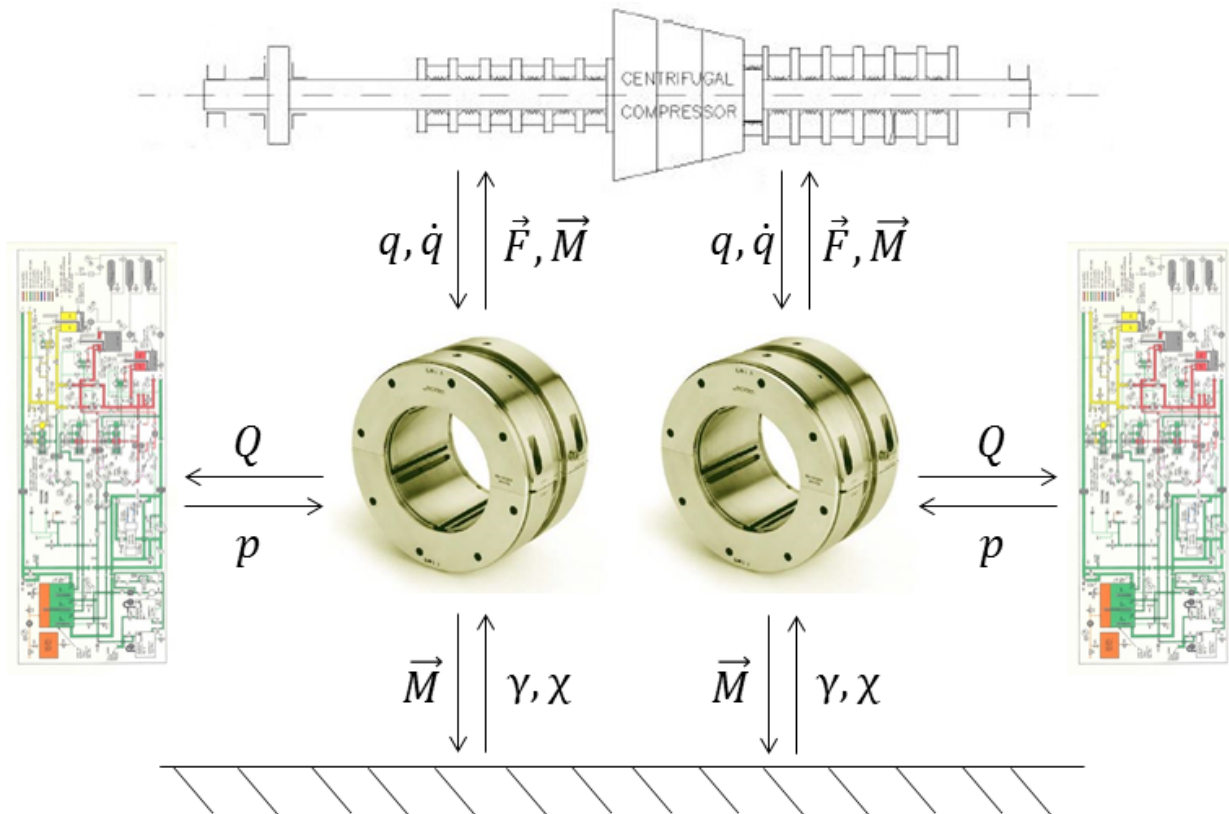


Figure 2.5: Complete model scheme

## 2.3 Step 3: ThermoElastoHydroDynamic aspects

The third model (complete model of a centrifugal compressor rotor supported by two TPJBs with five pads), whose architecture is shown in Figure 2.6, analyzes the thermal, elastic and fluid dynamic aspects affecting the bearing during operation, and it can be efficiently coupled with rotor dynamic models.

The elements that compose the model are:

- ten oil film models;
- ten pad models (with BRICK elements);
- ten lubricant supply plant models;
- rotor FEM model (with BEAM elements);
- rotor fraction model (with BRICK elements).

These components have been fully realized through the software *COMSOL Multiphysics*<sup>®</sup>4.4 which, being a software for finite element analysis, allows to model in a satisfactory way even complex real machines. The models components are completely coupled together, and the calculations required for the resolution of the case study are directly managed by the software itself. In the next chapter the architecture and the characteristics of the model will be exposed.

The oil film model is based on the coupling between the Reynolds equation and the energy equation; this is a 3D model realized through the use of two-dimensional elements. The outputs are the forces and moments that, due to the pressure field, acting on the pads and on the rotor, the lubricant temperature field and the lubricant flow rates within the oil film; the inputs are displacements, velocities and temperatures of the rotor and the pads, and the pressures and temperatures of the fluid in the lubricant supply plant.

The lubricant supply plant model has been developed using lumped parameters elements

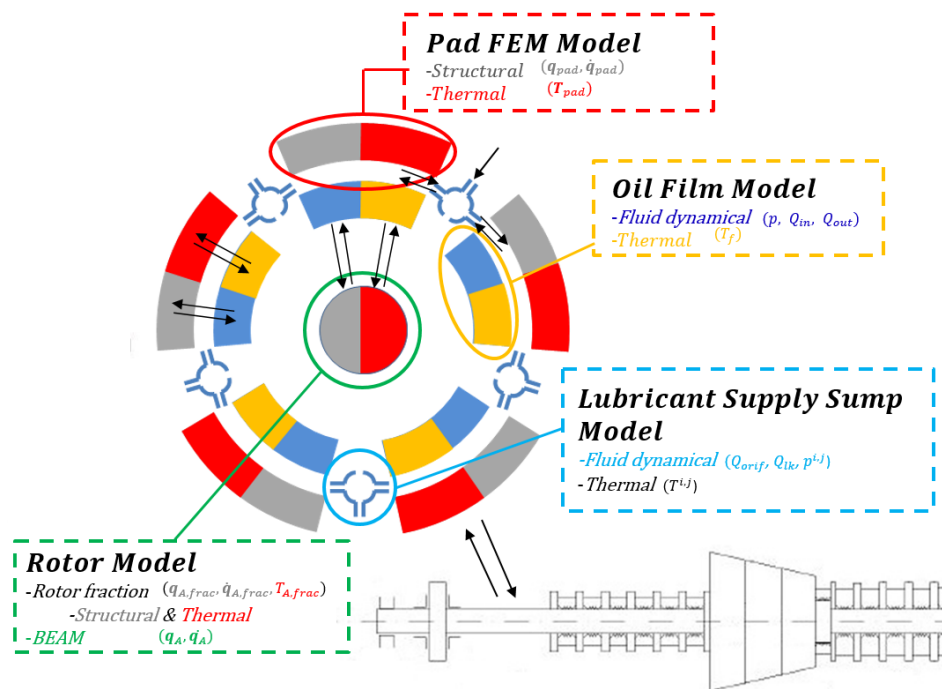


Figure 2.6: General architecture of the complete model.

that simulate the lubricant dynamics and the thermal behavior in the lubricant supply plant; the outputs are the temperature and the pressure within the system and the supply and leakage flow rates, while the inputs are the supply pressure, the input and output flow rates and the output lubricant temperature.

The pad model is a 3D model based on the Finite Element Method; in fact, in addition to the dynamic aspects still studied by lumped parameters elements, this model also studied the elastic and thermal aspects by a FEM model and simulates the deformation and temperature fields that develop in the pad, due to the presence of the fluid film in the system. The outputs that it generates are velocity, deformation and temperature of the pad, while the inputs are the loads due to the pressure field within the fluid film and the oil film temperature.

The rotor model simulates displacements, deformations and heat exchange of the rotor and similarly to the pad model is divided into two distinct sub-models, with different inputs and outputs. There is, in fact, a first part of the rotor FEM model realized through

BEAM elements that has the task of modeling the rotor motion, and a second part composed by two 3D solid elements that study the deformation and the thermal fields of the rotor fractions contained in the two bearings. The inputs needed by the two sub-models are the loads that the bearings exert on the rotor, the lubricant temperature and the possible external loads.

This third model reproduces a Tilting Pad Journal Bearing with five pad produced by *Kingsbury*<sup>®</sup>(Figure 2.3) and the rotor of a centrifugal compressor (Figure 2.7); the data of these two components have been provided by General Electric Oil & Gas Nuovo Pignone, in order to validate the proposed approach through the comparison with an experimental data set that will be shown in the next chapters. The developed model analyses for the physical phenomena involved in the system in the time domain, by performing a *transient* simulation. This integration is done through a *time dependent* study which uses the BDF multistep method; the resolution of each step is assigned to the *Segregated* solver implemented in the software *COMSOL Multiphysics*<sup>®</sup>4.4, which allows to treat the system variables in a decoupled way and to choose the order in which the various phenomena need to be analysed in order to avoid an inadequate coupling between the model equations; in this model the solver step has been set so that the analysis starts from the rotor motion resolution.

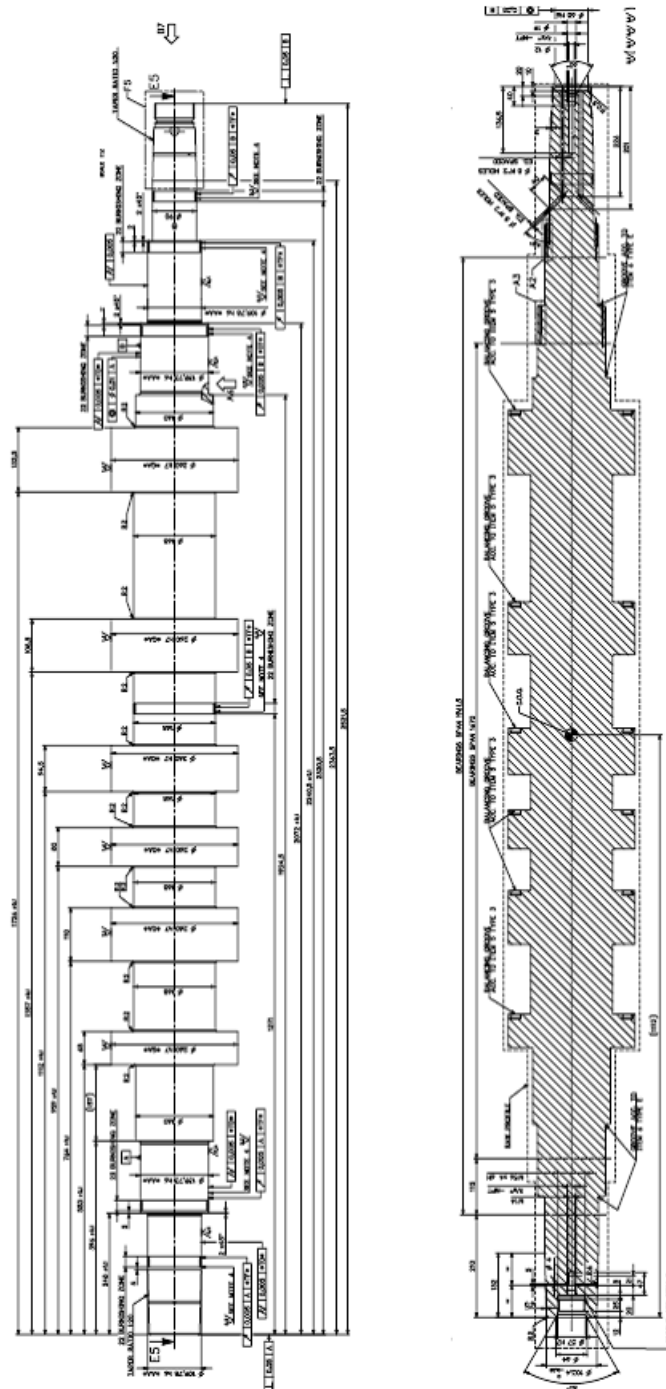


Figure 2.7: Constructive drawing for the considered rotor of a centrifugal compressor. All data are “owned and reserved” and obtained by permission of GE O&G Nuovo Pignone “GE ©2014 - All Rights Reserved”

## Step 1: Fluid dynamical aspects

The first modeling step realized for the development of a complete tilting pad journal bearing model concerns the comprehension and the representation of the typical fluid dynamical characteristics of a TPJB. The model has been developed in order to correctly represent the forces due to the oil film pressure, the motion of the mechanical components of the system and the dynamical behavior of the lubricant supply plant, and order to validate the fluid dynamical results obtainable from a single bearing model.

In the following sections the components of the model, the modeling approach and the numerical tools used to develop and solve the model will be explained in detail.

### 3.1 Softwares

The first model is based, as previously illustrated, on the coupled use of two commercial softwares: *COMSOL Multiphysics*<sup>®</sup>4.4 for the modeling of the oil film and the solution of the Reynolds equation and *MATLAB*<sup>®</sup>R2013a for the assembly of the whole rotor-bearing model and its time dependent solution.

*COMSOL Multiphysics*<sup>®</sup>4.4 is a software that allows to perform analyses and simulations of various physical phenomena through the Finite Elements Method, with the possibility to couple different phenomena (whence the attribute *multiphysics*). Like many other FEM programs *COMSOL Multiphysics*<sup>®</sup>4.4 allows to work on the model geometry, realizing it directly or importing it from a CAD software. Furthermore it is possible to modify the equations that rule the considered physics: the physics modules implemented in the software are already provided with all the equations needed by the respective physical phenomena but it is always possible to modify them or to add other equations in order to develop a model more consistent with the characteristic of a specific project.

In this thesis, the *MEMS* module (acronym of *MicroElectroMechanical Systems*) has been used, in order to analyze systems with micrometer dimensions, in particular taking advantage of the *Thin - Film Flow Branch* interface, an interface specifically developed for lubrication analyses (Figure 3.1). The generic scheme of a system modeled through

PHYSICS INTERFACE	ID	SPACE DIMENSION	GEOMETRIC ENTITY LEVEL
Thin-Film Flow, Shell	tfs	3D	Boundaries
Thin-Film Flow, Edge	tfs	2D, 2D axisymmetric	Boundaries
Thin-Film Flow, Domain	tff	2D	Domains

Figure 3.1: Typical analyses with the *Thin Film Flow* interface

the *Thin - Film Flow* interface is reported in Figure 3.2: it is a thin fluid film enclosed between two solid surfaces in relative motion, represented in the numerical model as a bidimensional surface; the hypothesis underlying this model is the typical assumption

from the lubrication theory that the total oil film thickness  $h = h_w + h_b$ , where  $h_w$  and  $h_b$  are respectively the distances of the *solid wall* and the *channel base* from a central reference surface, is much smaller than the other characteristic dimensions of the system. The body in the upper position is denoted in *COMSOL Multiphysics*<sup>®</sup>4.4 as *moving solid*: it is the solid supported by the lubrication effects due to the oil film pressure; the body located beneath the oil film is instead denoted as *channel base* and represents the statoric part of the kinematic couple. Both the elements can perform arbitrary motions; it is

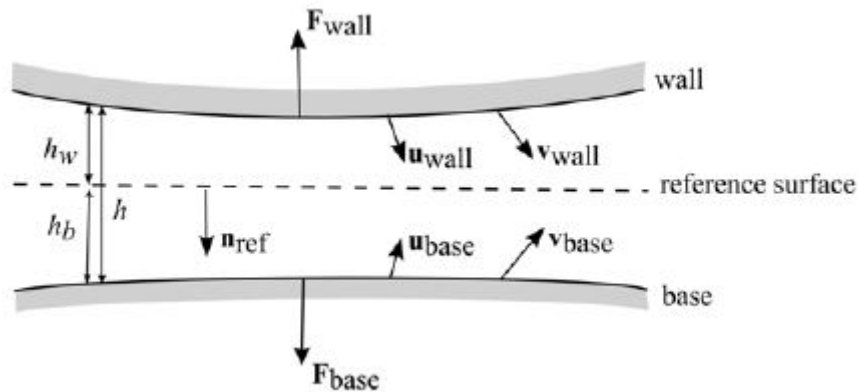


Figure 3.2: *Thin Film Flow* model scheme

possible to distinguish two fundamental situations, where their motion with respect to their boundaries orientation is mainly normal or tangential [20].

*COMSOL Multiphysics*<sup>®</sup>4.4 allows to formulate the lubrication problem represented by the Reynolds equation also in the frequency domain, in addition to its classical formulation. *MATLAB*<sup>®</sup>R2013a is a high level programming language and an interactive environment for numerical computing, analysis, data processing and programming. In this work the *ode15s* solver, implemented in *MATLAB*<sup>®</sup>R2013a for the solution of systems of ordinary differential equations, has been used; its characteristics will be explained in detail later. The softwares used for this work can be connected in real time through a tool denoted as *LiveLink*<sup>®</sup> for *MATLAB*<sup>®</sup>, which allows to use *COMSOL Multiphysics*<sup>®</sup>4.4 directly through *MATLAB*<sup>®</sup>R2013a.



## 3.2 Model structure

In Figure 3.3 the input and output variables of the model components are reported.

The state vector, containing all the dependent variables of the differential equations

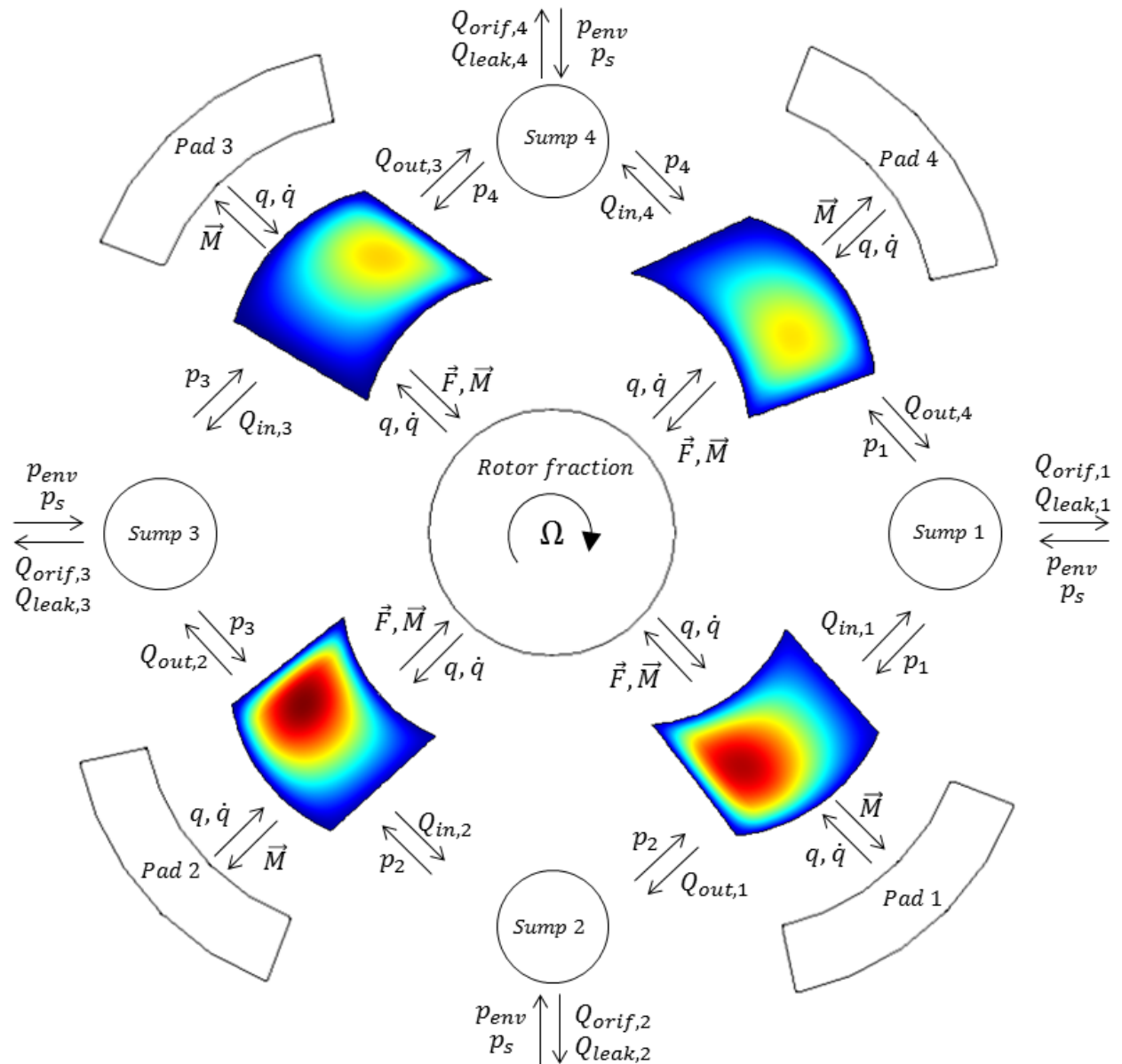


Figure 3.3: Developed model

constituting the model and their first time derivatives, is provided to the *ode15s* solver

with the following formulation:

$$\mathbf{Y} = \left\{ \begin{array}{c} p_{sump,1} \\ \gamma_1 \\ \dot{\gamma}_1 \\ \chi_1 \\ \dot{\chi}_1 \\ \vdots \\ \vdots \\ x \\ \dot{x} \\ \phi_y \\ \dot{\phi}_y \\ y \\ \dot{y} \\ \phi_{x'} \\ \dot{\phi}_{x'} \\ z \\ \dot{z} \\ \vartheta \\ \dot{\vartheta} \end{array} \right\} \quad (3.1)$$

The  $i$ -th oil film model, solved in *COMSOL Multiphysics*<sup>®</sup>4.4, provides the forces  $F_{xA,i}$ ,  $F_{yA,i}$ ,  $F_{zA,i}$  and moments  $M_{xA,i}$ ,  $M_{yA,i}$ ,  $M_{zA,i}$  to the rotor fraction model, the moments  $M_{tilt,i}$  e  $M_{pitch,i}$  needed to solve the pad dynamical model and the flow rates  $Q_{in,i}$ ,  $Q_{out,i}$ ,  $Q_{left,i}$  e  $Q_{right,i}$  then provided as inputs to the supply plant model. The  $i$ -th pad dynamical model receives as inputs the moments due to the oil film and provides as outputs its rotation angles  $\gamma_i$  and  $\chi_i$  and their velocities. The  $i$ -th sump performs a flow balance and provides its pressure  $p_{sump,i}$ , needed as a boundary conditions on the leading edge of the  $i$ -th pad and on the trailing edge of the  $(i - 1)$ -th pad; the inputs of the model are

the flow rates calculated with the oil film model and the supply and leakage flow rates, respectively  $Q_{orif,i}$  and  $Q_{leak,i}$ , computed within the sump model itself with respect to the supply and environment pressure. The dynamical model of the rotor fraction, receives the forces and moments exerted by the oil films and provides its translational and rotational positions  $x, y, z, \phi_y, \phi_{x'}, \vartheta$  and velocities.

## 3.3 Oil film modeling

The fundamental component of the developed bearing model is the FEM model of the oil film interposed between the tilting pads and the rotor. The solution of the fluid dynamical problems allows to compute all the quantities needed to determine the temporal evolution of the remaining components. In the following section, the fundamentals of the classical lubrication theory will be explained, to provide a useful basis for the understanding of the proposed model.

### 3.3.1 Lubrication theory

In generic terms, a *machine* is a group of components arranged in order to do work, moving subjected to appropriate forces. Two components in contact with each other on portions of their surfaces constitute a *kinematic couple*. In the mechanical field kinematic couples are an essential element: with their specific configuration they define the motion and the forces exerted on the components. Generally in systems where the constituting components are in relative motion (i.e. when the kinematic couple leaves at least one unconstrained degree of freedom) the direct contact between the kinematic surfaces is partially or completely avoided in order to reduce the friction coefficient due to the contact between solid elements, the energy dissipation caused by the surfaces overheating and the wear of the components. The free space between the surfaces of the kinematic couple can be filled with a lubricant fluid (liquid or gas depending on the specific application), which must be able to react to the normal forces exchanged by the members of the couple and to generate small tangential forces [21].

The lubrication of a kinematic couple can be classified as follows:

- dry contact between low friction surfaces (e.g. bushing);
- boundary lubrication, where the contact is still present but the lubricant is able to sensibly reduce the friction coefficient;

- mixed lubrication, where the metal-metal contact occurs only where the surfaces rugosity is higher;
- fluid dynamical lubrication, where the relative motion of the couple elements generates a supporting effect and the contact can be completely avoided;
- fluid static lubrication, where an external device generates an overpressure in the oil film in order to avoid contact even in absence of relative motion.

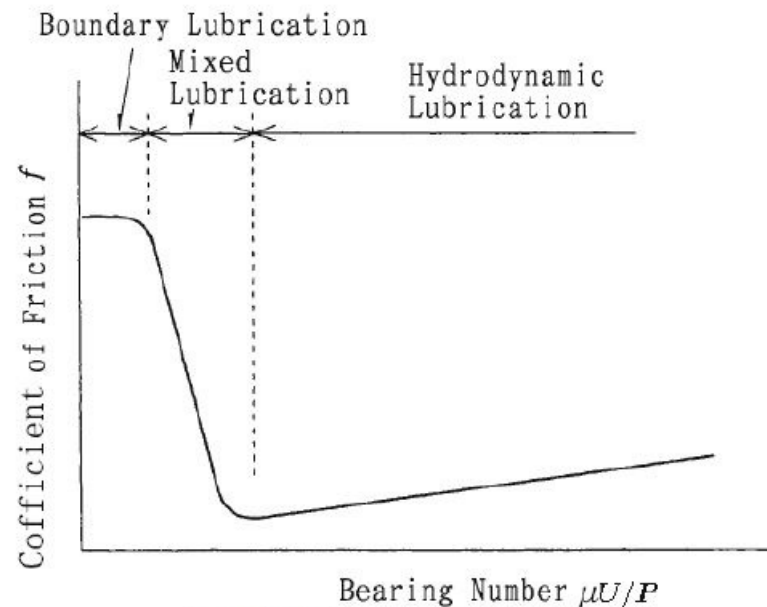


Figure 3.4: Stribeck diagram

Lubrication is a fluid dynamical phenomenon and consequently can be represented through the Navier-Stokes equations. Given the geometrical and physical peculiarities of a lubrication problem, these complex equations can be simplified obtaining the Reynolds equation; the fluids considered in order to accomplish this simplification are Newtonian fluids characterized by a viscosity which depends only on temperature and pressure. The viscosity is a fundamental parameter in lubrication applications since it represents a measure of the resistance opposed by the fluid to be dragged by tangential forces. The viscosity generates in the fluid a velocity gradient (that in a fluid dynamical analysis leads

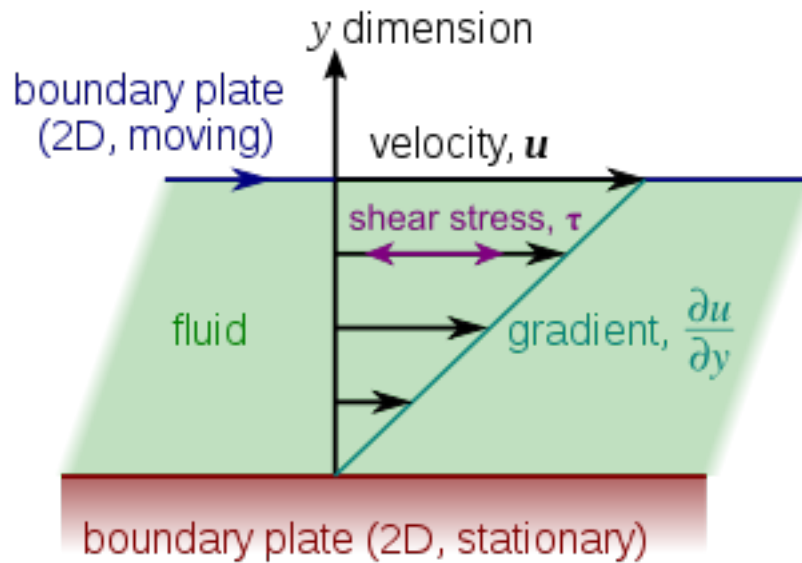


Figure 3.5: Bi-dimensional motion of the fluid inside the oil film

to the definition of the boundary layer) directly connected to its definition:

$$\mu = \frac{F h}{A u}, \quad (3.2)$$

where  $F$  is the force acting on the considered kinematic element,  $A$  and  $h$  define the geometry of the fluid volume and  $u$  is the fluid velocity. From the definition it can be noted that viscosity is measured in  $[Pa \cdot s]$ .

The ability of the fluid to react to normal forces originates from the presence, inside the oil film, of a pressure field assuming higher values with respect to the external pressure; this overpressure can be generated by the coupled effects of the oil film geometry and of the fluid velocity field (for the fluid dynamical lubrication) or by the action of an external supply device (for the fluid static lubrication).

The physical system analyzed according to the Reynolds equation is composed by two elements in relative motion with a fluid interposed. The oil film thickness is smaller than the other characteristic dimensions of the system and this allows for some fundamental simplification with respect to a complete fluid dynamical analysis such as the possibility to neglect the curvature of the surfaces enclosing the fluid. Furthermore it can be assumed

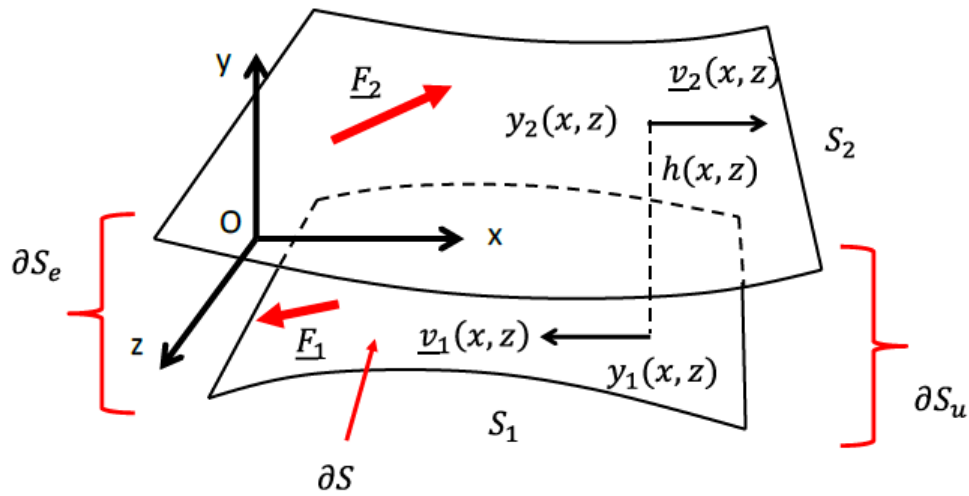


Figure 3.6: Physical system analyzed according to the Reynolds equation

that the flow is in steady state conditions inside the control volume that contains the oil film. It is possible to formulate a problem where the dimensions of the oil film and the motions of the elements of the kinematic couple are known and the pressure (and the fluid stress distribution) and velocity fields inside the oil film, the forces due to the overpressure and the flow rate needed to maintain the desired operating conditions are calculated through the solution of the Reynolds equation.  $S_1$  and  $S_2$  denote the geometry of the two boundaries that enclose the oil film and  $\partial S_e$  and  $\partial S_u$  denote the surfaces where the lubricant enter or exit the control volume. With respect to the fixed reference system, the velocities  $\mathbf{v}_1 = [u_1(x, z) \ v_1(x, z) \ w_1(x, z)]^T$  and  $\mathbf{v}_2 = [u_2(x, z) \ v_2(x, z) \ w_2(x, z)]^T$  (supposed known) identify the motions of the two kinematic elements and the vectors  $\mathbf{F}_1$  and  $\mathbf{F}_2$  represent the forces acting on them. The assumptions necessary to simplify the problem are the following:

- the flow inside the oil film is laminar and in steady state conditions;
- mass and inertia forces acting on the fluid can be neglected with respect to viscous forces;

- the fluid is incompressible and homogeneous inside the oil film;
- the fluid viscosity is uniform inside the oil film.

Under these hypotheses it is possible to formulate the fluid stress tensor as follows:

$$\sigma_{ij} = -p\delta_{ij} + \mu \left( \frac{\partial v_j}{\partial x_i} + \frac{\partial v_i}{\partial x_j} \right), \quad (3.3)$$

where  $p$  is the pressure inside the oil film,  $\delta_{ij}$  is the Kronecker delta,  $v_i$  is a generic component of the velocity vector and  $x_i$  is the generic spatial variable. Navier-Stokes and continuity equations can be simplified as follows:

$$-\nabla p + \mu \Delta \mathbf{v} = 0, \quad (3.4)$$

$$\operatorname{div} \mathbf{v} = 0, \quad (3.5)$$

and need the following boundary conditions:

$$\mathbf{v} = \mathbf{v}_1 \quad \text{on} \quad S_1, \quad (3.6)$$

$$\mathbf{v} = \mathbf{v}_2 \quad \text{on} \quad S_2, \quad (3.7)$$

$$p = p_a \quad \text{on} \quad \partial S, \quad (3.8)$$

where  $p_a$  is the environment pressure.

In the extended formulation, the problem is represented by the following system of equations:

$$\left\{ \begin{array}{l} -\frac{\partial p}{\partial x} + \mu \left( \frac{\partial^2 u}{\partial x^2} + \frac{\partial^2 u}{\partial y^2} + \frac{\partial^2 u}{\partial z^2} \right) = 0 \\ -\frac{\partial p}{\partial y} + \mu \left( \frac{\partial^2 v}{\partial x^2} + \frac{\partial^2 v}{\partial y^2} + \frac{\partial^2 v}{\partial z^2} \right) = 0 \\ -\frac{\partial p}{\partial z} + \mu \left( \frac{\partial^2 w}{\partial x^2} + \frac{\partial^2 w}{\partial y^2} + \frac{\partial^2 w}{\partial z^2} \right) = 0 \\ u = u_1 \quad v = v_1 \quad w = w_1 \quad \text{on} \quad S_1 \\ u = u_2 \quad v = v_2 \quad w = w_2 \quad \text{on} \quad S_2 \\ p = p_a \quad \text{on} \quad \partial S \end{array} \right. \quad (3.9)$$



Considering the typical lubrication problems represented by the previous equations, it is possible to introduce other simplifying hypotheses; they are the following:

- the  $v$  component of the velocity vector and its first and second spatial derivatives can be neglected inside the oil film (with the exception of the areas near the border  $S_1$  and  $S_2$ ), in order to neglect the fluid motion in the vertical direction;
- the first and second spatial derivatives of the velocity components  $u$  and  $w$  with respect to  $x$  and  $z$  can be neglected compared to their derivatives with respect to  $y$  and with respect pressure, in order to neglect tangential stresses generated by velocity variations in the  $x$  and  $y$  directions.

The equations of motion assume the following form:

$$\begin{cases} \frac{\partial p}{\partial x} = \mu \frac{\partial^2 u}{\partial y^2} \\ \frac{\partial p}{\partial y} = 0 \\ \frac{\partial p}{\partial z} = \mu \frac{\partial^2 w}{\partial y^2} \end{cases}, \quad (3.10)$$

where the pressure  $p$  is not a function of  $y$ , i.e.  $p = p(x, z)$ . Integrating the first and the third equations and using the previously shown boundary conditions, it is possible to obtain the following pressure dependent formulation of the velocity components:

$$u = \frac{1}{2\mu} \frac{\partial p}{\partial x} (y - y_1)(y - y_2) + \frac{u_2 - u_1}{y_2 - y_1} (y - y_1) + u_1, \quad (3.11)$$

$$w = \frac{1}{2\mu} \frac{\partial p}{\partial z} (y - y_1)(y - y_2) + \frac{w_2 - w_1}{y_2 - y_1} (y - y_1) + w_1. \quad (3.12)$$

To solve the lubrication problem and calculate the three variables  $u$ ,  $w$  and  $p$ , it is possible to integrate the continuity equation with respect to  $y$ :

$$\int_{y_1}^{y_2} \frac{\partial u}{\partial x} dy + \int_{y_1}^{y_2} \frac{\partial w}{\partial z} dy = - \int_{y_1}^{y_2} \frac{\partial v}{\partial y} dy = - (v_2 - v_1). \quad (3.13)$$

Solving the integrals and introducing the oil film thickness (supposed known) as follows:

$$h(x, z) = y_2(x, z) - y_1(x, z), \quad (3.14)$$

it is possible to obtain the following partial derivatives equation where the only dependent variable is the pressure  $p$ :

$$\begin{aligned} \frac{\partial}{\partial x} \left( h^3 \frac{\partial p}{\partial x} \right) + \frac{\partial}{\partial z} \left( h^3 \frac{\partial p}{\partial z} \right) = 12\mu (v_2 - v_1) + 6\mu h \left[ \frac{\partial(u_1+u_2)}{\partial x} + \frac{\partial(w_1+w_2)}{\partial z} \right] + \\ -6\mu \left[ (u_2 - u_1) \frac{\partial(y_1+y_2)}{\partial x} + (w_2 - w_1) \frac{\partial(y_1+y_2)}{\partial z} \right]. \end{aligned} \quad (3.15)$$

This equation is known as the generalized Reynolds equation and is representative of large part of practical lubrication problems. The left part of the equation represents the action of the pressure  $p$  on the fluid motion inside the oil film; the first term of the right part is the squeeze term (since it is due to the normal motion of the two elements of the kinematic couple), while the second and the third terms are purely hydrodynamic terms, due to the drag effect exerted by the solid boundary of the oil film on the fluid.

With this equation, imposing appropriate pressure boundary conditions and supposing to know the velocity and the geometry of the kinematic couple, it is possible to determine the pressure and velocity fields for the fluid inside the oil film.

Furthermore, it is possible to calculate the external loads needed to maintain the motion of the kinematic couple:

$$\mathbf{F}_1 = \int_{S_1} (\boldsymbol{\sigma} \cdot \mathbf{n}_1 + p_a \mathbf{n}_1) dS_1, \quad (3.16)$$

$$\mathbf{F}_2 = \int_{S_2} (\boldsymbol{\sigma} \cdot \mathbf{n}_2 + p_a \mathbf{n}_2) dS_2, \quad (3.17)$$

where  $\mathbf{n}_1$  and  $\mathbf{n}_2$  are the normalized normal vectors respectively of the surfaces  $S_1$  and  $S_2$  and the fluid stress tensor can be expressed as follows:

$$\boldsymbol{\sigma} = \begin{bmatrix} \sigma_x & \tau_{xy} & \tau_{xz} \\ \dots & \sigma_y & \tau_{yz} \\ \dots & \dots & \sigma_z \end{bmatrix} = \begin{bmatrix} -p & \mu \frac{\partial u}{\partial y} & \mu \left( \frac{\partial w}{\partial x} + \frac{\partial u}{\partial z} \right) \\ \dots & -p & \mu \frac{\partial w}{\partial y} \\ \dots & \dots & -p \end{bmatrix}. \quad (3.18)$$

Finally, it is possible to calculate the lubricant flow rate  $Q$  needed for the correct operation of the kinematic couple:

$$Q = \int_{\partial S_u} \mathbf{v} \cdot \mathbf{n} dS = - \int_{\partial S_e} \mathbf{v} \cdot \mathbf{n} dS, \quad (3.19)$$

where  $\mathbf{n}$  is the normalized normal vector for the oil film boundary  $\partial S$ .

### 3.3.2 Oil film sub-model

Through the CAD tool implemented in *COMSOL Multiphysics*®4.4 it is possible to draw the geometric surface where the Reynolds equation must be solved. In order to solve

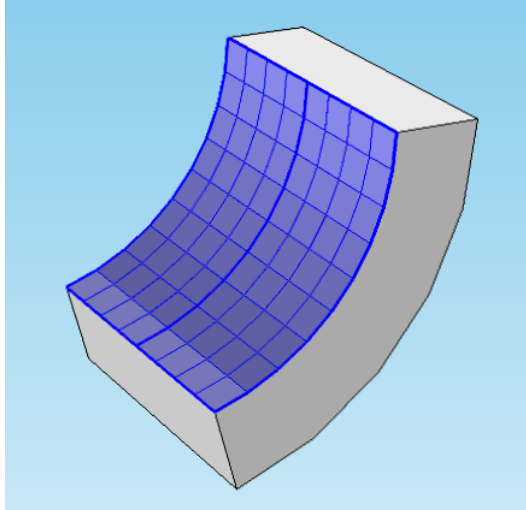


Figure 3.7: 3D pad model with 2D oil film mesh

this equation, it is necessary to implement in the model some mathematical functions representative of the rotor fraction peripheral speed (i.e. the *channel base* velocity) and the oil film thickness. Typically, to efficiently complete this calculation, all the relative motions between the two moving solid are assigned to only one of them: the *solid wall* (i.e. the pad surface) is assumed to have zero velocity and to develop the oil film thickness formulation all the relative motions are assigned to *channel base*.

Referring to a fixed reference system with its origin in the geometric center of the bearing, it is necessary to use the following rotation matrices (see Figure 3.8):

$$\mathbf{R}_1 = \begin{bmatrix} 1 & 0 & 0 \\ 0 & \cos \phi_{x'} & \sin \phi_{x'} \\ 0 & -\sin \phi_{x'} & \cos \phi_{x'} \end{bmatrix}, \quad (3.20)$$

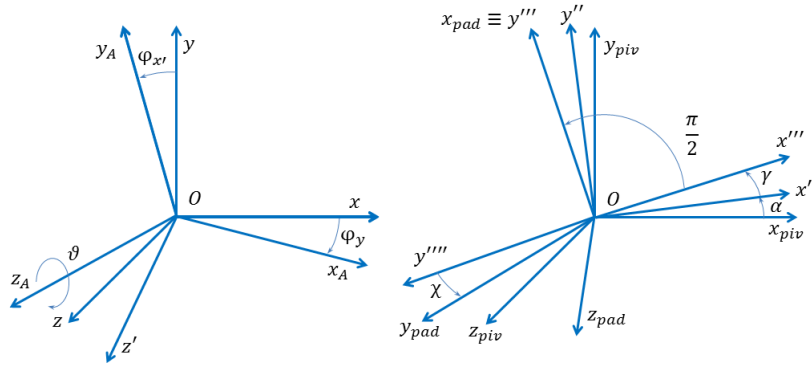


Figure 3.8: Reference systems

$$\mathbf{R}_2 = \begin{bmatrix} \cos \phi_y & 0 & -\sin \phi_y \\ 0 & 1 & 0 \\ \sin \phi_y & 0 & \cos \phi_y \end{bmatrix}, \quad (3.21)$$

$$\mathbf{R}_3 = \begin{bmatrix} \cos \theta & \sin \theta & 0 \\ -\sin \theta & \cos \theta & 0 \\ 0 & 0 & 1 \end{bmatrix}, \quad (3.22)$$

where  $\mathbf{R}_1$  represents the rotor fraction pitch motion,  $\mathbf{R}_2$  represents its yaw motion and  $\mathbf{R}_3$  takes into account the rotor spin speed and allows to introduce the moving reference system rigidly connected to the rotor fraction.

Referring to this moving reference system it is possible to identify, through the cylindrical coordinates  $z_A$  and  $\varphi$ , the position of a generic point located on the rotor surface:

$$\mathbf{M}^A = \begin{Bmatrix} (R - h_0) \cos \varphi \\ (R - h_0) \sin \varphi \\ z_A \end{Bmatrix}, \quad (3.23)$$

where  $R$  and  $h_0$  are the bearing radius and clearance. Referring then to the fixed reference system located in the bearing center (considering the rotor generic motion), this point can be identified as follows:

$$\mathbf{M} = \mathbf{O}\mathbf{O}_A + \mathbf{R}_1^T \mathbf{R}_2^T \mathbf{R}_3^T \mathbf{M}^A. \quad (3.24)$$

Calculating the matrices products, linearizing the trigonometric functions and neglecting the second order terms, it is possible to obtain the following vector for the identification of the generic rotor surface point:

$$\mathbf{M} = \left\{ \begin{array}{l} x_{O_A} + (R - h_0) \cos(\varphi + \theta) + z\phi_y \\ y_{O_A} + (R - h_0) \sin(\varphi + \theta) - z\phi_{x'} \\ z_{O_A} - (R - h_0)\phi_y \cos(\varphi + \theta) + (R - h_0)\phi_{x'} \sin(\varphi + \theta) + z \end{array} \right\}, \quad (3.25)$$

and this, through a time derivative, with  $\Omega = \dot{\theta}$ , it is then possible to calculate its velocity:

$$\mathbf{v}_M = \left\{ \begin{array}{l} U \\ V \\ W \end{array} \right\} = \left\{ \begin{array}{l} \dot{x}_{O_A} - (R - h_0)\Omega \sin\varphi + z\dot{\phi}_y \\ \dot{y}_{O_A} + (R - h_0)\Omega \cos\varphi - z\dot{\phi}_{x'} \\ \dot{z}_{O_A} + (R - h_0) \left[ (\Omega\phi_{x'} - \dot{\phi}_y) \cos\varphi + (\Omega\phi_y + \dot{\phi}_{x'}) \sin\varphi \right] \end{array} \right\}. \quad (3.26)$$

With an analogous procedure it is then possible to find an analytical expression that

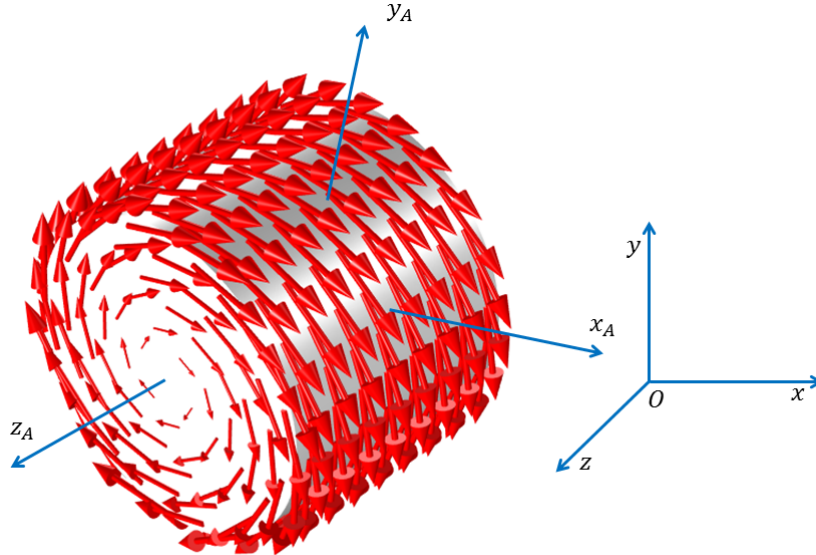


Figure 3.9: Rotor peripheral velocity

allows to calculate the oil film thickness from the rotor and pads positions and velocities. Neglecting the rotor proper rotation, it is necessary to express the position of a generic point on the rotor surface in the reference system rigidly connected to the pad; thus two

further rotations (i.e. the two possible tilt angles of the pad) must be taken into account, in addition to the necessary translations. In order to identify the oil film thickness, it is finally necessary to calculate the difference between the coordinates of the rotor point and those of the corresponding point on the pad surface. For the generic rotor point, identifying for the sake of synthesis the vector components with  $a$ ,  $b$  and  $c$ , the coordinates are the following:

$$\begin{aligned} \mathbf{M} &= \mathbf{OO}_A + \mathbf{R}_1^T \mathbf{R}_2^T \mathbf{M}^A = \\ &= \left\{ \begin{array}{l} x_{O_A} + (R - h_0) \cos \varphi \cos \phi_y + z \phi_y \\ y_{O_A} + (R - h_0) \cos \varphi \sin \phi_{x'} \sin \phi_y + (R - h_0) \sin \varphi \cos \phi_{x'} - z \sin \phi_{x'} \cos \phi_y \\ z_{O_A} - (R - h_0) \cos \varphi \cos \phi_{x'} \sin \phi_y + (R - h_0) \sin \varphi \sin \phi_{x'} + z \cos \phi_{x'} \cos \phi_y \end{array} \right\} \quad (3.27) \\ &= \left\{ \begin{array}{l} a \\ b \\ c \end{array} \right\}. \end{aligned}$$

Identifying with  $\alpha$  the pivot angle with respect to the fixed central reference system,  $\mathbf{M}$  can be formulated in the reference system with the same orientation of the fixed one and with its origin in correspondence of the pivot as follows:

$$\mathbf{M}_{piv} = \left\{ \begin{array}{l} a - R \cos \alpha \\ b - R \sin \alpha \\ c \end{array} \right\}. \quad (3.28)$$

To take into account a reference system rotation of  $\alpha$ , the two tilt angles  $\gamma$  and  $\chi$ , and a further  $\frac{\pi}{2}$  rotation (in order to correctly orient the normal vectors of the pad surface), the following rotation matrices must be used:

$$\mathbf{R}_4 = \begin{bmatrix} \cos \alpha & \sin \alpha & 0 \\ -\sin \alpha & \cos \alpha & 0 \\ 0 & 0 & 1 \end{bmatrix}, \quad (3.29)$$

$$\mathbf{R}_5 = \begin{bmatrix} \cos \gamma & \sin \gamma & 0 \\ -\sin \gamma & \cos \gamma & 0 \\ 0 & 0 & 1 \end{bmatrix} \approx \begin{bmatrix} 1 & \gamma & 0 \\ -\gamma & 1 & 0 \\ 0 & 0 & 1 \end{bmatrix}, \quad (3.30)$$

$$\mathbf{R}_6 = \begin{bmatrix} \cos \chi & 0 & -\sin \chi \\ 0 & 1 & 0 \\ \sin \chi & 0 & \cos \chi \end{bmatrix} \approx \begin{bmatrix} 1 & 0 & -\chi \\ 0 & 1 & 0 \\ \chi & 0 & 1 \end{bmatrix}, \quad (3.31)$$

$$\mathbf{R}_7 = \begin{bmatrix} \cos \frac{\pi}{2} & \sin \frac{\pi}{2} & 0 \\ -\sin \frac{\pi}{2} & \cos \frac{\pi}{2} & 0 \\ 0 & 0 & 1 \end{bmatrix} = \begin{bmatrix} 0 & 1 & 0 \\ -1 & 0 & 0 \\ 0 & 0 & 1 \end{bmatrix}, \quad (3.32)$$

where  $\mathbf{R}_4$  represents the pivot angular position,  $\mathbf{R}_5$  and  $\mathbf{R}_6$  represent the two pad tilt angles (being small angles the respective rotation matrices can be linearized) and  $\mathbf{R}_7$  takes into account the orientation of the *solid wall* normal vectors required by the software (they must be pointing towards the bearing center). The rotor point is then expressed as follows:

$$\mathbf{M}_{pad} = \mathbf{R}_4 \mathbf{R}_5 \mathbf{R}_6 \mathbf{R}_7 \mathbf{M}_{piv}. \quad (3.33)$$

To identify the coordinate of the generic point on the pad surface, a further reference system due to the bearing preload must be considered, denoting with  $\beta$  the angular coordinate of the point in the preloaded reference system. The reference system changes performed for the pad point are the following:

$$\mathbf{P}_{prel} = \begin{Bmatrix} (R + CC) \cos \beta \\ (R + CC) \sin \beta \\ z \end{Bmatrix}, \quad (3.34)$$

$$\mathbf{P}_{piv} = \begin{Bmatrix} (R + CC) \cos \beta - (R + CC) \cos \alpha \\ (R + CC) \sin \beta - (R + CC) \sin \alpha \\ z \end{Bmatrix}, \quad (3.35)$$

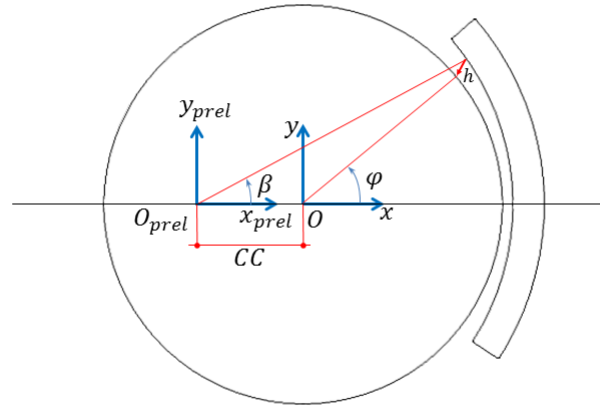


Figure 3.10: Bearing preload and reference angles

$$\mathbf{P}_{pad} = \mathbf{R}_4 \mathbf{R}_7 \mathbf{P}_{piv}. \quad (3.36)$$

Finally the two position vectors expressed in the same reference system can be compared, evaluating their difference and formulating the oil film thickness as follows:

$$\begin{aligned} h = \mathbf{M}_{pad}|_y - \mathbf{P}_{pad}|_y = & -[x_{O_A} + (R - h_0) \cos \varphi \cos \phi_y + z \sin \phi_y - R \cos \alpha] \cos \alpha + \\ & -[y_{O_A} + (R - h_0) \cos \varphi \sin \phi_{x'} \sin \phi_y + (R - h_0) \sin \varphi \cos \phi_{x'} - z \sin \phi_{x'} \cos \phi_y + \\ & -R \sin \alpha] \sin \alpha - \gamma [(R \cos \alpha - x_{O_A} - (R - h_0) \cos \varphi \cos \phi_y - z \sin \phi_y) \sin \alpha + \\ & + (y_{O_A} + (R - h_0) \cos \varphi \sin \phi_{x'} \sin \phi_y + (R - h_0) \sin \varphi \cos \phi_{x'} - z \sin \phi_{x'} \cos \phi_y + \\ & -R \sin \alpha) \cos \alpha] + \chi [z_{O_A} - (R - h_0) \cos \varphi \cos \phi_{x'} \sin \phi_y + (R - h_0) \sin \varphi \cos \phi_{x'} + \\ & + z \cos \phi_{x'} \cos \phi_y] + (R + CC) (\cos \beta - \cos \alpha) \cos \alpha + (R + CC) (\sin \beta - \sin \alpha) \sin \alpha. \end{aligned} \quad (3.37)$$

COMSOL *Multiphysics*®4.4 includes a vast lubricant library, useful for different kinds of analyses. In the proposed model, in order to obtain results as near as possible to the experimental data used for the validation, a custom lubricant model has been implemented to better represent the properties of the fluid used in the real bearing. The considered lubricant is denominated *ISO VG32* by ISO standards. Fluid properties have been modeled through polynomial equations as functions of the fluid temperature and pressure. Polynomial equations allows to simplify the numerical operations inside



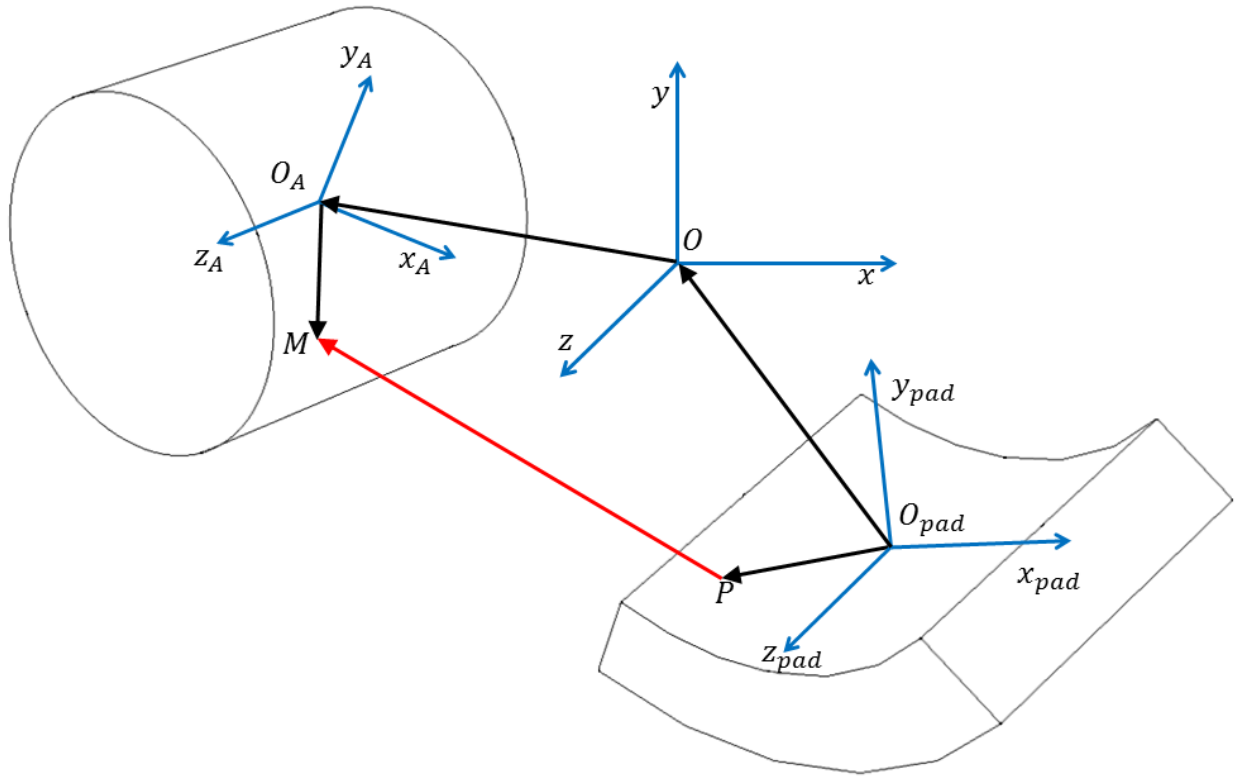


Figure 3.11: Oil film thickness

the model, in particular referring to the possibility to perform exact derivatives while maintaining a satisfying level of approximation. The considered properties are four; the specific volume is calculated as follows:

$$\nu_s = \frac{1}{\rho} = \nu_{s0} \left[ 1 + a_{p1} (p - p_{ref}) + a_{p2} (p - p_{ref})^2 + a_{t1} (T - T_{ref}) + a_{t2} (T - T_{ref})^2 + a_{pt} (p - p_{ref}) (T - T_{ref}) \right]; \quad (3.38)$$

the absolute viscosity is computed according to the following equation:

$$\mu = \mu_0 10^\psi, \quad (3.39)$$

where:

$$\psi = b_{p1} (p - p_{ref}) + b_{t1} (T - T_{ref}) + b_{t2} (T - T_{ref})^2; \quad (3.40)$$



the pad edges; all these information are exchanged continuously during the simulation of the model since they are provided by the ODE components of the model; the fluid dynamical problem, after the calculation of the pressure field, can provide to the other models its outputs.

In particular, the quantities calculated from the solution of the pressure field are the lubricant flow rates and the forces and moments exerted on rotor and pad. Identifying

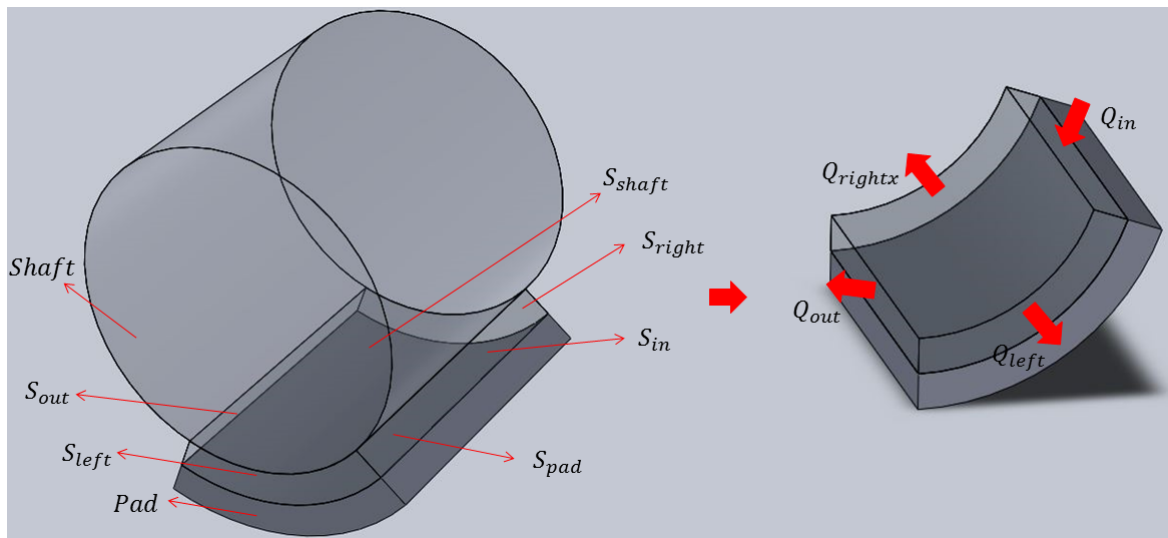


Figure 3.13: Control volume

the boundaries of the control volume enclosing the oil film as reported in Figure 3.13, it is possible to compute the pad edges lubricant flow rates as follows:

$$Q_{in} = \int_{S_{in}} \mathbf{v} \cdot \mathbf{n} dS, \quad (3.43)$$

$$Q_{out} = \int_{S_{out}} \mathbf{v} \cdot \mathbf{n} dS, \quad (3.44)$$

$$Q_{left} = \int_{S_{left}} \mathbf{v} \cdot \mathbf{n} dS, \quad (3.45)$$

$$Q_{right} = \int_{S_{right}} \mathbf{v} \cdot \mathbf{n} dS. \quad (3.46)$$

In order to compute the forces, by integrating the pressure field on the pad surface it is possible to obtain the loads acting on it. For the rotor the direct integration is not possible since in the developed oil film model the only physical surface is the pad one: it is necessary to perform a force balance imposing the equilibrium of the control volume in order to obtain the loads exerted on the rotor fraction. Identifying with  $\mathbf{f} = [f_x, f_y, f_z]^T$  the surface forces due to the fluid stress, the following forces and moments exerted on the rotor by the  $i$ -th pad can be computed:

$$F_{xA,i} = - \int_{S_{in,i}} f_x dS - \int_{S_{out,i}} f_x dS - \int_{S_{pad,i}} f_x dS - \int_{S_{right,i}} f_x dS - \int_{S_{left,i}} f_x dS, \quad (3.47)$$

$$F_{yA,i} = - \int_{S_{in,i}} f_y dS - \int_{S_{out,i}} f_y dS - \int_{S_{pad,i}} f_y dS - \int_{S_{right,i}} f_y dS - \int_{S_{left,i}} f_y dS, \quad (3.48)$$

$$F_{zA,i} = - \int_{S_{in,i}} f_z dS - \int_{S_{out,i}} f_z dS - \int_{S_{pad,i}} f_z dS - \int_{S_{right,i}} f_z dS - \int_{S_{left,i}} f_z dS, \quad (3.49)$$

$$\begin{aligned} M_{xA,i} = & - \int_{S_{in,i}} -f_y \cdot z dS - \int_{S_{out,i}} -f_y \cdot z dS - \int_{S_{pad,i}} -f_y \cdot z dS - \int_{S_{right,i}} -f_y \cdot z dS + \\ & - \int_{S_{left,i}} -f_y \cdot z dS - \int_{S_{in,i}} f_z \cdot y dS - \int_{S_{out,i}} f_z \cdot y dS - \int_{S_{pad,i}} f_z \cdot y dS + \\ & - \int_{S_{right,i}} f_z \cdot y dS - \int_{S_{left,i}} f_z \cdot y dS, \end{aligned} \quad (3.50)$$

$$\begin{aligned} M_{yA,i} = & - \int_{S_{in,i}} f_x \cdot z dS - \int_{S_{out,i}} f_x \cdot z dS - \int_{S_{pad,i}} f_x \cdot z dS - \int_{S_{right,i}} f_x \cdot z dS + \\ & - \int_{S_{left,i}} f_x \cdot z dS - \int_{S_{in,i}} -f_z \cdot x dS - \int_{S_{out,i}} -f_z \cdot x dS + \\ & - \int_{S_{pad,i}} -f_z \cdot x dS - \int_{S_{right,i}} -f_z \cdot x dS - \int_{S_{left,i}} -f_z \cdot x dS, \end{aligned} \quad (3.51)$$

$$\begin{aligned} M_{zA,i} = & - \int_{S_{in,i}} -f_x \cdot y dS - \int_{S_{out,i}} -f_x \cdot y dS - \int_{S_{pad,i}} -f_x \cdot y dS - \int_{S_{right,i}} -f_x \cdot y dS + \\ & - \int_{S_{left,i}} -f_x \cdot y dS - \int_{S_{in,i}} f_y \cdot x dS - \int_{S_{out,i}} f_y \cdot x dS + \\ & - \int_{S_{pad,i}} f_y \cdot x dS - \int_{S_{right,i}} f_y \cdot x dS - \int_{S_{left,i}} f_y \cdot x dS. \end{aligned} \quad (3.52)$$

By summing the contributes of the  $n_p$  pads, the forces and moments acting globally on the rotor can be calculated:

$$F_{xA} = \sum_{i=1}^{n_p} F_{xA,i}, \quad (3.53)$$

$$F_{yA} = \sum_{i=1}^{n_p} F_{yA,i}, \quad (3.54)$$

$$F_{zA} = \sum_{i=1}^{n_p} F_{zA,i}, \quad (3.55)$$

$$M_{xA} = \sum_{i=1}^{n_p} M_{xA,i}, \quad (3.56)$$

$$M_{yA} = \sum_{i=1}^{n_p} M_{yA,i}, \quad (3.57)$$

$$M_{zA} = \sum_{i=1}^{n_p} M_{zA,i}. \quad (3.58)$$

For the pad, the only loads that have to be considered are the moments corresponding to its tilt angles (in order to determine the pad dynamical behavior), referring, for the moments calculation, to the position of the pivot:

$$M_{pitch} = \int_{S_{pad}} f_x \cdot z dS + \int_{S_{pad}} -f_z \cdot (x - R \cos \alpha) dS, \quad (3.59)$$

$$M_{tilt} = \int_{S_{pad}} -f_x \cdot (R \cos \alpha + y) dS + \int_{S_{pad}} f_y \cdot (x - R \cos \alpha) dS. \quad (3.60)$$

## 3.4 Supply sump modeling

In the cavity interposed between two adjacent pads there are some orifices needed to introduce in the bearing the lubricant flow rate coming from the hydraulic network of the power plant, while from its side boundaries the leakage flow rate exits towards the external environment; furthermore, inside the cavity the flow rates exiting an oil film and entering the next mix: the balance between these flow rates affects the pressure level on the pads edges. This fluid cavity, with the duct elements connected to it, has been modeled according to a lumped parameters approach; in the following section the basis of this modeling approach will be explained.

### 3.4.1 Lumped parameters modeling approach

A dynamic system can be modeled as a series of elements that receive from the external environment some inputs and consequently produce certain outputs. For the description of a dynamic system, a set of *state variables* suitable to identify the system configuration in a certain time instant is needed: the representation chosen for the system must provide information concerning the behavior of its outputs as a function of its inputs. The

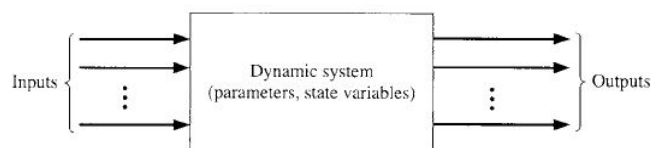


Figure 3.14: Generic dynamic system

lumped parameters modeling approach for dynamic systems is not specifically intended for lubrication applications: indeed it is a tool useful for modeling in many fields of analysis, from mechanics to electromagnetism.

Lumped parameters modeling, particularly for the fluid dynamical field considered in this work, is based on the discretization of the physical system and its properties in

order to obtain a simplified system where the elements, fluid, electrical or structural, are represented by the same formulation. Different elements exchange energy and their formulation is based on the analysis of a control volume with inputs and outputs, according to the typical dynamic system scheme. In order to represent different dynamic system with analogous differential equation it is necessary to identify the analogous variables between the systems as reported in Figure 3.15. The lumped elements that

System type	Mechanical translational	Mechanical rotational	Electrical	Fluid	Thermal
A-type variable	Velocity, $v$	Velocity, $\Omega$	Voltage, $e$	Pressure, $P$	Temperature, $T$
A-type element	Mass, $m$	Mass moment of inertia, $J$	Capacitor, $C$	Fluid Capacitor, $C_f$	Thermal capacitor, $C_h$
Elemental equations	$F = m \frac{dv}{dt}$	$T = J \frac{d\Omega}{dt}$	$i = C \frac{de}{dt}$	$Q_f = C_f \frac{dP}{dt}$	$Q_h = C_h \frac{dT}{dt}$
Energy stored	Kinetic	Kinetic	Electric field	Potential	Thermal
Energy equations	$\mathcal{E}_k = \frac{1}{2}mv^2$	$\mathcal{E}_k = \frac{1}{2}J\Omega^2$	$\mathcal{E}_e = \frac{1}{2}Ce^2$	$\mathcal{E}_p = \frac{1}{2}C_f P^2$	$\mathcal{E}_t = \frac{1}{2}C_h T^2$
T-type variable	Force, $F$	Torque, $T$	Current, $i$	Fluid flow rate, $Q_f$	Heat flow rate, $Q_h$
T-type element	Compliance, $1/k$	Compliance, $1/K$	Inductor, $L$	Inertor, $I$	None
Elemental equations	$v = \frac{1}{k} \frac{dF}{dt}$	$\Omega = \frac{1}{K} \frac{dT}{dt}$	$e = L \frac{di}{dt}$	$P = I \frac{dQ_f}{dt}$	
Energy stored	Potential	Potential	Magnetic field	Kinetic	
Energy equations	$\mathcal{E}_p = \frac{1}{2k}F^2$	$\mathcal{E}_p = \frac{1}{2K}T^2$	$\mathcal{E}_m = \frac{1}{2}Li^2$	$\mathcal{E}_k = \frac{1}{2}IQ_f^2$	
D-type element	Damper, $b$	Rotational damper, $B$	Resistor, $R$	Fluid resistor, $R_f$	Thermal resistor, $R_h$
Elemental equations	$F = bv$	$T = B\Omega$	$i = \frac{1}{R}e$	$Q_f = \frac{1}{R_f}P$	$Q_h = \frac{1}{R_h}T$
Rate of energy dissipated	$\frac{dE_D}{dt} = Fv$ $= \frac{1}{b}F^2$ $= bv^2$	$\frac{dE_D}{dt} = T\Omega$ $= \frac{1}{B}T^2$ $= B\Omega^2$	$\frac{dE_D}{dt} = ie$ $= Ri^2$ $= \frac{1}{R}e^2$	$\frac{dE_D}{dt} = Q_f P$ $= R_f Q_f^2$ $= \frac{1}{R_f} P^2$	$\frac{dE_D}{dt} = Q_h$

Figure 3.15: Variables for lumped parameters modeling approach

constitute a fluid network are denoted (using an electrical notation) as resistive, capacitive and inertial elements, corresponding in the mechanical field to the mass, spring and damper elements typically used for the analyses of linear dynamics (i.e. vibrations mechanical systems); with them it is possible to develop a fluid circuit equivalent to the considered three dimensional system. To formulate the characteristic equations of the lumped elements, the flow in a duct with constant cross section must be considered. A viscous flow generally involves many phenomena that break its uniformity; the lumped parameters modeling approach is based on a one-dimensional representation of the system and assumes the fluid properties to be constant in the duct cross section. It is then

possible to analyze a complex network discretizing it with a certain number of elements with constant properties: these properties can vary inside the element as functions of time but they are spatially uniform. It is possible to use the continuity equation, the energy equation and the momentum equation in order to obtain the formulation of the single lumped elements. It is important to underline that the possible linearity of a lumped parameter model is linked to the constancy of the elements resistance, capacitance and inertia, following the principle to linearize the real system behavior near an operating point.

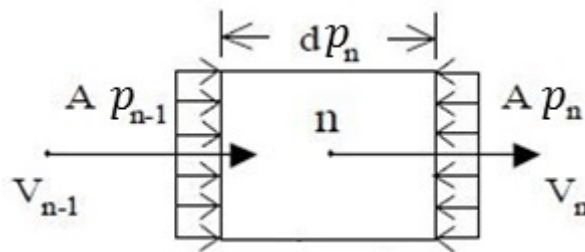


Figure 3.16: Control volume for the  $n$ -th element

### Capacitive element

The capacitance of a fluid is due to the intrinsic compressibility of real fluids; it reveals itself as a mass accumulation or release, related to the mass flow that crosses the boundaries of the considered control volume. The mathematical formulation

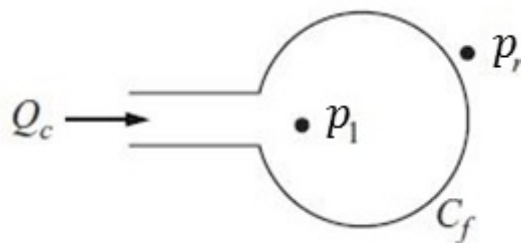


Figure 3.17: Generic capacitive element

representative of the capacitive element can be obtained from the continuity equation,



where the pressure  $p$  inside the element is referred to an external reference pressure  $p_r$ :

$$\frac{\partial}{\partial t} \int_V \rho dV + \int_{\partial V} (\rho \mathbf{v}) \cdot \mathbf{n} dA = 0. \quad (3.61)$$

Referring to Figure 3.17, the flow rate accumulated inside the element is analogous to the electric charge stored inside a capacitor. The fundamental equation of the fluid capacitive element is the following:

$$Q_c = C_f \frac{dp_{1r}}{dt}, \quad (3.62)$$

where  $C_f$  is the fluid *capacitance*. The simplest form of fluid capacitance arises when the compressibility of a fluid, enclosed in a rigid container, is subjected to pressure oscillations due to the variations of the amount of gathered fluid. This pressure variation leads to the definition of the bulk modulus, which represents the pressure variation  $dp$  needed to obtain a certain volume variation  $dV$  for a fluid volume  $V$ . This property is defined as follows:

$$\beta = \frac{dp}{\frac{dV}{V}}. \quad (3.63)$$

The capacitance for a certain volume of fluid inside a rigid vessel can then be calculated according to the following equation:

$$C_f = \frac{V}{\beta}, \quad (3.64)$$

or

$$C_f = \frac{\Delta V}{\Delta p}. \quad (3.65)$$

The capacitive element stores energy proportionally to the square of the variable  $p$ ; this stored potential energy is given by:

$$E_P = \frac{C_f}{2} p_{1r}^2. \quad (3.66)$$

Consequently the capacitive element, with a behavior analogous to that of the mass element in the mechanical field, stores energy and contributes to weaken vibrations and load oscillations within the circuit, thus avoiding, in fluid dynamical field, sudden pressure variations.

### Inertial element

The inertia of a fluid is a characteristic related to its mass and velocity: it is then linked to the fluid motion and kinetic energy. The behavior of the inertial element can be analyzed



Figure 3.18: Generic inertial element

from the momentum equation, derived for a fluid from the Newton's Second Law:

$$\sum \mathbf{F}_V = \frac{\partial}{\partial t} \int_V \mathbf{v} \rho dV + \int_{\partial V} \mathbf{v} \rho (\mathbf{v} \cdot \mathbf{n}) dA, \quad (3.67)$$

where a balance between momenta is performed inside the control volume and on its boundaries. The fundamental equation for the inertial element is the following:

$$p_{12} = I \frac{dQ_I}{dt}, \quad (3.68)$$

where  $I$  is the fluid *inertia*. For an incompressible non viscous fluid, in a uniform duct with length  $l$  and cross section  $A$ , it is given by:

$$I = \frac{\rho}{A} l. \quad (3.69)$$

The kinetic energy stored in the element is given by:

$$E_K = \frac{I}{2} Q_I^2, \quad (3.70)$$

thus the inertial element contributes to avoid sudden flow rate variations.

### Resistive element

The resistance of a fluid is due to the presence of viscous effects: it is then related to an energy dissipation caused by friction and other phenomena. This energy dissipation

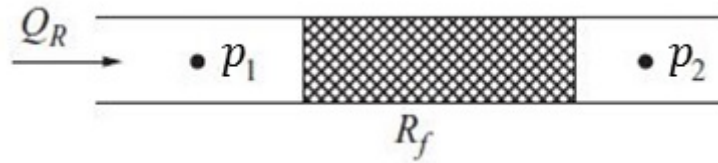


Figure 3.19: Generic resistive element

involves a pressure drop for the flow that is directly related to the volumetric flow rate. The analysis of the resistive element is based on the energy equation for a fluid, derived from the First Principle of Thermodynamics:

$$\frac{\partial}{\partial t} \int_V e \rho dV + \int_{\partial V} e \rho (\mathbf{v} \cdot \mathbf{n}) dA = \dot{Q}_{net\,in} + \dot{W}_{shaft\,in}. \quad (3.71)$$

The fundamental equation for the resistive elements is the following:

$$p_{12} = R_f Q_R, \quad (3.72)$$

where  $R_f$  is the fluid *resistance*.

If the flow becomes turbulent or passes through an orifice, the relationship between the flow rate and the pressure drop through the element is no more linear and the losses must be evaluated with fluid dynamical techniques. An important approximate relationship is the one representing the flow through an orifice previously cited:

$$Q = A_0 C_d \sqrt{\frac{2}{\rho} p_{12}}, \quad (3.73)$$

where  $A_0$  is the cross section of the orifice; if the flow becomes turbulent or for gas flows with high Mach numbers the relationship must be properly corrected using an appropriate *power law* [22].

### 3.4.2 Sump sub-model

The sump has been modeled as a capacitive element: the balance between the flow rates entering and exiting it, with the lubricant bulk modulus, affects the pressure level

inside the sump, that must then be provided as a boundary condition for the oil films. The flow rates involved in the balance are calculated according to the resistive element formulation: the supply flow rate is computed considering the pressure drop between the supply pressure and the sump pressure, while the leakage flow rate is computed considering the drop between the sump pressure and the environment pressure. The

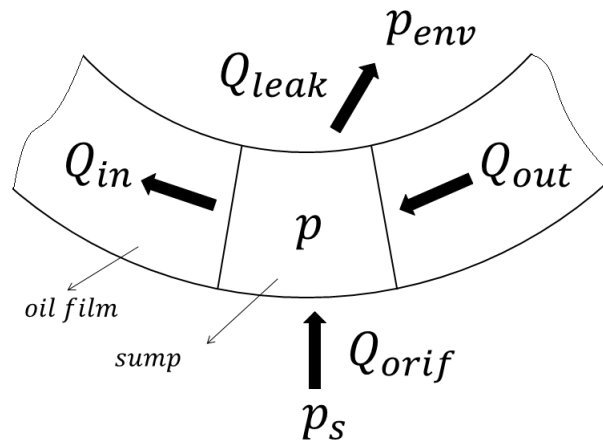


Figure 3.20: Scheme of the sump interposed between two adjacent pads

flow coefficients of the two resistive elements have been properly tuned; furthermore the leakage flow rate must be zero if the sump pressure is below the environment pressure. It is useful to highlight how the oil films adjacent to the sump, even if modeled as previously illustrated, behave as resistive elements with respect to the sump, since for a certain pressure drop they provide the lubricant flow rates that pass through them. The flow rates are computed according to the following equations:

$$Q_{orif} = C_{d,orif} \left( \frac{\pi d^2}{4} \right) \sqrt{\frac{2(p_s - p_{sump})}{\rho}}, \quad (3.74)$$

$$\begin{cases} Q_{leak} = C_{d,leak} A_{sump} \sqrt{\frac{2(p_{sump} - p_{env})}{\rho}} & \text{if } p_{sump} > p_{env} \\ Q_{leak} = 0 & \text{if } p_{sump} \leq p_{env} \end{cases} \quad (3.75)$$

where  $C_{d,orif}$  and  $C_{d,leak}$  are the resistive elements flow coefficients,  $d$  is the diameter of the supply orifices,  $A_{sump}$  is the cross section of the sump through which the leakage flow

rate passes and  $\rho$  is the lubricant density.

The pressure inside the sump is then calculated according to the following ordinary differential equation (derived from Equation 3.62):

$$\frac{dp_{sump}}{dt} = \frac{\beta}{V} (Q_{in} - Q_{out} + Q_{orif} - Q_{leak}), \quad (3.76)$$

where  $\beta$  is the lubricant bulk modulus and  $V$  is the sump volume.

### 3.5 Pad sub-model

In order to calculate the pad rotations and hence their influence on the rotor behaviour, it is necessary to model their motion. Each pad has two possible degrees of freedom, corresponding to its tilt angles; as reported in Figure 3.22,  $\gamma$  is the principal tilt angle, defined with respect to an axis parallel to the geometrical symmetry axis of the machine, while  $\chi$  is the secondary tilt angle (i.e. the *pitch* angle), defined with respect to a circumferentially tangential axis (this angle is important if the rotor and the bearing are strongly misaligned). The pad moments of inertia have been calculated, in order to obtain

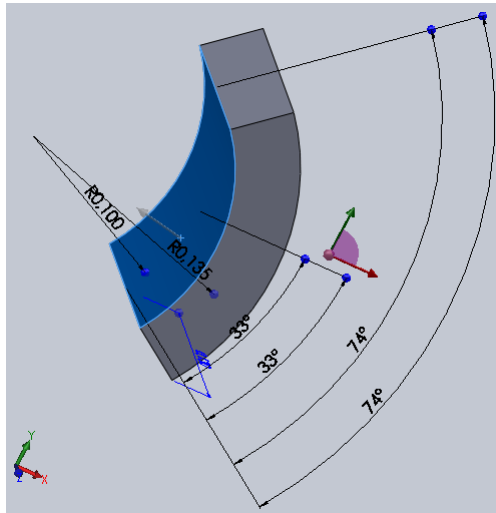


Figure 3.21: Calculation of pad moments of inertia

realistic results, with the inertial properties tool of a CAD software. Considering the moments due to the pressure field inside the oil film it is then possible to formulate the pad equations of motion as follows:

$$\begin{cases} J_{p,pad}\ddot{\gamma} = M_{tilt} \\ J_{t,pad}\ddot{\chi} = M_{pitch} \end{cases} \quad (3.77)$$

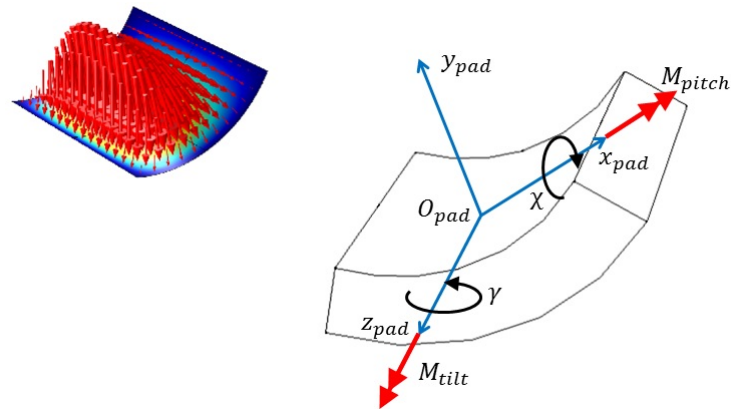


Figure 3.22: Pressure and forces acting on the tilting pad

## 3.6 Rotor modeling

The last element included in the model is the rotor fraction, based on the classical four degrees of freedom rotor model where, decoupling the flexural motions from the axial and torsional ones, the analysis is focused on the two transverse translations of the rotor and on their respective rotations. In the following section, the fundamentals of rotordynamics will be exposed to provide a better understanding of the proposed modeling approach.

### 3.6.1 Rotordynamics

*Rotordynamics* is the branch of the mechanical systems dynamics that analyzes systems where at least one a component (i.e. the *rotor*), rotates with a significant angular momentum. According to ISO standards, a rotor is a body suspended on a series of cylindrical hinges (bearings) which let it rotate about a fixed axis. This definition can be too strict in some cases (there can be rotors without bearings, like celestial bodies); however this work refers exactly to a *fixed rotor*.

The rotor, in its undeformed configuration, has a well defined rotational axis, generally coincident with one of its central principal axes of inertia. This condition is exactly

verified only for a perfectly balanced rotor; in most cases the *unbalance*, which represents the difference from the ideal condition, is small and can be considered as a small perturbation. Consequently, it is possible to assume that also the rotor linear and angular displacements are small (with the exception of the rotor proper rotation). These two assumptions allow to linearize the rotor equations of motion, obtaining a formulation analogous to that of a classical linear dynamic system. In the general form, for a linear rotor with  $n$  degrees of freedom, the equations of motions can be expressed as follows:

$$\mathbf{M}\ddot{\mathbf{q}}(t) + (\mathbf{C} + \mathbf{G})\dot{\mathbf{q}}(t) + (\mathbf{K} + \mathbf{H})\mathbf{q}(t) = \mathbf{f}(t), \quad (3.78)$$

where  $\mathbf{q}(t)$  is a vector containing the generalized coordinates with respect to an inertial reference system,  $\mathbf{M}$  is the symmetric mass matrix,  $\mathbf{C}$  is the symmetric damping matrix,  $\mathbf{G}$  is the skew-symmetric gyroscopic matrix,  $\mathbf{K}$  is the symmetric stiffness matrix,  $\mathbf{H}$  is the skew-symmetric circulatory matrix and  $\mathbf{f}(t)$  is a time dependent vector containing external loads.

In the analysis of rotating systems, one of the most important loads is often that due the rotor unbalance, a time dependent load with an amplitude proportional to the square of the rotor angular velocity and a frequency equal to it. The gyroscopic matrix contains inertial conservative terms due to the gyroscopic moments acting on the rotating components of the system; if the equations of motion are referred to a non inertial reference system,  $\mathbf{G}$  includes also terms due to Coriolis acceleration. The matrix  $\mathbf{H}$  contains non conservative terms due to the internal damping of the rotating components and, with fluid dynamical linearized bearings, to the fluid damping and cross-coupled stiffness terms; a matrix like this can generate instability phenomena. The presence of these two skew-symmetric matrices distinguishes the rotordynamical equations of motion from those of classical dynamic systems; both  $\mathbf{G}$  and  $\mathbf{H}$  are proportional to the rotor angular velocity  $\Omega$ : when it is zero the equations degenerate in the non rotating formulation.

As usual with dynamic systems, from the equations of motion it is possible to analyze the free response of the system, calculating its eigenvalues. The classical solution for the



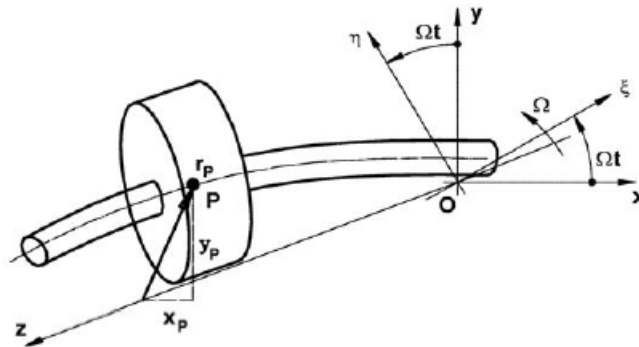


Figure 3.23: Simple rotor scheme

free vibrations of the system can be expressed in the complex form:

$$\mathbf{q}(t) = \mathbf{q}_0 e^{st}, \quad (3.79)$$

where the imaginary part of  $s = \sigma + i\omega$  is the natural frequency of the system. Since the rotational velocity appears explicitly in the equations of motion, the natural frequencies calculated from the analysis of the free response of the system are velocity dependent. This behavior is generally reported in the Campbell diagram, where the rotor natural frequencies are reported as functions of the rotor spin speed; the unbalance load (dependent on the rotor velocity) can be plotted in the same diagram in order to identify, from the intersections between the curves, the possible system resonances. In rotordynamics such resonances, due to synchronous load like the unbalance, are called critical speeds. These concepts are important only within the linear assumption, because the definition of natural frequency holds only for linear systems; when dealing with non linear system the approach must be slightly different.

After the free motion analysis of the rotor, typically its dynamical response to synchronous or non synchronous loads is analyzed in the frequency domain. For the unbalance response (whose formulation is reported for the four degrees of freedom rotor) the results are similar to those of classical dynamic systems; considering then loads with a frequency multiple of the rotor spin speed, it is possible to draw the rotor waterfall plot, where the rotor response is reported in all its operating range.

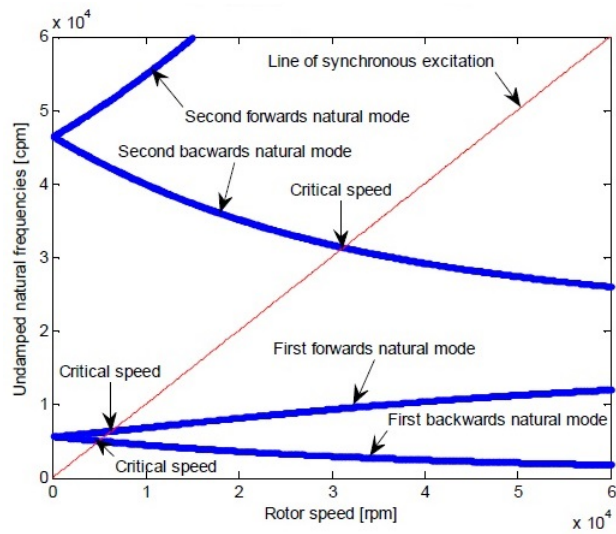


Figure 3.24: Campbell diagram

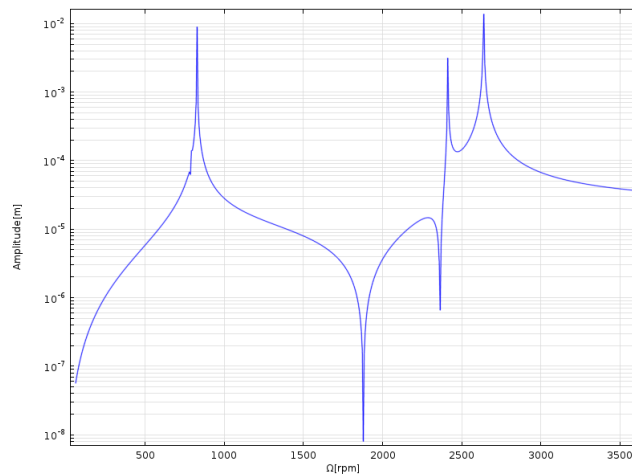


Figure 3.25: Unbalance response

Skipping the most simple rotor models (e.g. the Jeffcott rotor), in the following section the four degrees of freedom rotor model (a model which includes the gyroscopic effects in the analysis) will be presented, in order to introduce the fundamentals of a rotordynamical analysis and be able to extend those results to more complex models. The 4 DOFs rotor model represents a mass-less flexible rotor rigidly connected to a rigid disk and supported by rigid bearings or a rigid rotor on flexible supports. The rotor center

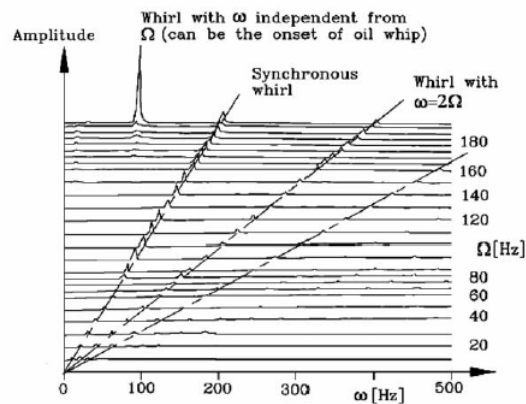


Figure 3.26: Waterfall plot of the rotor forced response

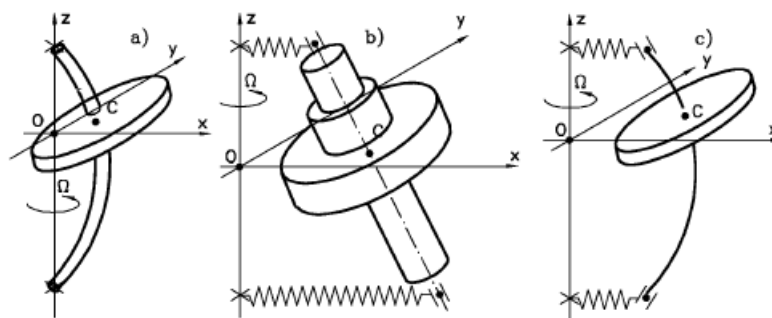


Figure 3.27: Rotor with 4 degrees of freedom

of gravity  $P$  does not coincide with the geometrical center  $C$  of the shaft: this eccentricity, denoted by  $\epsilon$ , originates the previously illustrated unbalance. Furthermore, the symmetry axis does not coincide with the rotational axis, with an angular displacement denoted as  $\chi$ . Consequently an unbalance force and an unbalance moment act on the rotor. The system has six degrees of freedom: the reduction to only four DOFs is due to the decoupling between flexural, axial and torsional motions which lead to the analysis of two rotations and two translations.

Using the reference systems reported in Figure 3.28, and taking into account the forces exerted by the supports as linear springs with stiffness  $K_{ij}$ , the equations of motion for



### 3.6.2 Rotor fraction sub-model

The rotor fraction enclosed in the bearing represents the connection between the bearing and the complete rotor model which will be introduced in the next Chapter. It is a cylindrical rigid body, with a length equal to the bearing length and diameter equal to  $2R - 2h_0$ . Consequently, its dynamical behavior is only affected by its inertial characteristics, mass and moments of inertia, and it is modeled according to a system of ordinary differential equations based on the four degrees of freedom rotor model. The rotor fraction degrees of freedom considered for the vibration analysis are the two

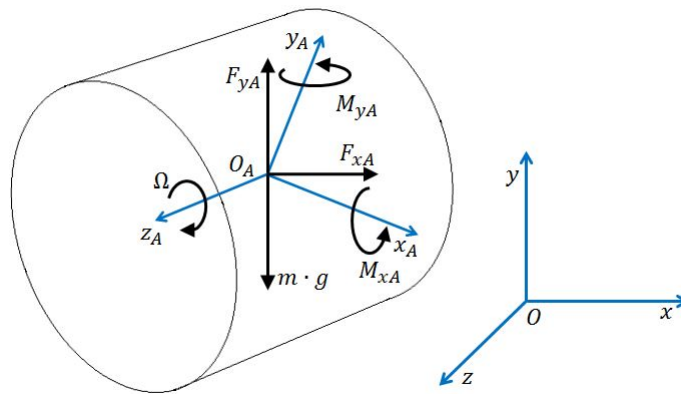


Figure 3.29: Rotor fraction and forces acting on it

*flexural* translations and the two rotations denoted as pitch and yaw. This simplification is based on the assumptions that the tilting pad journal bearings does not affect the axial behavior of the system (eventually controlled by a thrust bearing) and that the system is not affected by torsional vibrations (phenomenon for which it can be useful to develop a separate analysis). Referring to a fixed reference system with its origin in the bearing center and to a reference system rigidly connected to the rotor fraction (with its origin in the disk center of gravity), the equations of motion of the rotor fraction characterized by a spin speed  $\Omega$  and subjected to its own weight and to the bearing forces can be formulated

as follows:

$$\left\{ \begin{array}{l} m\ddot{x} = F_{xA} \\ m\ddot{y} = F_{yA} - m \cdot g \\ J_t\ddot{\phi}_{x'} + J_p\Omega\dot{\phi}_y = M_{xA} \\ J_t\ddot{\phi}_y - J_p\Omega\dot{\phi}_{x'} = M_{yA} \end{array} \right. \quad (3.84)$$

## 3.7 Numerical solvers

The developed model is divided, as previously illustrated, in a *transient* part where the system evolves in the time domain and a steady state part, repeated for each time step of the transient simulation. The solution of the system of ordinary differential equations representative of the transient part is performed by the *ode15s* solver implemented in *MATLAB*<sup>®</sup> *R2013a*, while the steady state solution of the Reynolds equation (strongly nonlinear) is due to the *BiCGStab* implemented in *COMSOL Multiphysics*<sup>®</sup> 4.4, which takes advantage of the Newton's method for the solution of non linear equations and of the *Incomplete LU* method for the factorization of the system matrices.

### 3.7.1 ode15s

The *ode15s* solver, whose name denotes a solver for ordinary differential equations (ODE) with a variable order (from 1 to 5) for *stiff* problems, is a numerical solver developed for the solution of equations with the following formulation:

$$M(t) y' = f(t, y), \quad (3.85)$$

where  $M(t)$  is the mass matrix, considering over a time interval  $[t_0, t_f]$  and a set of appropriate initial values  $y(t_0) = y_0$ . Before a brief presentation of the solver characteristics it is necessary to underline that it is specifically recommended for the solution of stiff problems that require the use of an implicit solver. The definition of *stiffness* is not completely straightforward and is based on the analysis of the eigenvalues of the system Jacobian matrix:

$$J = \partial_y f(t, y) = \left( \frac{\partial f_i}{\partial y_j} \right), i = 1, \dots, n, j = 1, \dots, n. \quad (3.86)$$

In particular, stiffness phenomena are typical when some components of the solution evolve more rapidly than the others (this phenomenon is present in the developed model) [23].

The first approach to the solution of stiff problems through implicit solvers is represented by the Backward Differences Formulas (BDF), used to approximate the derivatives of the unknown function in order to solve a system of algebraic equations. The formula with order  $k$  for the step with  $h$  amplitude between  $(t_n, y_n)$  and  $(t_{n+1}, y_{n+1})$  is expressed as follows:

$$\sum_{m=1}^k \frac{1}{m} \nabla^m y_{n+1} - hF(t_{n+1}, y_{n+1}) = 0, \quad (3.87)$$

setting up the iterations with:

$$y_{n+1}^{(0)} = \sum_{m=0}^k \nabla^m y_n. \quad (3.88)$$

This algebraic equation is solved with respect to  $y_{n+1}$  with the Newton's method. This kind of formula is generally used with a constant stepping. To improve the stability of the method, the above mentioned formula can be modified as follows:

$$\sum_{m=1}^k \frac{1}{m} \nabla^m y_{n+1} - hF(t_{n+1}, y_{n+1}) - k\gamma_k (y_{n+1} - y_{n+1}^{(0)}) = 0, \quad (3.89)$$

denominated Numerical Differentiation Formulas, NDF.  $k$  is a scalar parameter and the coefficient  $\gamma_k$  is given by  $\gamma_k = \sum_{j=1}^k \frac{1}{j}$ . The role of the term which distinguishes the NDF from the BDF is shown by the following identity:

$$y_{n+1} - y_{n+1}^{(0)} = \nabla^{k+1} y_{n+1}. \quad (3.90)$$

In order to minimize the error,  $k$  must be chosen as a function of the order of the problem [24].

The *ode15s* solver code is an implementation of the NDF in terms of BDF with quasi-constant stepping. The equation:

$$\sum_{m=1}^k \frac{1}{m} \nabla^m y_{n+1} = \gamma_k (y_{n+1} - y_{n+1}^{(0)}) + \sum_{m=1}^k \gamma_k \nabla^m y_n, \quad (3.91)$$

shows that the equation presented for the NDF is equivalent to:

$$(1 - k) \gamma_k (y_{n+1} - y_{n+1}^{(0)}) + \sum_{m=1}^k \gamma_k \nabla^m y_n - hF(t_{n+1}, y_{n+1}) = 0. \quad (3.92)$$



### 3.7.2 BiCGStab

*BiCGStab*, abbreviation of BiConjugate Gradient Stabilized, is an algorithm for the solution of systems of equations based on the Krylov method. It is a powerful algorithm, both in terms of computational times and of resources consumption. Considering a system like the following:

$$\mathbf{Ax} = \mathbf{b}, \quad (3.93)$$

direct methods are those which perform a factorization of the system matrix in order to invert it. In systems with sparse matrices it is preferable to use iterative methods like the BiCGStab. These methods start from an approximate solution and modify its components at each iterative step, in order to minimize the residual norm. Most of the iterative techniques for the solution of large problems are based on projective methods which extract an approximation of the solution from a particular sub-space of  $\mathbb{R}^n$  with dimension  $m$  denoted by  $K$ . To uniquely determine the solution,  $m$  orthogonality constraints must be imposed between the residual  $\mathbf{b} - \mathbf{Ax}$  and  $m$  particular vectors. The Krylov sub-space  $K$ , on which the BiCGStab method is based, is the space generated by vectors  $p(A)r_0$ , where  $p$  is a polynomial. To make the basis of the sub-space stable it is necessary to extract an orthonormal basis; to obtain this basis the Lanczos biorthogonalization algorithm can be used [25]. The BiCGStab method originates from this procedure, formulating the residual as a product of two polynomials  $\psi_j(A)\varphi_j(A)$ . The algorithm is the following:

Calculate  $\mathbf{r}_0 := \mathbf{Ax}_0$

Choose  $\mathbf{r}_0^*$  arbitrarily

Put  $\mathbf{p}_0 := \mathbf{r}_0$

**for**  $j = 0, 1, \dots$  until convergence

$$\alpha_j := (\mathbf{r}_j, \mathbf{r}_0^*) / (\mathbf{Ap}_j, \mathbf{r}_0^*)$$

$$\mathbf{s}_j := \mathbf{r}_j - \alpha_j \mathbf{Ap}_j$$

$$\omega_j := (\mathbf{As}_j, \mathbf{s}_j) / (\mathbf{As}_j, \mathbf{As}_j)$$

$$\begin{aligned}
\mathbf{x}_{j+1} &:= \mathbf{x}_j + \alpha_j \mathbf{p}_j + \omega_j \mathbf{s}_j \\
\mathbf{r}_{j+1} &:= \mathbf{s}_j - \omega_j \mathbf{A} \mathbf{s}_j \\
\beta_j &:= \frac{(\mathbf{r}_{j+1}, \mathbf{r}_0^*)}{(\mathbf{r}_j, \mathbf{r}_0^*)} \cdot \frac{\alpha_j}{\omega_j} \\
\mathbf{p}_{j+1} &:= \mathbf{r}_{j+1} + \beta_j (\mathbf{p}_j - \omega_j \mathbf{A} \mathbf{p}_j)
\end{aligned}$$

**end for**

The convergence of the algorithm is often more irregular with respect to other methods like *GMRES*. As shown in the algorithm, *BiCGStab* uses two matrices products for each iteration, thus requiring two preconditioning steps for each iteration. During the calculation the software performs continuously an estimate of the error and if it is small enough to satisfy the convergence criterion (Equation 3.94), a solution is provided:

$$\rho |\mathbf{M}^{-1} (\mathbf{b} - \mathbf{A} \mathbf{x})| < tol \cdot |\mathbf{M}^{-1} \mathbf{b}|, \quad (3.94)$$

where  $\mathbf{M}$  is the preconditioning matrix [25].

$\mathbf{M}$  is determined by the preconditioning algorithm chosen for the solution; this choice affects the calculation time since the preconditioning phase can sometimes require more time than the iterative solution itself. For the proposed model, the *BiCGStab* method is coupled with an *Incomplete LU* algorithm for the preconditioning. This method is an approximate version of the classical LU factorization: instead of decomposing exactly the system with  $\mathbf{A} = \mathbf{L}\mathbf{U}$ , where  $\mathbf{L}$  and  $\mathbf{U}$  are respectively the lower and upper triangular matrices, the factorization is approximated as  $\mathbf{A} \approx \mathbf{L}\mathbf{U}$ , a formulation more suitable for problems characterized by large and sparse matrices, like those arising from FEM models. Furthermore, the *BiCGStab* method takes advantage of the Newton's method for the solution of non linear equations. This method is based on the linear approximation principle: referring to Figure 3.30, the solution  $r$  of the equation  $f(x) = 0$  is calculated iterating from a first estimate  $x_0$ , with  $h = r - x_0$ . If  $h$  is small, the function  $f$  can be linearly approximated as follows:

$$0 = f(r) = f(x_0 + h) \approx f(x_0) + hf'(x_0), \quad (3.95)$$

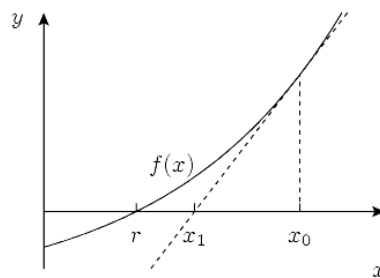


Figure 3.30: Newton's method for the solution of nonlinear systems

from which a new estimate of the solution can be computed:

$$x_1 = x_0 - \frac{f(x_0)}{f'(x_0)}. \quad (3.96)$$

The formulation for the generic  $n$ -th iteration is the following:

$$x_{n+1} = x_n - \frac{f(x_n)}{f'(x_n)}, \quad (3.97)$$

and the iterative procedure continues until an appropriate convergence criterion is satisfied.

## Step 2: Rotor dynamical aspects

The second modeling step realized in order to develop a complete bearing model deals with the coupling between the single bearing model previously exposed and a rotor FEM model. The passage from the analysis of the motion of a single rotor fraction to the dynamical analysis of the complete rotor is essential to allow the model to accurately represent the rotor dynamical phenomena involved in the bearing operation in addition to the previously analyzed fluid dynamical ones. In order to realize a correct coupling between the bearing model and the complete rotor, the whole model has been upgraded and subjected to a further experimental validation.

In the following sections, the developments introduced with the second modeling step in order to implement the rotor dynamical effects in the model will be explained.

## 4.1 Software

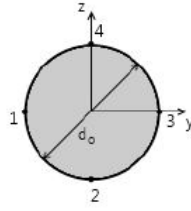
The second modeling step developed in this thesis has been completely implemented in *COMSOL Multiphysics*<sup>®</sup>4.4; all the components are directly realized in the same software through the following interfaces:

- *Thin - Film Flow Branch* for the oil film modeling;
- *Beam Interface* for the rotor FEM modeling;
- *Global ODEs and DAEs Interface* to add the ordinary differential equations that represent the dynamical behavior of pads and sumps.

The *Beam Interface* is used to perform structural analysis concerning slender elements like beams or rotors, which can be completely described through the properties of their cross sections (e.g. area, moments of inertia, density). Two different mathematical formulations are available for the BEAM element: the Euler BEAM and the Timoshenko BEAM; the latter has been used in the proposed model in order to introduce the effects due to the rotor spin speed. The elements can be loaded with forces and moments acting in every direction, with distributed or lumped loads; furthermore many possible structural constraints are available. The dependent variables for a component modeled through the *Beam Interface* are the generalized displacements of the element nodes:

$$\begin{matrix} u & v & w \\ thx & thy & thz \end{matrix} \quad (4.1)$$

from which the strains and stresses of the system can be calculated according to the classic FEM formulation exposed later. The cross section assigned to the BEAMS constituting the rotor has a circular shape; referring to Figure 4.1, the section properties needed for the analysis are the following:

Figure 4.1: Cross section of the *BEAM* element

$$\begin{aligned}
 A &= \frac{\pi d_0^2}{4}, \\
 I_{zz} &= \frac{\pi d_0^4}{64} = I_{yy}, \\
 I_{xx} &= \frac{\pi d_0^4}{32}, \\
 W_t &= \frac{\pi d_0^3}{16}.
 \end{aligned} \tag{4.2}$$

In order to obtain consistent results it is essential to correctly define the element local reference system, with the  $x$  axis coincident with the *BEAM* axis [26].

The *Global ODEs and DAEs Interface* is used to add to the model global equations (both

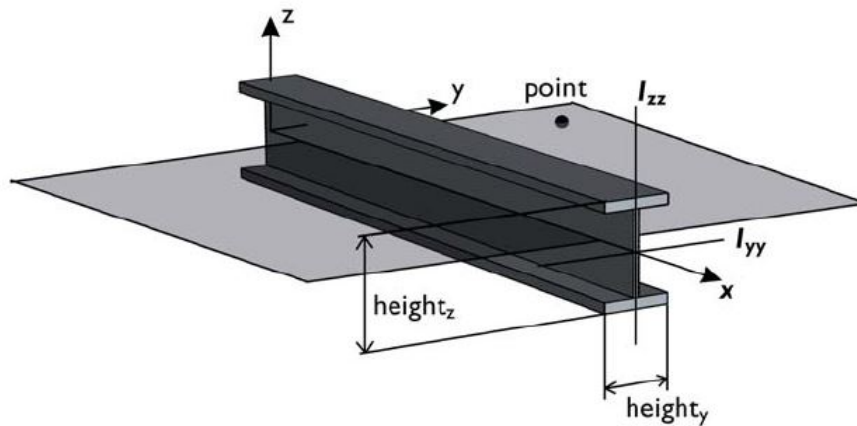


Figure 4.2: Element local reference system

differential and algebraic) that are independent from the spatial coordinates of the FEM model. The necessity to use this interface arises from the interactions between the oil film model (i.e. a FEM model) and external elements like the tilting pads and the supply sumps. If differential equations are added to the model, they require appropriate initial values for each variable and for its first time derivative. In particular, the equations are

implemented with the following formulation:

$$\begin{cases} f(u, \dot{u}, \ddot{u}, t) = 0 \\ u(t_0) = u_0 \\ \dot{u}(t_0) = \dot{u}_0 \end{cases} \quad (4.3)$$

where  $u$  is the dependent variable of the new equation [20].

## 4.2 Model structure

The upgraded model has a structure analogous to that exposed in the previous Chapter, with the essential difference that all the components are directly implemented in *COMSOL Multiphysics*<sup>®</sup>4.4, without the division of the problem in a steady state and a transient part. This simplifies the interactions between the various components but it is necessary to correctly interface the *physics* used for the modeling. In particular, it is necessary to distinguish the dependent variables of each physics in order to obtain a solution. This problem primarily concerns the interaction between the oil film and the supply sump, since pressure is the dependent variable for both components: *COMSOL Multiphysics*<sup>®</sup>4.4 allows to avoid this conflict through the function *nojac*, which establishes an order in the numerical solution of the model components and excludes its argument expression from the calculation of the Jacobian for the considered integration step.

The inputs and outputs are similar to those shown for the previous model: the  $i$ -th oil film provides the forces  $F_{xA,i}$ ,  $F_{yA,i}$ ,  $F_{zA,i}$  and the moments  $M_{xA,i}$ ,  $M_{yA,i}$ ,  $M_{zA,i}$  (calculated integrating the pressure field inside the oil film) applied to the rotor in the node corresponding to the bearing center; furthermore it provides the moments  $M_{tilt,i}$  and  $M_{pitch,i}$  needed to determine the pad dynamical motion and the lubricant flow rates  $Q_{in,i}$ ,  $Q_{out,i}$ ,  $Q_{left,i}$  and  $Q_{right,i}$  necessary as inputs for the sump model. The  $i$ -th pad model, subjected to the moments due to the oil film pressure field, provides the pad tilt angles  $\gamma_i$  and  $\chi_i$  and their respective velocities, needed by the *Thin - Film Flow Branch* to compute the oil film thickness. The  $i$ -th supply sump performs a balance between its input flow rates, calculating the pressure  $p_{sump,i}$  needed as a boundary condition for the adjacent pads (the previously mentioned variable conflict arises from the imposition as a boundary condition of a quantity that is the dependent variable of another component, calculated according to this boundary condition itself); analogously to the previous modeling step, the supply flow rate  $Q_{orif,i}$  and the leakage flow rate  $Q_{leak,i}$  are computed with respect to the supply and environment pressure. The rotor model, with the possibility to apply



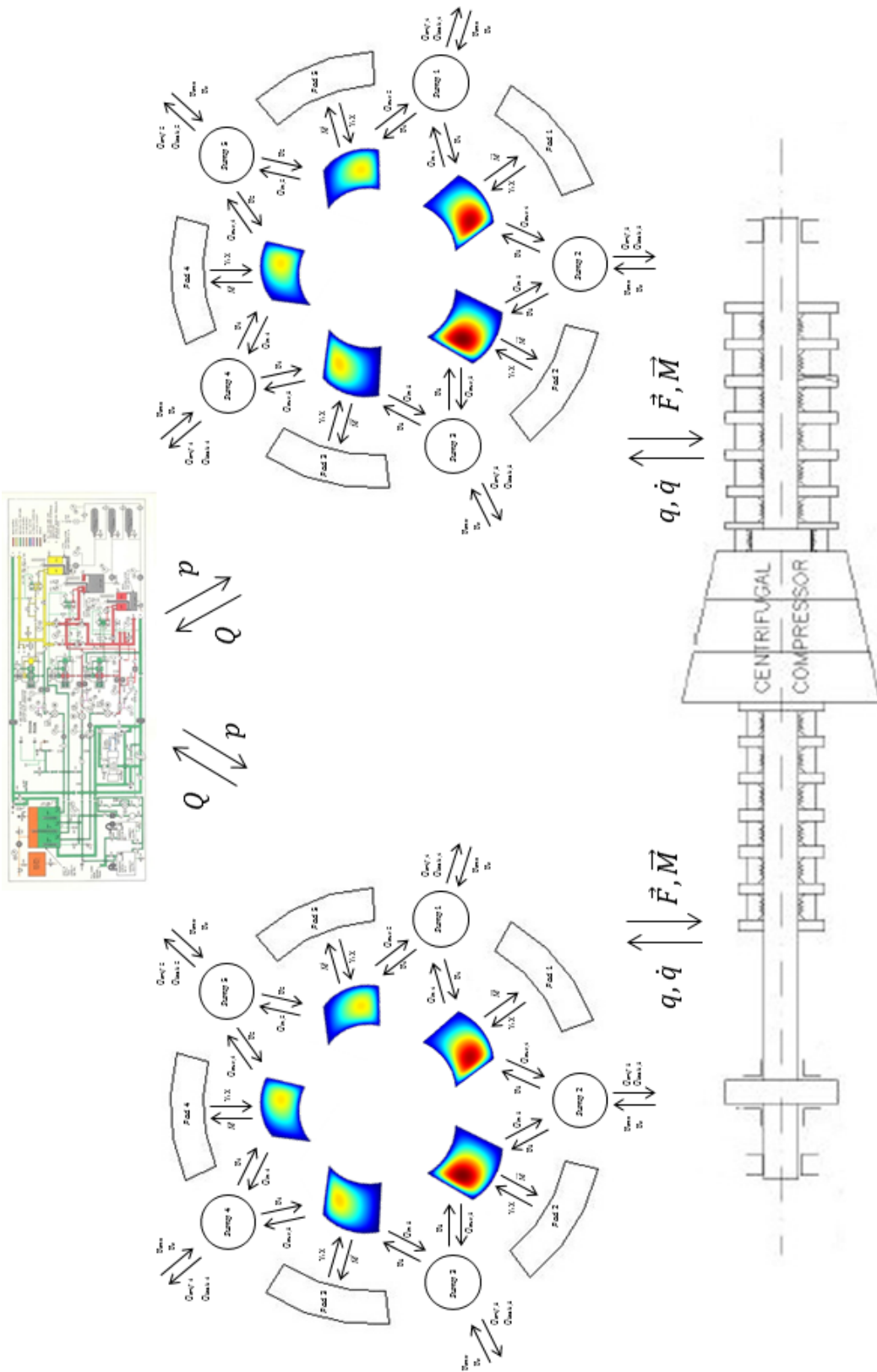


Figure 4.3: Complete rotor dynamical model

an unbalance load, receives as inputs the loads exerted by the oil films and evolves (in the time domain or in the frequency domain) providing its generalized displacements (translations and rotations)  $u_i, v_i, w_i, thx_i, thy_i, thz_i$  and their respective velocities  $ut_i, vt_i, wt_i, thxt_i, thyt_i, thzt_i$ , calculated in the nodes corresponding to the bearings locations.

The interactions between the various components are reported in Figure 4.3. The state vector containing the dependent variables of the whole model is expressed as follows:

$$\mathbf{Y} = \left\{ \begin{array}{c} p_f \\ u_1 \\ v_1 \\ w_1 \\ thx_1 \\ thy_1 \\ thz_1 \\ \vdots \\ \gamma_1 \\ \vdots \\ \chi_1 \\ \vdots \\ p_{sump,1} \\ \vdots \\ p_{sump,2n_{pad}} \end{array} \right\}. \quad (4.4)$$

## 4.3 Rotor modeling

The novelty with respect to the previous model is represented by the complete rotor model. The presence of the whole rotor allows to evaluate and accurately validate the rotor dynamical performances of the model; for the previous model such an evaluation was impossible due to the excessive simplification of the considered rotor model, while with the present model it is possible to analyze the behavior of the complete system, taking into account rotor flexibility and rotor dynamical effects due to the presence of elements connected to the rotor. In the following section, the fundamentals of FEM rotor dynamical analyses will be explained briefly in order to clarify the chosen modeling approach.

### 4.3.1 Rotor FEM modeling

The previously considered 4 DOFs rotor model allows to understand and model the main rotor dynamical phenomena but it is too simplified to be successfully used in the analysis of the behavior of modern rotors. Most engineering problems concern complex rotors with multiple interactions. Consequently, the usual approach is to discretize the system in order to obtain a problem represented by ordinary differential equations: the infinite DOFs continuous model represented in terms of partial differential equations is substituted by a discrete model with a finite number of DOFs; this approach is generally denoted as *Finite Element Method* (FEM). The FEM modeling approach is based on the discretization of the considered system in a certain number of regions denominated *finite elements* of finite dimensions, in contrast with the infinitesimal elements characteristic of a classical continuous analysis. It is possible to assume that an element deforms according to the linear combination of a set of functions of the spatial coordinates, denominated *shape functions*, weighted through a certain number of parameters denoted as element degrees of freedom which represent the generalized displacements of the element nodes.





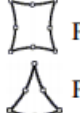



Element Order	2D Solid	3D Solid	3D Shell	Line Elements
Linear	 PLANE42 PLANE182	 SOLID45 SOLID185	 SHELL63 SHELL181	 BEAM3/44 BEAM188
Quadratic	 PLANE82/183 PLANE2	 SOLID95/186 SOLID92/187	 SHELL93	 BEAM189

Figure 4.4: Typical FEM elements

Consequently, the displacements  $\mathbf{u}(x, y, z)$  of a generic element point with coordinates  $x, y, z$  can be expressed as follows:

$$\mathbf{u}(x, y, z, t) = \mathbf{N}(x, y, z) \mathbf{q}(t), \quad (4.5)$$

where  $\mathbf{u}$  is a time and space dependent vector containing the displacements,  $\mathbf{q}$  is a time dependent vector containing the generalized displacements of the element nodes and  $\mathbf{N}$  is the shape functions matrix. Assuming the displacements in a certain direction to be dependent only on the nodal displacement in the same direction, the previous equation can be written in a more simple formulation:

$$\begin{Bmatrix} u(x, y, z, t) \\ v(x, y, z, t) \\ w(x, y, z, t) \end{Bmatrix} = \begin{bmatrix} \mathbf{N}(x, y, z) & 0 & 0 \\ 0 & \mathbf{N}(x, y, z) & 0 \\ 0 & 0 & \mathbf{N}(x, y, z) \end{bmatrix} \begin{Bmatrix} \mathbf{q}_x(t) \\ \mathbf{q}_y(t) \\ \mathbf{q}_z(t) \end{Bmatrix}. \quad (4.6)$$

The shape functions can be chosen arbitrarily; however they must satisfy certain conditions to be able to coherently represent the problem. Performing the derivative of the previous equation with respect to displacements, the relationship between strain and generalized coordinates can be formulated as follows:

$$\boldsymbol{\varepsilon}(x, y, z, t) = \mathbf{B}(x, y, z) \mathbf{q}(t), \quad (4.7)$$

where  $\mathbf{B}$  is a matrix containing the spatial derivatives of the shape functions and  $\boldsymbol{\varepsilon}$  is a vector containing the components of the strain tensor. Considering the material stiffness

matrix  $\mathbf{E}$ , the stress can be computed as follows:

$$\boldsymbol{\sigma}(x, y, z, t) = \mathbf{E}\boldsymbol{\varepsilon}. \quad (4.8)$$

Then, through the definition of elastic potential energy, it is possible to obtain the element stiffness matrix, which is, together with the shape functions, one of the fundamental components of a FEM analysis:

$$\mathbf{K} = \int_V \mathbf{B}^T \mathbf{E} \mathbf{B} dV. \quad (4.9)$$

Performing the time derivative of the displacements and considering the definition of kinetic energy, it is then possible to obtain the element mass matrix:

$$\mathbf{M} = \int_V \rho \mathbf{N}^T \mathbf{N} dV, \quad (4.10)$$

where  $\rho$  is the material density.

Finally the equations of motion for the element can be formulated as follows:

$$\mathbf{M}\ddot{\mathbf{q}} + \mathbf{K}\mathbf{q} = \mathbf{f}(t), \quad (4.11)$$

where  $\mathbf{f}$  is a vector containing the loads acting on the element.

The previously exposed relationships have a general validity for FEM analyses in the structural field. For a rotor dynamical analysis the most used elements are the BEAM elements, suitable to represent the behavior of structure with a prevalent direction (i.e. length with respect to cross section). The various formulations available for this elements differ for the number of nodes and DOFs. The main formulations are the Euler one, which does not consider the deformations due to shear stresses, and the Timoshenko one, which includes this kind of deformation. The latter formulation is the most diffused in rotordynamics, since it allows to easily introduce phenomena due to rotation. The Timoshenko BEAM has 2 nodes, each with 6 DOFs, and represents a prismatic homogenous beam with uncoupled axial, torsional and flexural behavior. The vector containing its nodal displacements can be expressed as follows:

$$\mathbf{q} = [u_1, v_1, w_1, \theta x_1, \theta y_1, \theta z_1, u_2, v_2, w_2, \theta x_2, \theta y_2, \theta z_2]^T. \quad (4.12)$$

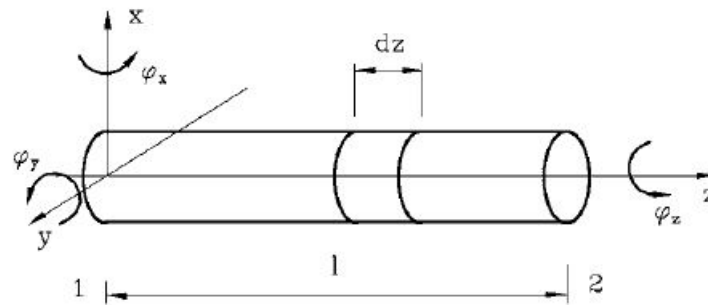


Figure 4.5: Scheme of the BEAM element

For a correct definition of the element, its shape functions include the *shear factor*, denoted by  $k$ , a parameter which takes into account the beam deformations due to shear stresses [1].

Finally, in rotor dynamical analysis, lumped masses or disk elements connected to the

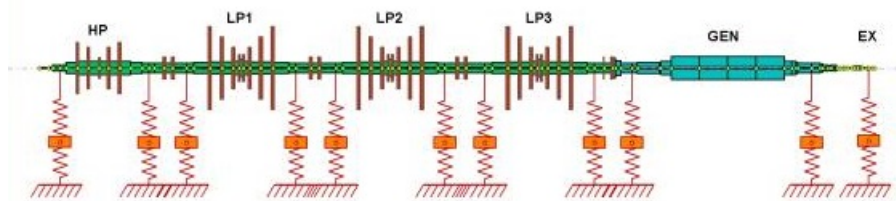


Figure 4.6: Rotor discretization

BEAM structure are widely used in order to represent the effects due to mechanical elements assembled on the rotor; in fact rotor dynamical analyses mainly concern the behavior of turbomachines, which are typically connected to impellers, ducts and many other components. The formulation of this lumped elements and their gyroscopic effects will be discussed in the following section.

Finally, the techniques to introduce a bearing model in a rotor dynamical analysis have been exposed in the introductory Chapter, when dealing with state-of-the-art bearing models.

### 4.3.2 Complete rotor dynamical model

Firstly, in order to develop the complete model, two whole bearings have been modeled in *COMSOL Multiphysics*<sup>®</sup>4.4, while in the previous modeling step only a single pad, called back repeatedly, was implemented for the lubrication analysis. The bearing model has

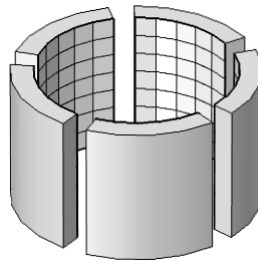


Figure 4.7: Bearing with five tilting pads and oil film mesh

then been upgraded in order to solve simultaneously all the ten oil film models enclosed in the two bearings for the rotor support: the new model is nearer to a fully-3D model and its FEM degrees of freedom have slightly increased with respect to the first modeling step.

The rotor has been modeled through the *COMSOL Multiphysics*<sup>®</sup>4.4 *Beam Interface*. Furthermore, some elements needed for the rotor dynamical analysis have been added to the rotor model.

It is possible to add lumped masses by assigning to the chosen node the punctual mass value  $m_p$ . This element, sometimes used even in this simplified formulation, can be easily enriched to represent a disk assembled on the rotor. The *Disk* element is then introduced assigning the following information:

$$\begin{cases} m_p \\ J_p \\ J_t \end{cases}, \quad (4.13)$$

where  $J_p$  and  $J_t$  are respectively the polar and transverse disk moments of inertia. This element can be loaded with lumped moments in order to represent its gyroscopic effects:

$$\begin{cases} M_{gyr,x} = -\frac{1}{2}\rho\pi r_d^4 t \Omega \dot{\phi}_y = -J_t \Omega \dot{\phi}_y \\ M_{gyr,y} = \frac{1}{2}\rho\pi r_d^4 t \Omega \dot{\phi}_{x'} = J_t \Omega \dot{\phi}_{x'} \end{cases}, \quad (4.14)$$

where  $t$  and  $r_d$  are the disk thickness and radius. For a rotating body like a compressor rotor, the gyroscopic moments are the reactions to a rotation, denoted as precession, about an axis orthogonal to the spin speed axis; hence they are directed orthogonally with respect to both axes. In addition to the rotor dynamical effects due to lumped elements



Figure 4.8: Example of a centrifugal impeller schematized as a Disk element

connected to the rotor, the model must also include the gyroscopic effects that act on the rotor regardless of other elements: the gyroscopic moments acting on the BEAM elements must be applied as distributed loads, according to the following formulation (where the rotor performs its proper rotation about the  $z$  axis):

$$\begin{cases} M_{gyr,x} = -\frac{1}{32}\rho\pi d_0^4 \Omega \dot{\phi}_y \\ M_{gyr,y} = \frac{1}{32}\rho\pi d_0^4 \Omega \dot{\phi}_{x'} \end{cases}. \quad (4.15)$$

Using the *COMSOL Multiphysics*®4.4 internal variables *beam.rho* and *beam.area* it is possible to directly take into account all the section and material variations without the need to apply separate loads.

A typical rotor dynamical analysis is firstly performed without external loads to evaluate the system eigenvalues and then in presence of an unbalance load. This load can be



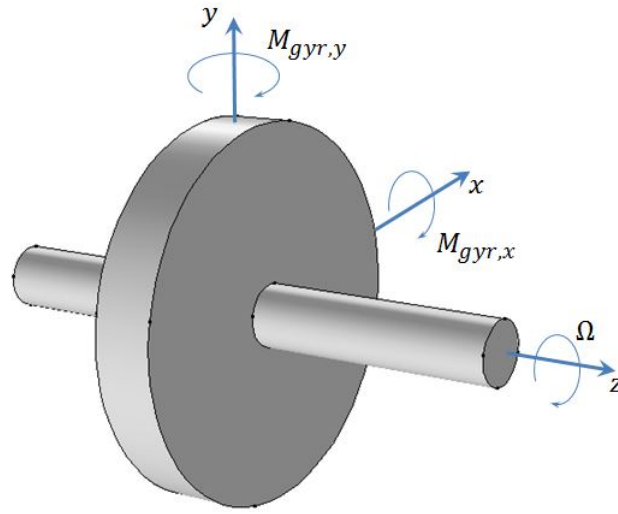


Figure 4.9: Gyroscopic moments

expressed as follows:

$$\begin{cases} F_{unb,x} = m_{res}\epsilon\Omega^2 \sin(\Omega t) \\ F_{unb,y} = m_{res}\epsilon\Omega^2 \cos(\Omega t) \end{cases}, \quad (4.16)$$

where  $m_{res}$  is the residual mass responsible for the rotor unbalance and  $\epsilon$  is its distance from the rotor geometrical center. This formulation is valid for analyses in the time domain; to analyze the rotor frequency response the load must be modified as follows (with  $\Omega = 2\pi f$ ):

$$\begin{cases} F_{unb,x} = -im_{res}\epsilon(2\pi f)^2 e^{i2\pi ft} \\ F_{unb,y} = m_{res}\epsilon(2\pi f)^2 e^{i2\pi ft} \end{cases}. \quad (4.17)$$

where the term  $-i$  represent a  $\frac{\pi}{2}$  phase shift between the two components of the load. An analogous modification must be realized for the ordinary differential equations of the pad and sump models.

For linear rotor dynamical models, the rotor weight can be neglected, since a static load does not affect the eigenvalues or the frequency response of the system. The proposed model, due to the presence of fluid dynamical bearings, is highly non linear and it is not possible to neglect the rotor own weight, both in a transient analysis in the time domain and in a steady state study in the frequency domain. *COMSOL Multiphysics*<sup>®</sup>4.4

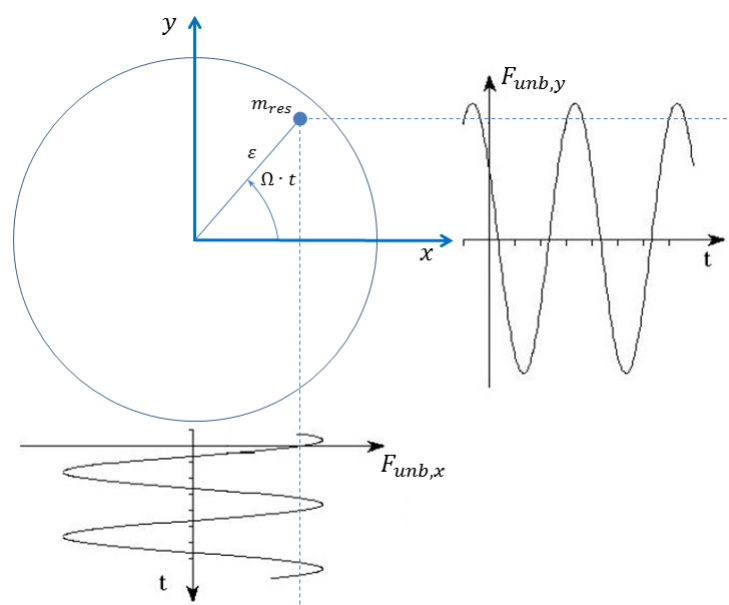


Figure 4.10: Unbalance loads

allows to include in the model the static force due to weight through the function *gravity*, which assigns an acceleration equal to  $g$  to each element with inertial properties: this contribution can be used in the time domain, where an acceleration is equivalent to a force through the mass, and in the frequency domain, where forces cannot be formulated as constant loads.

The ordinary differential equations representative of the pads and sumps dynamical

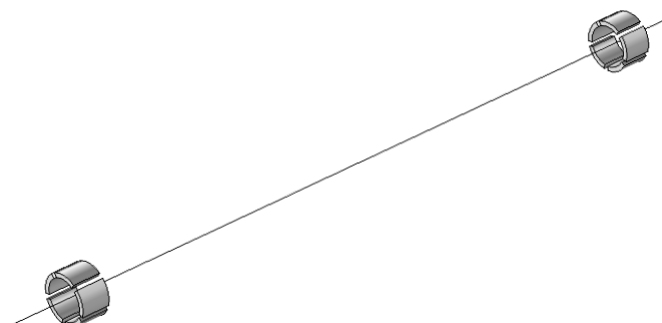


Figure 4.11: Rotor supported by two bearings

behavior are implemented in the model with the *Global ODEs and DAEs Interface*, using the formulation exposed in the previous Chapter. In order to use simulate the model in the frequency domain, those equations must be expressed following the typical procedure of a small vibrations analysis. Referring to the tilt angle  $\gamma$ , if its motion is oscillatory about an equilibrium position it can be expressed as follows:

$$\gamma = \gamma_0 e^{i\omega t} = \gamma_0 e^{i2\pi f t}. \quad (4.18)$$

Consequently its first and second derivatives can be expressed as:

$$\frac{d\gamma}{dt} = i2\pi f \gamma_0 e^{i2\pi f t}, \quad (4.19)$$

and

$$\frac{d^2\gamma}{dt^2} = -(2\pi f)^2 \gamma_0 e^{i2\pi f t}. \quad (4.20)$$

Substituting these expressions and analogous ones for the secondary tilt angle  $\chi$  in the pad equations of motion, their formulation can be modified as follows:

$$\begin{cases} -J_{p,pad} (2\pi f)^2 \gamma_0 e^{i2\pi f t} = M_{tilt,0} e^{i2\pi f t} \\ -J_{t,pad} (2\pi f)^2 \chi_0 e^{i2\pi f t} = M_{pitch,0} e^{i2\pi f t} \end{cases}, \quad (4.21)$$

where the loads are expressed as oscillatory quantities, being computed through a perturbation of the oil film pressure field. Simplifying the  $e^{i2\pi f t}$  term, the equations are implemented in the model as follows:

$$\begin{cases} -J_{p,pad} (2\pi f)^2 \gamma_0 = M_{tilt,0} \\ -J_{t,pad} (2\pi f)^2 \chi_0 = M_{pitch,0}. \end{cases} \quad (4.22)$$

With the same procedure, the sump equation can be implemented as follows:

$$i2\pi f p_0 = \frac{\beta}{V} (Q_{in,0} - Q_{out,0} + Q_{orif,0} - Q_{leak,0}). \quad (4.23)$$

## 4.4 Numerical solvers

### 4.4.1 Double Dogleg

For the solution of the numerical problem in the time domain the new model uses the BiCGStab algorithm previously illustrated. For the analysis in the frequency domain, given the strong non linearity of the model, the Newton's method is inappropriate to efficiently find a solution; hence the new model resorts on the *Double Dogleg* method implemented in *COMSOL Multiphysics*<sup>®</sup>4.4 for the solution of steady state problems.

The Double Dogleg is a *Newton trust region* method, able to vary both the direction and the length of the iterative step in the solution of non linear equations  $\mathbf{f}(\mathbf{x}) = 0$  with  $\mathbf{f} : \mathbb{R}^n \mapsto \mathbb{R}^n$ . The method minimizes the following quadratic form:

$$m_k(s) = \frac{1}{2} \|F_k + F'_k s\|^2 = \frac{1}{2} F_k^T F_k + \left( F_k'^T F_k^T \right)^T s + \frac{1}{2} s^T F_k'^T F'_k s, \quad (4.24)$$

where the step  $s$  must be limited by the trust region radius  $\delta_k$ , i.e.  $\|s\| \leq \delta_k$ . Both the Cauchy point, which represent the point which minimizes  $m$  in the gradient direction, and the Newton point are used. For each iterative step the algorithm dynamically adjusts the trust region dimension, taking into account the estimated and calculated decreases of  $m$ . The Double Dogleg step is determined by a convex combination of Cauchy and Newton steps. Referring to Figure 4.12,  $x_{k+1} = x_k + s_k$  is computed through a segment

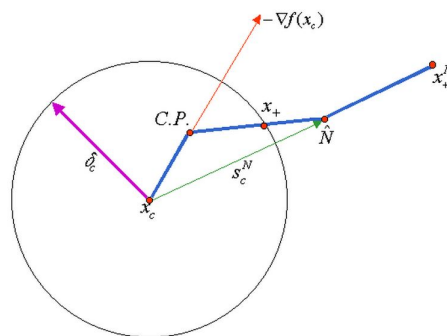


Figure 4.12: Double Dogleg method

path to approximate  $s$ . The first segment connects the origin to the Cauchy point while the

second connects the Cauchy point to the Newton point; the intersection between this path and the trust region boundary is denoted by  $x_{k+1}$ . For complex problems it is possible to begin the computation with a damped Newton method.

The algorithm provides a solution if the residual norm, properly scaled, is smaller than an appropriate tolerance  $\|SF_k\| \leq tol$  [27].

## Step 3: ThermoElastoHydroDynamic aspects

In the third modelling step, in addition to the fluid dynamic and rotor dynamic aspects affecting a system composed by two TPJBs and a rotor in the complete model, thermal and elastic aspects involving all the system elements have also been taken into account; in particular the proposed model includes the thermal exchange inside the oil film due to the viscous dissipation, the thermal mixing that develops inside the lubricant supply plant due to the presence of lubricant at different temperatures and the deformation suffered by pads and rotor due to the pressure and temperature fields and the heat fluxes exchanged in the system.

In the following sections, the developments introduced with the third modeling step in order to implement thermo-elasto-hydrodynamic effects in the model will be explained.

## 5.1 Software

All the model components have been implemented in *COMSOL Multiphysics*<sup>®</sup>4.4 and in particular the following *physics* have been used:

- *Thin-Film Flow Branch* for the fluid dynamics modelling of the oil film;
- *BEAM Interface* for the rotor modelling;
- *Global ODEs and DAEs Interface* to add the Ordinary Differential Equations that represent the pads motion and the temperature and the pressure in the lubricant supply plant;
- *Coefficient Form Boundary Interface* for the heat exchange modelling within the oil film;
- *Solid Mechanics Interface* for the elastic deformation modelling of the pads and the rotor fractions;
- *Heat Transfer Solid Interface* for the heat exchange modelling within all the solid components of the system.

The *Structural mechanics Interface* is used for the study of the behavior of mechanical structures and can therefore be used to perform static analysis for the determination of stresses and deformations or to perform dynamic analysis in order to obtain the frequencies and the modes of vibration of a structure.

The *Heat Transfer Solid Interface* allows to simulate various phenomena that characterize the heat transfer: convection, conduction and radiation. This module allows to study the generation and flow of thermal energy that occurs inside solids and therefore can be used for the simulation of the behavior of all those components in which heat exchange phenomena occurs (e.g. heat exchangers, electronic components and steam and gas turbines).

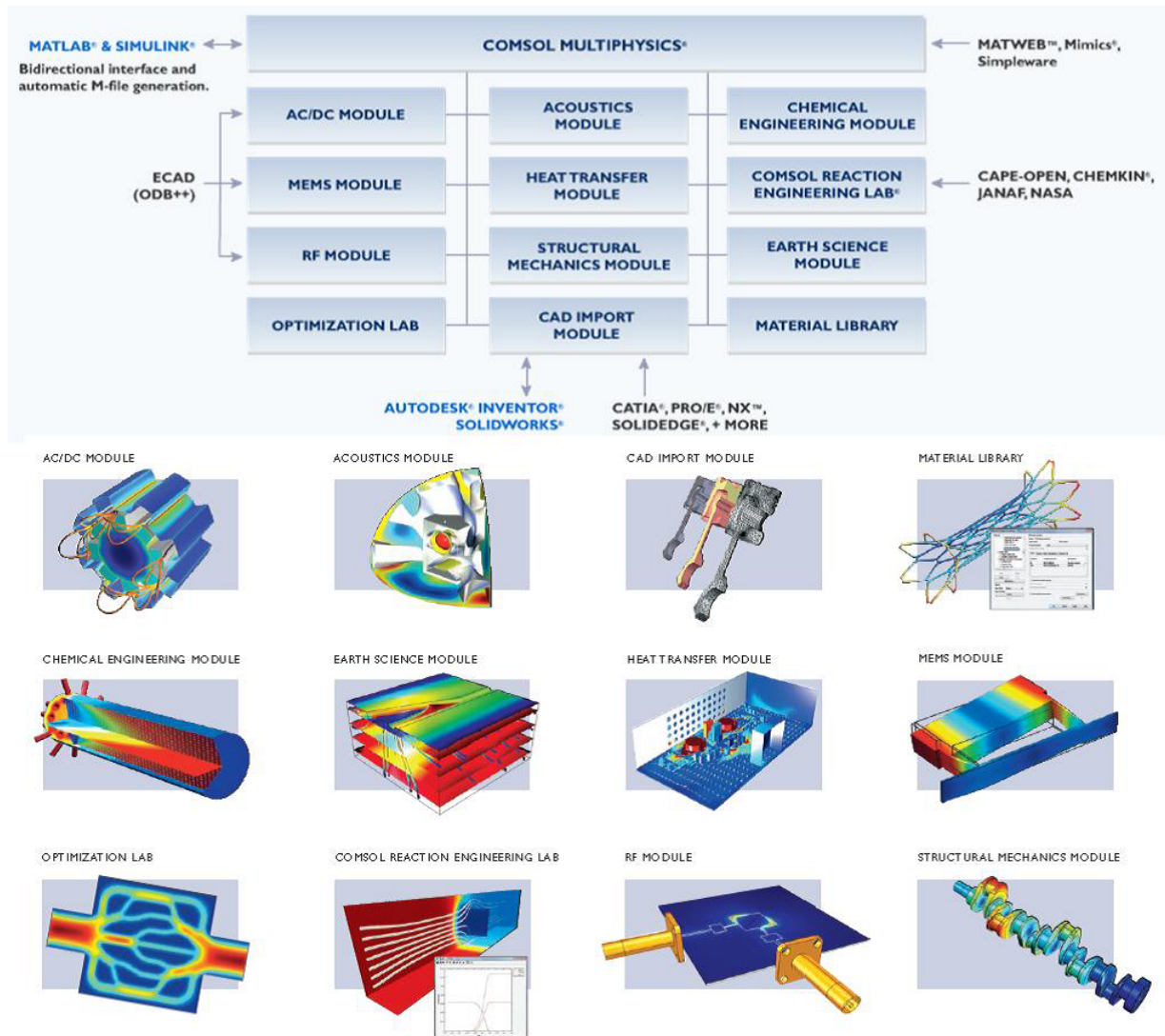


Figure 5.1: Modules available in the software *COMSOL Multiphysics*® 4.4.



## 5.2 Model structure

All the model components have been developed directly in *COMSOL Multiphysics*<sup>®</sup>4.4. This choice simplifies the analyses of the interactions between the various elements, but at the same time requires the different *physics* to be interfaced with each other in a correct way, i.e. it becomes necessary that the dependent variables of each *physics* used for the modelling are distinct from one another, in order to allow the model resolution. This caution is necessary because it is possible that different *physics* belonging to the model are characterized by the same dependent variable (such as the oil film and the lubricant supply plant, for both of which in fact the dependent variable is the pressure  $p$ ). In this case it is appropriate to solve this conflict. This is useful when the contribution to the Jacobian of the variable is not desired (as in its case), or when the computational weight of the calculation. Figure 5.2 shows the inputs and outputs of the various components. The following section shows how the different *physics* exchange the information in order to solve the problem.

The  $i$ -th oil film model provides the forces  $F_{xA,i}$ ,  $F_{yA,i}$ ,  $F_{zA,i}$  and the moments  $M_{xA,i}$ ,  $M_{yA,i}$ ,  $M_{zA,i}$ , needed by the rotor model to determine its motion, the moments  $M_{tilt,i}$  and  $M_{pitch,i}$  affecting the pad motion, the flow rate  $Q_{in}$ ,  $Q_{out}$ ,  $Q_{bord}$  which act as inputs for the  $i$ -th lubricant supply plant model and the lubricant temperature  $T_f$  to be provided to the rotor and pad models to evaluate their thermal deformation.

The  $i$ -th lubricant supply plant model performs a balance between the flow rates above mentioned and generates as output the pressure  $p_{pozz,i}$  to be used as a boundary condition on the leading edge of the  $i$ -th pad and on the trailing edge of the  $(i - 1)$ -th pad; it also simulates the mixing between the lubricant flow rates from the outside and that coming from the  $(i - 1)$ -th pad, providing as a further output the temperature  $T$  inside the lubricant supply plant. The supply  $Q_{orif,i}$  and leakage  $Q_{traf,i}$  flow rates are calculated at ambient temperature and pressure.

The  $i$ -th pad model, subjected to the thermal and structural loads mentioned above,

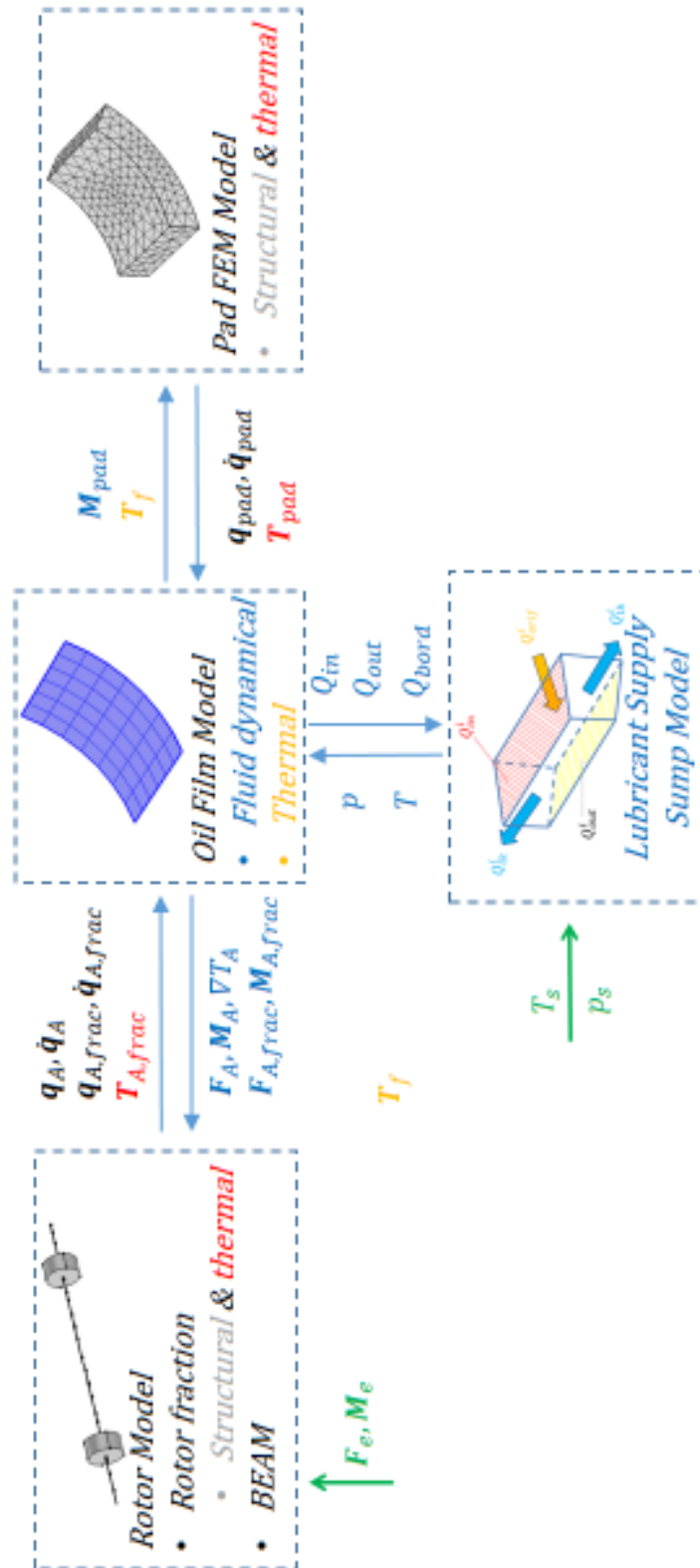


Figure 5.2: Structure of the developed model.

provides the rigid displacements (tilt angles  $\gamma_i$  and  $\chi_i$ ), velocities, pad deformation and pad temperature, to be supplied as boundary condition to the oil film model.

The rotor model, on which it is possible to apply a over hung forcing due to the imbalance, receives as inputs the loads generated by the bearings and the bearings temperature, and provides as output the temperature  $T_A$  and the displacement  $q_A$  of the rotor, which are provided to the oil film model and used for the direct calculation of the fluid film thickness.

## 5.3 Oil film modeling

Concerning the oil film, the novelty with respect to the previous modeling steps consists of the analyses of the thermal effects inside the oil films. The presence of these effects strongly influences the lubricant performances by varying its viscosity.

### 5.3.1 Thermal modeling

The study of the heat exchange phenomena which develop within a hydrodynamic bearing is of fundamental importance, since the temperature distribution directly influences the performances of these components. The Navier-Stokes equations describing the fluid motion contain the viscosity and density of the fluid itself, which significantly affect the pressure distribution that is generated in the oil film (and therefore the bearing performance) and have values that vary as a function of the lubricant temperature. Therefore, in order to develop a reliable model of the hydrodynamic bearing, it will have to take into account the influence that the temperature has on the lubricant properties.

As already mentioned in the previous chapter, the lubricant used in the present work has a viscosity value (i.e. the fluid resistance to the shear forces) that varies as a function of temperature. A high value of this variable brings benefits in terms of lubrication (e.g. better separation of the surfaces, see Chapter 3.3.1) and disadvantages in terms of energy dissipation, in fact, a higher viscosity leads a greater amount of mechanical energy to be dissipated in thermal energy, causing an increase of the lubricant temperature  $T_f$ .

The viscosity is strongly dependent on the temperature and its increase leads to a significant viscosity decrease. For a correct operation of the bearings it is, therefore fundamental to keep under control the lubricant temperature: in fact if this reaches a critical value of lubricant oxidation can occur, providing a drastic reduction of the fluid film thickness, which consequently loses its lubricant properties.

In the literature there are various equations describing the relationship between temperature and viscosity; among these the most accurate is that which related the dynamic viscosity  $\mu$  with the absolute temperature  $T$  as follows:

$$\mu(T) = \mu_0 \cdot e^{-\beta(T-T_0)}, \quad (5.1)$$

where  $\mu_0$  is the viscosity at the reference temperature  $T_0$  and  $\beta$  is the thermal expansion coefficient.

As well as the viscosity, also the lubricant density decreases with increasing temperature; an empirical formulation is reported in [28] and is expressed as follows:

$$\rho(T) = \rho_0 [1 - \varepsilon(T - T_0)], \quad (5.2)$$

where  $\rho_0$  is the density at the reference temperature  $T_0$  and  $\varepsilon$  is the volume expansion coefficient. In the present work the study of the heat exchange within the lubricant is

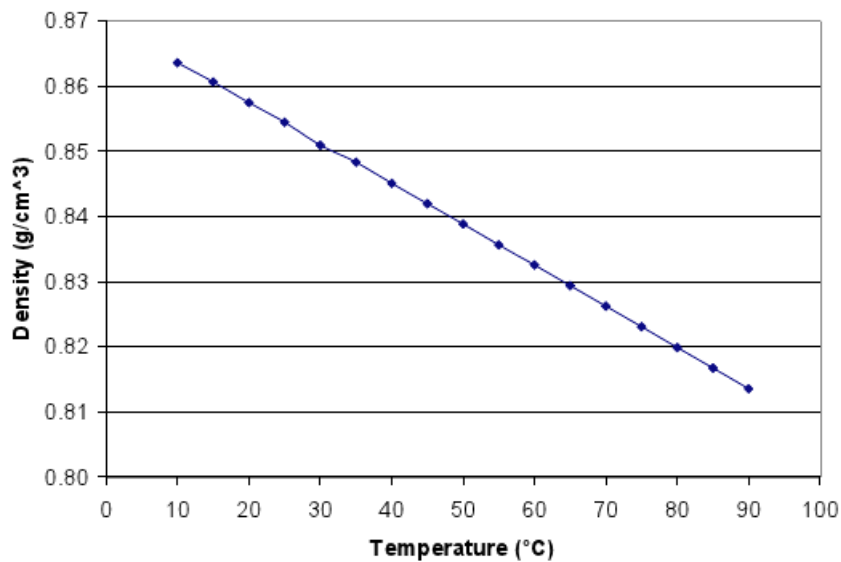


Figure 5.3: Trend of the density-temperature relationship for a generic lubricant.

carried out through the *Coefficient Form of Boundary* interface of *COMSOL Multiphysics*, which allows the users to implement the PDEs (*Partial Differential Equations*) necessary to analyze the considered problem.

This, like the oil film model, is a 2D problem and the equations that compose it, are solved by the software using the rotor  $T_A$  and pads  $T_{pad}$  temperatures obtained from models that will be described in the following chapters.

Considering the velocity field obtained through the fluid dynamic analysis of the lubricant, the temperature  $T_f$  inside the lubricant can be obtained using the energy equation:

$$\rho C_p \frac{\partial T_f}{\partial t} + \nabla \cdot (-\lambda \nabla T_f) + \beta \cdot \nabla T_f = \mathbf{f}_{visc}, \quad (5.3)$$

where  $C_p$  is the thermal capacity of the lubricant at constant pressure,  $\lambda$  is the thermal conductivity,  $\beta$  is a vector defined by the following relationship:

$$\beta = \begin{Bmatrix} \rho C_p \cdot u \\ \rho C_p \cdot v \\ \rho C_p \cdot w \end{Bmatrix}, \quad (5.4)$$

and  $\mathbf{f}_{visc}$  is the viscous dissipation due to the lubricant motion, which contributes to the energy equation as a heat source, and is defined as:

$$\begin{aligned} \mathbf{f}_{visc} = & 2\mu \left[ \left( \frac{\partial u}{\partial x} \right)^2 + \left( \frac{\partial v}{\partial y} \right)^2 + \left( \frac{\partial w}{\partial z} \right)^2 \right] + \\ & + \mu \left[ \left( \frac{\partial v}{\partial x} + \frac{\partial u}{\partial y} \right)^2 + \left( \frac{\partial w}{\partial v} + \frac{\partial v}{\partial w} \right)^2 + \left( \frac{\partial u}{\partial z} + \frac{\partial w}{\partial x} \right)^2 \right] + \\ & - \frac{2}{3}\mu \left( \frac{\partial u}{\partial x} + \frac{\partial v}{\partial y} + \frac{\partial w}{\partial z} \right)^2 \end{aligned}, \quad (5.5)$$

where  $\mu$  is the dynamic viscosity and  $u$ ,  $v$  and  $w$  are the components of the velocity field. In the *Coefficient Form Boundary* interface it is possible to impose both *Dirichlet boundary conditions* and *Neumann boundary conditions*; the first ones are imposed on the leading edge of the  $i$ -th pad and specify the variable value on the domain boundary; the second ones are imposed on the trailing edge and on the side edges of the  $i$ -th pad and specify the values that the derivative of the variable will assume on the considered domain boundary. These boundary conditions can be expressed as follows:

$$\begin{cases} T_f = T^i \text{ on } S_3 \\ \mathbf{n} \cdot (-\lambda \nabla T_f) = 0 \text{ on } S_1, S_2, S_4 \end{cases}, \quad (5.6)$$

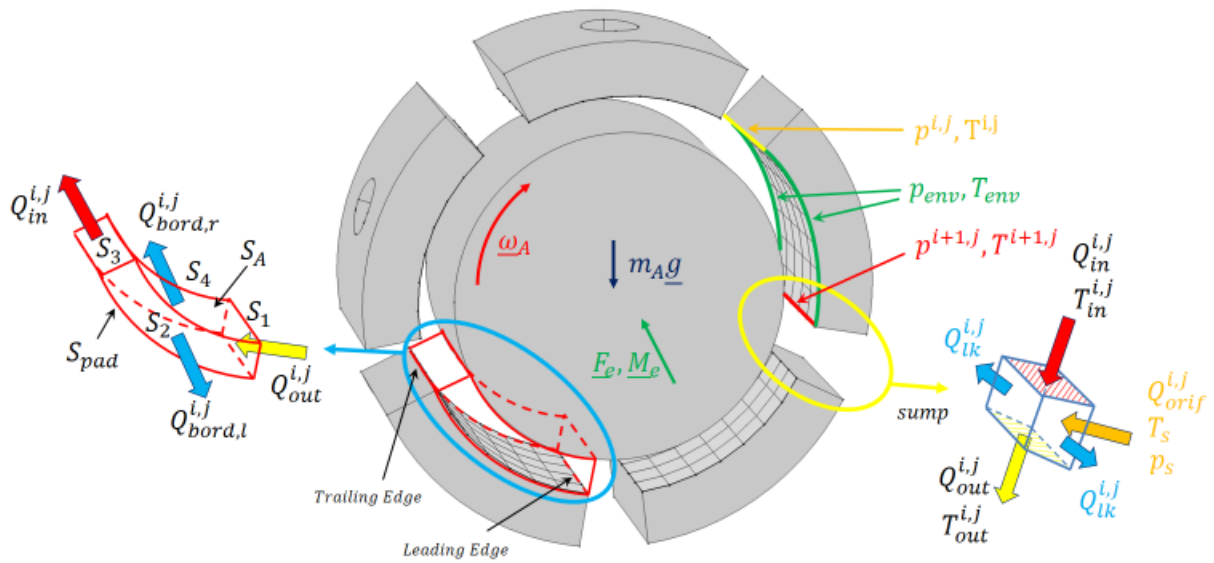


Figure 5.4: TPJB structure, lubricant supply plant and control volume.

where  $S_1$ ,  $S_2$ ,  $S_3$  and  $S_4$  are respectively the leading edge, the trailing edge and the two side edges of the control volume (reported in Figure 5.4) and  $T^i$  is the temperature of the lubricant supply plant preceding the  $i$ -th pad.

## 5.4 Supply sump modeling

Concerning the lubricant supply plant, the novelty with respect to the previous modeling step, is represented by the modeling of the thermal effects inside the lubricant supply plant. Basically, the model consists of an energy mixing equation between the lubricant flow rate of the previous pad and the flow rate supplied from the outside. In this way it is possible to obtain the lubricant temperature needed as a boundary condition on the leading edge of the next pad.

### 5.4.1 Thermal modeling

As previously mentioned and as shown in Figure 5.4, within the  $i$ -th lubricant supply plant the mixing between the lubricant flow rate from the outside  $Q_{orif}$  and that coming from the previous pad  $Q_{in}$  which are at different temperatures ( $T_s$  and  $T_{in}$ ).

The resultant lubricant flow has an intermediate temperature value between  $T_s$  and  $T_{in}$ , and can be considered as resulting from the convective and conduction heat transfer within the sump.

The energy balance that determines the lubricant temperature that comes out from the lubricant supply plant  $T_{out}$  used as boundary condition in the energy equation of the oil film model (Equation 5.3), can be expressed as follows:

$$T_{out} = \frac{Q_{in}}{Q_{out}} T_{in} + \frac{Q_{orif}}{Q_{out}} T_s, \quad (5.7)$$

where the temperature at which thermal equilibrium is reached, is calculated by assigning weights for the two temperatures,  $T_s$  and  $T_{in}$ , according to the two flow rate values,  $Q_{orif}$  and  $Q_{in}$ , compared to the total flow rate that coming out from the lubricant supply plant  $Q_{out}$  (see Figure 5.4).

The lubricant supply plant model is very important in order to obtain an accurate model in particular for the part concerning to the thermal exchange. This model, in fact, considering the mixing that occurs between the two lubricant flow rates allows to



optimally compute the temperature field which develops in the fluid and in the solid components of the system. Without an appropriate consideration of these phenomena, it would not be possible to obtain reliable results in terms of thermal instability.

As regards the pressure calculation inside the lubricant supply plant, this has less effect on the rotor dynamic results; its importance lays instead on the possibility of accurately calculating the lubricant flow rate required for a correct operation of the Tilting Pad Journal Bearing.

## 5.5 Pad modeling

Concerning the pad, the novelty with respect to the previous modeling step, is that the pad model is a 3D model that simulates the dynamical, structural and thermal behavior of the tilting pads that compose the bearing. The model analyzes the rigid rotational motions that each pad describes around its pivot following the displacement of the rotor, but it also simulates both the elastic and thermal deformations of the pads and the thermal field developed within them, due to the presence of the fluid films.

The inputs are the loads generated by the fluid films ( $M_{z,pad}$  and  $M_{x,pad}$ ), the temperature ( $T_f$ ) and the pressure ( $p$ ) of the lubricant; the outputs are position, velocity and temperature of the pads (respectively  $\mathbf{q}_{pad}$ ,  $\dot{\mathbf{q}}_{pad}$  and  $T_{pad}$ ).

### 5.5.1 Pad FEM modeling

The type of elements used for the pads FEM modeling are BRICK elements, which are widely used in the modeling of solid structural elements where there is not a negligible dimension compared to the others. These elements are able to represent a three-dimensional stress state. The BRICK elements have eight nodes, each node has three degree of freedom, each one corresponding to a translation. The natural or isoparametric coordinates of these elements are the coordinates  $\xi$ ,  $\eta$  and  $\mu$  shown in Figure 5.5; which vary from a minimum value of  $-1$  to a maximum of  $1$  with a zero value in the middle.

The components of the displacements vector have the following form:

$$u = \sum_{i=1}^m n_i(\xi, \eta, \mu) \cdot u_i, \quad (5.8)$$

$$v = \sum_{i=1}^m n_i(\xi, \eta, \mu) \cdot v_i, \quad (5.9)$$

$$w = \sum_{i=1}^m n_i(\xi, \eta, \mu) \cdot w_i, \quad (5.10)$$

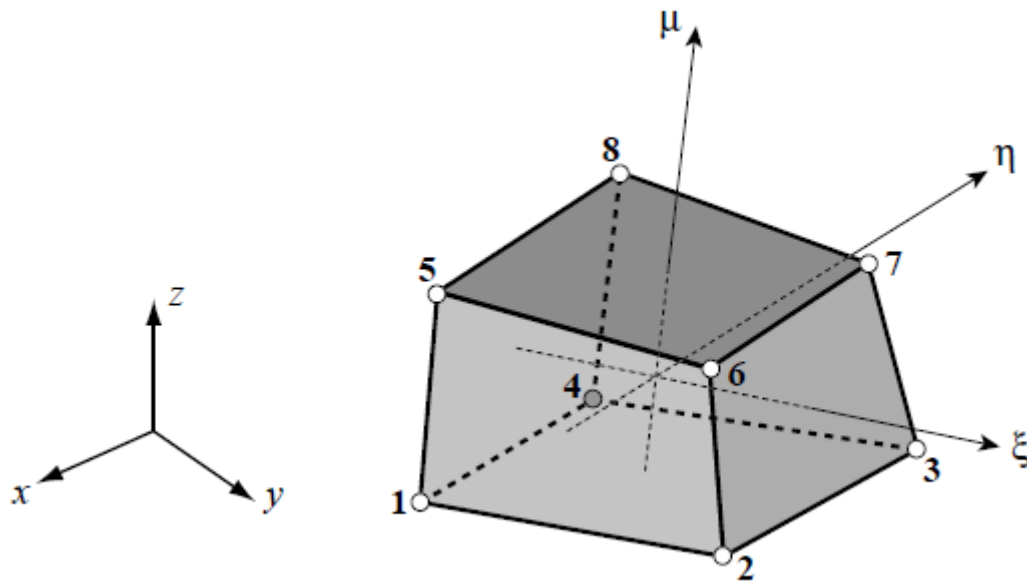


Figure 5.5: Scheme of a BRICK element.

where  $u_i, v_i, w_i$  are the nodal displacements of the element, and  $n_i$  are the shape functions.

### 5.5.2 Theory of the thermal modeling

As already mentioned in the previous chapters, the study of the heat exchange phenomena which develop within a hydrodynamic bearing is of fundamental importance because it directly affects the bearing performance.

It has already been seen how it is necessary to control the lubricant temperature in order to preserve its lubricating properties; at the same time also the temperature of the solid components of the bearing and of the rotor must be object of study, since an excessive temperature level would change the bearing geometry thus reducing lift and dynamic response; furthermore it can also lead to a further increase of instability phenomena due to excessive deformation.

In general terms the heat exchange is meant as the phenomenon that involves an energy flow due to the temperature difference between the considered bodies. This phenomenon

can occur with three different mechanisms: *conduction*, *convection* and *radiation*. In the

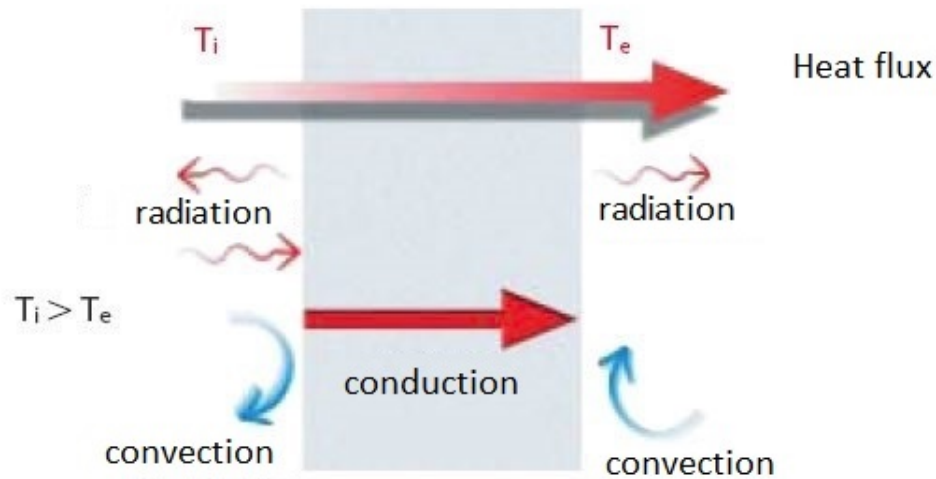


Figure 5.6: Heat exchange typologies.

specific case of hydrodynamic bearings, the fluid motion is determined by the rotor rotation: the fluid adheres to the rotor surfaces and is dragged inside the space between the rotor and the pads. The presence of fluid in motion involves a convective heat transfer and leads to a temperature rise due to viscous stresses. The thermal energy thus generated is then transmitted by conduction to the pads and to the rotor.

As mentioned above, in the realized model only the heat transfer phenomena due to convection and conduction are considered, therefore neglecting the contribution due to the radiation. This hypothesis is acceptable because the pads are flooded by the lubricant, i.e. the majority of the thermal energy that these exchange with the environment is transported by convection by the moving fluid.

The study of the heat transfer mechanisms is based on the *first law of thermodynamics* or *law of conservation of energy*, which in steady state conditions has the following form [29]:

$$\rho C_p \mathbf{u} \cdot \nabla T - k \nabla^2 T = \boldsymbol{\tau} : \mathbf{S}, \quad (5.11)$$

where  $\rho$  is the material density,  $C_p$  is the specific heat,  $\mathbf{u}$  is the velocity field,  $T$  is the absolute temperature,  $k$  is the thermal conductivity,  $\boldsymbol{\tau}$  is the viscous stress tensor and  $\mathbf{S}$  is

the strain rate tensor.

The first and the second term of the equation represent respectively the amount of thermal energy exchanged by convection and conduction, while the term  $\tau : \mathbf{S}$  is the expression in compact form of the operation  $\sum_{ij} \tau_{ij} S_{ij}$ , and represents the part of the mechanical energy which is transformed into thermal energy causing the temperature increase of the fluid (i.e. it is the term describing the mechanical energy dissipation due to the fluid viscosity).

## Conduction heat transfer

From a macroscopic point of view, the thermal conduction occurs as thermal energy is exchanged within bodies or among solid, liquid or gaseous bodies in contact with each another, without macroscopic material movement. The heat exchange is due to the transfer of molecular kinetic energy from high temperature areas to adjacent areas with lower temperature. In the particular case of metallic solids, in addition to this mechanism, the transported energy component due to the electrons motion should be also considered. The entity of thermal energy that is exchanged or that propagates in the considered body, depends on its geometry and characteristics as well as on the temperature difference among the body regions involved in the heat exchange phenomenon.

Consider a body composed by homogeneous material (uniform structure of the material at each point) and isotropic (thermophysical properties independent of the direction) whose two ends are located at a mutual distance equal to  $\Delta x$  and maintained at different and uniform temperatures  $T_1$  and  $T_2$ , with  $T_1 > T_2$ , as shown in Figure 5.7: under the assumption of one-dimensional flow, it follows that the temperature difference leads to a flux of thermal power  $q_x$  through the section  $A$ , which can be expressed as follows:

$$q_x \propto A \frac{\Delta T}{\Delta x}, \quad (5.12)$$

i.e. there is a direct proportionality among heat flux, temperature difference and section area, and an inverse proportionality between heat flux and length.

The proportionality factor is called *thermal conduction coefficient* or *material thermal*

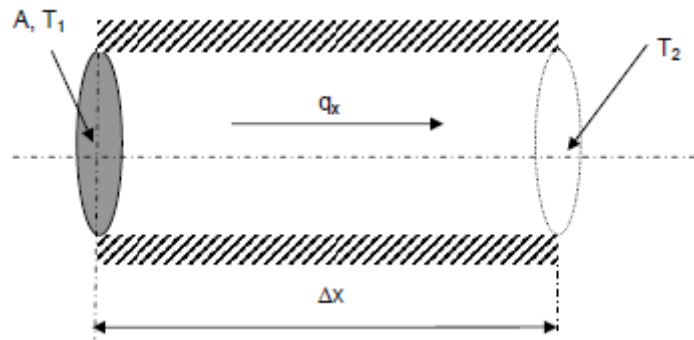


Figure 5.7: Heat flux through a cylinder

*conductivity*  $\lambda$ . This coefficient is a physical property of the material and characterizes its behaviour.

Equation 5.12 can be rewritten using the *Fourier postulate*:

$$q_x = -\lambda A \frac{\Delta T}{\Delta x}, \quad (5.13)$$

where the minus sign indicates that the direction of the heat flux must correspond with the temperature decreasing. This means that the heat transmission occurs in the opposite direction to the temperature gradient, i.e. from the hotter zone to the colder one, in accordance with the second law of the thermodynamics.

That above scenario is the simplest case of thermal conduction. One way to provide a more general treatment of the phenomenon is to perform an energy balance for an infinitesimal volume element  $dV$  of a generic body, as shown in Figure 5.8.

The general form of the energy conservation equation, limited only to the heat fluxes, is given by:

$$\dot{E}_{in} + \dot{E}_g - \dot{E}_{out} = \dot{E}_{st}, \quad (5.14)$$

where  $\dot{E}_{in}$  is the input thermal power,  $\dot{E}_{out}$  is the outgoing thermal power,  $\dot{E}_g$  is the thermal power generated within the element and  $\dot{E}_{st}$  is the thermal power stored within the element. It is possible to explicit the relationship as follows:

$$(q_x + q_y + q_z) + \dot{E}_g - (q_{x+dx} + q_{y+dy} + q_{z+dz}) = \dot{E}_{st}, \quad (5.15)$$

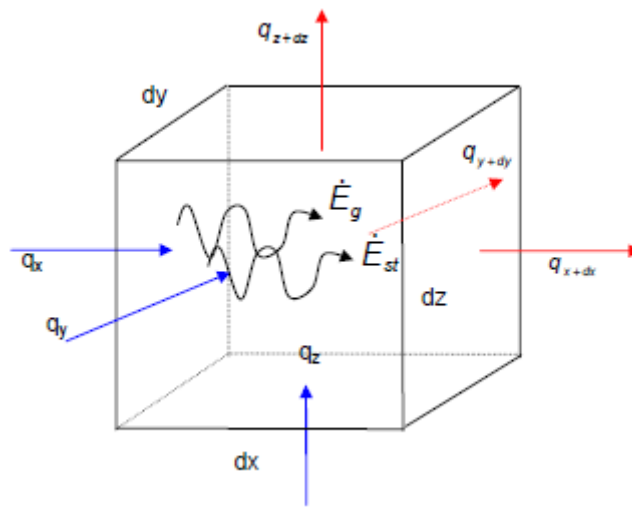


Figure 5.8: Energy balance of infinitesimal element  $dV$ .

where the first three terms  $q_x$ ,  $q_y$ ,  $q_z$  represent the incoming heat fluxes in the direction of each axis, each perpendicular to a volume surface, and the terms  $q_{x+dx}$ ,  $q_{y+dy}$  and  $q_{z+dz}$  represent the outgoing thermal fluxes in each direction through the opposite surface.

Equation 5.15 can be expressed using the Taylor series and obtaining:

$$q_{x+dx} = q_x + \frac{\partial q_x}{\partial x} dx, \quad (5.16)$$

$$q_{y+dy} = q_y + \frac{\partial q_y}{\partial y} dy, \quad (5.17)$$

$$q_{z+dz} = q_z + \frac{\partial q_z}{\partial z} dz. \quad (5.18)$$

All these terms are conductive heat fluxes and therefore, considering the the Fourier's law previously described (Equation 5.13), can be expressed as follows:

$$q_x = -\lambda \frac{\partial T}{\partial z} dy dz, \quad (5.19)$$

$$q_y = -\lambda \frac{\partial T}{\partial z} dx dz, \quad (5.20)$$

$$q_z = -\lambda \frac{\partial T}{\partial z} dy dx, \quad (5.21)$$

where the products  $dydz$ ,  $dx dz$  and  $dy dx$  represent the surfaces areas of the volume crossed by the heat flows in all directions. Therefore the output terms can be expressed as follows:

$$q_{x+dx} = - \left[ \lambda \cdot (dy \cdot dz) \cdot \frac{\partial T}{\partial x} + \frac{\partial}{\partial x} \left( \lambda \cdot (dy \cdot dz) \cdot \frac{\partial T}{\partial x} \right) \cdot dx \right], \quad (5.22)$$

$$q_{y+dy} = - \left[ \lambda \cdot (dx \cdot dz) \cdot \frac{\partial T}{\partial y} + \frac{\partial}{\partial y} \left( \lambda \cdot (dx \cdot dz) \cdot \frac{\partial T}{\partial y} \right) \cdot dy \right], \quad (5.23)$$

$$q_{z+dz} = - \left[ \lambda \cdot (dx \cdot dy) \cdot \frac{\partial T}{\partial z} + \frac{\partial}{\partial z} \left( \lambda \cdot (dx \cdot dy) \cdot \frac{\partial T}{\partial z} \right) \cdot dz \right]. \quad (5.24)$$

Along each direction the resulting flux is equal to the difference between the incoming and the outgoing fluxes, then:

$$q_x - q_{x+dx} = \frac{\partial}{\partial x} \left( \lambda \cdot (dy \cdot dz) \cdot \frac{\partial T}{\partial x} \right) = \frac{\partial}{\partial x} \left( \lambda \cdot \frac{\partial T}{\partial x} \right) \cdot dx \cdot dy \cdot dz, \quad (5.25)$$

$$q_y - q_{y+dy} = \frac{\partial}{\partial y} \left( \lambda \cdot \frac{\partial T}{\partial y} \right) \cdot dx \cdot dy \cdot dz, \quad (5.26)$$

$$q_z - q_{z+dz} = \frac{\partial}{\partial z} \left( \lambda \cdot \frac{\partial T}{\partial z} \right) \cdot dx \cdot dy \cdot dz. \quad (5.27)$$

As regards the internal generation, assuming that  $H$  is the thermal power generated per volume unit, uniform throughout the infinitesimal volume  $dV$ , it can be expressed as follows:

$$\dot{E}_g = H \cdot dx \cdot dy \cdot dz. \quad (5.28)$$

The mass  $\delta M$  of the considered material for the stored thermal capacity can be expressed as the product between the density  $\rho$  and the volume  $dV$ :

$$\delta M = \rho \cdot dx \cdot dy \cdot dz, \quad (5.29)$$



and the stored thermal power will be determined by the temperature variation in the time  $\tau$  for the specific heat at constant pressure of the material  $c_p$ , i.e. it is equal to the time variation of the internal energy  $U$  of the control volume:

$$\dot{E}_{st} = \rho c_p \frac{\partial T}{\partial \tau} \cdot dx \cdot dy \cdot dz. \quad (5.30)$$

The conduction equation in the most general form, becomes, for an arbitrary volume  $dV$ :

$$\frac{\partial}{\partial x} \left( \lambda \frac{\partial T}{\partial x} \right) + \frac{\partial}{\partial y} \left( \lambda \frac{\partial T}{\partial y} \right) + \frac{\partial}{\partial z} \left( \lambda \frac{\partial T}{\partial z} \right) + H = \rho c_p \frac{\partial T}{\partial \tau}. \quad (5.31)$$

Introducing the thermal diffusivity  $a$  (i.e. the ratio between the capacity of a material to conduct thermal energy and its ability to store energy), and considering  $\lambda$  to be constant (isotropic and homogeneous), the Fourier equation can be written as follows:

$$a \cdot \left( \frac{\partial^2 T}{\partial x^2} + \frac{\partial^2 T}{\partial y^2} + \frac{\partial^2 T}{\partial z^2} \right) = \frac{\partial T}{\partial \tau}. \quad (5.32)$$

If the system is in steady state conditions and there is no internal energy variation, it is possible to obtain the Poisson's equation:

$$\frac{\partial^2 T}{\partial x^2} + \frac{\partial^2 T}{\partial y^2} + \frac{\partial^2 T}{\partial z^2} + \frac{H}{\lambda} = 0. \quad (5.33)$$

Without internal energy generation and in steady state conditions, it is then possible to obtain the Laplace's equation:

$$\frac{\partial^2 T}{\partial x^2} + \frac{\partial^2 T}{\partial y^2} + \frac{\partial^2 T}{\partial z^2} = 0. \quad (5.34)$$

## Convective heat transfer

As previously mentioned, in addition to conduction, there is a second heat transfer phenomenon that affects the developed model; this phenomenon is called *thermal convection* and occurs when at least one of the two bodies between which the heat exchange occurs, is a fluid (in this case the lubricant). This phenomenon occurs if the fluid is moving with respect to the other body with which heat is exchanged.

Therefore, convection can take place between a solid and a gas, between a liquid and a gas, between two immiscible liquids or, as in our case, between a solid and a liquid. In general it can be said that convection occurs inside the fluid in a limited space that begins at the interface between the fluid and the other body and ends at a distance which depends on the considered system.

The relative motion of the fluid can have different causes. It can, for example, be due to mechanical devices or natural phenomena (wind, sea currents, etc..) that impose the fluid velocity. Convection is then denoted as *forced*. Instead, when the motion is generated by the heat exchange itself: the process modifies the physical characteristics of the fluid, in particular its density, and this generates a mass displacement, since fluid volumes with lower density tend to rise and to be replaced by volumes of fluid with higher density; the convection is denoted as *natural* or *free*. The distinction between the two types of convection is not clear and often in real situations they coexist. These are two extreme situations where it is often useful to bring back the real phenomena to obtain useful analytical representations. The microscopic procedures of energy transmission involved

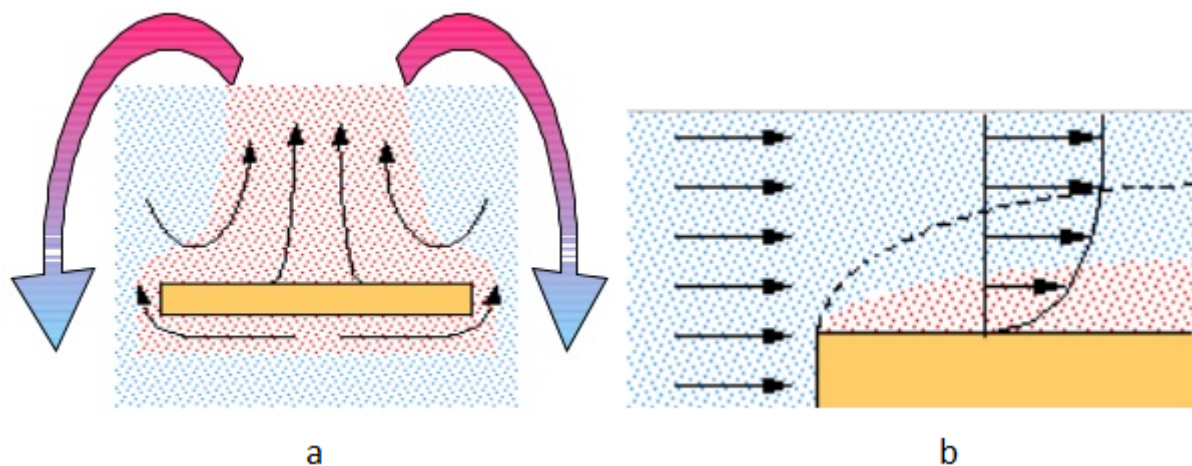


Figure 5.9: Schematization of the natural convection (a) and of the forced convection (b).

in the convection process are the same as that in the case of the conduction. The main difference is that, being the fluid in motion, the material motion that conveys this energy in the space and in the time is added to the energy transport due to molecular interactions.

If the fluid remains motionless, the internal heat transfer mechanism would be that of conduction and the energy would be transmitted among the material particles without macroscopic motion.

Having said that, it is essential to analyze the motion that the lubricant assumes inside the system.

It is important to remember that the fluid motion can be characterized by two different flow regimes, denoted as *laminar* and *turbulent*. In the laminar regime, the fluid proceeds in an orderly and regular way: the flux lines, which correspond to the particles trajectories, are parallel to each other. Therefore there is no mixing among different parts of the fluid system in motion and it is possible to identify for the various physical quantities at every fluid point and for each time instant a numerical well-defined value. Otherwise, in the case of turbulent motion, the fluid trajectories are twisty and complex, with continuous mixing processes within the flux among fluid masses of different areas. The distortions in the flow lines, if amplified, cause the establishment of a more chaotic and random motion regime in which the local physical quantities vary in time and in space without following determinable laws.

Between the laminar and the turbulent region, the flow is defined as *transitional* (see Figure 5.10). Considering for example the fluid motion inside a pipe, the effect of the

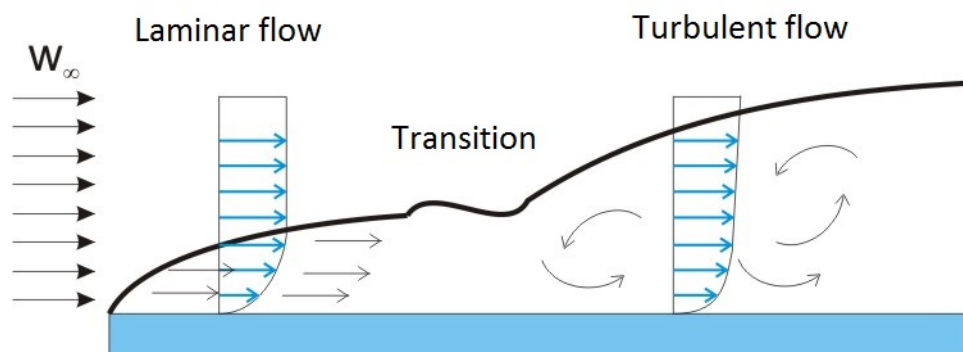


Figure 5.10: Transition between laminar and turbulent flow on a flat plate.

turbulent contribution generates more uniform velocity and temperature profiles: the velocity gradient (and hence the value of the tangential stress  $\tau$ ) in the area close to the

surface is much higher in turbulent regime with respect to the laminar one and such higher gradients contribute to increase the heat exchange near the surface.

The onset of a particular regime is related to the system conditions: the fluid properties (density  $\rho$  and viscosity  $\mu$ ), the velocity value  $w$ , the surface roughness of the surface of the solid in contact with the fluid and the geometric characteristics of the considered system through a characteristic dimension  $d$ . In other words the onset of the turbulence is linked to the ratio of inertial forces and viscous forces (or friction): if this is in favor of the first one, the flow regime is turbulent. More in general, the flow regime can be identified by a dimensionless parameter that takes into account all these quantities and which corresponds to the relationship between inertial forces and viscous forces, that is the Reynolds number:

$$Re = \frac{\rho dw}{\mu}. \quad (5.35)$$

Generally high  $Re$  values correspond to a turbulent flow, and low values of the Reynolds number involve a laminar flow.

In the following paragraphs the heat exchange process associated with the convection will be briefly described.

Consider a fluid at temperature  $T_\infty$  which moves at velocity  $u_\infty$  along a surface of area  $A$  and arbitrary shape. This surface has a uniform temperature  $T_s$  different from  $T_\infty$ . The heat flux  $q$  exchanged by convection between the surface and the fluid in each point of the considered surface can be expressed by the *Newton's relation*:

$$q = h \cdot (T_s - T_\infty), \quad (5.36)$$

where  $h$  is the *local heat transfer coefficient by convection*.

The thermal power  $\dot{Q}_c$  exchanged from the whole surface  $A$ , since the motion conditions vary along the surface itself, can be obtained as follows:

$$\dot{Q}_c = \int_A q \cdot dA = (T_\infty - T_s) \cdot \int_A h \cdot dA. \quad (5.37)$$

By defining an *average heat exchange coefficient for the convection*  $h_m$  given by:

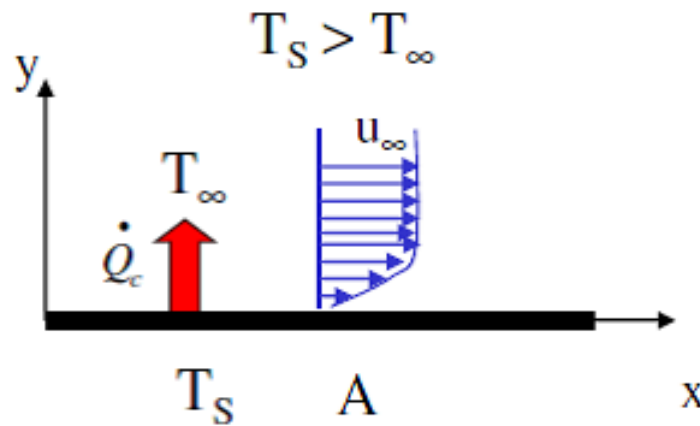


Figure 5.11: Convection on the flat plate.

$$h_m = \frac{1}{A} \cdot \int_a h \cdot dA, \quad (5.38)$$

it is possible to express the exchanged thermal power as:

$$\dot{Q}_c = h_m \cdot A \cdot (T_\infty - T_s). \quad (5.39)$$

It is interesting to notice that, within the boundary layer, for a generic distance  $x$  from the inlet edge and for an infinitesimal area  $dA$ , at distance  $y = 0$  from the wall, the heat exchange relationship that equals the convective heat flow to the conductive one (calculated using the Fourier postulate expressed by the Equation 5.13) can be applied. Indicating with  $k$  the thermal conductivity of the fluid:

$$q = h \cdot (T_s - T_\infty) = -k \frac{\partial T}{\partial y} \Big|_{y=0}. \quad (5.40)$$

In correspondence of the surface, since there is no fluid motion, the thermal energy is moved by conduction. It can therefore express the convective heat transfer coefficient in the following way:

$$h = \frac{-k \cdot \frac{\partial T}{\partial y} \Big|_{y=0}}{(T_s - T_\infty)}, \quad (5.41)$$

which indicates the strong influence of the temperature gradient that is present in correspondence of the surface of separation between fluid and wall, on the convective

heat transfer.

Indicating with  $L$  a length characterizing the system geometry, Equation 5.40 becomes:

$$q = L \cdot h \cdot (T_s - T_\infty) = -L \cdot k \cdot \left. \frac{\partial T}{\partial y} \right|_{y=0}, \quad (5.42)$$

and

$$L \cdot \frac{h}{k} = -\frac{L}{(T_s - T_\infty)} \cdot \left. \frac{\partial T}{\partial y} \right|_{y=0}. \quad (5.43)$$

The dimensionless group  $\frac{hl}{k}$  is called *Nusselt number* ( $Nu$ ) and represents the ratio between the heat exchanged by convection (between the surface and the fluid), and the heat that the same surface would exchange by conduction through a stationary fluid layer of thickness  $L$ . The higher the value of the Nusselt number, the greater the influence of the mass transport is in the heat exchange phenomenon.

Concerning the thermal exchange due to convection, it is easy to see how the main problem in the analysis of this phenomenon is the determination of the convective heat exchange coefficient  $h$ .

In this regard, due to the difficulty in solving analytically the constitutive equations above mentioned, it is almost essential to take advantage of the experimental investigation of physical models, supported by the dimensional analysis; this method allows to generalize the experimental results through the use of the dimensionless numbers, each of which comprises a group of some of the physical quantities which the convective phenomenon depends on. Those dimensionless groups are obtained through the use of the *Buckingham  $\pi$  theorem*, which states that if an equation, which describes a physical phenomenon, is dimensionally homogeneous (i.e., changing the units of measure the equation does not change), it can be reduced to a relationship among a full set of dimensionless groups.

In particular, it uses the following dimensionless groups:

- Reynolds number:

$$Re = \frac{\rho dw}{\mu}, \quad (5.44)$$

which represents the ratio between the inertia forces and frictional forces;

- Nusselt number:

$$Nu = \frac{hL}{k}, \quad (5.45)$$

which represents the real incidence of the convective heat transfer mechanisms with respect to the conductive one;

- Prandtl number:

$$Pr = \frac{c_p \mu}{k}, \quad (5.46)$$

which represents the relationship between the availability of the fluid to transport momentum and its availability to transport heat, and depends on the nature of the medium and its physical state;

- Grashof number:

$$Gr = \frac{g\beta(T_s - T_\infty)L^3}{\nu^2}, \quad (5.47)$$

which represents the ratio between the inertia forces of flotation and the squared friction forces.

The relationship that is experimentally used between those dimensionless numbers is generally expressed as follows:

$$Nu = f(Re, Gr, Pr), \quad (5.48)$$

which, through the use of experimental data, can be written in the following form:

$$Nu = C \cdot Re^a \cdot Gr^b \cdot Pr^c, \quad (5.49)$$

where  $C$ ,  $a$ ,  $b$  and  $c$  are coefficients obtained experimentally.

### 5.5.3 Thermal modeling

In the developed model the heat exchange inside the pads is driven by the fluid movement which, due to the rotation of the rotor, adheres to the journal surface and is dragged in proximity of the pads, with a consequent temperature increase; the thermal energy generated by this phenomenon is then transferred inside the pad.

The study of heat transfer phenomena in solid components, is simulated through the *Heat Transfer by Solid* interface of the software *COMSOL Multiphysics*®4.4, usually used where there is need to model any heat exchange phenomenon. The energy equation implemented within the proposed model can be written as follows:

$$\rho c_p \frac{\partial T}{\partial t} + \rho c_p \mathbf{u} \cdot \nabla T = \nabla \cdot (k \nabla T) + Q, \quad (5.50)$$

where  $\mathbf{u}$  is the lubricant velocity field and  $Q$  is the heat source.

The initial temperature of the whole pad is set to 293.15[K], which is equal to the ambient temperature. Concerning the boundary conditions, a forced convection, due to the fluid motion, has been imposed on the pad surface in contact with the oil films (Figure 5.12). This kind of boundary condition can be set through the *Convective Heat Flux* function,

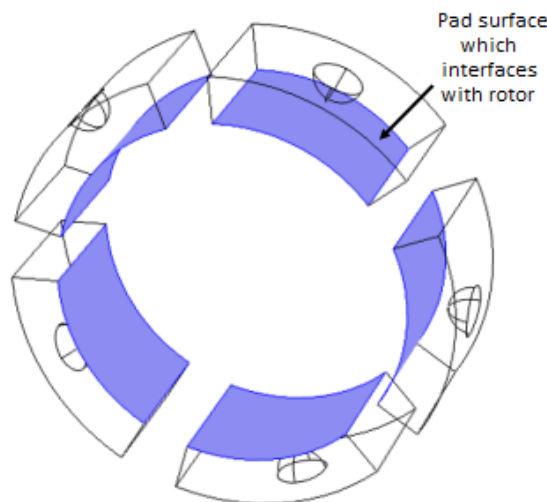


Figure 5.12: Pads Surfaces concerned by the convective heat transfer with the lubricant.

which allows to use different types of correlations for the calculation of the convective



coefficient  $h$ ; in this model the *Average Transfer Coefficient* method, which calculates the convection coefficient as a function of the motion field of the fluid film and the value of the area on which the heat exchange occurs, has been chosen.

In accordance with the Equation 5.40, the heat exchange between pad and lubricant inside the oil film, is expressed by the following equation:

$$\mathbf{n} \cdot (-\lambda \nabla T_{pad}) = h_{film} (T_f - T_{pad}), \quad (5.51)$$

where  $\mathbf{n}$  is the normal vector at the pad surface,  $h_{film}$  is the convective heat transfer coefficient between the pad and the fluid film,  $T_f$  and  $T_{pad}$  are respectively the fluid film and pad temperatures.

The remaining pad surfaces are also interested by convective phenomena: indeed they are in contact with the supply lubricant, which is at a temperature  $T_s$ , generally different from the pads one; this generates a convective heat exchange in correspondence of the surfaces shown in Figure 5.13. for this surfaces, the heat transfer coefficient is not calculated

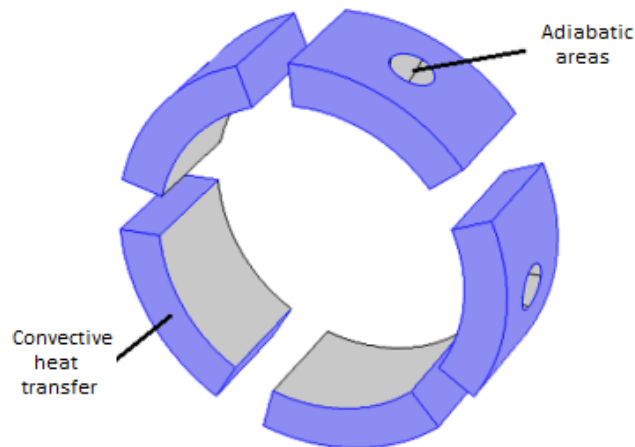


Figure 5.13: Pads Surfaces subjected to heat exchange and adiabatic surfaces.

through an empirical correlation but, since the fluid is stationary, a value of  $h$  equal to  $50[W/m^2K]$  has been chosen. Even in this case, in accordance with the Equation 5.40, the heat exchange that interests such surfaces is defined by the relationship:

$$\mathbf{n} \cdot (-\lambda \nabla T_{pad}) = h_{pad} (T_s - T_{pad}), \quad (5.52)$$

where  $h_{pad}$  is the convective heat transfer coefficient between the pad and the lubricant within which it is immersed,  $T_s$  and  $T_{pad}$  are respectively the supply and pad temperatures.

For a correct analysis of the model a possible thermal exchange should be considered even in the spherical surface of the pivot; however in this work, due to the reduced lubricant quantity that comes in contact with the pivot, the author chose such pad portions to be thermally insulated (gray spherical sections in Figure 5.13), imposing a heat exchange equal to zero in the spherical surface of the pivot:

$$\mathbf{n} \cdot (-\lambda \nabla T_{pad}) = 0. \quad (5.53)$$

As specified in the Chapter 5.5.1, the pads model is a 3D FEM model composed by BRICK elements. In contrast with the dynamic/structural study, which was carried out in the time domain using *transient* analysis, the pads thermal behavior was evaluated through stationary tests, i.e. *steady state* tests. This choice is due to the high computational weight that a *transient* analyses of a solid body would involve; thus, in order to reduce calculation times, the study of the pads thermal behavior is carried out through several *steady state* tests, one for each step of the dynamic problem carried out in the time domain.

Considering the previously shown boundary conditions and taking into account the classical equations of the FEM modeling, the equations that describe the pads thermal behavior are defined as follows:

$$\mathbf{K}_{pad}^t \cdot \mathbf{T}_{pad} = \mathbf{Q}_{pad}, \quad (5.54)$$

where  $\mathbf{K}_{pad}^t$  is the pad thermal stiffness matrix and  $\mathbf{Q}_{pad}$  is the heat source due to the fluid film.

#### 5.5.4 Elastic modeling

As previously mentioned, the pressure field that develops in the fluid film during the bearing operation acts both on the rotor and on the pads causing their deformation

and tilting motion; furthermore, the temperature field that develops within the pads contributes to their deformation. The purpose of this submodel is to determine the elastic behavior of the pad.

Under the hypothesis of homogeneous, isotropic and linear elastic material, the elastic properties of the pads are expressed through the constants  $E$  (Young's modulus),  $\nu$  (Poisson's ratio) and  $G$  (shear modulus), related among them by the following relation:

$$G = \frac{E}{2(1 + \nu)}. \quad (5.55)$$

The connection between deformations and displacements is given by the compatibility equations which, considering a Cartesian system such as that shown in Figure 5.14, have the following form:

$$\varepsilon_x = \frac{\partial u}{\partial x}, \quad \varepsilon_y = \frac{\partial v}{\partial y}, \quad \varepsilon_z = \frac{\partial w}{\partial z}, \quad (5.56)$$

$$\gamma_{xy} = \frac{\partial u}{\partial y} + \frac{\partial v}{\partial x}, \quad \gamma_{yz} = \frac{\partial v}{\partial z} + \frac{\partial w}{\partial y}, \quad \gamma_{xz} = \frac{\partial w}{\partial x} + \frac{\partial u}{\partial z}, \quad (5.57)$$

where  $\varepsilon_x, \varepsilon_y, \varepsilon_z$  are the linear deformation along the respective axes,  $\gamma_{xy}, \gamma_{yz}, \gamma_{xz}$  are the tangential sliding and  $u, v, w$  are the displacements.

The connection between stress and deformation for a linear isotropic material is expressed by the following equation:

$$\begin{Bmatrix} \sigma_x \\ \sigma_y \\ \sigma_z \\ \tau_{xy} \\ \tau_{yz} \\ \tau_{xz} \end{Bmatrix} = \frac{E}{(1 + \nu)(1 - 2\nu)} \begin{bmatrix} 1 - \nu & \nu & \nu & 0 & 0 & 0 \\ \nu & 1 - \nu & \nu & 0 & 0 & 0 \\ \nu & \nu & 1 - \nu & 0 & 0 & 0 \\ 0 & 0 & 0 & \frac{1-2\nu}{2} & 0 & 0 \\ 0 & 0 & 0 & 0 & \frac{1-2\nu}{2} & 0 \\ 0 & 0 & 0 & 0 & 0 & \frac{1-2\nu}{2} \end{bmatrix} \cdot \begin{Bmatrix} \varepsilon_x \\ \varepsilon_y \\ \varepsilon_z \\ \gamma_{xy} \\ \gamma_{yz} \\ \gamma_{xz} \end{Bmatrix}, \quad (5.58)$$

where  $\sigma_x, \sigma_y, \sigma_z$  are the normal stresses, and  $\tau_{xy}, \tau_{yz}, \tau_{xz}$  are the shear stress.

For a three-dimensional effort, the equilibrium equations can be expressed as follows:

$$-\frac{\partial \sigma_x}{\partial x} - \frac{\partial \tau_{xy}}{\partial y} - \frac{\partial \tau_{zy}}{\partial z} = F_x, \quad (5.59)$$

$$-\frac{\partial \sigma_y}{\partial y} - \frac{\partial \tau_{xy}}{\partial x} - \frac{\partial \tau_{zy}}{\partial z} = F_y, \quad (5.60)$$

$$-\frac{\partial \sigma_z}{\partial z} - \frac{\partial \tau_{yz}}{\partial y} - \frac{\partial \tau_{xz}}{\partial x} = F_z, \quad (5.61)$$

where the terms  $F_x$ ,  $F_y$  and  $F_z$  represent the volume forces. In this work the elastic

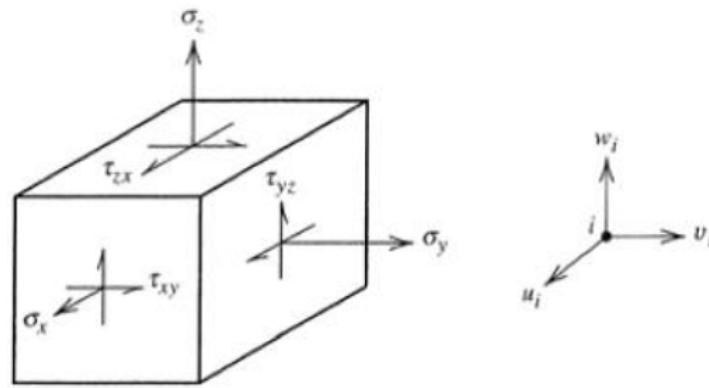


Figure 5.14: Reference system of the considered 3D solid.

modeling of the solid components it was performed using the *Solid Mechanics* interface of *COMSOL Multiphysics*. This interface is useful to perform both static and dynamic structural analysis of any type of geometry and with different types of stresses.

Replacing in the equilibrium Equations 5.59, 5.60, 5.61 the relationship between stress and deformation found in the Equation 5.58 and the relationship between deformations and displacements found in the Equations 5.56 and 5.57, it is possible to obtain for the formulation of the elastic problem [30], i.e. the Navier equations:

$$-(\lambda + \mu)\nabla(\nabla \cdot \mathbf{q}) - \mu\nabla^2 \mathbf{q} = \mathbf{F}, \quad (5.62)$$

where  $\mathbf{q}$  is the displacement field,  $\mathbf{F}$  is the volume forces vector,  $\mu$  is the Lamé's first parameter (equal to  $G$  and defined in the Equation 5.55) and  $\lambda$  is the Lamé's second parameter, defined as follows:

$$\lambda = \frac{\nu E}{(1 + \nu)(2 - 2\nu)}. \quad (5.63)$$

The Navier equations are implemented within the *Solid Mechanics* interface used in the model.

For a correct analysis of the model also the flexibility of the spherical pivot interface, since a possible deformation in the operating phase greatly affects the system behavior, especially in the more demanding operating conditions, i.e. with high temperature and pressure values within the fluid film. However in the present work, the spherical pivot has been considered rigid: *Fixed Constraint* has been used as a boundary condition imposing a displacement field equal to zero in the pivot interface (Figure 5.15):

$$\mathbf{q}_{pad} = 0. \quad (5.64)$$

The load on pads is set with the *Boundary Load* command, which directly applies the

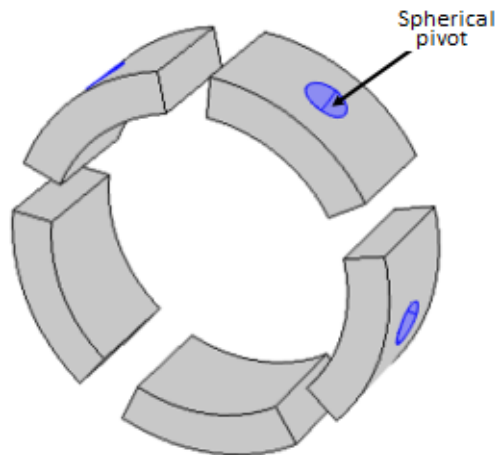


Figure 5.15: Spherical pivot surfaces with zero displacement.

pressure generated by the fluid film (calculated in the submodel previously described) on the considered surfaces, as shown in Figure 5.12.

In addition to the elastic deformation due to the pressure field, the model takes also into account the thermal deformation due to the pad temperature distribution. These are fundamental for a correct analysis of the system because they modify the pad geometry and, consequently, the oil film geometry. In accordance with Equation 5.58, it is possible

to define the elastic stiffness matrix  $\mathbf{D}$  as:

$$\mathbf{D} = \frac{E}{(1 + \nu)(1 - 2\nu)} \begin{bmatrix} 1 - \nu & \nu & \nu & 0 & 0 & 0 \\ \nu & 1 - \nu & \nu & 0 & 0 & 0 \\ \nu & \nu & 1 - \nu & 0 & 0 & 0 \\ 0 & 0 & 0 & \frac{1-2\nu}{2} & 0 & 0 \\ 0 & 0 & 0 & 0 & \frac{1-2\nu}{2} & 0 \\ 0 & 0 & 0 & 0 & 0 & \frac{1-2\nu}{2} \end{bmatrix}. \quad (5.65)$$

In addition, defining the thermal expansion tensor  $\alpha_T$  as:

$$\alpha_T = \begin{bmatrix} \alpha & 0 & 0 \\ 0 & \alpha & 0 \\ 0 & 0 & \alpha \end{bmatrix}, \quad (5.66)$$

it is possible to calculate the pad overall deformation  $\varepsilon$ :

$$\varepsilon = \mathbf{D}^{-1} \boldsymbol{\sigma} + \alpha_T \Delta T, \quad (5.67)$$

where  $\boldsymbol{\sigma}$  is the stress tensor.

As described in Chapter 5.5.1, the elastic analyses of the pad is performed through a FEM discretization of the continuous system, using BRICK type elements.

In terms of computational weight it is possible to do the same considerations expressed for the thermal behavior study of the pads. In this regard, in order to reduce the calculation times, the elastic modeling of the pads was not carried out in time domain, but rather through more *steady state* tests, one for each step of the dynamic problem carried out in the time domain.

Taking into account the previously shown boundary conditions, and considering the classical equations of the FEM modeling, the equations that describes the structural behavior of the pads is defined as follows:

$$\mathbf{K}_{pad} \cdot \mathbf{q}_{pad} = \mathbf{f}_{pad}, \quad (5.68)$$

where  $\mathbf{K}_{pad}$  and  $\mathbf{q}_{pad}$  are respectively the stiffness matrix and the vector of the pad displacements.

Finally, remembering Equation 5.54, it is possible to write the equations system describing the whole thermo-elastic behavior of the pads:

$$\begin{bmatrix} \mathbf{K}_{pad} & \mathbf{K}_{pad}^{ut} \\ \mathbf{0} & \mathbf{K}_{pad}^t \end{bmatrix} \begin{Bmatrix} \mathbf{q}_{pad} \\ \mathbf{T}_{pad} \end{Bmatrix} = \begin{Bmatrix} \mathbf{f}_{pad} \\ \mathbf{Q}_{pad} \end{Bmatrix}, \quad (5.69)$$

where  $\mathbf{K}_{pad}^{ut}$  is the thermo-elastic stiffness matrix of the pad.

## 5.6 Rotor modeling

As shown in Figure 5.16 the rotor model is a 3D model composed by BEAM elements connected to two appropriately created solid parts through the 3D design tool Software of *COMSOL Multiphysics*. The two solids representing the rotor fractions enclosed in the bearings allow to analyze the influence that the bearings have on the rotor thermo-structural behaviour. This model therefore provides both the rotor FEM modeling and

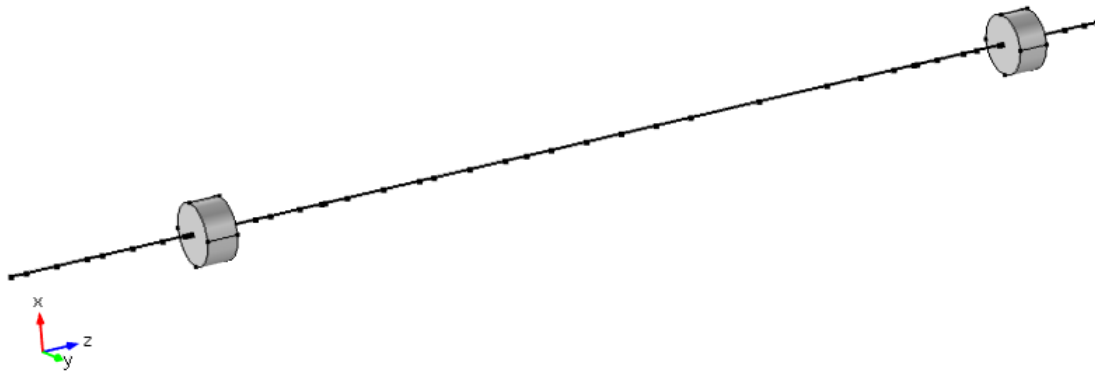


Figure 5.16: Rotor discretization with BEAM elements and rotor solid fractions.

the modeling of deformation and temperature field that are created, as a result of the lubricant motion inside the bearings. In this regard, the inputs are forces and moments generated by the bearings ( $F_{x,A}$ ,  $F_{y,A}$ ,  $F_{z,A}$ ,  $M_{x,A}$ ,  $M_{y,a}$  and  $M_{z,a}$ ), the bearing temperature field ( $T$ ) and possible external loads ( $\mathbf{F}_e$  and  $\mathbf{M}_e$ ). The outputs are the temperature ( $T_A$ ) and the displacement ( $\mathbf{q}_a$ ) of the rotor (needed to calculate the fluid film thickness).

### 5.6.1 Elastic modeling

As previously mentioned this submodel aims to evaluate motion, deformation and temperature of the rotor. In the present work the motion calculation is give, to modeling through rotor BEAM elements; as it regards the deformations and the temperature calculation, a different way has been followed.

The rotor fractions enclosed in the two bearings (shown in green in Figure 5.17) are not



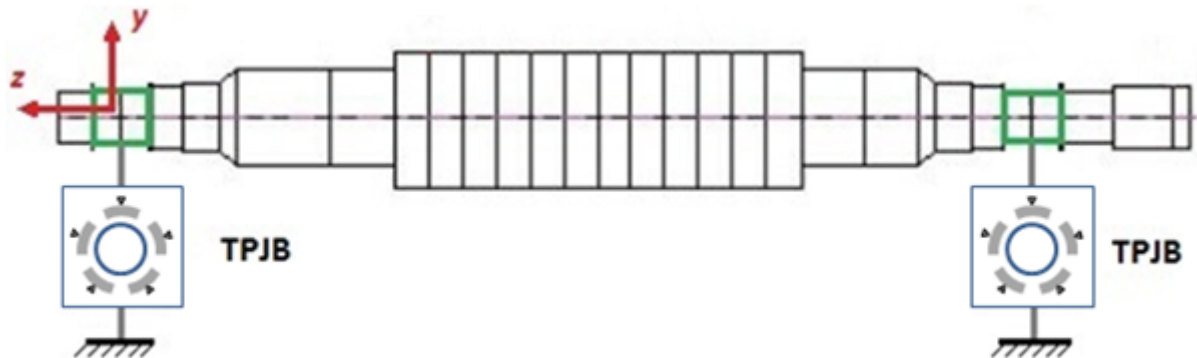


Figure 5.17: Rotor and rotor fractions modeled by solid elements.

modeled exclusively through BEAM elements, but through solid elements: using the 3D drawing tools and the physics *Solid Mechanics* in the software *COMSOL Multiphysics*, it will be possible to analyze the rotor fractions. These rotor fractions represent the connection between the bearing and the whole model of the rotor; each rotor fraction has a cylindrical section with a thickness that coincides with the axial length of the bearing. The elastic modeling of this sub-model is based on the same physical principles discussed in Chapter 5.5.4, because it represents the same elastic deformation problem of a solid component seen for the bearing pads, and has been modeled using the same interface *Solid Mechanics*. Another analogy is that for modeling the solid component 3D elements of BRICK type have been used; the characteristics of these elements are exposed in chapter 5.5.1.

Being a solid component, and then computationally heavier than a rotor model made by BEAM elements, the structural analysis and, as we will see later, also thermal have been realized through *steady state* analyses.

The equation that describes the structural behavior of the rotor fraction is defined as follows:

$$\mathbf{K}_{A,frac} \cdot \mathbf{q}_{A,frac} = \mathbf{f}_{A,frac}, \quad (5.70)$$

where  $\mathbf{K}_{A,frac}$  and  $\mathbf{q}_{A,frac}$  are respectively the stiffness matrix and the rotor displacement.

### 5.6.2 Thermal modeling

Regarding the thermal behavior of the rotor, and in particular of the solid parts through which this has been modeled, it is referred to the already exposed theory in Chapter 5.5.2, having to also model in this case a heat exchange between the components which occurs through convection and conduction processes, according to the equation:

$$\rho c_p \frac{\partial T}{\partial t} + \rho c_p \mathbf{u} \cdot \nabla T = \nabla \cdot (k \nabla T) + Q. \quad (5.71)$$

The boundary conditions used for the following sub-model were modeled using the

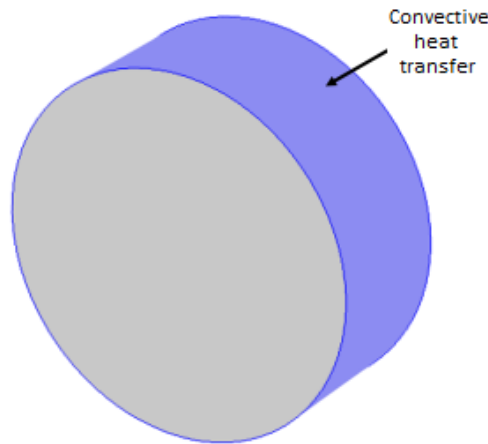


Figure 5.18: Part of the rotor fraction that exchanges heat with the fluid film by convection.

same interface *Heat Transfer in Solids* of *Comsol* seen for the pads thermal modeling: firstly an initial temperature of the whole rotor fraction has been imposed equal to 293.15[K], with the convective boundary condition an heat exchange between the outer surface of the rotor enclosed within the bearing and the fluid film (Figure 5.18); this is shown into the following equation:

$$\mathbf{n} \cdot (-\lambda \nabla T_{A,frac}) = h_{film} (T_f - T_{A,frac}), \quad (5.72)$$

where  $h_{film}$  is the convective heat transfer coefficient between the rotor and the fluid film,  $T_f$  and  $T_{A,frac}$  are respectively the fluid film temperature and the temperature of the rotor outer surface.

Another boundary condition is modeled considering instead a conductive heat exchange inside the rotor, which develops through the plane surfaces of the rotor fraction, as shown in Figure 5.19. In accordance with Equation 5.13 it is possible to express this boundary

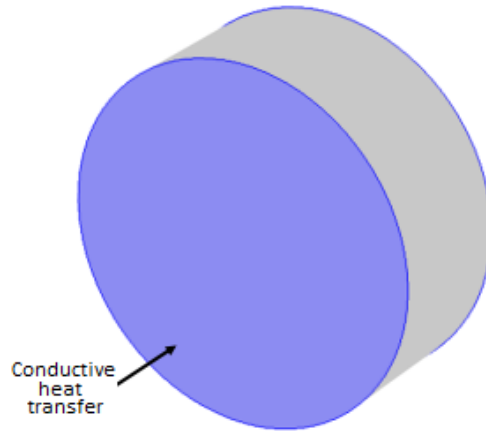


Figure 5.19: Parts of the rotor that exchange heat through conduction process.

condition as:

$$\mathbf{n} \cdot (-\lambda \nabla T_{A,frac}) = d_A \lambda (T_{env} - T_{A,frac}), \quad (5.73)$$

where  $\lambda$  is the thermal conduction coefficient of the rotor and  $d_A$  represents the distance between the surface of the considered rotor and the rotor portion that is in thermal equilibrium with the external environment.

As already mentioned, even the study of the rotor thermal behaviour has been carried out by *steady state* analysis of the 3D FEM model composed by BRICK elements.

The heat exchange inside the rotor fraction is controlled by the following equation:

$$\mathbf{K}_{A,frac}^t \cdot \mathbf{T}_{A,frac} = \mathbf{Q}_{A,frac}, \quad (5.74)$$

where  $\mathbf{K}_{A,frac}^t$  is the thermal stiffness matrix of the rotor and  $\mathbf{Q}_{A,frac}$  is the heat source due to the presence of the fluid film.

Following what has been said about the rotor thermal behavior, and remembering Equation 5.70 that describes the deformations, the thermo-structural behavior of this component can be described according to an equation analogous to Equation 5.69, seen

for the pads, but with different contributions:

$$\begin{bmatrix} \mathbf{K}_{A,frac} & \mathbf{K}_{A,frac}^{ut} \\ \mathbf{0} & \mathbf{K}_{A,frac}^t \end{bmatrix} \begin{Bmatrix} \mathbf{q}_{A,frac} \\ \mathbf{T}_{A,frac} \end{Bmatrix} = \begin{Bmatrix} \mathbf{f}_{A,frac} \\ \mathbf{Q}_{A,frac} \end{Bmatrix}, \quad (5.75)$$

where  $\mathbf{K}_{A,frac}^{ut}$  is the thermo-elastic stiffness matrix of the rotor.

The thermo-elastic study of this component is essential in view of the whole model: by this analysis in fact it is possible to estimate the rotor deformation value, which directly affects the geometry of the fluid film inside the bearing and then its operation; but especially through the knowledge of the thermal field inside the rotor fraction, it is possible to properly evaluate the temperature gradient that will then be applied to the rotor BEAM model.

## 5.7 Numerical solvers

The developed model involves the carrying out of *transient* simulations which analyzes the behavior of the system in the time domain. This analysis is done by setting a *Time Dependent* study in the software *COMSOL Multiphysics*<sup>®</sup>4.4. This type of study uses the BDF multistep method, which calculates and uses information from a previous step, to calculate and solve the next steps. The solution of each step is realized using the *Segregated* solver. The *Segregated* solver can be used both for stationary studies and for

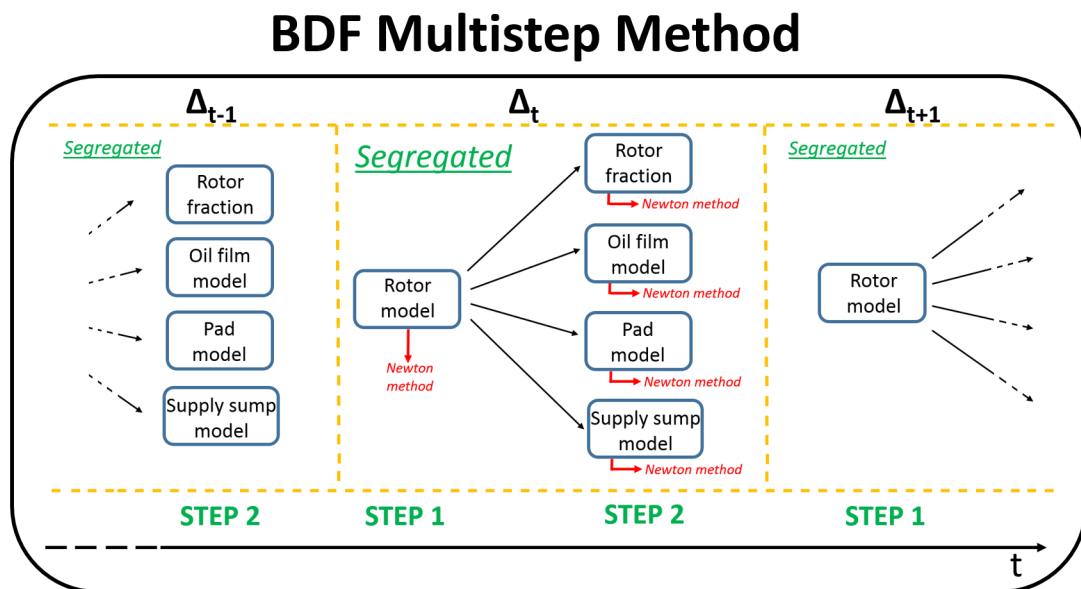


Figure 5.20: Conceptual map of the realized model.

time domain studies. This solver manages the components of the modeled system using a “segregated” approach that does not deal with the system variables in a coupled way, but in a decoupled one, dividing the total solution of the system in multiple steps [20].

Each step uses a simplified version of Newton’s method. This method is based on the linear approximation principle: you find the root  $r$  of a function  $f(x) = 0$  iterating from an initial estimate of the solution  $x_0$ , with  $h = r - x_0$ .

With  $h$  small, it is possible to approximate the function  $f$  linearly with:

$$0 = f(r) = f(x_0 + h) \approx f(x_0) + hf'(x_0), \quad (5.76)$$

from which a new estimate of the solution can be obtained by:

$$x_1 = x_0 - \frac{f(x_0)}{f'(x_0)}. \quad (5.77)$$

Generalizing for the  $n$ -th iteration is then:

$$x_{n+1} = x_n - \frac{f(x_n)}{f'(x_n)}, \quad (5.78)$$

Alternatively to this type of solver, *Comsol* allows to use the *Fully Coupled Solver*, it can

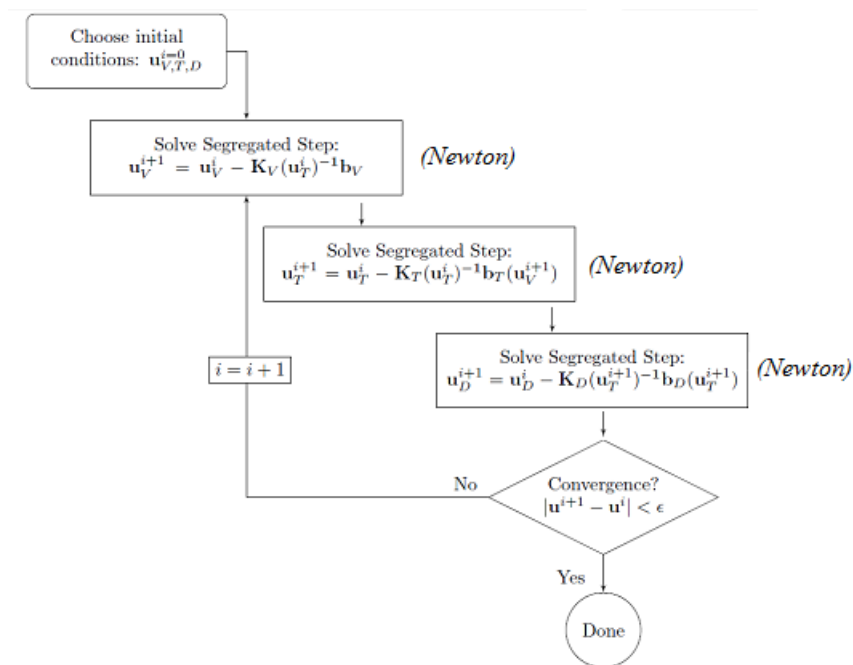


Figure 5.21: Modeling approach used by the *Segregated* solver.

also be used in the time domain, but it is not suitable for the resolution of this model given the strong non-linearity of the analyzed system. In this regard it can be said that the advantages encountered in the use of the *Segregated* solver in the simulation, are manifold: firstly it is a more streamlined resolution method and therefore less computationally expensive, but mostly (as it will be described below) it allows to arbitrarily decide in what sequence the various physical steps should be resolved, providing therefore a direct management on the variables flow among the elements of the proposed model.

As previously said the *Segregated* solver established by the user allows to subdivide the system solution in different steps solved in the order with which they were included in the model. In each step the variable to be solved must be specified (and thus the relative physical ambient), and the type of solver (direct or iterative) of the linear system.

In the present work it was decided to assign to the first step the BEAM physics: this means that in the first part of the analysis the solver will calculate the variables associated with that interface using as boundary conditions the inputs provided by the other physics, which then coincide with the initial conditions of the system. Upon reaching convergence, the solver will automatically switch to the resolution of the second step in which all the remaining other physical ambients were placed (i.e. the rotor fraction, the oil film model, the supply sump model and the pad model).

## Experimental data

In order to validate the developed models through the comparison with experimental data, some simulations have been performed evaluating the most important quantities involved in the bearing operation. The experimental tests used as a reference have been carried out by General Electric Oil & Gas. In particular three main test cases have been considered: the first one concerns the fluid dynamical behavior of tilting pad journal bearings, the second test case aims at the evaluation of the rotor dynamical characteristics of a turbomachine supported by two tilting pad journal bearings while the third one has been designed to highlight the Morton effect, detecting the pads temperatures. The three test cases have been used for the experimental validation of the three modeling steps carried out in this thesis (the fluid dynamical step, the rotor dynamical step and the ThermoElastoHydroDynamic step). In the following sections, the experimental apparatus and procedures will be described separately:

- Test case 1: experimental apparatus and data for the fluid dynamical validation;
- Test case 2: experimental apparatus and data for the rotor dynamical validation;
- Test case 3: experimental apparatus and data for the ThermoElastoHydroDynamic validation.



## 6.1 Test case 1: Fluid dynamical characteristics

In order to validate the first model developed in this thesis, an experimental data set obtained by General Electric Oil & Gas in the Massa-Carrara testing plant (reported in Figure 6.1) has been used. The tests have been carried out evaluating the bearings performances during the start-up and shut-down phases, varying the lubricant supply pressure and temperature and realistically reproducing the interactions between the bearings and the supply plant. The lubricant flow rate is provided by two centrifugal pumps, operated by two asynchronous motors. With a manual valve it is possible to

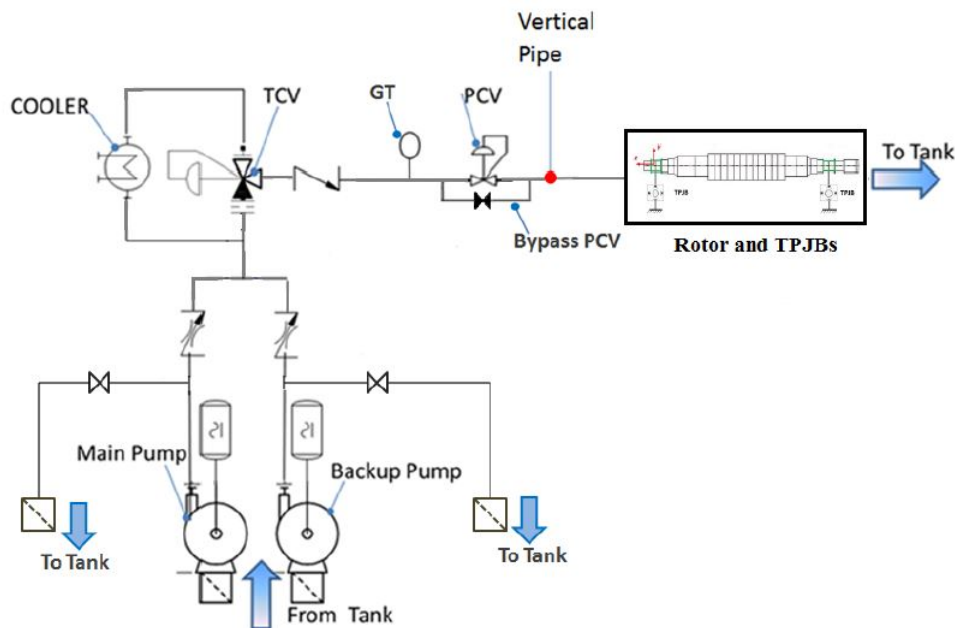


Figure 6.1: Scheme of the experimental plant located in Massa-Carrara. All data are “owned and reserved” and obtained by permission of GE O&G Nuovo Pignone “GE ©2014 - All Rights Reserved”

simulate the failure of the duct upstream the check-valves. The plant includes then a cooler which operates in parallel with an orifice; these ducts are connected through a 3-way Temperature Control Valve (TCV), used to control the temperature downstream the valve (with a GE-NP MARKVI controller). Downstream the TCV the plant contains a

filter, a pressurized gas-tank and a Pressure Control Valve (PCV). The gas-tank is used to compensate the lubricant flow rate during transient phases, when the voltage is low or in presence of a failure. The PCV is a self regulated valve used to control the pressure level downstream the valve itself, with a bypass branch in parallel. Finally the tilting pad bearings are located after a vertical pipe. Additional orifices, check-valves and bypass valves are located throughout the plant to simulate other known pressure losses. The rotor used in this testing plant (and in the second test case) is a centrifugal compressor for the process of natural gas denoted with the code 3BLC1005.

The data reported in Table 6.1 have been obtained evaluating the pressure drop across the bearings, i.e. between the supply pressure and the environment pressure, and the lubricant flow rate through the bearing supply orifices in steady state conditions, with variable lubricant inlet temperature and variable rotor spin speed; in particular the temperature levels include a design temperature (50°C) and a high temperature (65°C, with the cooler connected to the hydraulic network).

The lubricant temperature is measured downstream the TCV, the rotor spin speed is measured directly on the rotor and the pressure drop is evaluated through a calibrated orifice upstream the bearing. Finally, the flow rate is measured with a probe located downstream the bearing. This flow rate is evaluated for the whole bearing, thus its value has been used for the validation comparing it with the sum of the supply flow rates calculated for all the sumps included in the bearing:

$$Q_{orif} = \sum_{i=1}^{n_p} Q_{orif,i}. \quad (6.1)$$

Pressure [Pa]	Velocity [rad/s]	Temperature [K]	Flow rate [l/min]
0.50	396.8879	323.59	62.81
0.52	396.5737	323.65	63.14
0.52	399.1917	323.68	63.23
0.51	396.8879	323.62	63.13
0.51	397.8303	323.61	63.02
0.51	398.4587	335.71	65.70
0.51	395.9454	336.36	65.79
0.20	396.8565	336.36	45.77
0.21	397.0659	336.11	45.67
0.17	397.3068	337.35	37.79
1.08	396.8879	336.94	92.93
1.11	396.7832	336.43	93.04
1.06	396.5737	323.26	89.31
1.06	397.7256	323.93	89.21
0.23	398.8775	323.18	41.84
0.23	396.4690	323.93	42.05
0.24	399.1917	323.65	44.18
0.25	395.5265	326.09	44.60
0.50	399.2964	323.55	60.36
0.49	396.4690	323.55	62.17

Table 6.1: Experimental flow rates for the GEJB200M-05 bearing. All data are “owned and reserved” and obtained by permission of GE O&G Nuovo Pignone “GE ©2014 - All Rights Reserved”

## 6.2 Test case 2: Rotor dynamical characteristics

The experimental tests used for the validation of the second modeling step have been performed by General Electric Oil & Gas according to API 617 Standards. The 3BLC1005

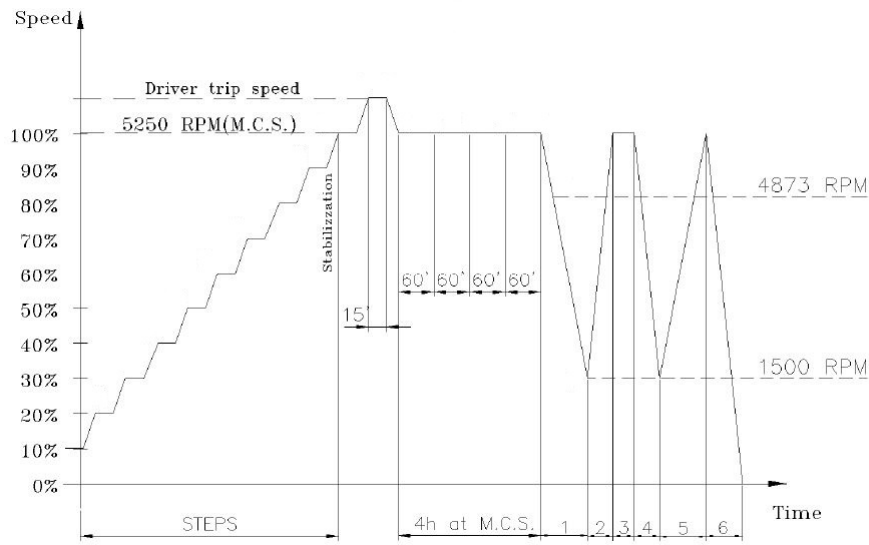


Figure 6.2: Experimental procedure concerning the 3BLC1005 centrifugal compressor. All data are “owned and reserved” and obtained by permission of GE O&G Nuovo Pignone “GE ©2014 - All Rights Reserved”

compressor has been mechanically tested under vacuum, with a pressure inside the casing equal to 0,02 MPa. The lubricant used for the testing is the ISO VG32, with an inlet temperature equal to 42°C: the testing procedure begins with a start-up phase, accelerating gradually the rotor, then the compressor operates for 4 hours at design speed. After the steady state phase the rotor is repeatedly decelerated and accelerated, varying the lubricant temperature and hence its viscosity, until a maximum temperature equal to 48°C. Finally, the run-down phase of the machine is monitored. All the phases of the testing procedure (reported in Figure 6.2) last long enough to allow the bearings and the rotor to reach a dynamical equilibrium condition. The acceleration and deceleration phases aim to highlight the presence of critical speeds in the rotor operating range, in order to correctly determine how to operate the rotor. Furthermore, to better highlight

the resonance behavior of the rotor, some tests with an unbalance mass located on one of the rotor ends (*overhung* configuration) can be performed.

During the testing procedure the rotor vibration amplitudes and other quantities significant in a bearing analysis (e.g. pressure and temperature) are measured. The results of the run-up and unbalance tests are reported in Figures 6.3 and 6.4 as Bode plots where the amplitudes and phases of the vertical and horizontal vibrations in the bearings locations are reported as a function of the rotor spin speed.

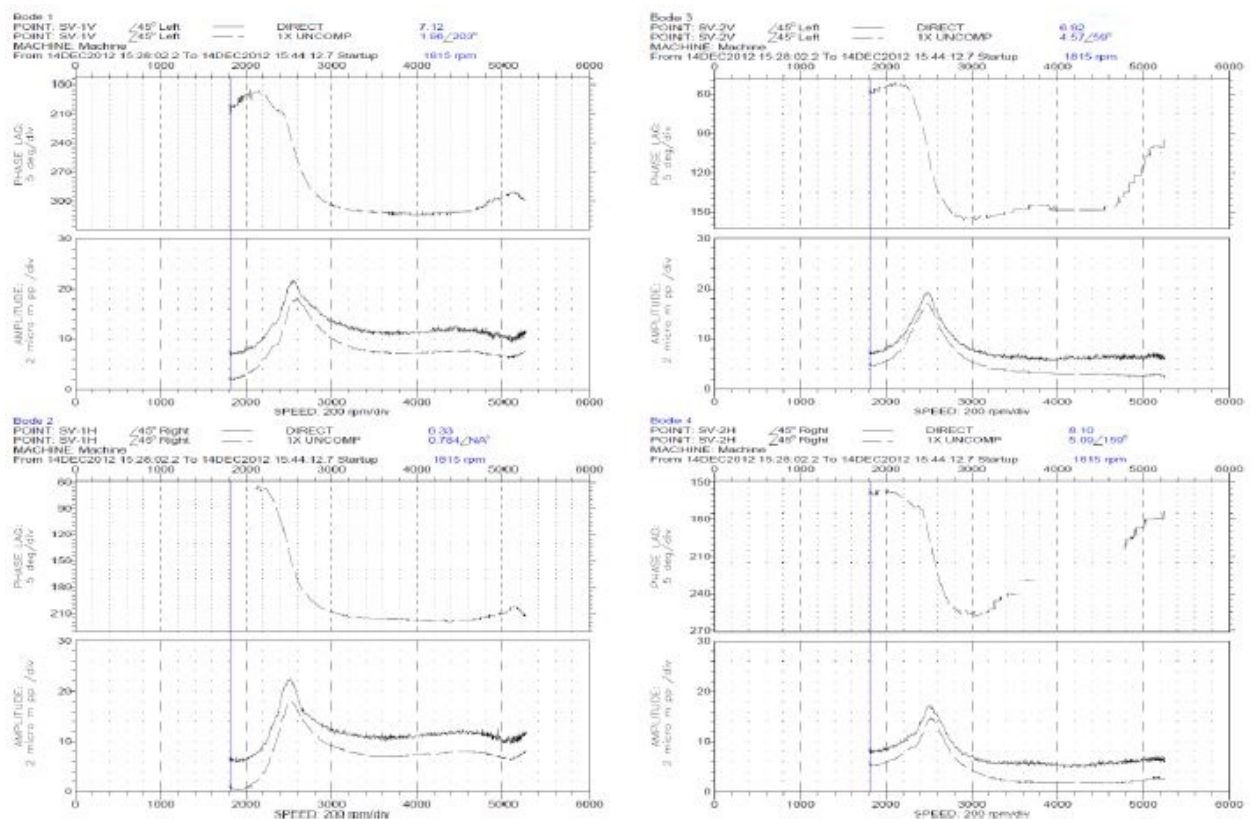


Figure 6.3: Run up phase for the 3BLC1005 compressor. All data are “owned and reserved” and obtained by permission of GE O&G Nuovo Pignone “GE ©2014 - All Rights Reserved”

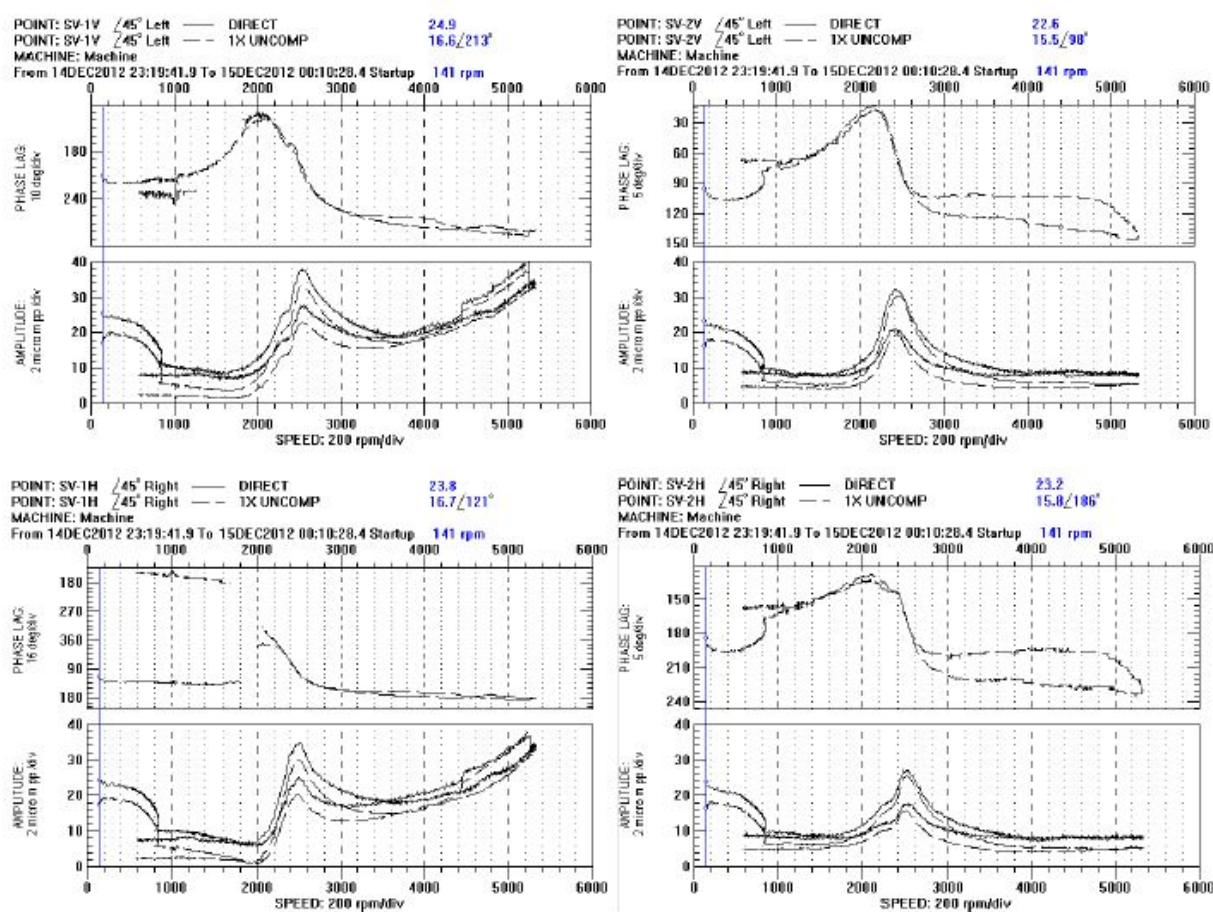


Figure 6.4: Unbalance response for the 3BLC1005 compressor. All data are “owned and reserved” and obtained by permission of GE O&G Nuovo Pignone “GE ©2014 - All Rights Reserved”

### 6.3 Test case 3: ThermoElastoHydroDynamic characteristics

The model proposed in the third step has been developed on the basis of technical data relating to a test rig specially built to study the possible onset of thermal instability in a centrifugal compressor supported by two TPJBs. The compressor which is shown mounted on the test rig in Figure 6.5 represents a scale model of a real machine, on which the onset of thermal instability in particular operating phases has been observed. The characteristics of the test rig together with the testing procedure will be illustrated below.

The considered test rig was developed to evaluate the rotor behavior both in the start-up and shutdown phases, and in some steady operating conditions, in order to highlight the onset or absence of thermal instability.

The proposed TEHD model has been developed taking into account the main characteristics and functioning conditions of the test rig shown in Table 6.2, and validated through a comparison with experimental data sets supplied by General Electric Oil & Gas. The test rig shown in Figure 6.5, includes a series of disks which represent the



Figure 6.5: Test rig.

gyroscopic effects produced by the centrifugal impellers of the compressor. The bearings that support the rotor are Tilting Pad Journal Bearings, with five pads, set in the Load On Pivot (LOP) configuration (load acting on the spherical pivot), whose technical data are reported in Table 6.2. The rotor is driven by an electric motor connected to the drive-end side of the rotor through a flexible coupling, and a gearbox which allows to reach the rotor maximum speed. In correspondence of the Non-Drive End bearing, i.e. the side on which the unbalance mass is placed, the test rig is equipped with eight

<i>Rotor:</i>	
Total mass of the rotor	450 [kg]
Rotor length	2.5 [m]
Young's modulus	210 [GPa]
Poisson's ratio	0.31
Specific heat capacity	475 [J/kgK]
Thermal conductivity	44.5 [W/mK]
Thermal expansion	$12.3 \cdot 10^{-6}$ [1/K]
Rotational velocity of the rotor $\omega_A$	8000 ÷ 20000 [rpm]
<i>Bearings:</i>	
Bearing radius	70 [mm]
Pad thickness	19 [mm]
Bearing axial length	56 [mm]
Radial clearance of the bearing	0.124 [mm]
Radial clearance of the pad	0.07 [mm]
Pad angle	56.3°
Pivot offset	50%
Type of lubricant	ISO VG 46

Table 6.2: Main characteristics and operating conditions of the test rig and of its TPJBs.

thermocouples positioned directly on the rotor surface and connected with an external telemetry device, as shown Figure 6.7; thermocouples rotate with the rotor and then allow to measure the temperature profile that during the operating phase is spread on the rotor. This temperature value is sent as a wireless signal to the rotor-antenna included in the telemetry system. In addition to the thermocouples, there are also resistance thermometers on the pad and proximity sensors respectively mounted at the bearings midspan and at the rotor Non-Drive End. The resistance thermometers measure the fluid film temperature inside the bearing; the proximity sensors instead, using the eddy currents, estimate the rotor vibration value on two different planes and are characterized by an uncertainty of the about 5%. In order to evaluate the rotor sensitivity to the overhung disk (considering the second critical velocity of the rotor), the test rig can be equipped with disks of different size; by varying their size, and therefore their weight, it is possible to shift the second critical speed of the rotor: as it is possible to see from Table 6.4 the frequency of the second critical speed tends to lower with the increase of the disc



weight, while the first critical velocity remains unchanged. Regarding the tests, with the aim of minimizing the power dissipation due to the aerodynamic resistance on the rotor, they were carried out within a bunker in which the vacuum has been done previously. The lubricant used in the tests (whose characteristics are shown in Table 6.3) is referred to as ISO VG 46 by the ISO standards, and has been supplied to the system at a temperature of about  $40^{\circ}\text{C}$  [31]. As shown in Figure 6.8, the preliminary phase of the tests consists

<i>ISO VG 46</i>	
Density at $15^{\circ}\text{C}$	0.856 [kg/L]
Kinematic viscosity at $40^{\circ}\text{C}$	43.8 [ $\text{mm}^2/\text{s}$ ]
kinematic viscosity at $100^{\circ}\text{C}$	7 [ $\text{mm}^2/\text{s}$ ]
Viscosity index	115
Pour point	$-15 [^{\circ}\text{C}]$
Flash point	$232 [^{\circ}\text{C}]$

Table 6.3: Main characteristics of the lubricant ISO VG 46.

in the rotor start-up, up to the operating velocity, immediately followed by a drastic reduction of the velocity; this step has the task of identifying the critical velocities of

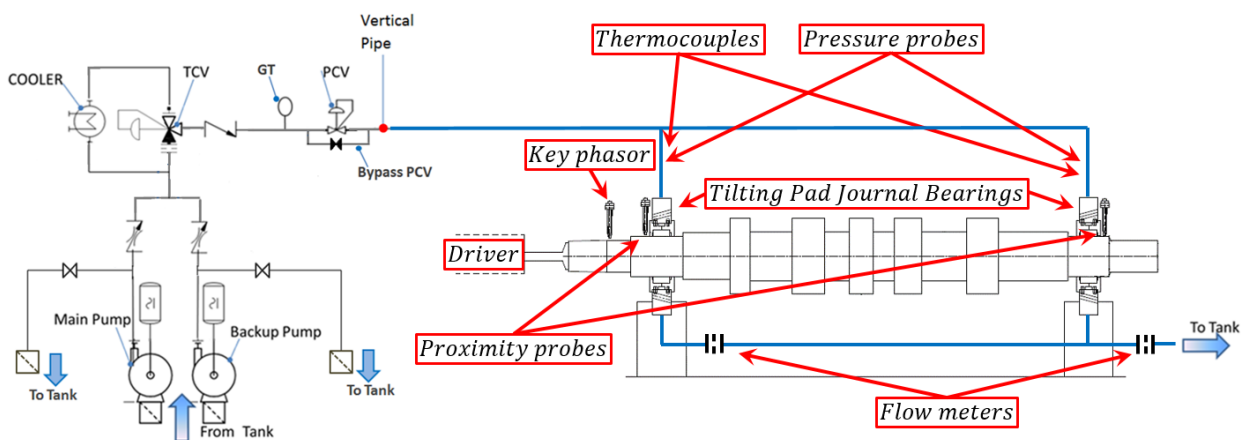


Figure 6.6: Simplified scheme of the experimental test rig.

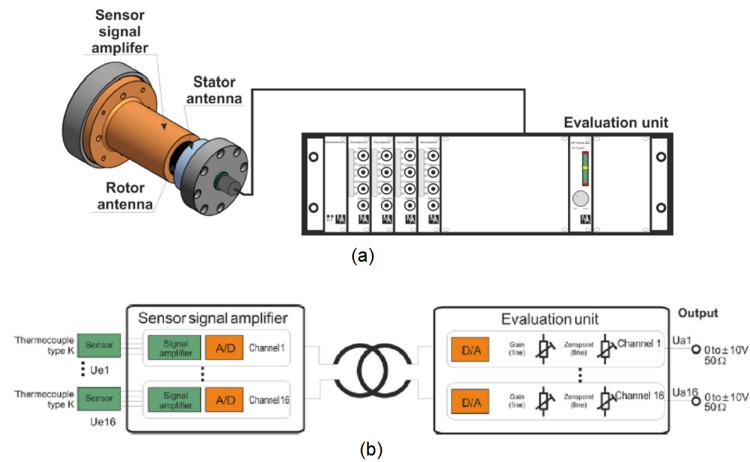


Figure 6.7: Sensors and signal acquisition system.

the rotor. This first phase is followed by another one in which the rotor is subjected to a continuous series of velocity increments (each lasting five minutes); this second step has the task of detecting the possible onset of thermal instability phenomena. Finally the test proceeds with the shutting down of the machine.

In accordance with the Table 6.4 and for the validation of the proposed model, the complete testing procedure was repeated with three different configurations:

- end of the rotor without additional disks, W3 configuration;
- end of the rotor equipped with a disc of  $10\text{kg}$ , W2 configuration;
- end of the rotor equipped with a disc of  $20\text{kg}$ , W1 configuration;

in these configurations, the distance between the Non-Drive End of the rotor and the center of mass of the disk is respectively equal to  $215[\text{mm}]$  (W3 configuration),  $249[\text{mm}]$  (W2 configuration),  $301[\text{mm}]$  (W1 configuration).

In accordance with the API Standard 684 [32], the unbalance used to excite the first and the second critical velocity of the rotor is equal to  $0.26\text{ kg} \cdot \text{mm}$ . To trigger the first critical velocity, the unbalance is placed at the bearings midspan and also the measurement is taken at the midspan; to trigger the second critical velocity, the disk is placed at the

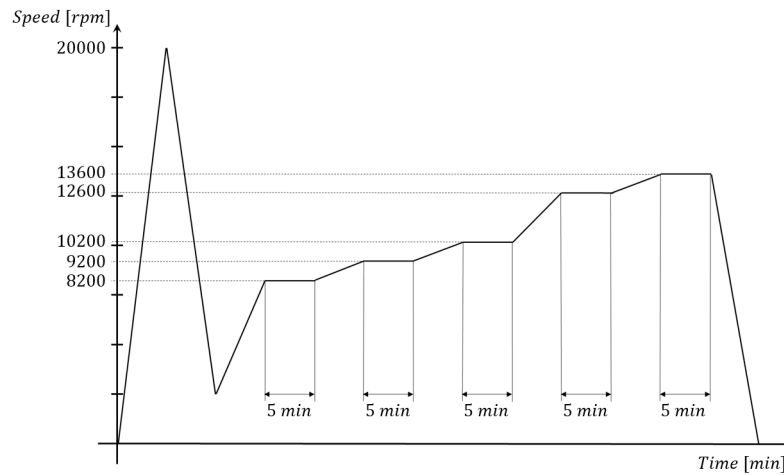


Figure 6.8: Experimental procedure to evaluate the onset of the thermal instability.

Non-Drive End of the rotor and the measurement is carried out in correspondence of the Non-Drive End bearing. The model validation was made through a comparison of

Configuration	I critical V. Velocity [rpm]	II critical V. Velocity [rpm]
W3	5000	15000
W2	5000	13000
W1	5000	8000

Table 6.4: Rotor critical velocity for the considered configurations.

the following experimental data:

- amplitude and phase of the rotor vibrations, acquired both on the plane coincident with the bearings midspan and on the corresponding plane to the Non Drive-End bearing;
- rotor temperature in correspondence of the Non Drive-End bearing, to evaluate the onset of the thermal instability;

- pads temperature of the Non Drive-End bearing to evaluate the onset of the thermal instability (measured at 25% and 75% of the first pad, which is the most loaded, and at 75% of the second pad).

All the measurements are subjected to appropriate acceptance criteria according to API Standard 684 [32].

The experimental tests have shown that the onset of thermal instability is connected to the second critical velocity, and is influenced by the presence of the overhung mass.

## Models numerical validation

Referring to the experimental data exposed in the previous Chapter, the models have been simulated reproducing the testing conditions and verifying their outputs through the comparison with the quantities measured experimentally. The validation follows the three modeling steps realized:

- Step 1: validation of the fluid dynamical characteristics through the comparison with the results of the Test case 1;
- Step 2: validation of the rotor dynamical characteristics through the comparison with the results of the Test case 2;
- Step 3: validation of the ThermoElastoHydroDynamic characteristics through the comparison with the results of the Test case 3.

In the following sections the most important numerical results and the comparison between numerical and experimental data are reported.

## 7.1 Step 1: Fluid dynamical characteristics

The simulations performed for the first model are based on the data provided by General Electric Oil & Gas reported in Table 6.1. The other parameters, principally geometrical, needed to set up the model are reported in the Table 7.1.

The simulation time is long enough to allow the system to reach its dynamical equilibrium, which consists of an equilibrium point. The results concern, in addition to the lubricant flow rates used for the validation of the model, the dynamical behavior of the various components of the system. In Figures 7.1 and 7.2 the displacements of the rotor fraction center of gravity are reported, highlighting how the rotor, due to its own weight, moves downwards.

Consistently with these displacements, the pads more distant from the rotor position (i.e.

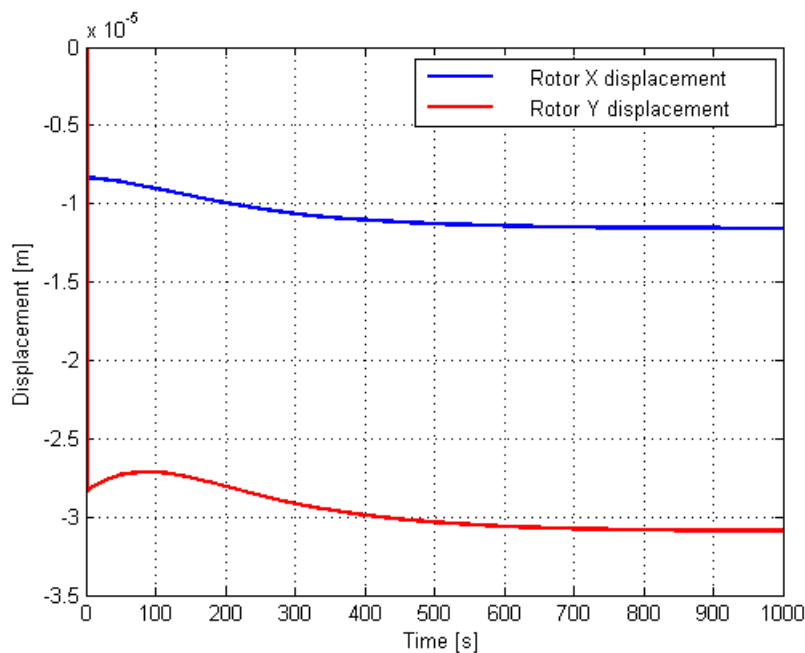


Figure 7.1: Rotor fraction X and Y displacements.

that located in the upper part of the bearing) are more tilted, since with a higher oil film thickness a higher tilt angle is needed in order to generate the correct supporting effect.

Quantity	Value	Description
$R$	$0,08\ m$	Bearing radius
$h_0$	$2,54 \cdot 10^{-4}\ m$	Bearing radial clearance
$CC$	$3,71 \cdot 10^{-4}\ m$	Pad radial clearance
$n_p$	4	Pads number
$\alpha_1$	$-\pi/4\ rad$	First pad pivot location
$\alpha_2$	$-(3\pi)/4\ rad$	Second pad pivot location
$\alpha_3$	$-(5\pi)/4\ rad$	Third pad pivot location
$\alpha_4$	$-(7\pi)/4\ rad$	Fourth pad pivot location
$\psi_{pad}$	$74^\circ$	Pad opening angle
$\psi_{piv}$	$41^\circ$	Pivot angular offset
$t_{fin}$	1000 s	Simulation time
$\beta$	$1,4 \cdot 10^7\ Pa$	Lubricant bulk modulus
$A_{sump}$	$1,1 \cdot 10^{-3}\ m^2$	Sump leakage area
$V$	$1,54 \cdot 10^{-4}\ m^3$	Sump volume
$C_{d,orif}$	0,6587	Supply orifice coefficient
$C_{d,leak}$	0,0178	Leakage orifice coefficient
$p_{env}$	100000 Pa	Environment pressure
$J_{pad}$	$1,13 \cdot 10^{-2}\ kg \cdot m^2$	Pad polar moment of inertia
$J_{t,pad}$	$9,24 \cdot 10^{-3}\ kg \cdot m^2$	Pad transverse moment of inertia
$m_{rot}$	100 kg	Rotor fraction mass
$J_{rot}$	$4\ kg \cdot m^2$	Rotor fraction polar moment of inertia
$J_{t,rot}$	$420\ kg \cdot m^2$	Rotor fraction transverse moment of inertia

Table 7.1: Parameters considered for the model of a single bearing

Analogous considerations can be made for the sump pressure: in steady state conditions the pressure is higher in the sumps nearer to the rotor fraction center of gravity;

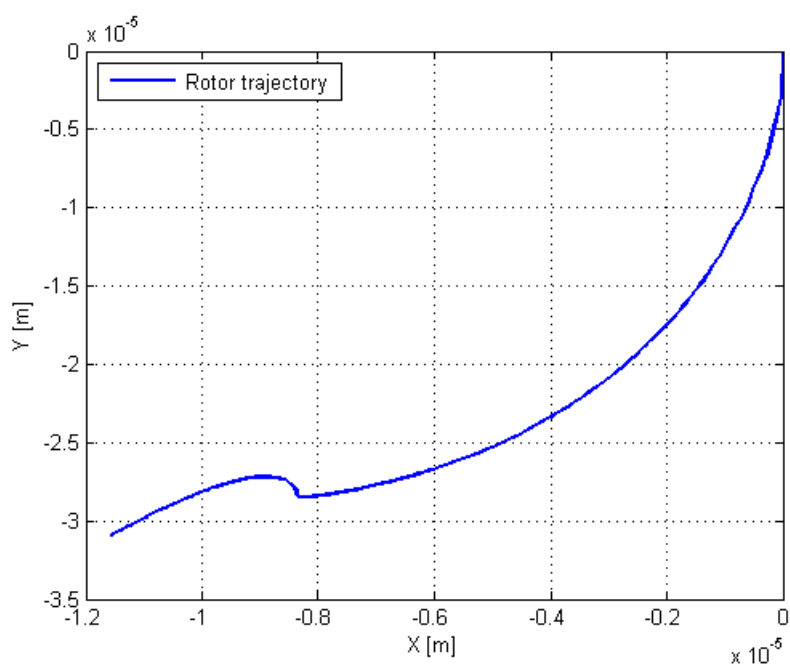


Figure 7.2: Rotor fraction trajectory.

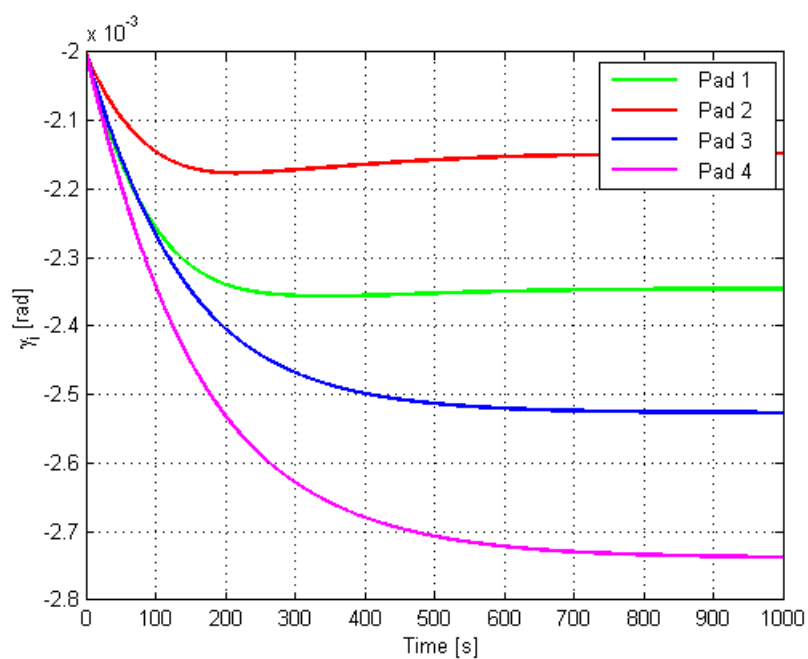


Figure 7.3: Pads tilt angles.



consistently with the dynamical behavior of the rotor, the supply flow rate entering the sumps increases until the system reaches its equilibrium condition.

In Figures 7.6 and 7.7 the pressure and velocity fields inside the oil films are reported. In

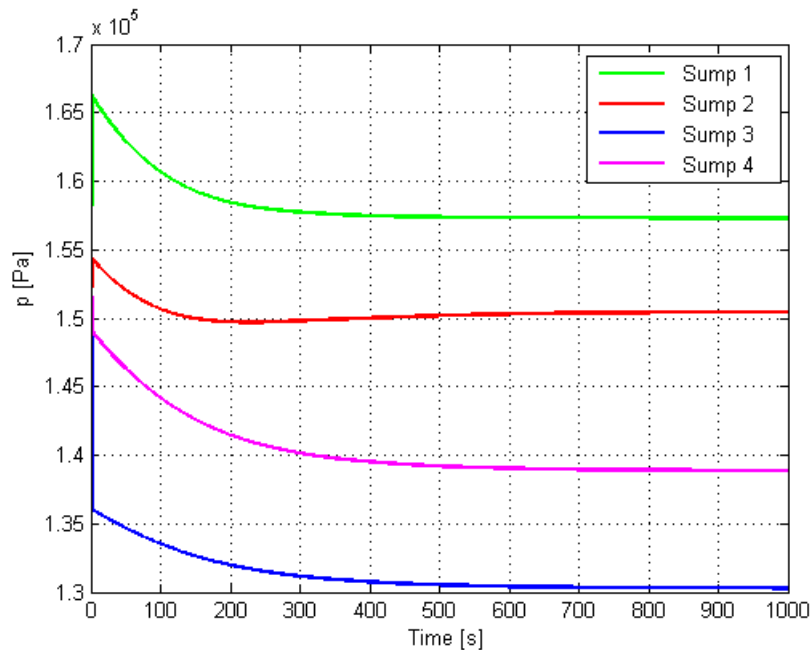


Figure 7.4: Sumps pressures.

Figure 7.6 the color scale represents the pressure level and it is possible to highlight how in each pad the pressure maximum is nearer to the pad trailing edge; in Figure 7.7 the color scale represents the velocity magnitude while the vectors represent the direction of the fluid velocity field.

Furthermore, measuring the pressure and the oil film thickness along the pad mean lines (reported in Figure 7.8) it is possible to obtain the typical results found in literature, noting how the higher pressure levels correspond to the pads with the lower oil film thicknesses (i.e. the ones nearer to the rotor position). In Figures 7.9 and 7.10 the pressure and oil film thickness referred to the last simulation instant are reported; those results are reported as a function of the local curvilinear coordinate  $S_{tang}$  with its origin located in correspondence of the pad pivot (see Figure 7.8).

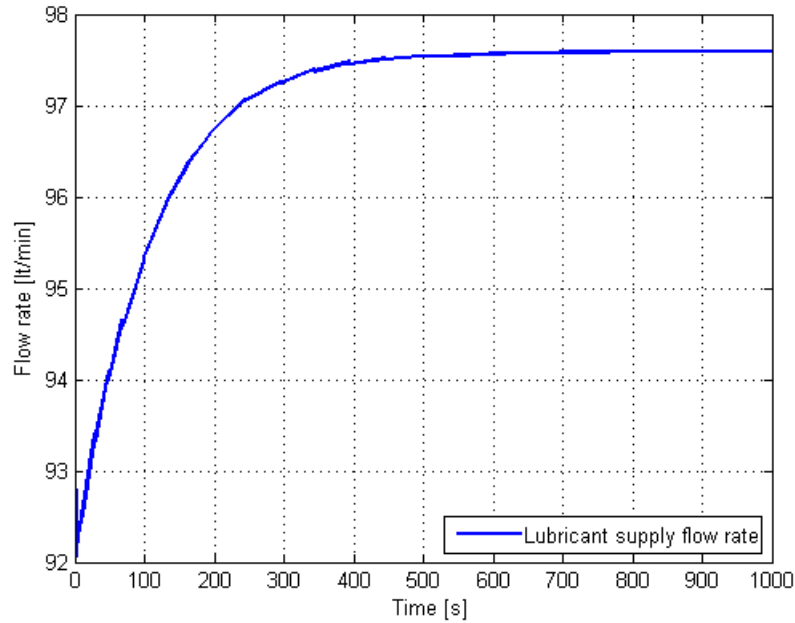


Figure 7.5: Lubricant supply flow rate for the complete bearing.

The comparisons between the experimental data provided by General Electric Oil & Gas, the numerical supply flow rates calculated with the proposed model and the flow rates obtained according to the two resistive element formulas previously illustrated are reported in Figures 7.11 and 7.12:

$$Q_{orif}^{id} = A_0 C_d \sqrt{\frac{2}{\rho} (p_s^{meas} - p_{env})},$$

$$Q_{orif}^{GENP} = D^2 k_{GENP} \frac{\beta^2}{\sqrt{1-\beta^2}} \sqrt{\frac{(p_s^{meas} - p_{env})}{\rho}}.$$

The results obtained with the developed model show an excellent agreement with the experimental data, in particular in the high pressure operating range, where the lumped parameters models differ more from the experimental data. In Figures 7.13 and 7.14 the relative errors of the calculated flow rates with respect to experimental values are reported: in the whole supply pressure range the error of the proposed model remains very low.

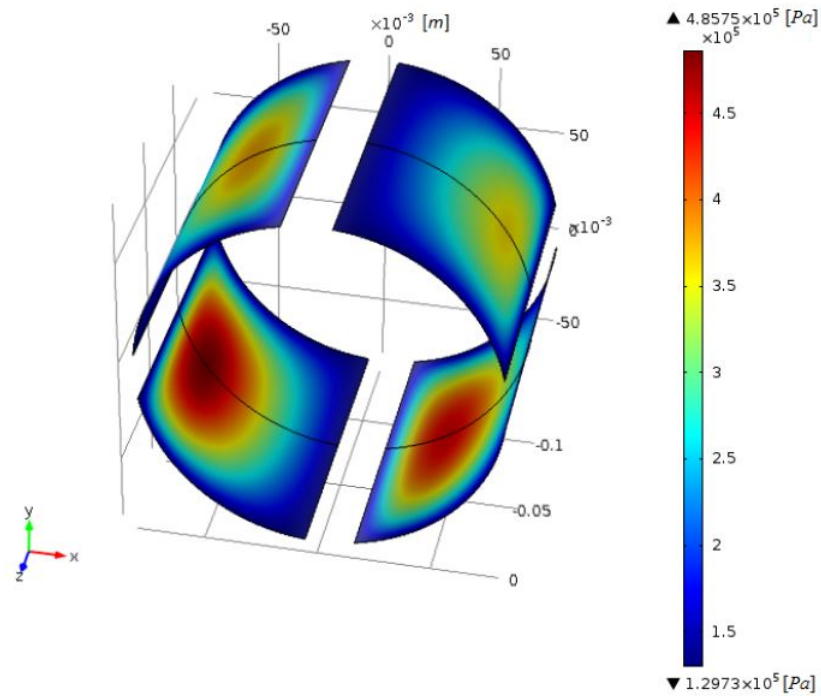


Figure 7.6: Pressure field inside the oil films.

$D$	$1,25 \cdot 10^{-1} m$
$\beta$	0,121
$A_0$	$5,0265 \cdot 10^{-5} m^2$
$C_d$	0,6689
$\rho$	$880 kg/m^3$

Table 7.2: Parameters used in the orifice lumped parameters formulas

### 7.1.1 Model performances

The developed model is based on a bidimensional discretization of the oil film, in order to realize a geometrically 3D model while maintaining low the number of elements and hence of degrees of freedom. Consequently the simulations, although longer with respect to lumped parameters models simulation times, are less time consuming with

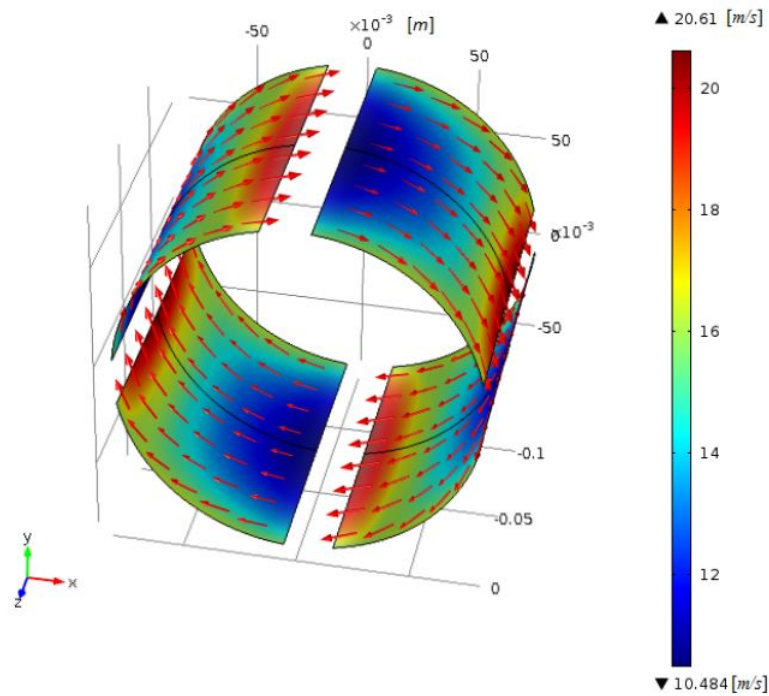


Figure 7.7: Velocity field inside the oil films.

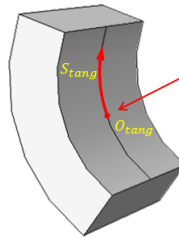


Figure 7.8: Pads mean lines (for the pressure measurement).

respect to fully-3D models. The proposed model is built with 70 QUAD elements (for the discretization of a single oil film), reaching a total of 945 FEM degrees of freedom, to be added to the 18 DOFs due to the ODEs models implemented in *MATLAB*<sup>®</sup> *R2013a*; the simulation of a 1000 seconds transient phase requires 90 minutes of computational time. The fully-3D model for the CFD analysis of the same bearing (with the same accuracy) would require about 6450 BRICK elements for the discretization of the fluid parts, raising the computational time to about 40 hours.

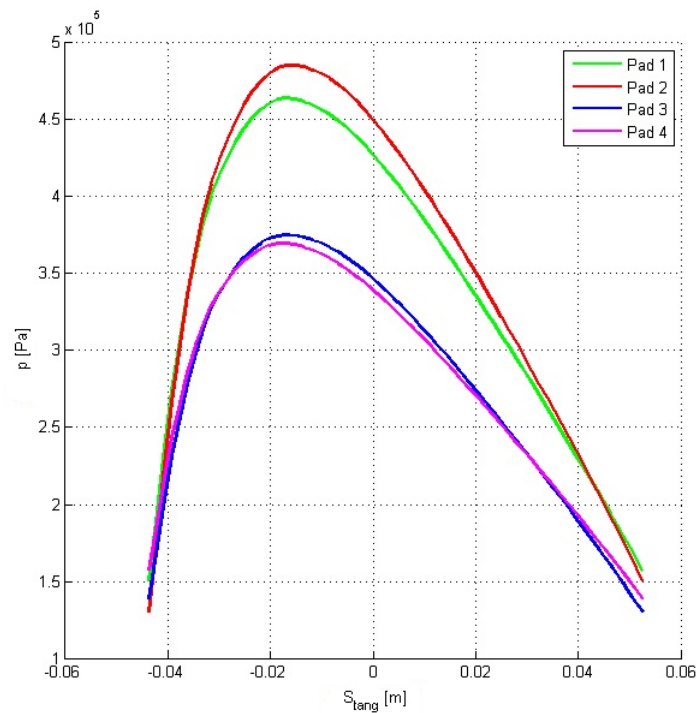


Figure 7.9: Pressure level in the pads mean lines.

Quantity	Value	Description
$MaxStep$	50 s	<i>ode15s</i> maximum integration step-size
$RelTol$	$10^{-3}$	<i>ode15s</i> relative tolerance
$AbsTol$	$210^{-4}$	<i>ode15s</i> absolute tolerance
$MaxLinIt$	$10^4$	<i>BiCGStab</i> maximum iterations number
$MaxIter$	4	Newton's method maximum iterations number
$TolF$	$2,5 \cdot 10^{-6}$	Newton's method relative tolerance
$mes$	0,000304 m	Minimum element dimension
$Mes$	0,00169 m	Maximum element dimension
$MeGR$	1,3	Maximum element growth rate

Table 7.3: Numerical solvers tolerances and mesh features (Step 1)

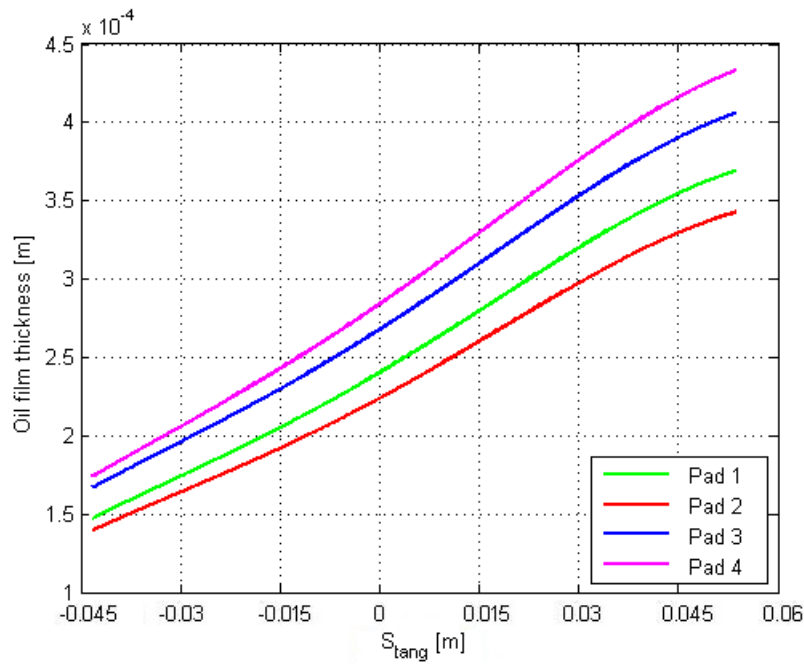


Figure 7.10: Oil film thickness in the pads mean lines.

CPU	Intel CORE i7
Clock frequency	2.20 GHz
RAM memory	8 Gb
Operating system	Windows 7-64 bit

Table 7.4: Characteristics of the computer used for the simulations

	Fully-3D reference model	MDM Lab model
Simulation time	1000 s	1000 s
Computational time	144000 s	5400 s

Table 7.5: Comparison between computational times (Step 1)

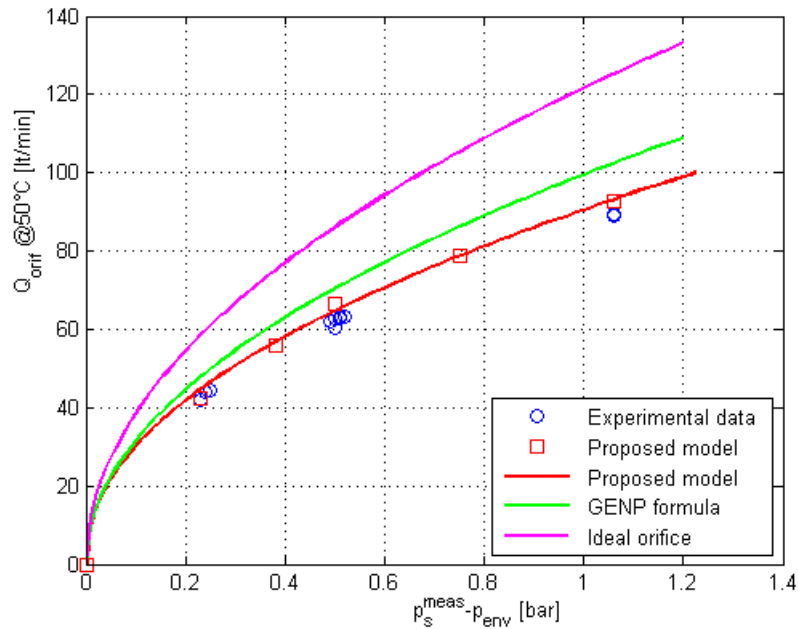


Figure 7.11: Comparison between the experimental, theoretical and numerical flow rates (50°C). All data are “owned and reserved” and obtained by permission of GE O&G Nuovo Pignone “GE ©2014 - All Rights Reserved”

## 7.2 Step 2: Rotor dynamical characteristics

The parameters used for the simulation of the complete rotor-bearings model are reported in Table 7.6; a harmonic load due to the unbalance mass has been applied on the rotor drive-end (i.e. the end where the compressor is coupled with a steam turbine driver) to perform a frequency domain analysis, while the run-up transient phase in the time domain has been simulated without the unbalance load.

The comparison with the experimental data concerns the vibration amplitudes in some specific points of the rotor. In this section most of the exposed results deal with the rotor dynamical characteristics of the system, since the bearing results, even if numerically different, are conceptually analogous to those reported in the previous section. The dynamic characteristics of the considered bearings are reported in Figure 7.17: they can

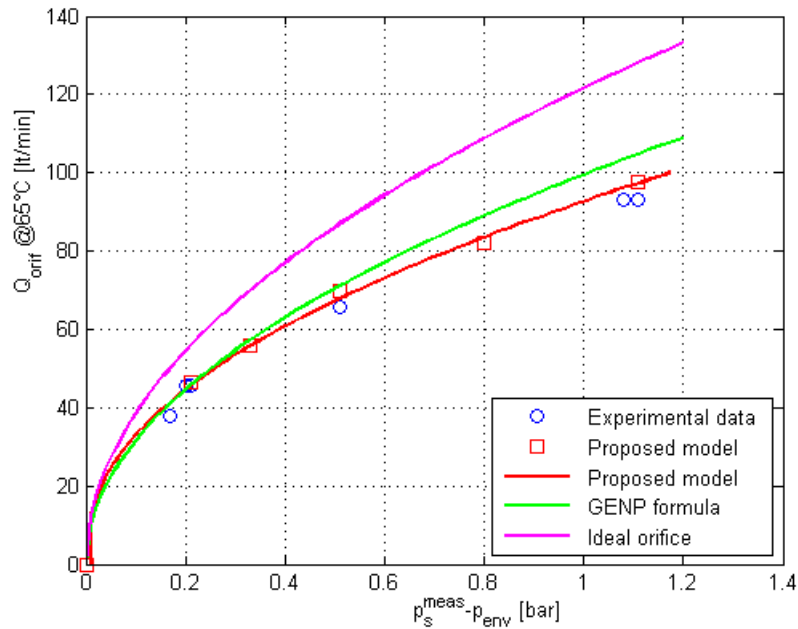


Figure 7.12: Comparison between the experimental, theoretical and numerical flow rates (65°C). All data are “owned and reserved” and obtained by permission of GE O&G Nuovo Pignone “GE ©2014 - All Rights Reserved”

be used to develop a reference lumped parameters bearing model (linearized model).

The first set of simulations evaluate the frequency response of the complete model. The horizontal and vertical vibration amplitudes (in correspondence of the bearings locations and of the drive-end of the rotor) are reported in Figures 7.18 and 7.19 as a function of the rotor spin speed: it is possible to highlight a first rotor critical speed at 2500 rpm, while the second critical speed has been experimentally detected outside the rotor operating range, at 6000 rpm. In correspondence of the non-drive-end bearing (i.e. the bearing located on the opposite end with respect to the steam turbine driver) the vibration amplitude decreases after the critical speed while in the drive-end bearing location and in the drive-end itself the amplitude increases monotonically after this first peak. At about 4000 rpm it is possible to note further peaks which, although their origin needs to be further investigated, can be detected also in the experimental data provided by General Electric



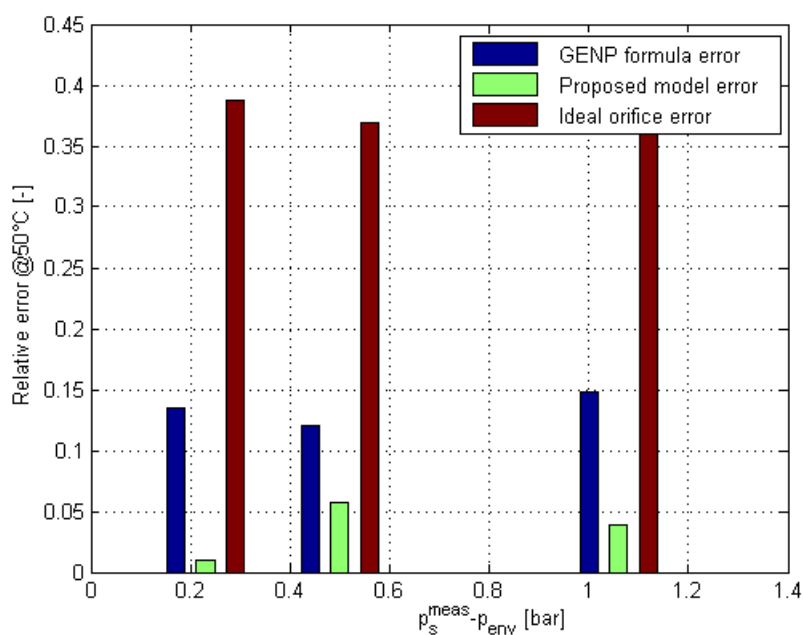


Figure 7.13: Relative errors (50°C)

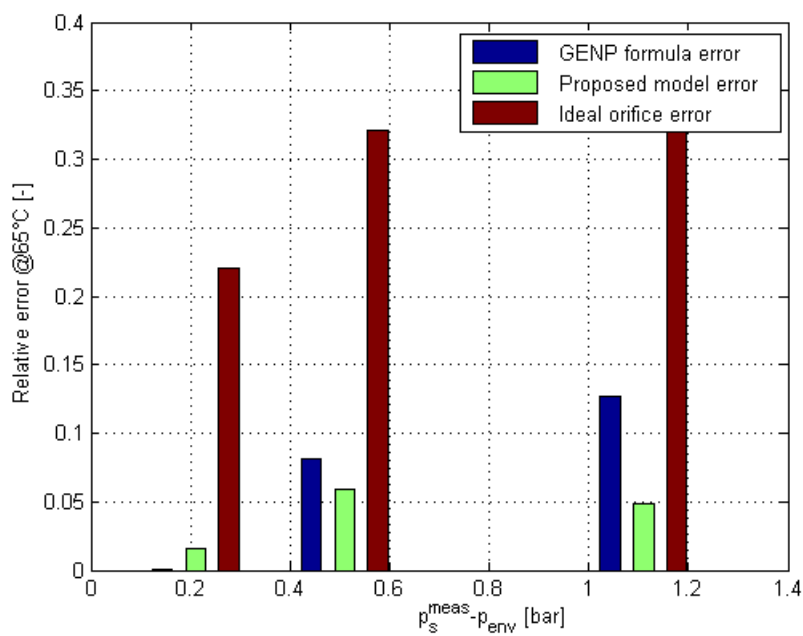


Figure 7.14: Relative errors (65°C)

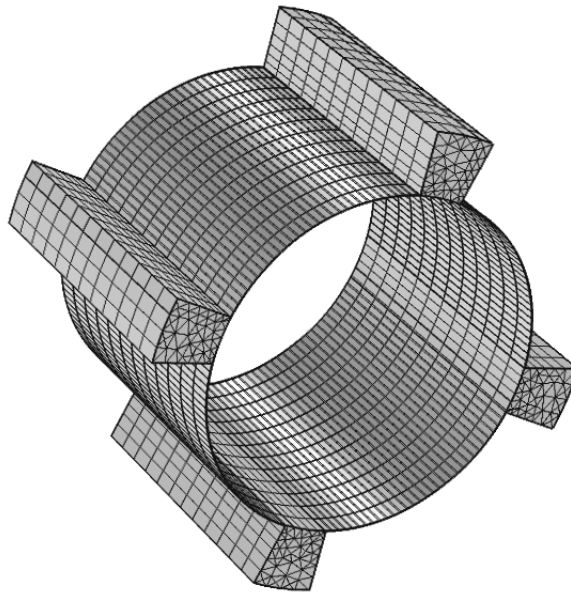


Figure 7.15: Mesh for the CFD analysis of the considered bearing



Figure 7.16: Unbalance load on the rotor end

Oil & Gas. The results obtained with these simulations show a good agreement with the experimental data; furthermore, the vibration amplitudes are lower than the limit established by the API standards in the whole compressor operating range: the crossing of the first critical speed does not affect the safe operation of the machine. In order to complete the model validation, the compressor run-up phase has been simulated in the time domain, evaluating the crossing of the first critical speed without the unbalance load. The simulations analyze a 10 seconds transient phase with the rotor subjected to a constant acceleration from  $100 \text{ rad/s}$  to  $600 \text{ rad/s}$ . In Figure 7.22 the vibrations in correspondence of the bearings locations are reported; furthermore, the orbit performed by the rotor in correspondence of the DE (drive-end) bearing with an angular velocity equal to  $550 \text{ rad/s}$  is reported in Figure 7.25.

Quantity	Value	Description
$R$	$0,11\text{ m}$	Bearing radius
$h_0$	$1,92 \cdot 10^{-4}\text{ m}$	Bearing radial clearance
$CC$	$2,0 \cdot 10^{-4}\text{ m}$	Pad radial clearance
$n_p$	5	Pads number
$\alpha_1$	$(17\pi)/10\text{ rad}$	First pad pivot location
$\alpha_2$	$(13\pi)/10\text{ rad}$	Second pad pivot location
$\alpha_3$	$(9\pi)/10\text{ rad}$	Third pad pivot location
$\alpha_4$	$\pi/2\text{ rad}$	Fourth pad pivot location
$\alpha_5$	$\pi/10\text{ rad}$	Fifth pad pivot location
$\psi_{pad}$	$60^\circ$	Pad opening angle
$\psi_{piv}$	$36^\circ$	Pivot angular offset
$A_{sump}$	$1,3 \cdot 10^{-3}\text{ m}^2$	Sump leakage area
$V$	$1,97 \cdot 10^{-4}\text{ m}^3$	Sump volume
$J_{pad}$	$6,1 \cdot 10^{-3}\text{ kg} \cdot \text{m}^2$	Pad polar moment of inertia
$t_{fin}$	10 s	Simulation time
$m_{res} \cdot \epsilon$	9500 g · mm	Unbalance

Table 7.6: Parameters considered for the complete model

By applying the Fourier transform to the vibrations time histories it is possible to detect the principal frequency components of the rotor vibrations, highlighting the peak due to the first critical speed (where the vibration level is still acceptable according to API Standards).

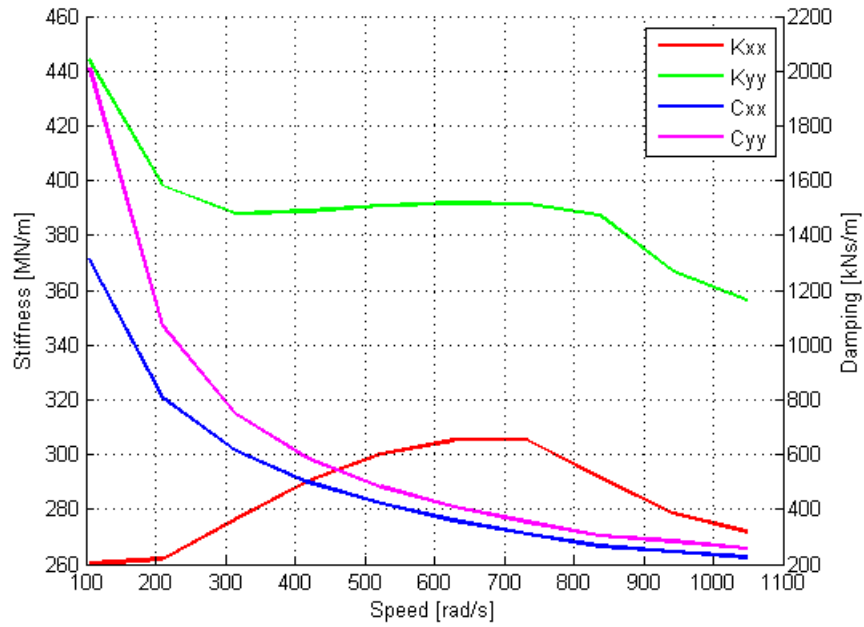


Figure 7.17: Dynamical characteristics of the considered bearings

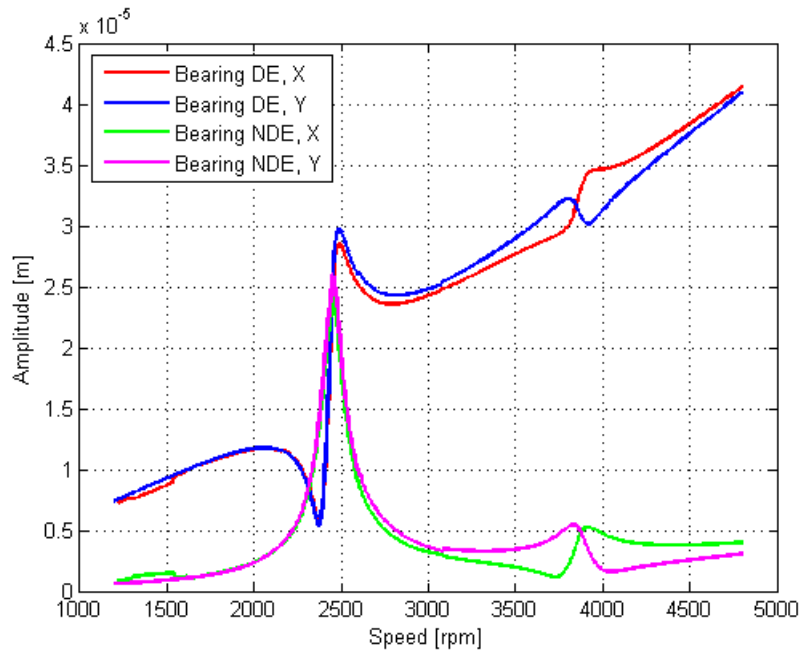


Figure 7.18: Rotor frequency response obtained with the complete model

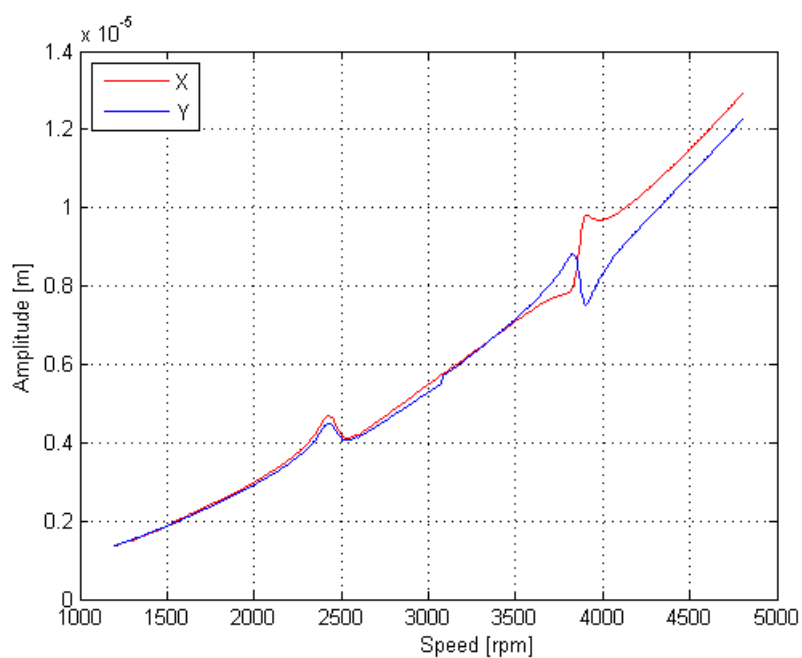


Figure 7.19: Vibration amplitude for the rotor drive-end

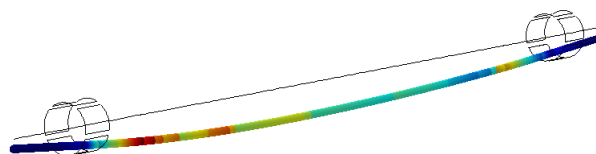


Figure 7.20: Generic rotor deformation (transient simulation)

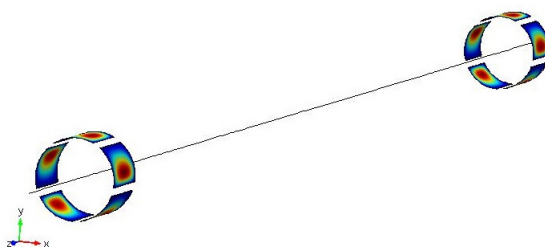


Figure 7.21: Generic pressure field inside the oil films (transient simulation)

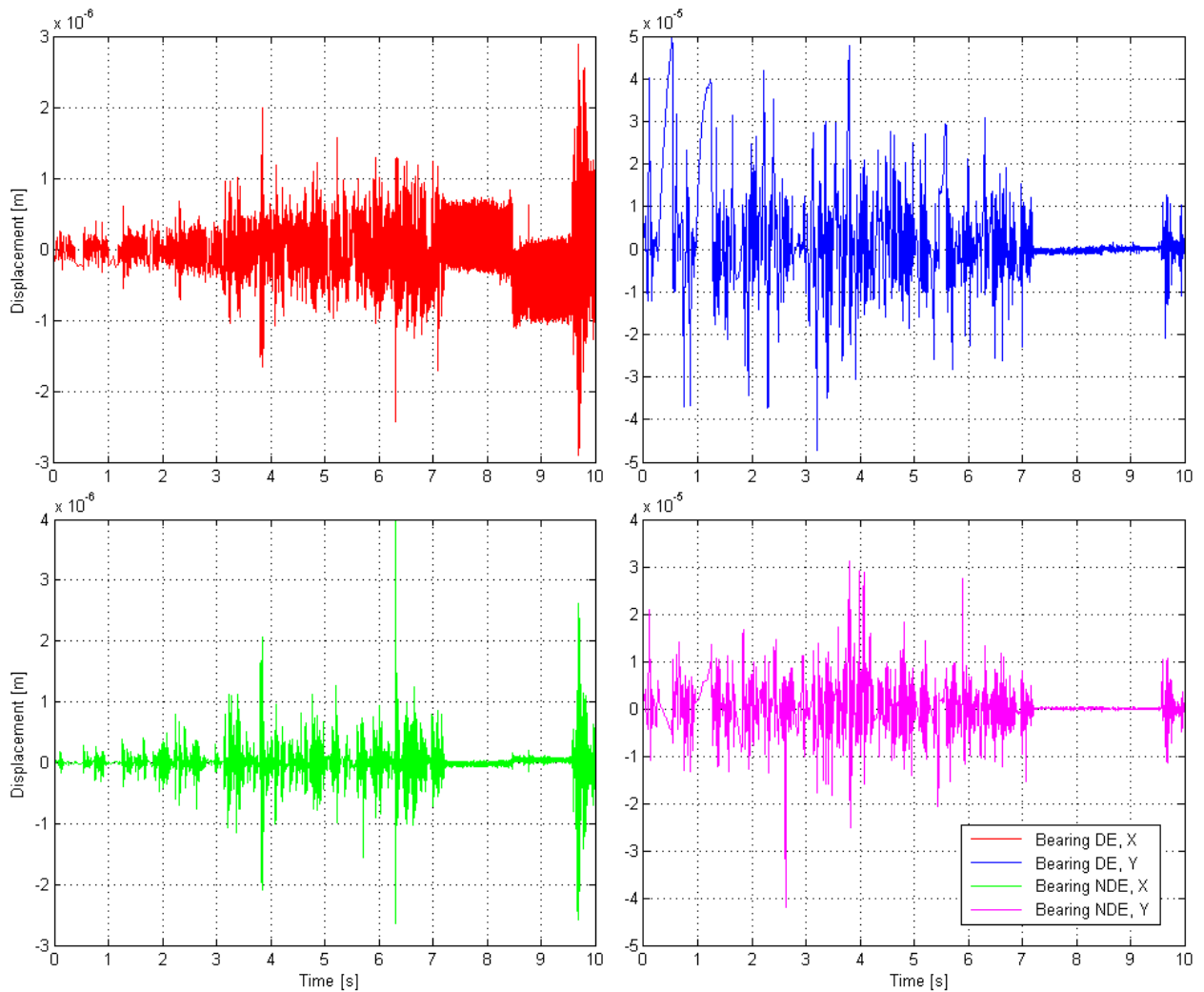


Figure 7.22: Rotor displacements time history

### 7.2.1 Model performances

The model is built with 350 QUAD elements (for the discretization of the ten oil films) and 41 BEAM elements (for the rotor), reaching a total of 1998 FEM degrees of freedom, to be added to the 30 DOFs implemented with the ordinary differential equations for the pad and supply sump dynamics. A 10 seconds simulation in the time domain requires about 2 hours of computational time. A fully-3D reference model, built with about 100000 BRICK elements, would require about 100 hours of computation. In the frequency domain an

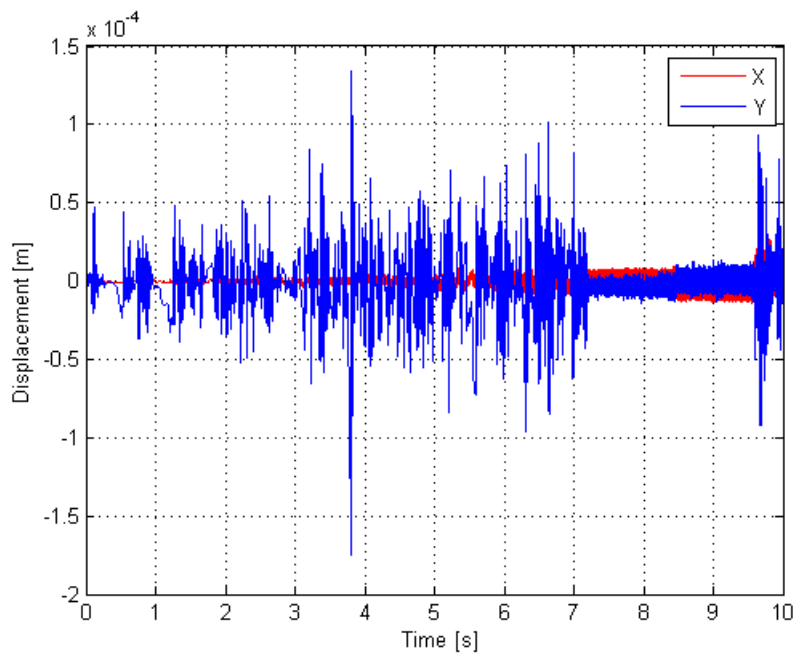


Figure 7.23: Rotor displacements time history (drive-end)

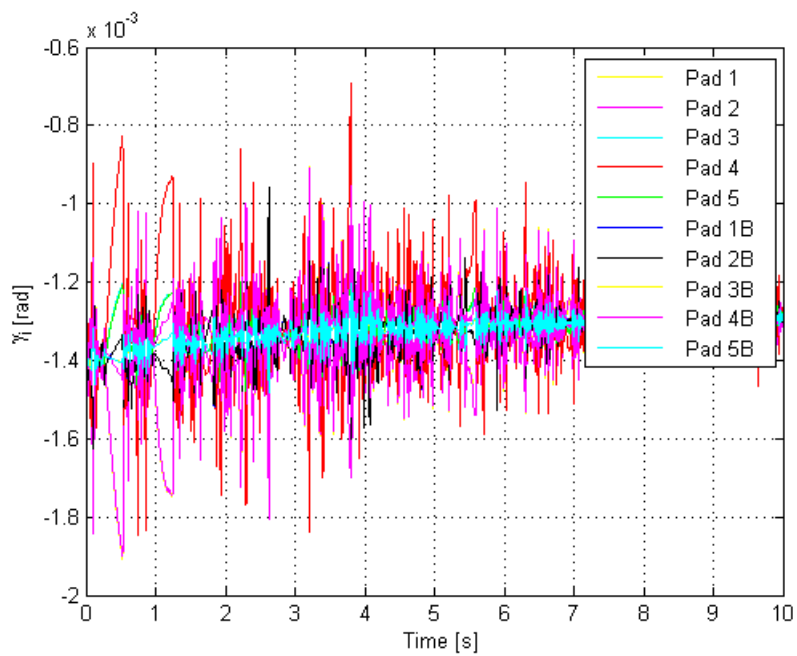


Figure 7.24: Pads tilt angles time history

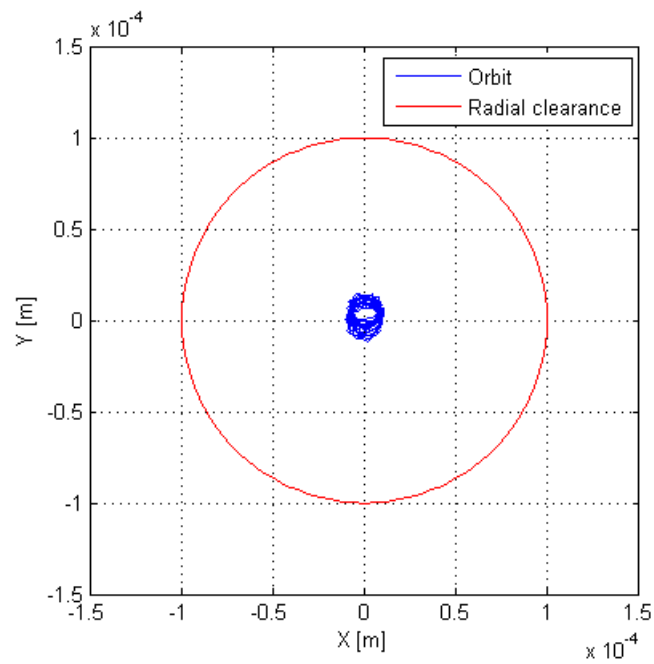


Figure 7.25: Rotor orbit (drive-end bearing)

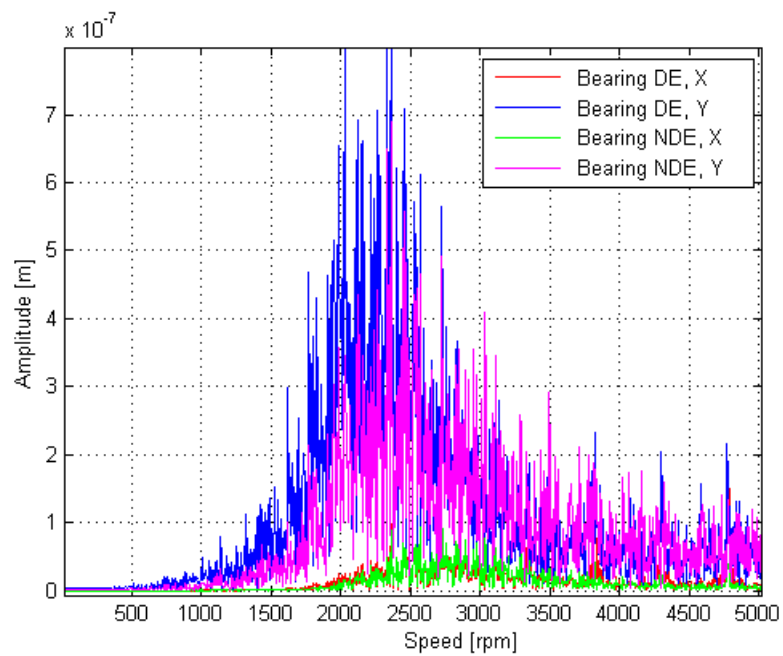


Figure 7.26: Fourier transform of the rotor vibration (bearings locations)



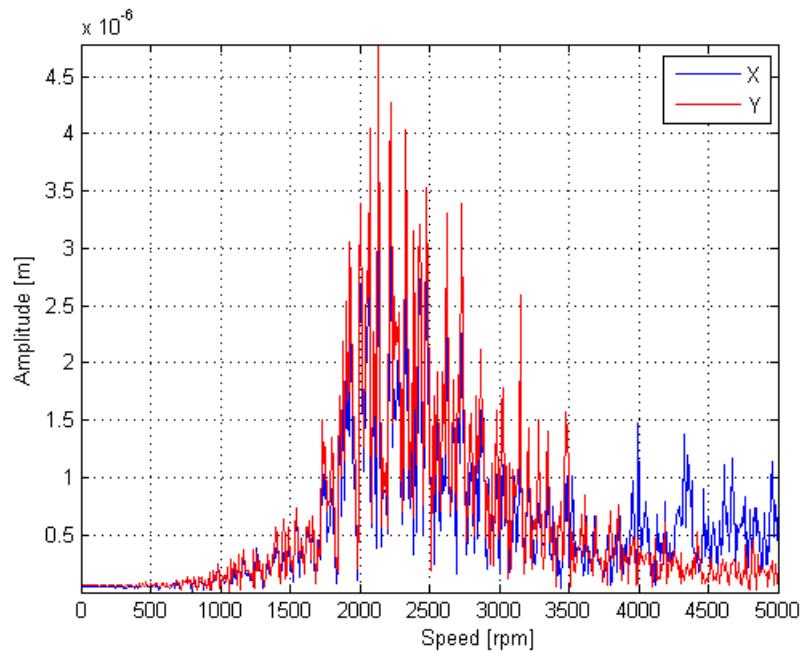


Figure 7.27: Fourier transform of the rotor vibration (rotor drive-end)

Quantity	Value	Description
$MaxLinIt$	$10^4$	<i>BiCGStab</i> maximum iterations number
$DDogIter$	25	Double Dogleg method maximum iterations number
$DDogTolF$	$2,5 \cdot 10^{-6}$	Double Dogleg method relative tolerance
$mes$	0,000304 m	Minimum element dimension
$Mes$	0,1 m	Maximum element dimension
$MeGR$	1,3	Maximum element growth rate

Table 7.7: Numerical solvers tolerances and mesh features (Step 2)

analysis with the developed model in the range from 20 to 100  $Hz$  requires 90 seconds of computational time, a value which is quite near the 40 seconds required by a reference lumped parameters model.

	Lumped parameters reference model	Complete MDM Lab model
Frequency range	20 ÷ 100 Hz	20 ÷ 100 Hz
Computational time	40 s	90 s
	Fully-3D reference model	Complete MDM Lab model
Simulation time	10 s	10 s
Computational time	360000 s	7200 s

Table 7.8: Comparison between computational times (Step 2)

### 7.3 Step 3: ThermoElastoHydroDynamic characteristics

In this section, some of the numerical results obtained with the third modeling step, its preliminary validation with a model available in literature [33] and the comparisons, referring to different model components and different physical quantities, with the experimental data provided by *General Electric Nuovo Pignone Spa* will be exposed, with the ultimate goal of evaluating the reliability of the proposed model.

Futhermore, some results useful to highlight the TEHD behaviour of the system will be shown. In particular the following results will be reported:

- the comparison between the experimental and numerical values of the bearing eccentricity in its equilibrium position, and a first model validation with literature data;
- the comparison between the experimental and numerical values of the pressure ( $p$ ), temperature ( $T_f$ ) and oil film thickness ( $h$ );
- the temperature ( $T_{pad}$ ) and the deformation ( $q_{pad}$ ) of the pad of the Non-Drive End bearing;
- the temperature ( $T_A$ ) and the deformation ( $q_A$ ) of the rotor fraction enclosed in the Non-Drive End bearing.

### 7.3.1 Static results and preliminary validation

The first comparison concerns the static eccentricity assumed by the rotor in its equilibrium position; the experimental results refer to tests carried out on the Non-Drive End bearing, with an imposed load equal to half of the rotor weight and a *Load On Pivot* (LOP) configuration; these static results can be used in order to exploit the proposed model for the calculation of the bearing dynamic coefficients, i.e. of the damping [C] and stiffness [K] matrices.

In Figure 7.28 the numerical and experimental values of eccentricity as a function of the rotor rotational velocity are shown; it is possible to highlight a good agreement

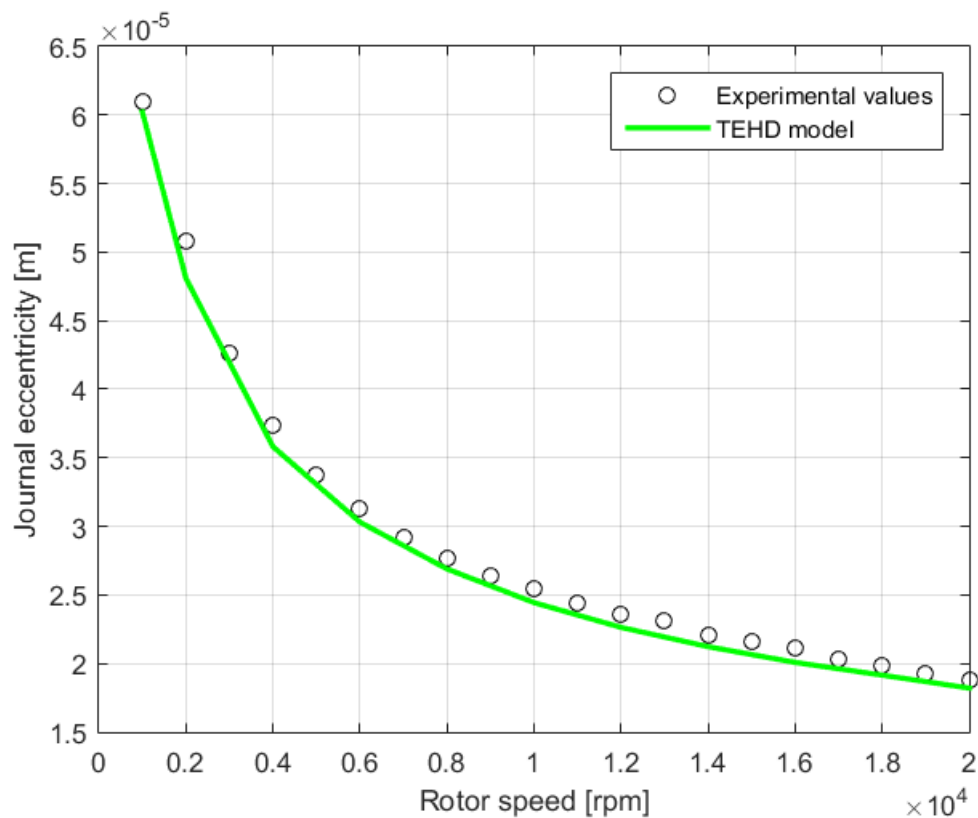


Figure 7.28: Comparison between the static eccentricity of the bearing obtained with the proposed model and that obtained from the experimental tests.

between the results obtained with the proposed TEHD model and those coming from

the experimental tests: the bearing eccentricity decreases as the rotor rotational velocity increases, since also the supporting action provided by the fluid films increases. In any static operating condition, the eccentricity remains well below the limit imposed for a correct operation of the bearing. Excessive values could instead be achieved if the bearing was subjected to a high unbalance load generated the rotor rotation, and particularly in presence of an overhung mass, since this configuration can be sometimes affected by the onset of thermal instability phenomena. A preliminary validation of this TEHD

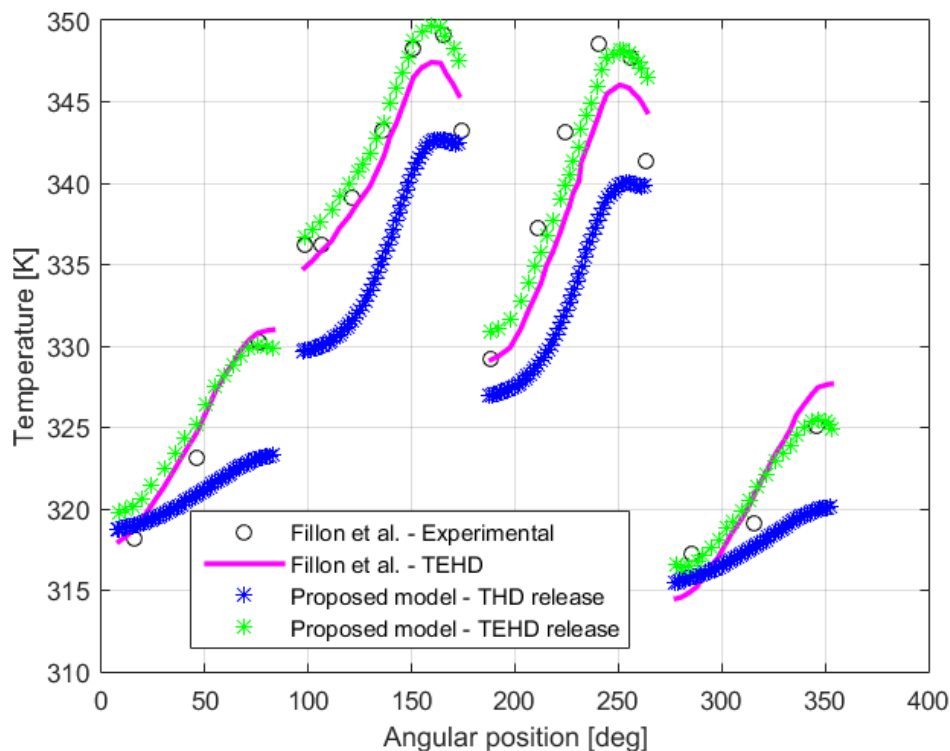


Figure 7.29: Comparison between the numerical and experimental values of the temperature range shown in [33], and the results obtained by the proposed THD model and the TEHD model (4000 rpm and an applied load of 10 kN).

model has been performed by considering a number of results available in the literature. In Figure 7.29 the comparison between the numerical and experimental values of the temperature field exposed in [33] is shown, and those obtained with the developed TEHD

model and the previous THD model, which does not consider the elastic effects of the rotor-bearing system.

The results refer to tests carried out on a TPJB with four pads which support a rotor with a rotation velocity equal to 4000 rpm and with an applied load equal to 10 kN, in a *Load Between Pivot* (LBP) configuration.

In accordance with Figure 7.29, the highest temperature values can be found in correspondence of the two most heavily loaded pads. The results obtained with the TEHD model show substantial agreement with those exposed in literature [33]; the agreement is not as good with the THD model, which tends to underestimate the temperature field that develops on the pads.

### 7.3.2 Experimental validation of the oil film model

This part of the model validation focuses on the characteristics that the fluid film within the bearing assumes during the system operation. The considered variables are the thickness ( $h$ ), the pressure ( $p$ ) and the temperature ( $T_f$ ) of the oil film, measured in correspondence of a rotor rotational velocity equal to 8000 rpm.

The comparisons have been highlighted considering experimental data and numerical results obtained with the TEHD model and from previous HD and THD releases of the model, which do not consider the heat transfer phenomena and elastic deformation present in the bearings and in the rotor. All the analyzed variables are measured circumferentially on the fluid film and their value are those recorded at the last step of the performed transient analysis, i.e. equal to 240 seconds.

In Figure 7.30 the values of the oil film thickness measured on the Non-Drive End bearing are shown: the oil film thickness is minimum in correspondence of the most loaded pads and on each pad the thickness value decreases from the leading edge to the trailing edge. The TEHD model shows minimum values of  $h$ , this is due to a decrease of the bearing radial clearance at high rotational velocities (Figure 7.35). Figure 7.31 shows the pressure

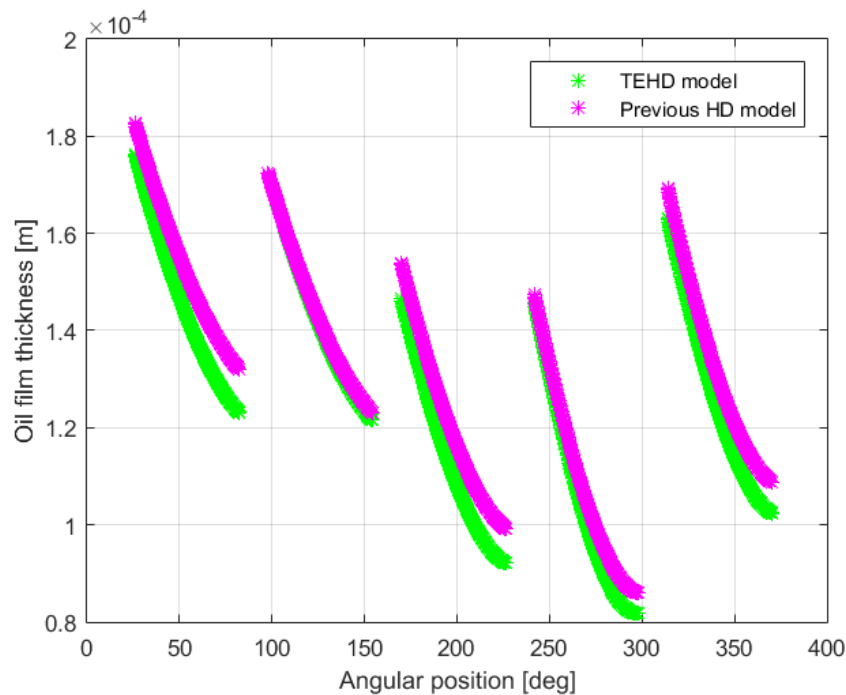


Figure 7.30: Comparison between the oil film thickness obtained with the third modeling step (TEHD) and with the previously developed model (HD), with a rotor rotational velocity equal to 8000 rpm and an applied load equal to half of the rotor mass (LOP configuration) together with an unbalance force.

values measured on the Non-Drive End bearing: it is possible to highlight how the higher levels of pressure are detected where the oil film thickness on the pads is lower.

Globally, the highest pressure values are obtained with the TEHD model: this is due to the fact that if the solid components are flexible, a part of the pressure generated within the oil film contributes to the pads deformation while the remaining part contributes to the sustenance of the rotor. In Figure 7.32 the temperature values measured on the Non-Drive End bearing are reported: the highest temperature values are obtained in correspondence of the most loaded pads. Furthermore on each pad there is an increasing temperature profile from the leading edge to the trailing edge: this is due to the viscous dissipation within the lubricant, which tends to raise the temperature and is maximum

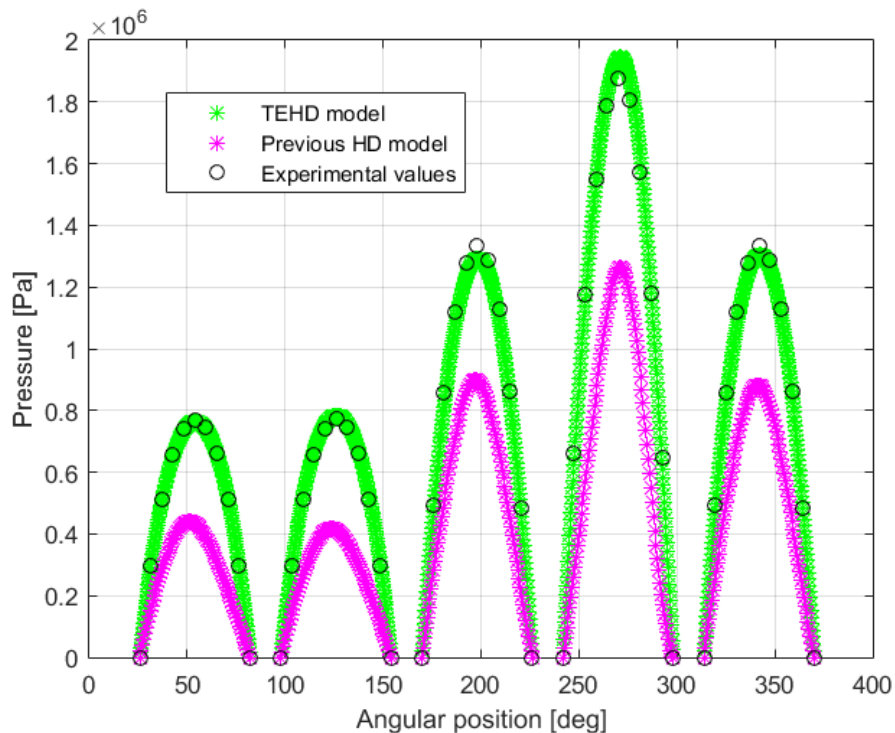


Figure 7.31: Comparison between the pressure field obtained with the third modelling step (TEHD) and with the previously developed model (HD), with a rotor rotational velocity equal to 8000 rpm and an applied load equal to half of the rotor mass (LOP configuration) together with an unbalance force.

in correspondence of the minimum oil film thickness (i.e. where the lubricant velocity is maximum).

For the pressure and temperature fields, it is possible to highlight how the numerical results obtained with the proposed TEHD model are in good agreement with the experimental data. Figures 7.31 and 7.32, allow to highlight how the introduction of further physical phenomena in the analysis has enhanced the accuracy of the TEHD model with respect to the previously developed HD and THD models, in which a lower number of physical phenomena has been considered.

Figure 7.32 shows how the temperature values obtained with the THD model are quite different from the experimental results, in particular in correspondence of the pads

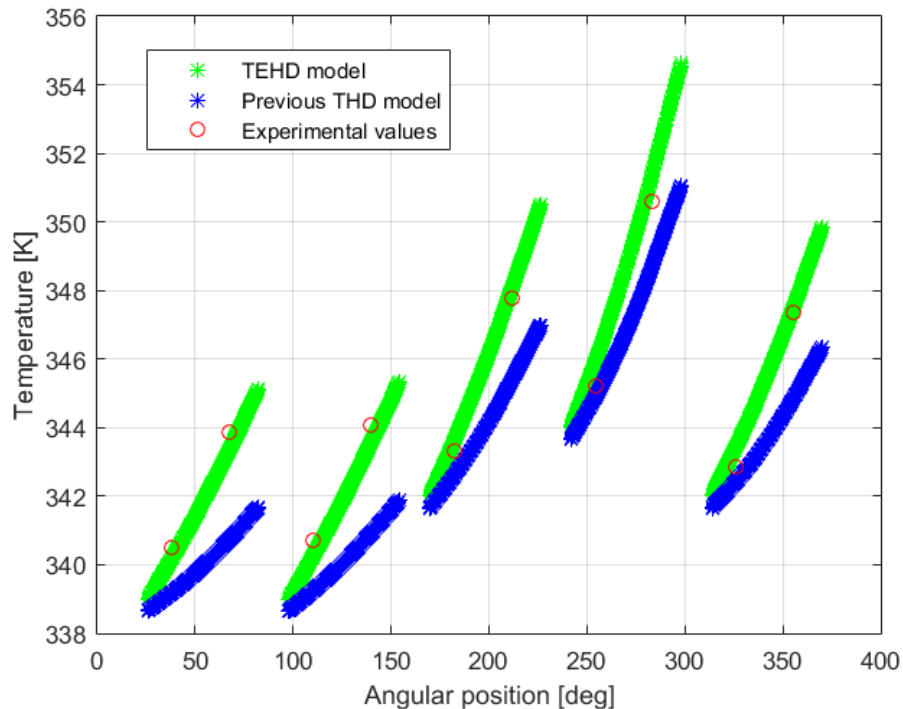


Figure 7.32: Comparison between the temperature field obtained with the third modelling step (TEHD) and with the previously developed model (THD), with a rotor rotational velocity equal to 8000 rpm and an applied load equal to half of the rotor mass (LOP configuration) together with an unbalance force.

trailing edges; this is due to the fact that in the trailing edges the temperature and the thermal deformations are greater, and a hypothesis of deformation equal to zero on the pads (such as that made in the THD model) leads to excessively distort the data. Furthermore, in Figure 7.32, it is possible to see how the temperature monotonically increases along the pad profile, differently with respect to TEHD models found in literature, which show a maximum value of temperature followed by a decrease in correspondence of the trailing edge. This discrepancy can be due to the bearing rotation velocity: the temperature decrease is due to the pads deformation that causes, in correspondence of the trailing edge, a strong increase of the oil film thickness with a consequent decrease of viscous dissipation within the lubricant. Since the bearings



considered in the present work are designed to operate at very high velocities, in the considered operative condition the pad deformation is not high enough to cause a temperature decrease according to the process above described.

### 7.3.3 Numerical results of the rotor and pad models

This last part of the discussion concerns primarily the thermal and elastic phenomena which develop on the solid parts of the model, and in particular provides a three-dimensional and two-dimensional representation of the temperature and deformation fields that occur on the pads and on the rotor.

Figure 7.33 shows, using a color scale, the temperature and the deformation that develop on the Non-Drive End bearing with a rotational velocity equal to 8000 rpm; the deformation includes both the thermal contribution generated by the heat exchange with the oil film and the elastic contribution due to the pressure applied by the oil film. It is possible to highlight as higher temperatures correspond to higher deformations; in the considered operating conditions, this means that, due to the high pads thickness, deformations due to thermal contributions are larger than those due to the elastic contribution. Moreover, the highest temperatures occur in correspondence of the pad trailing edges, i.e. where the lubricant temperature reaches higher values.

It is of particular interest to note how the temperature field developed on the pads reflects the boundary conditions applied to them: the pads outer surfaces are cooled through the convective heat exchange with the lubricant, at the supply temperature  $T_s$ ; this heat exchange, however, is not enough to dissipate the entire heat produced inside the oil film by the viscous dissipation. Therefore, the temperature field of the pads follows the temperature profile within the fluid film without ever reaching the supply temperature  $T_s$ . These results are in agreement with those found in literature, considering, for example, the TEHD model proposed by Palazzolo [19]. Figure 7.34 shows the pads deformation measured on the pads midline, i.e. the line that is located

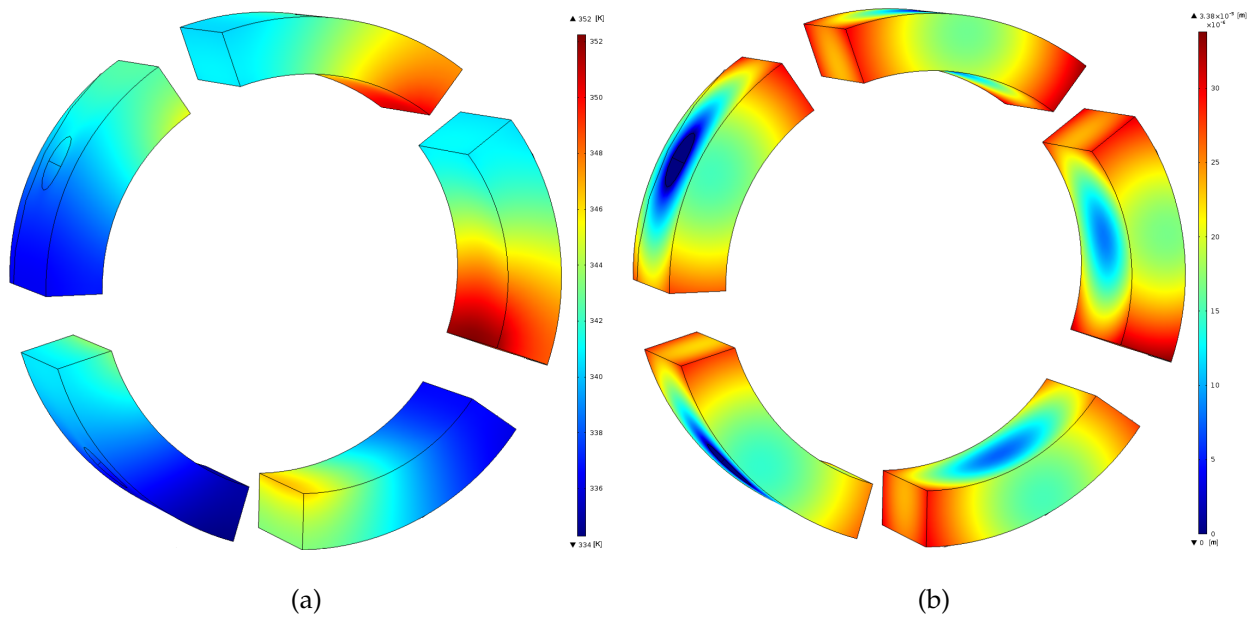


Figure 7.33: 3D representation of the temperature (a) and of the thermo-elastic deformation (b) fields of the Non-Drive End bearing pads with a rotor rotational velocity equal to 8000 rpm and an applied load equal to half of the rotor mass (LOP configuration) together with an unbalance force (TEHD modelling step).

circumferentially on the pads centerline; these results are an excerpt of those shown in Figure 7.33.b and it is possible to highlight how the minimum displacements can be found in correspondence with the pads pivots, while the deformation in the leading edge and in the trailing edge are maximum [34]. This deformation causes a variation in the curvature of the pads profiles, and hence a variation of the bearing preload.

As it is possible to see in Figure 7.35 the bearing radial clearance has not a constant value, and its variation can be attributed to the deformation of rotor and pads: the thermo-elastic load that acts on these solid components causes a deformation which tends to gradually decrease the value of the bearing radial clearance. A representative value of this variation may be calculated by performing an average on the five pads: Figure 7.35 shows the variation of the radial clearance as a function of the rotor rotational velocity. In particular, the bearing clearance decreases as the rotor speed increases: in fact, a high

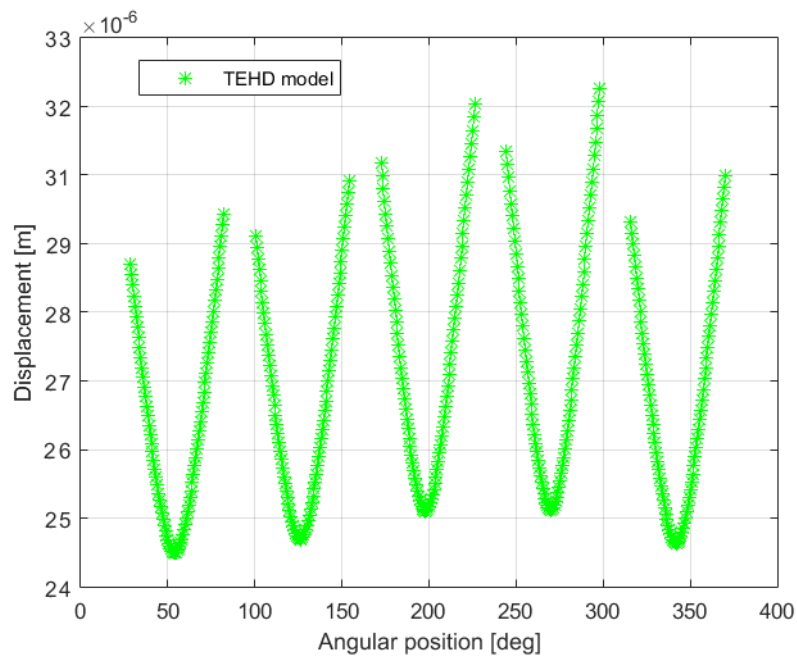


Figure 7.34: Deformation field obtained with the TEHD model on the Non-Drive End bearing pads, with a rotor rotational velocity equal to 8000 rpm and an applied load equal to half of the rotor mass (LOP configuration) together with an unbalance force.

value of the rotational velocity leads to a rise in the oil film temperature with a consequent increase of the deformation of rotor and pads (the clearance reduction is mainly due to the rotor thermal expansion). These results are in agreement with those found in literature considering, for example, the TEHD model proposed by Fillon [33].

Figure 7.36.a shows a three-dimensional representation of the temperature field in the rotor fraction enclosed within the Non-Drive End bearing, with a rotational velocity equal to 8000 rpm. From the color scale it is possible to highlight how, due to the rotor rotation, the temperature field on the rotor surface is characterized by the presence of cold and a hot zone, consistently with the result found in literature [33]: the temperature on the journal has a sinusoidal profile due to the rotor motion. In fact, due to the unbalance load applied on the overhung disk, the rotor performs a synchronous orbit while rotates around its axis: this leads to a condition in which a rotor part is always in contact with a

higher oil film thickness zone, while the opposite side is always in contact with a lower oil film thickness zone; then, the second part will be more heated than the other, thus generating a sinusoidal trend of the rotor temperature. This effect can trigger thermal instability phenomena, but in the considered operating conditions the temperature gap between the two opposite rotor sides is not high enough to generate this type of behavior. Figure 7.36.b shows the stresses field on the NDE side of the rotor and the temperature gradient due to the bearing thermal loads applied on the Non-Drive End rotor fraction, with a rotational velocity equal to 8000 rpm, the temperature gradient greatly contribute to the rotor deformation. The maximum stress occurs near to the NDE bearing, due to the unbalance load applied in correspondence of the rotor overhang; however, in the considered operating conditions, the stress value is not high in any case. The temperature gradient is calculated according to the thermal load found in correspondence of the

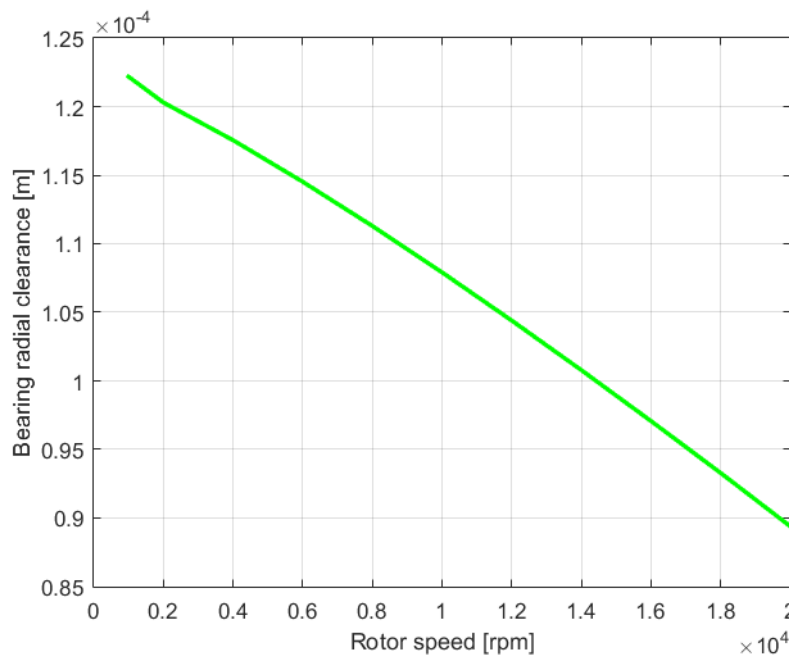


Figure 7.35: Bearing radial clearance variation obtained with the TEHD model for the NDE bearing, with a rotor rotational velocity equal to 8000 rpm and an applied load equal to half of the rotor mass (LOP configuration) together with an unbalance force.

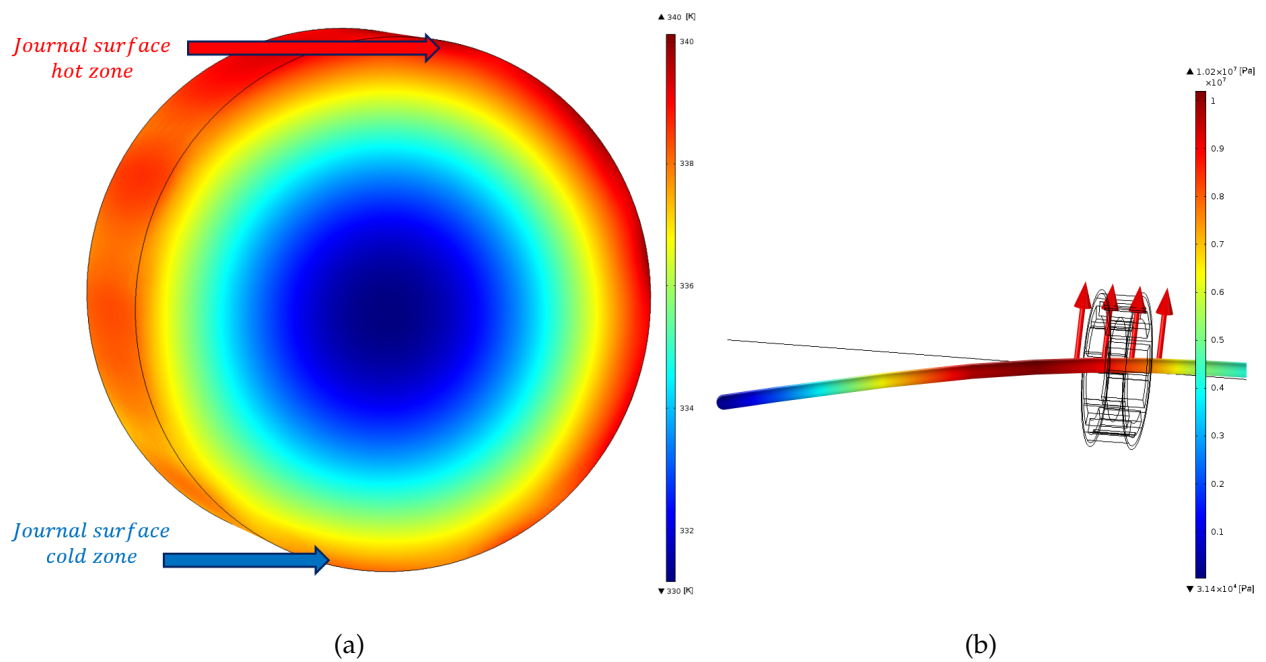


Figure 7.36: 3D representation of the temperature field in the rotor fraction enclosed in the Non-Drive End bearing (a), of the stresses and of the temperature gradient due to the bearing (b); with a rotor rotational velocity equal to 8000 rpm and an applied load equal to half of the rotor mass (LOP configuration) together with an unbalance force.

considered rotor fraction, and applied directly to the BEAM elements used for the rotor modeling (as described in Chapter 3.6.1). Since the rotor rotates around its  $z$  axis and the temperature distribution has a sinusoidal trend, the temperature gradient applied on the BEAM elements is represented by a rotating vector; this type of coupling is at the base of the onset of the thermal instability phenomenon known as *Morton effect*.

### 7.3.4 Model performances

The realized model is based on different types of finite element discretization. Each oil film model (i.e. one for each pad) was discretized with 35 2D QUAD elements. Concerning the solid components, each pad has been discretized with 4200 3D BRICK

elements, while the rotor model is composed by 41 3D BEAM elements; in addition, the rotor fractions enclosed in the two bearings have been discretized using 21600 3D BRICK elements. All these elements account for a total of 1,527,032 degrees of freedom, which must be added to the 40 degrees of freedom related to the implementation of ordinary differential equations that model the pads motion and the dynamics of the lubricant supply plant. The choice of two-dimensional elements for the oil film discretization allows, to avoid the huge computational efforts required by a fully 3d cfd model, while preserving the possibility to perform a geometrically and kinematically 3d analysis. Consequently the simulations, although substantially longer in comparison to the classical lumped parameters models, are less time-consuming with respect to the fully three-dimensional bearing models present in literature. The simulations were performed using a machine with the characteristics shown in Table 7.9: a simulation of 3 seconds requires about 46 minutes of computing time.

CPU	Intel CORE i7
clock frequency	2.30 GHz
RAM memory	16 Gb
$\frac{\text{machine time [s]}}{\text{time to be simulated [s]}}$	15.3

Table 7.9: Machine features and calculation time.

## Conclusions and future developments

In the last years, the development trend in the turbomachinery field has pushed towards ever higher rotational speeds and loads, since the machine rotational speed directly influences the efficiency of the system. In this scenario, Tilting Pad Journal Bearings have almost completely substituted the more unstable Fixed Geometry Journal Bearings. The typical TPJB models found in literature deal with the different aspects of the bearings behaviour separately, often using simplified lumped parameters approach: many models consider only the fluid dynamic aspect, considering the calculation of lubricant flow rate, while others analyze the rotor dynamic characteristics of the system simplifying the bearings action through their stiffness and damping matrices. Those models present great advantages from the computational point of view, but their accuracy and their ability to investigate the physical interactions involved in the bearings operation are insufficient to improve the efficiency of modern rotor dynamic systems; furthermore, modern rotor dynamic research topics involve the analysis of the couplings between the elements of a rotor dynamic system, with the aim of understanding how to enlarge the machine operating range and avoid particular instability phenomena: a simplified model is, by its own definition, inappropriate to carry on such analyses. Some authors performed an intermediate step, coupling a lower number of physical phenomena or analyzing

the coupled behavior of simpler bearings, or developed a completely three dimensional models which deals with many of the physical phenomena involved in TPJBs operation, coupling the classical thermal-fluid dynamic analysis performed on the oil films to the elastic and thermal study of the solid elements. All those models are characterized by a great accuracy but their computational times still represent a great limit to their applicability.

In this work an innovative Tilting Pad Journal Bearing model has been developed and experimentally validated; the proposed model allows to analyze simultaneously the ThermoElastoHydroDynamic (TEHD) characteristics of the system and is suitable to be used in the industrial field. The main objective of the proposed modelling approach is to partially overcome the limitations of existing models, providing results as accurate as those obtainable with fully-3D CFD model (good accuracy) but with computational times comparable to those of lumped parameter models (good numerical efficiency). The result is to obtain a time-efficient unique model with a high numerical efficiency, since a power plant can contain a large number of different bearings. Furthermore, the proposed model is characterized by a strong modularity, necessary for complex transient simulations of complete plants and for the easy representation of different kind of bearings. In fact, the modularity of the proposed model allows the variation of the bearing layout, also considering different kind of lubricants and of supply plant.

The complete model (rotor-bearings system) has been realized and verified following three separate modeling step: a first single bearing model has been developed to validate the fluid dynamical performances of the system and its extension (i.e. coupling with a FEM rotor model) provided the possibility to verify the rotor dynamical behavior of the proposed model; finally, the third modeling step focused on the thermal and elastic behaviours of the system.

The results obtained simulating the developed model show a good agreement with the experimental data used as a reference, from the hydraulic point of view (evaluating the lubricant flow rates and pressures of the system), from the dynamical one (analyzing the



interactions between rotor and bearings) and from the ThermoElastoHydroDynamic one (considering all the physical interactions between rotor and bearings). The third release of the proposed model has been preliminary validated considering a set of numerical and experimental results found in literature, concerning a four pads TPJB with a rotational speed equal to 4000 rpm and an applied load of 10 kn, and then through a set of experimental results provided by General Electric Oil & Gas concerning an experimental campaign on a full rotor supported by two five pads TPJBs. The proposed results show the comparison between the experimental measurements and the results obtained with the TEHD and other previous releases of the proposed model, in order to validate the model and show the accuracy improvement due to the introduction of further physical phenomena in the model. From the thesis has emerged how there is a strong influence of the thermo-elastic phenomena on the system behaviour (especially in the transient phases), thus bringing out the industrial importance of having a time-efficient bearing model that models not only the fluid dynamic and/or rotor dynamic aspects.

The computational times are low in spite of the complexity of the model: the proposed model can thus aim to partially replace the classical lumped parameters models. The whole model is composed by different types of FEM elements and even lumped parameters components. It includes about 1 million degrees of freedom but is characterized by a good numerical efficiency.

On the basis of this thesis some papers have already been realized and others are under construction; furthermore it is possible for a new research topic on bearings to originate from this work with the cooperation of General Electric Oil & Gas.

Many future developments can stem from this thesis. From a rotor dynamical point of view a first step can be the introduction of a basement model for the rotor, in order to include the dynamical coupling between the motions of rotor and structure. The modelling of such components becomes important especially when on the same basement are installed more rotors: in this case it is necessary to highlight the coupled effects between bearings belonging to different rotors. Initially the baseplate will be modelled

through a lumped parameters approach, using joining elements between the various bearings; in a second step FEM models of the baselpates will be coupled to the rotor-bearings model itself.

Furthermore, the pivot flexibility can be introduced in the model, since it influences the total stiffness and damping characteristics of the bearing. In fact, its flexibility influences the bearing clearance and thus its dynamic characteristics. Moreover, being a kinematic pair, it will present losses to be taken into account in the calculation of the pad rotations. This part should be realized in the same way of the pad and rotor fraction models.

From a fluid dynamical point of view a further step is represented by the use of a turbulence model for the oil film in order to analyze the behavior of a machine in the widest operating range. The turbulent motion arises especially for certain ranges of viscosity and when the bearing is characterized by large dimensions: in these conditions it is possible to demonstrate how the heat transfer phenomena are more significant than in other operating conditions. It will also be necessary to consider a relationship concerning the temperature variation along the oil film thickness (which is higher close to the pad and lower in the interface in contact with the rotor), especially to investigate thermal instability effects. Starting from the current oil film model, simply two equations should be added: an additional equation for the current laminar Reynolds equation, to take into account the turbulent regime; and another to calculate the temperatures to be applied on the pads and rotor surfaces from the oil film temperature field.

Furthermore it can be useful to extract from the complete model some heuristic relationships that take into account, statically and dynamically, the typical 3D effects neglected by a classical lumped parameters model. The use of heuristic relationships is especially important in the preliminary phases of a project, when a first layout should be defined without significant computational effort.

The developed model can be easily modified in order to analyze tilting pad thrust bearings.

Under the SIR program (Scientific Independence of Young Researchers) project, the

design and construction of a complete rotordynamic test rig (rotor mounted on two Tilting Pad Journal Bearings) is in progress, to test the performances of various bearings (in term of size and pad numbers) and allow further upgrades of the model developed during this PhD course.

Each of these proposed future developments will need to be subjected to further

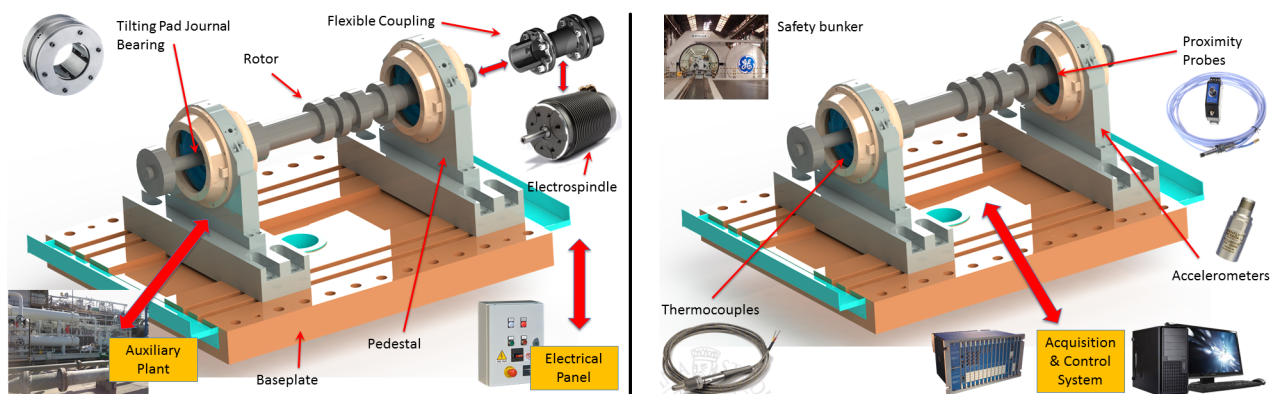


Figure 8.1: UNIFI test rig layout

experimental validations.

The final aim of this research work is to produce a reliable analysis tool for the rotor dynamical field which, being able to accurately represent the complex phenomena involved in Tilting Pad Journal Bearings operations, could provide essential information for the design and safe operation of a plant.

## Publications

This section shows the previews of the publications realized during the Ph.D. program, inherent to the proposed research project. The work was greeted with considerable interest and has led both to publications in high impact factor journals:

- ASME Journal of Computational and Nonlinear Dynamics;
- ASME Journal of Vibration and Acoustics;
- Tribology International;

and to positive opinions in several international congresses regarding the rotordynamic topic:

- 9<sup>th</sup> IFToMM International Conference on Rotor Dynamics;
- IDETC/CIE 2015 ASME International Design Engineering Technical Conferences and Computers & Information in Engineering Conference;
- ASME TURBO EXPO 2016 Turbomachinery Technical Conference & Exposition;
- 4<sup>th</sup> Joint International Conference on Multibody System Dynamics IMSD.

## Development and Preliminary Validation of Efficient 3D Models of Tilting Pad Journal Bearings

Roberto Conti, Amedeo Frilli, Emanuele Galardi, Enrico Meli,  
Daniele Nocciolini, Luca Pugi, Andrea Rindi and Stefano Rossin

**Abstract** This paper mainly focuses on the development of efficient three-dimensional (3D) models of TPJBs, able to contemporaneously simulate both the rotor dynamics of the system and the lubricant supply plant. The proposed modelling approach tries to obtain a good compromise between the typical accuracy of standard 3D models and the high numerical efficiency of simpler and less accurate models. In this work, the whole model has been developed and validated in collaboration with *Nuovo Pignone General Electric S.p.a.* which provided the required technical and physical data. In particular, the experimental data are referred to a suitable lube oil console system, built at the GE testing center in Massa-Carrara (MS, Italy) for the verification of plant components.

---

R. Conti (✉) · A. Frilli · E. Galardi · E. Meli · D. Nocciolini · L. Pugi · A. Rindi · S. Rossin  
Department of Industrial Engineering, University of Florence,  
via di S.Marta 3, 50139 Florence, Italy  
e-mail: roberto.conti@unifi.it  
URL: <http://www.dief.unifi.it/>; <http://www.ge.com/>

A. Frilli  
e-mail: amedeo.frilli@unifi.it

E. Galardi  
e-mail: emanuele.galardi@unifi.it

E. Meli  
e-mail: enrico.meli@unifi.it

D. Nocciolini  
e-mail: daniele.nocciolini@unifi.it

L. Pugi  
e-mail: luca.pugi@unifi.it

A. Rindi  
e-mail: andrea.rindi@unifi.it

S. Rossin  
e-mail: stefano.rossin@ge.com

© Springer International Publishing Switzerland 2015  
P. Pennacchi (ed.), *Proceedings of the 9th IFToMM International  
Conference on Rotor Dynamics, Mechanisms and Machine Science 21*,  
DOI 10.1007/978-3-319-06590-8\_65

793

R. Conti, E. Galardi, E. Meli, D. Nocciolini, L. Pugi, A. Rindi (2014). *Development and Preliminary Validation of Efficient 3D Models of Tilting Pad Journal Bearings*. Proceedings of IFTOMM ICORD 2014. p.1-10, IFTOMM ICORD 2014.

**Andrea Rindi**

Professor  
Department of Industrial Engineering,  
University of Florence,  
Florence 50139, Italy  
e-mail: andrea.rindi@unifi.it

**Stefano Rossin**

General Electric Oil & Gas,  
Florence 50127, Italy  
e-mail: stefano.rossin@ge.com

**R. Conti**

Department of Industrial Engineering,  
University of Florence,  
Florence 50139, Italy  
e-mail: roberto.conti@unifi.it

**A. Frilli**

Department of Industrial Engineering,  
University of Florence,  
Florence 50139, Italy  
e-mail: amedeo.frilli@unifi.it

**E. Galardi**

Department of Industrial Engineering,  
University of Florence,  
Florence 50139, Italy  
e-mail: emanuele.galardi@unifi.it

**E. Meli**

Department of Industrial Engineering,  
University of Florence,  
Florence 50139, Italy  
e-mail: enrico.meli@unifi.it

**D. Nocciolini**

Department of Industrial Engineering,  
University of Florence,  
Florence 50139, Italy  
e-mail: daniele.nocciolini@unifi.it

**L. Pugi**

Department of Industrial Engineering,  
University of Florence,  
Florence 50139, Italy  
e-mail: luca.pugi@unifi.it

## Efficient Models of Three-Dimensional Tilting Pad Journal Bearings for the Study of the Interactions Between Rotor and Lubricant Supply Plant

*In many industrial applications, tilting pad journal bearings (TPJBs) are increasingly used because they are very suitable both for high-speed and high external loads. Their study is fundamental in rotating machines and a compromise between accuracy and numerical efficiency is mandatory to achieve reliable results in a reasonable time. This paper mainly focuses on the development of efficient three-dimensional (3D) models of TPJBs, in order to contemporaneously describe both the rotor dynamics of the system and the lubricant supply plant in long simulations (from the initial transient phase to the steady-state condition). Usually, these two aspects are studied separately, but their interactions must be considered if an accurate description of the whole system is needed. The proposed model architecture considers all the six degrees-of-freedom (DOFs) between supporting structures and rotors and can be applied to different types of TJPB layout with different lubricant supply plants. In this research activity, the whole model has been developed and validated in collaboration with Nuovo Pignone General Electric S.p.a. which provided the required technical and experimental data. [DOI: 10.1115/1.4030509]*

### 1 Introduction

The present paper deals with the development of an efficient numerical model for the simulation of the dynamic behavior of TPJBs (Fig. 1). TPJBs are particular fluid dynamical bearings widely used in turbomachinery: the continuous increase of turbomachines rotational speed, with the aim of improving the machines aerodynamic performances, has brought the classical fixed geometry journal bearing to the limits of their operating range. The intrinsic problems in operating at high-speed with fixed geometry bearings (e.g., the onset of instability phenomena like *oil whip* and *oil whirl* due to the coupling between the forces exerted by the bearing on the rotor in the transverse directions) have led to the introduction of the TPJBs in order to achieve

satisfactory performances even in very challenging operating conditions. In a TPJB, the bearing surface delimiting the oil film is not a complete cylinder but is divided in a certain number of sectors capable, through appropriate constraints, of one or more rotations: the bearing geometry is no more fixed and is able to follow the rotor motion and to adjust to the dynamic loads applied to the system. Thanks to their dynamical characteristics, TPJBs are appropriate for high-speed applications and heavy external loads both in transient and steady-state operations (ensuring stability in both cases) [1–3]: the bearing operating range is wider with respect to fixed geometry bearings and this enables to operate the supported machine near or beyond its critical speeds.

TPJBs, due to their supporting action to a pressurized lubricant fluid (which also performs the secondary function of removing the heat generated in the rotor-bearing system), interposed between the rotor surface and the bearing pads surfaces: the lubricant is supplied by the hydraulic network used for all the auxiliary needs

Manuscript received October 1, 2014; final manuscript received April 27, 2015; published online July 17, 2015. Assoc. Editor: José L. Escalona.

Journal of Computational and Nonlinear Dynamics  
Copyright © 2016 by ASME

JANUARY 2016, Vol. 11 / 011011-1

Downloaded From: <http://computationalnonlinear.asmedigitalcollection.asme.org/> on 09/29/2016 Terms of Use: <http://www.asme.org/about-asme/terms-of-use>

R. Conti, A. Frilli, E. Galardi, E. Meli, D. Nocciolini, L. Pugi, A. Rindi, S. Rossin (2015). *Efficient Models of 3D Tilting Pad Journal Bearings for the Study of the Interactions between Rotor and Lubricant Supply Plant*. ASME JOURNAL OF COMPUTATIONAL AND NONLINEAR DYNAMICS, p. 1-16, ISSN: 1555-1423.

## DETC2015/VIB-46262

### A TILTING PAD JOURNAL BEARING MODEL FOR COUPLED FLUID DYNAMICAL - ROTOR DYNAMICAL ANALYSES

**R. Conti, A. Frilli, E. Galardi, E. Meli,  
D. Nocciolini, L. Pugi, A. Rindi**  
Department of Industrial Engineering (DIEF)  
University of Florence  
Via di Santa Marta n° 3, 50139  
Florence, Italy  
Email: [roberto.conti, amedeo.frilli,  
emanuele.galardi, enrico.meli, daniele.nocciolini,  
luca.pugi, andrea.rindi]@unifi.it

**Stefano Rossin**  
Consulting Engineer, Ph.D.  
General Electric Oil & Gas  
Via Felice Matteucci n° 2, 50127  
Florence, Italy  
Email: stefano.rossin@ge.com

#### ABSTRACT

*Turbomachines are continuously developing in order to reach higher levels of speed, power and efficiency and the classical Fixed Geometry Journal Bearings have been replaced by Tilting Pad Journal Bearings to avoid instability phenomena. In this paper, the authors propose an innovative quasi-3D TPJB modelling approach that allows the simultaneous and coupled analysis of the typical phenomena involved in TPJB operations. The authors focused on the accurate analysis of the interactions between the rotor and the lubricant supply plant and on the fluid dynamical effects due to the bearing that cause those couplings, aiming at reaching a good compromise between the accuracy and the numerical efficiency of the model (mandatory to analyze systems with many bearings). The TPJB model has been developed and experimentally validated in collaboration with Nuovo Pignone General Electric S.p.a. which provided the technical data of the system and the results of experimental tests.*

#### 1 Introduction

Tilting Pad Journal Bearings (TPJB, Figure 1) are extensively used for the support of compressors, pumps and turbines because they are more reliable with respect to fixed geometry

journal bearings and provide a greater stability in high speed applications, both for transient and steady state operating conditions, due to their possibility to adjust their response to the rotor motion. Consequently, due to the presence of several physical phenomena, the accurate modelling of TPJBs represents a challenging issue. Furthermore, the complexity of a turbomachinery system requires a compromise between the accuracy of the bearing model and its computational times.

The state-of-the-art models of the bearing fluid dynamical be-

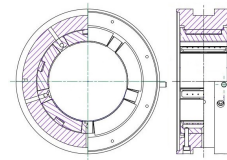


FIGURE 1. Tilting Pad Journal Bearing.

haviour are often based on simplified approaches (i.e. lumped parameters models) [18], [32], [33]. Analogously, rotor dynamical models including TPJBs usually employ lumped spring-

**Andrea Rindi**

Professor  
Department of Industrial Engineering,  
University of Florence,  
Florence 50100, Italy  
e-mail: andrea.rindi@unifi.it

**Stefano Rossin**

General Electric Oil & Gas,  
Florence 50100, Italy  
e-mail: stefano.rossin@ge.com

**R. Conti**

Department of Industrial Engineering,  
University of Florence,  
Florence 50100, Italy  
e-mail: roberto.conti@unifi.it

**A. Frilli**

Department of Industrial Engineering,  
University of Florence,  
Florence 50100, Italy  
e-mail: amedeo.frilli@unifi.it

**E. Galardi**

Department of Industrial Engineering,  
University of Florence,  
Florence 50100, Italy  
e-mail: emanuele.galardi@unifi.it

**E. Meli**

Department of Industrial Engineering,  
University of Florence,  
Florence 50100, Italy  
e-mail: enrico.meli@unifi.it

**D. Nocciolini**

Department of Industrial Engineering,  
University of Florence,  
Florence 50100, Italy  
e-mail: daniele.nocciolini@unifi.it

**L. Pugi**

Department of Industrial Engineering,  
University of Florence,  
Florence 50100, Italy  
e-mail: luca.pugi@unifi.it

## An Efficient Quasi-Three-Dimensional Model of Tilting Pad Journal Bearing for Turbomachinery Applications

*The constant increase of turbomachinery rotational speed has brought the design and the use of journal bearings to their very limits: tilting pad journal bearings (TPJBs) have been introduced for high-speed/high-load applications due to their intrinsic stability properties and can be used both in transient and steady-state operations obtaining superior performances. An accurate analysis of the TPJBs behavior is essential for a successful design and operation of the system; however, it is necessary to reach a compromise between the accuracy of the results provided by the TPJB model and its computational cost. This research paper exposes the development of an innovative and efficient quasi-3D TPJB modeling approach that allows the simultaneous analysis of the system rotordynamics and the supply plant behavior; the majority of existing models describe these aspects separately but their complex interaction must be taken into account to obtain a more accurate characterization of the system. Furthermore, the proposed model is characterized by a high numerical efficiency and modularity, allowing for complex transient simulations of the complete plant and for the representation of different kind of bearings. The TPJB model has been developed and experimentally validated in collaboration with an industrial partner which provided the technical data of the system and the results of experimental tests. [DOI: 10.1115/1.4031408]*

### 1 Introduction

Compressors, pumps, and turbines are used in many industrial fields in a wide range of sizes and powers. In the analysis of such rotating machines, TPJBs (Fig. 1) represent a key element, because they couple all the elements of the plant (i.e., supporting structures, rotors, lubricant supply plant), deeply affecting their behavior.

TPJBs are increasingly used in turbomachinery, because they present several advantages compared to fixed geometry journal bearings. In particular, TPJBs ensure stability in high-speed applications, even with heavy external loads, both for transient and

steady-state conditions, due to their possibility to follow the rotor motion and adapt to the system dynamical equilibrium. The complete rotor-bearing-plant system is very complex, due to the presence of a number of different dynamical phenomena, both mechanical and fluid dynamical; therefore, the accurate modeling of TPJBs represents a challenging issue. At the same time, the complexity of the system requires a compromise between the accuracy of the TPJB model and its numerical efficiency: in a single plant there could be a large number of bearings, so it is necessary that a bearing model returns reliable results in reasonable times.

The state-of-the-art models of the fluid dynamical behavior of the bearings (including simple representations of the supply plant) are often based on a simplified lumped parameters approach [1–4]. Analogously, rotor dynamical models of the TPJBs usually consist of lumped parameters spring-damper systems [5–8]. These models are very simple and characterized by small computational

Contributed by the Technical Committee on Vibration and Sound of ASME for publication in the JOURNAL OF VIBRATION AND ACOUSTICS. Manuscript received November 10, 2014; final manuscript received June 23, 2015; published online October 6, 2015. Assoc. Editor: Patrick S. Keogh.

R. Conti, A. Frilli, E. Galardi, E. Meli, D. Nocciolini, L. Pugi, A. Rindi, S. Rossin (2015). *An Efficient quasi-3D Model of Tilting Pad Journal Bearing for Turbomachinery Applications*. JOURNAL OF VIBRATION AND ACOUSTICS.





Contents lists available at ScienceDirect

Tribology International

journal homepage: [www.elsevier.com/locate/triboint](http://www.elsevier.com/locate/triboint)

## An efficient quasi-3D rotordynamic and fluid dynamic model of Tilting Pad Journal Bearing



R. Conti<sup>a</sup>, A. Frilli<sup>a</sup>, E. Galardi<sup>a</sup>, E. Meli<sup>a,\*</sup>, D. Nocciolini<sup>a</sup>, L. Pugi<sup>a</sup>, A. Rindi<sup>a</sup>, S. Rossin<sup>b</sup>

<sup>a</sup> MDM Lab-Department of Industrial Engineering-University of Florence, Via di Santa Marta n°3, Italy

<sup>b</sup> General Electric Nuovo Pignone, Via Felice Matteucci, Italy

### ARTICLE INFO

#### Article history:

Received 19 February 2016

Received in revised form

8 July 2016

Accepted 27 July 2016

Available online 2 August 2016

#### Keywords:

Tilting Pad Journal Bearing

Thin film lubrication

Hydrodynamic lubrication

Mineral oils

### ABSTRACT

Over the last few decades the use of Tilting Pad Journal Bearings (TPJBs) has spread due to their better performances in the most demanding operating conditions (i.e. in the presence of high loads and speeds). This research paper describes the development and experimental validation of a new quasi-3D TPJB model, able to analyze both the fluid dynamics (also including the supply plant) and rotor dynamics of the system and their complex interactions. The developed model is characterized by a high numerical efficiency, thus allowing for complex simulation tasks, and strongly modular, with the possibility to easily represent different layouts of TPJBs. The proposed model has been developed and experimentally validated in collaboration with *Nuovo Pignone General Electric S.p.a.* considering a complete plant test rig which includes rotor, bearings and lubrication circuit. Finally, an innovative heuristic law is proposed in order to predict the TPJB fluid dynamical characteristics taking into account the coupled effects neglected by classical simplified models.

© 2016 Elsevier Ltd. All rights reserved.

### 1. Introduction

Nowadays Tilting Pad Journal Bearings (TPJB, Fig. 1) are widely used for the support of rotating machinery in the full range of available sizes and powers, thus representing the coupling element between the different components of a plant (i.e. lubricant supply plant, supporting structures, rotors).

Compressors, turbines and pumps benefit from the presence of TPJBs because their performances largely overtake those of fixed geometry journal bearings [1,2]. Compared to classical journal bearings, TPJBs fit better for high speed applications [3] and for heavily loaded rotors thanks to the possibility to adjust their supporting action to the rotor motion, thus ensuring optimal stability [4–6] both in transient [7,8] and steady state conditions [9]. The behavior of the rotor-bearing-plant system depends on the complex interactions between the fluid dynamical (including the effects of the lubricant supply plant) and rotor dynamical phenomena involved in the process: an accurate modelling of both the aspects is mandatory for the correct design and operation of the entire plant. On the other hand, the system complexity itself (a

plant can include several different bearings) requires a TPJB model as computationally efficient as possible; therefore a compromise between the accuracy and the numerical efficiency of a TPJB model is necessary to fulfill industrial requirements.

The classical literature TPJBs models are often based on the lumped parameters approach [10–12]: from the rotor dynamical point of view TPJB are usually represented in terms of stiffness and damping matrices, whose forces are applied in the rotor node corresponding to the bearing center. While a procedure for the calculation of dynamic coefficients for journal bearings was already available [13], the first to develop a calculation method for Tilting Pad Journal Bearings was Lund [14]. Starting from that pioneering work, many researchers have investigated how to improve the lumped parameters dynamical representation of TPJBs: Tschoepe and Childs [15] and Brockwell et al. [16] experimentally validated the dynamic coefficients prediction taking into account pivot contact flexibility and different pad geometries; Wilkes and Childs [4] and Rodriguez and Childs [17] analyzed the influence of frequency and model degrees of freedom on the calculation of coefficients and on stability; Lihua et al. [18] investigated the calculation of dynamical coefficients in gas lubricated bearings and Cha et al. [19] analyzed the influence of pad compliance on the bearing dynamic characteristics. Similarly, from the hydraulic point of view the behavior of TPJBs within the lubrication auxiliary plant is typically treated as that of a lumped parameters orifice [13,20]. The numerical efficiency of these simplified models is very high and their use is widely diffused in many applications,

\* Corresponding author.

E-mail addresses: [roberto.conti@unifi.it](mailto:roberto.conti@unifi.it) (R. Conti), [amedeo.frilli@unifi.it](mailto:amedeo.frilli@unifi.it) (A. Frilli), [emanuele.galardi@unifi.it](mailto:emanuele.galardi@unifi.it) (E. Galardi), [enrico.meli@unifi.it](mailto:enrico.meli@unifi.it) (E. Meli), [daniele.nocciolini@unifi.it](mailto:daniele.nocciolini@unifi.it) (D. Nocciolini), [luca.pugi@unifi.it](mailto:luca.pugi@unifi.it) (L. Pugi), [andrea.rindi@unifi.it](mailto:andrea.rindi@unifi.it) (A. Rindi), [stefano.rossin@ge.com](mailto:stefano.rossin@ge.com) (S. Rossin).

<http://dx.doi.org/10.1016/j.triboint.2016.07.024>  
0301-679X/© 2016 Elsevier Ltd. All rights reserved.

R. Conti, E. Galardi, A. Frilli, E. Meli, D. Nocciolini, L. Pugi, A. Rindi, S. Rossin (2016). *An efficient quasi-3D rotordynamic and fluid dynamic model of Tilting Pad Journal Bearing*. Tribology International, p. 449-464, vol. 103.

GT2016-57401

### DEVELOPMENT AND VALIDATION OF AN EFFICIENT TEHD MODEL OF TILTING PAD JOURNAL BEARINGS

R. Conti, A. Frilli, E. Meli, D. Nocciolini,  
 S. Panconi, L. Pugi, A. Rindi

Department of Industrial Engineering  
 University of Florence

Email: [roberto.conti, amedeo.frilli, enrico.meli, daniele.nocciolini,  
 simone.panconi, luca.pugi, andrea.rindi]@unifi.it

S. Rossin

General Electric Nuovo Pignone  
 Italy

Email: stefano.rossin@ge.com

#### ABSTRACT

*The large success of Tilting Pad Journal Bearings (TPJBs) for the use in high speed/high load applications is due to their intrinsic stability properties, which allow superior rotor dynamic performances. TPJBs operation involves different physical phenomena, like the pads flexibility and the heat exchange between solids and fluids: an accurate analysis of these phenomena is fundamental in order to successfully employ TPJBs. In this paper, the authors, in cooperation with General Electric Nuovo Pignone, develop an innovative 3D TPJB modelling approach that allows an accurate analysis of the interactions between the fluid dynamic and thermal phenomena with the elastic behaviour of the solid components (ThermoElastoHydroDynamic analysis). The main objective of the proposed model is to provide accurate 3D results with low computational times. The TPJB model has been also experimentally validated, focusing on the thermal characteristics of the system and the interactions due to the TEHD behaviour of the bearing system.*

#### NOMENCLATURE

**A** Area.  
**C** Viscous damping matrix.  
 $C_d$  Duct flow coefficient.  
 $C_p$  Specific heat capacity at constant pressure.  
**D** Elastic stiffness matrix.  
**F** Force.  
**G** Gyroscopic effect matrix.

**H** Circulatory matrix.  
 $I_p$  Polar moment of inertia.  
 $I_t$  Transversal moment of inertia.  
**K** Bulk modulus.  
**K** Stiffness matrix.  
**M** Moment.  
**M** Mass matrix.  
 $Q$  Flow rate.  
**R** Radius.  
**S** Surface.  
**T** Temperature.  
 $Vol$  Volume.  
 $W_i$  Rotor section torsional modulus.  
 $d_0$  Rotor section diameter.  
**f** FEM generalized loads.  
 $f$  Frequency.  
 $h$  Oil film thickness.  
 $h$  Convective heat transfer coefficient.  
 $m$  Mass.  
**n** Outgoing unitary vector.  
 $p$  Pressure.  
**q** FEM generalized displacements.  
 $t$  Time.  
**v** Fluid velocity.  
**x** Position.  
 $\dot{x}$  Velocity.

*Greek Letters*

R. Conti, A. Frilli, E. Meli, D. Nocciolini, S. Panconi, L. Pugi, A. Rindi, S. Rossin (2016). *Development and Validation of an Efficient TEHD Model of Tilting Pad Journal Bearings*. Proceedings of the ASME TURBO EXPO 2016, p. 1-16.

## A New ThermoElastoHydroDynamic Tilting Pad Journal Bearings Model

Roberto Conti<sup>1</sup>, Amedeo Frilli<sup>1</sup>, Enrico Meli<sup>1</sup>, Daniele Nocciolini<sup>1</sup>, Simone Panconi<sup>1</sup>, Luca Pugi<sup>1</sup>,  
Andrea Rindi<sup>1</sup> and Stefano Rossin<sup>2</sup>

<sup>1</sup>Department of Industrial Engineering, University of Florence,

{roberto.conti, amedeo.frilli, enrico.meli, daniele.nocciolini, simone.panconi, luca.pugi, andrea.rindi}@unifi.it

<sup>2</sup>General Electric Oil & Gas, Florence, stefano.rossin@ge.com

The turbomachinery field is constantly pushing towards higher rotational speeds and loads; this development trend has led to the overcome of Fixed Geometry Journal Bearings and to the introduction of Tilting Pad Journal Bearings (TPJBs). TPJBs are characterized by superior dynamic performances and by a greater rotordynamic stability. Their operation involves many different physical phenomena (e.g. the elastic and thermal behaviour of the pads) and hence, an accurate analysis of their behaviour is essential in order to successfully and safely design and operate them. Moreover, in order to meet the industry requirements, it is important for a TPJB model to reach a good trade-off between the accuracy of the results and the computational costs.

In this paper, the authors, in collaboration with General Electric Nuovo Pignone, present a newly developed TPJB three-dimensional model which is able to perform a coupled analysis of the main physical phenomena involved in TPJBs operations. The main goal of the model is to analyze the interactions between the thermal and fluid dynamical behavior of the lubricant with the thermal and elastic behavior of the solid components, thus obtaining a complete TEHD model (ThermoElastoHydroDynamic analysis).

Most of the models found in literature analyze the behaviour of TPJBs with a lumped parameters approach (0D and 1D models), dealing separately with the different physical phenomena and neglecting their couplings [1]. While those models are characterized by a great computational efficiency and a low accuracy, it is also possible to find fully 3D models [2], [3] but their computational loads represent a great limit for the applicability at the industry level. The proposed model aims to reach a compromise between the characteristics of the State-of-the-Art models, obtaining accurate results from a coupled analysis with a great computational efficiency.

The developed model architecture is shown in Figure 1:

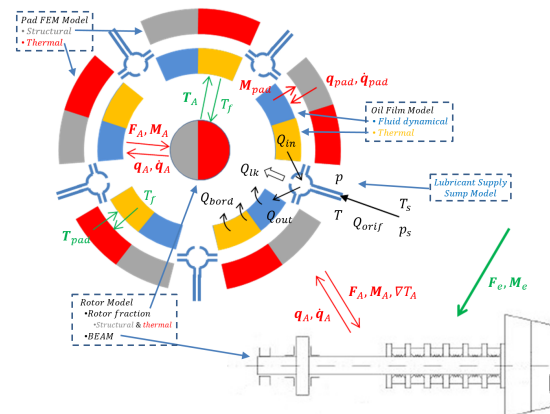


Fig. 1: General architecture of the whole model.

R. Conti, A. Frilli, E. Meli, D. Nocciolini, S. Panconi, L. Pugi, A. Rindi, S. Rossin (2016). *A New ThermoElastoHydroDynamic Tilting Pad Journal Bearings Model*. Proceedings of the International Conference on multibody System Dynamics-IMSD.

# Bibliography

- [1] G. Genta , *Dynamics of Rotating Systems* , Springer, January 2005; [4](#), [16](#), [76](#), [94](#)
- [2] J. C. Nicholas, *Tilting pad bearing design* , Proceedings of the Twenty-Third Turbomachinery Symposium, 1994; [9](#), [11](#)
- [3] J. C. Nicholas, *Lund's tilting pad journal bearing pad assembly method* , Transactions of the ASME, 448 / Vol. 125, October 2003; [15](#)
- [4] T. Dimond , A. Younan , P. Allaire *A Review of Tilting Pad Bearing Theory* , Hindawi Publishing Corporation, International Journal of Rotating Machinery Volume 2011; [18](#)
- [5] Knight, J. D., and Barrett, L. E., 1988, *textit*Analysis of tilting pad journal bearings with heat transfer effects, *Journal of Tribology*, 110(1), pp. 128-133; [19](#)
- [6] Gomiciaga, R., and Keogh, P. S., 1999, *Orbit Induced Journal Temperature Variation in Hydrodynamic Bearings*, *Journal of Tribology*, 121, pp; [19](#)
- [7] Monmousseau, P., Fillon, M., and Frene, J., 1998, *Transient thermoelastohydrodynamic study of tilting-pad journal bearings under dynamic loading*, *Journal of Engineering for Gas Turbines and Power*, 120, pp. 405-409; [20](#)

- [8] Monmousseau, P., and Fillon, M., 1999, *Frequency effects on the TEHD behaviour of a tilting-pad journal bearing under dynamic loading*, ASME Journal of Tribology, 121, pp. 321-326; [20](#)
- [9] Ettles, C. M. M., 1980, *The analysis and performance of pivoted pad journal bearings considering thermal and elastic effects*, Journal of Lubrication Technology, 102(2), pp. 182-192; [20](#)
- [10] Brockwell, K., Kelinbub, D., and Dmochowski, W., 1990, *Measurement and calculation of the dynamic operating characteristics of the five shoe, tilting pad journal bearing*, Tribology Transactions, 33(4), pp. 481-492; [20](#)
- [11] Constantinescu, V. N., 1967, *On the pressure equation for turbulent lubrication*, in Proceedings of the Conference on Lubrication and Wear, 182-183, pp. 132-134, IMechE, London, UK, 1967; [20](#)
- [12] Q. Chang, P. Yang, Y. Meng, S. Wen, *Thermoelastohydrodynamic analysis of the static performance of tilting-pad journal bearings with the Newton-Raphson method*, Tribology International 35 (2002) 225-234; [VI](#), [20](#), [21](#)
- [13] Brugier, D., and Pascal, M. T., 1989, *Influence of elastic deformations of turbo-generator tilting pad bearings on the static behavior and on the dynamic coefficients in different designs*, Journal of Tribology, 111(2), pp. 364-371; [21](#)
- [14] Kim, J., Palazzolo, A., and Gadangi, R., 1995, *Dynamic Characteristics of TEHD Tilt Pad Journal Bearing Simulation Including Multiple Mode Pad Flexibility Model*, J. Vib. Acoust., 117, pp. 123-135; [22](#)
- [15] H. Hashimoto, S. Wada, T. Marukawa, *Performance characteristics of large scale tilting pad journal bearings*, Bulletin of JSME, Vol.28, No. 242, August 1985; [VI](#), [22](#)

- [16] J. C. Nicholas, K. D. Wygant , *Tilting Pad Journal Bearing Pivot Design for High Load Applications* , Proc. No. 24 Turbomachinery Symposium, Houston, TX, pp. 33-47, 1995; [23](#)
- [17] Monmousseau, P., and Fillon, M., 2000, *Transient thermoelastohydrodynamic analysis for safe operating conditions of a tilting pad journal bearing during start-up*, *Tribology International*, 33(3-4), pp. 225-231; [23](#)
- [18] Kirk, R. G., Reedy, S. W., 1988, *Evaluation of Pivot Stiffness for Typical Tilting-Pad Journal Bearing Designs*, *ASME. J. Vib., Acoust., Stress, and Reliab*, 110(2), pp.165-171; [23](#)
- [19] Suh, J., and Palazzolo, A., 2015, *Three-Dimensional Dynamic Model of TEHD Tilting-Pad Journal Bearing-Part I: Theoretical Modeling*, *J. Tribol.* 137(4); [VI, 24, 185](#)
- [20] COMSOL Multiphysics 4.4 , *Reference Manual*; [40, 87, 141](#)
- [21] E. Funaioli , A. Maggiore , U. Meneghetti *Meccanica Applicata alle Macchine* , Patron Editore, 1987; [44](#)
- [22] B. T. Kulakowski, J. F. Gardner, J. L. Shearer, *Dynamic Modeling and Control of Engineering Systems*, Cambridge University Press, 2007, Cambridge Books Online; [67](#)
- [23] R. Ashino, M. Nagase, R. Vaillancourt, *Behind and Beyond the MATLAB ODE suite* , *Computers & Mathematics with Applications* Volume 40, Issues 45, August-September 2000; [79](#)
- [24] L. F. Shampine, M. W. Reichelt, *The MATLAB ODE suite* , *SIAM J. Sci. Comput.*, 18(1), 1997, pp. 1-22; [80](#)
- [25] L. T. Yang, R. P. Brent, *The improved BiCGStab method for large and sparse unsymmetric linear systems on parallel distributed memory architectures* , *Proceedings of the Fifth International Conference on Algorithms and Architectures for Parallel Processing (IEEE)*; [81, 82](#)

- [26] COMSOL Multiphysics 4.4 , *Structural Mechanics Module Users Guide*; [86](#)
- [27] S. Bellavia, M. Macconi, S. Pieraccini, *Constrained dogleg methods for nonlinear systems with simple bounds*, Springer, COMPUTATIONAL OPTIMIZATION AND APPLICATIONS, 53-3, 2012. [101](#)
- [28] D. Knežević, V. Savić, *Mathematical modeling of changing of dynamic viscosity, as a function of temperature and pressure, of mineral oils for hydraulic systems*, Mechanical Engineering Vol. 4, NÂ°1, 2006, pp. 27-34; [109](#)
- [29] COMSOL Multiphysics 4.4, *Heat Transfer Module Users Guide*; [116](#)
- [30] COMSOL Multiphysics 4.4, *Modeling Guide*; [132](#)
- [31] Nuovo Pignone General Electric SpA, *Technical note: 3BCL1010 mechanical running test, SOS0406484.*, Internal report of GE, 2014; [153](#)
- [32] 2005, API STD 684, *Rotordynamic Tutorial: Lateral Critical Speeds, Unbalance Response, Stability, Train Torsionals, and Rotor Balancing*, Second Edition, STANDARD by American Petroleum Institute; [154](#), [156](#)
- [33] Fillon, M., Bligoud, J. C., and Frene, J., 1992, *Experimental study of tilting-pad journal bearings comparison with theoretical thermoelastohydrodynamic results*, J. Tribol. 114(3), pp. 579-587; [XI](#), [178](#), [180](#), [181](#), [187](#)
- [34] San Andrés, L., and Li, Y., 2015, *Effect of Pad Flexibility on the Performance of Tilting Pad Journal Bearings: Benchmarking a Predictive Model*, Proceedings of the ASME Turbo Expo 2015: Turbine Technical Conference and Exposition, Montreal, Quebec, Canada, June 15-19, 2015;
- [35] B. J. Hamrock , *Fundamentals of Fluid Film Lubrication*, Mc-Graw-Hill-International Editions; [186](#)

- [36] Balbahadur, A.C., and Kirk, R.G., 2002, *textitPart I-Theoretical Model for a Synchronous Thermal Instability Operating in Overhung Rotors*, Proceedings of IFTOMM, Sixth International Conference on Rotor Dynamics, Sydney, Australia;
- [37] Conti, R., Frilli, A., Galardi, E., Meli, E., Nocciolini, D., Pugi, L., Rindi, A., and Rossin, S., 2015, *An efficient quasi-three-dimensional model of Tilting Pad Journal Bearing for turbomachinery applications*, Journal of Vibration and Acoustics, VIB-14-1434;
- [38] Conti, R., Frilli, A., Galardi, E., Meli, E., Nocciolini, D., Pugi, L., Rindi, A., and Rossin, S., 2015, *Efficient models of 3D Tilting Pad Journal Bearings for the study of the interactions between rotor and lubricant supply plant*, Journal of Computational and Nonlinear Dynamics (CND), pp. 1-16, CND-14-1228;
- [39] De Jongh, F. M., and Morton, P. G., 1994, *The Synchronous Instability of a Compressor Rotor Due to Bearing Journal Differential Heating*, ASME 1994 International Gas Turbine and Aeroengine Congress and Exposition;
- [40] C. Bonacina, A. Cavallini, L. Mattarolo, *Trasmissione del Calore*, CLEUP, Padova, 1992;
- [41] M.N. Ozisik, *Heat Conduction*, J. Wiley, Inc, Second Edition, 1993;
- [42] Y.A. Cengel, *Termodinamica e Trasmissione del Calore*, Mc Graw-Hill, 1998;
- [43] Friswell, M.I., Penny, J.E.T., Garvey, S.D., and Lees, A.W., 2010, *Dynamics of Rotating Machines*, Cambridge University Press, Cambridge, UK;
- [44] Murphy, B.T., and Lorenz, J.A., 2010, *Simplified Morton Effect Analysis for Synchronous Spiral Instability*, Journal of Vibration and Acoustics, 132;
- [45] Rao, J. S., 1983, *Instability of Rotors in Fluid Film Bearings*, J. Vib. Acoust. 105, pp. 274-279;
- [46] Genta, G., 1993, *Vibration of Structures and Machines-Practical Aspects*, Springer-Verlag, New York, NY, USA;



- [47] *Modular Tilting Pad Thrust Bearings*, Waukesha Bearings Brochure, [www.waukbearings.com](http://www.waukbearings.com);
- [48] G. Genta , *Vibration Dynamics and Control* , Springer;
- [49] O. Reynolds , *On the Theory of Lubrication and its Application to Mr. B. Tower's Experiments* , Philosophical Transactions of Royal Society of London, Vol. 177, Pt. 1, 1886, pp. 157-234;
- [50] G. W. Stachowiak, A. W. Batchelor , *Engineering Tribology Book* , Butterworth-Heinemann;
- [51] M. Mikami, M. Kumagai, S. Uno, H. Hashimoto , *Static and Dynamic Characteristics of Rolling-Pad Journal Bearings in Super-Laminar Flow Regime* , Transactions ASME, Journal of Tribology, Vol. 110, 1988, pp. 73-79;
- [52] D. Markin, D. M. C. McCarthy, S. B. Glavatskih , *A FEM Approach to Simulation of Tilting-Pad Thrust Bearing Assemblies* , Tribology International, Vol. 36, 2002, pp. 807-814;
- [53] S. B. Glavatskih, M. Fillon, R. Larsson , *The Significance of Oil Thermal Properties on the Performance of a Tilting-Pad Thrust Bearing* , Journal of Tribology, Vol. 124, 2002, pp. 377-385;
- [54] T. Almqvist, S. B. Glavatskih, R. Larsson , *THD Analysis of Tilting Pad Thrust Bearing Comparison Between Theory and Experiments* , Journal of Tribology, Vol. 122, 2000;
- [55] E. Storteig, M White , *Dynamic Characteristics of Hydrodynamically Lubricated Fixed-Pad-Thrust Bearings* , Wear, Vol. 232, pp. 250-255, 1999;
- [56] Rotech Engineering Services , *Tilting Pad Journal Bearings: Principles of Operation* , [http://www.rotechconsulting.com/bearings\\_sub2.htm](http://www.rotechconsulting.com/bearings_sub2.htm), Delmont, PA, 2007;

- [57] K. Ikeda, T. Hirano, T. Yamashita, M. Mikami, H. Sakakida , *An Experimental Study of Static and Dynamic Characteristics of a 580 mm (22.8 in.) Direct Lubrication Tilting Pad Journal Bearing* , ASME/STLE International Joint Tribology Conference, Long Beach, California, USA, Paper No. TRIB2004-64064;
- [58] M. Cha, P. Isaksson, S. Glavatskih, *Influence of pad compliance on nonlinear dynamic characteristics of tilting pad journal bearings* , Tribology International 57, 2013;
- [59] Y. Hou, T. Lai, S. Chen, B. Ma, J. Liu, *Numerical analysis on the static performance of tilting pad journal gas bearing in subsystems* , Tribology International 61, 2013;
- [60] K. Sim, D. Kim, , *Thermohydrodynamic Analysis of Compliant Flexure Pivot Tilting Pad Gas Bearings* , transactions of the ASME, 032502-2 / Vol. 130, MAY 2008;
- [61] A. Cerda Varela, I. Ferreira Santos, *Stability Analysis of an Industrial Gas Compressor Supported by Tilting-Pad Bearings Under Different Lubrication Regimes* , Journal of Engineering for Gas Turbines and Power FEBRUARY 2012, Vol. 134 / 022504-1;
- [62] Z. Yan, L. Wang, G. Qiao, T. Zheng, *An analytical model for complete dynamical coefficients of a tilting-pad journal bearing* , Tribology International 43 (2010) 7-15;
- [63] Y. Lihua, L. Huiguang, Y. Lie, , *Dynamic stiffness and damping coefficients of aerodynamic tilting-pad journal bearings* , Tribology International 40 (2007) 13991410;
- [64] M. He, C. hunter Cloud, J. M. Byrne, *Fundamentals of fluid film journal bearing operation and modelling* , Proceedings of the Thirty-Fourth Turbomachinery Symposium, Turbomachinery Laboratory, Texas A&M University, College Station, Texas, 2005;
- [65] I. Abu-Mahfouz, M. L. Adams, *Numerical Study of Some Nonlinear Dynamics of a Rotor Supported on a Three-Pad Tilting Pad Journal Bearing* , Transactions of the ASME, 262 / Vol. 127, JUNE 2005;
- [66] Y. Tao, L. San Andrés, *A novel computational model for tilting pad journal bearings with soft pivot stiffness* , 32nd Turbomachinery Research Consortium Meeting, May 2012;

- [67] A. M. El-Butch, N. M. Ashour, *Transient analysis of misaligned elastic tilting pad journal bearing*, Tribology International 38 (2005) 41-48;
- [68] L. Ma, X. Zhang, *Numerical simulation of nonlinear oil film forces of tilting pad guide bearing in large hydro unit*, International Journal of Rotating Machinery 2000, Vol. 6, No. 5;
- [69] J. Chen, L. Curfman McInnes, H. Zhang, *Analysis and practical use of Flexible BiCGStab*, Preprint ANL/MCS-P3039-0912, Argonne National Laboratory, 2012;
- [70] G. Qiao, L. Wang, T. Zheng, *Linear stability analysis of a tilting pad journal bearing system*, Transactions of the ASME, 348 / Vol. 129, April 2007;
- [71] Lund, J. W., 1964, *Spring and Damping Coefficients for the Tilting Pad Journal Bearing*, ASLE Transactions, 42(4), pp. 342-352;
- [72] A. Zhu, Y. Yang, H. Xiao, W. Chen, *Swing characteristic of pads in four pad tilting pad bearing*, 2013, IEEE;
- [73] J. Schmied, A. Fedorov, B. S. Grigoriev, *Non synchronous tilting pad bearing characteristics*, Proceedings of the 8<sup>th</sup> IFToMM International Conference on Rotordynamics, September 2010, KIST, Seoul, Korea;
- [74] R. Eling, R. van Ostayen, D. Rixen, *Dynamics of rotors on hydrodynamic bearings*, Excerpt from the Proceedings of the 2013 COMSOL Conference in Rotterdam;
- [75] J. Ying, Y. Jiao, Z. Chen, *Nonlinear dynamic analysis of tilting pad journal bearing-rotor system*, Shock and Vibration 18 (2011) 45-52, IOS Press;
- [76] G. Shenoy, B. S. Shenoy, R. C. Thiagarajan, *Effects of structural forces on the dynamic performance of high speed rotating impellers*, Excerpt from the Proceedings of the 2012 COMSOL Conference in Bangalore;